PACIFIC EARTHQUAKE ENGINEERING RESEARCH CENTER

Fragility Basis for California Highway Overpass Bridge Seismic Decision Making

Kevin R. Mackie
and
Božidar Stojadinović

Department of Civil and Environmental Engineering
University of California, Berkeley

Fragility Basis for California Highway Overpass Bridge Seismic Decision Making

Kevin R. Mackie

Department of Civil and Environmental Engineering
University of California, Berkeley

Božidar Stojadinović

Department of Civil and Environmental Engineering
University of California, Berkeley

ABSTRACT

The seismic loss modeling of transportation networks is a multifaceted procedure for calculating monetary losses due to damage to the transportation links in an earthquake. This report focuses on providing a rational method to evaluate damage potential and to assess probable highway bridge losses for critical decision making regarding the post-earthquake safety and repair of a highway network. Loss fragilities were defined for each individual bridge using PEER's performance-based earthquake engineering framework. Decision variables were related to earthquake intensity through a series of disaggregated models (demand, damage, and loss). The fragilities provided in this report are intended for application in two ways. First, bridge designers may use them to investigate how variation of bridge design parameters is reflected in the amount of expected losses after an earthquake. Second, highway network planners may use bridge fragilities to more reliably evaluate the losses in a highway transportation network.

In the process of developing bridge fragilities, intensity measures were first coupled with engineering demand parameters to formulate probabilistic demand models. Two damage models were then formulated. Component damage models utilized experimental data to predict response levels at which observable damage states were reached. System damage models utilized finite element reliability analysis to predict the loss of lateral and vertical load-carrying capacity. Improved methods for computing system damage were introduced. Last, two loss models were formulated. Component damage states were described in terms of repair costs of returning bridges to full functionality. System load-loss states were described in terms of bridge traffic capacity and collapse prevention. System loss fragilities were enhanced using the same improved methods developed for damage models.

ACKNOWLEDGMENTS

CONTENTS

LIST OF FIGURES

LIST OF TABLES

LIST OF SYMBOLS

The following symbols or acronyms are used in this report.

a Demand model scalar (linear space)

A Demand model scalar (log space)

A_f Demand fragility surface coefficient

B, b Demand model slope

B_f Demand fragility surface coefficient

c_{dm} Damage model scalar (linear space)

C_{dm} Damage model scalar (log space)

C_f Demand fragility surface coefficient

df Statistical degrees of freedom

D Strong motion duration (sec)

D_c Column diameter (single bent)

D_{c1} Column diameter of left column (where appropriate)

D_{c2} Column diameter of right column (2 bent bridge) or middle column (3 bent)

D_{c3} Column diameter of right column (3 bent bridge)

D_{dm}, d_{dm} Damage model slope

D_f Total ground motion record duration

D_s Superstructure depth

DM Damage measure

DV Decision variable

e_{lm} Loss model scalar (linear scale)

E, E_f Young's modulus

EDP Engineering demand parameter

E_{lm} Loss model scalar (log scale)

f'_c Concrete 28 day unconfined compressive strength

f'_{cc} Maximum confined concrete compressive strength

F_{lm}, f_{lm} Loss model slope

f_y Steel reinforcement yield stress

G	Shear modulus
H	Column height above grade (single bent)
H_1	Column height above grade of left column (where appropriate)
H_2	Column height above grade of right column (2 bent) or middle (3 bent)
H_3	Column height above grade of right column (3 bent)
IM	Intensity measure
k	Stiffness (with subscript), or slope of hazard curve
k_{bb}	Euler buckling constant
K_{soil}	USGS soil group below grade of columns
L	Span length (single bent)
L_1	Span length of left span (where appropriate)
L_2	Span length of middle span (2 bent) or 2nd span from the left (3 bent)
L_3	Span length of 2nd span from right (3 bent)
LM	Large magnitude
LR	Large distance
LS	Limit state
m	Mass
M_{max}	Maximum column moment (k-in)
M_w	Moment magnitude
N	Column axial force, or uncorrected soil blow-counts
N_{60}, $N_{1,60}$	Corrected soil blow-counts
PDM	Probabilistic damage model
PLM	Probabilistic loss model
$PSDM$	Probabilistic seismic demand model
P_s	Column shear strength
p_{ult}	Ultimate bearing capacity of soil
R	Closest distance (km)
$Sa(T_1)$	1st mode spectral acceleration, 5% viscous damping
$Sd(T_1)$	1st mode spectral displacement, 5% viscous damping
$Sv(T_1)$	1st mode spectral velocity, 5% viscous damping
SM	Small magnitude
SR	Small distance

T_D	Strong motion duration (sec)
T_1	1st mode bridge period
T_2	2nd mode bridge period
u_y	Yield displacement
V_b	Column base-shear (k)
V_{max}	Maximum column shear force (k)
Wt	Additional dead weight of the superstructure (%)
x	Design parameter value
$\hat{\alpha}$	Uncorrelated reliability importance measure
$\tilde{\alpha}$	Normalized, uncorrelated reliability importance measure
α_h	SDOF oscillator hardening ratio
β_1, β_2	Coefficients for demand fragility surfaces
γ	Effective weight of soil (force/volume)
$\hat{\gamma}$	Reliability importance measure taking into account correlation
Δ	Drift ratio
Δ_L	Drift ratio of left column (where appropriate)
Δ_M	Drift ratio of middle column (3 bent)
Δ_R	Drift ratio of right column (where appropriate)
ε	Error term in mathematical model
$\varepsilon_{concrete}$	Concrete strain
ε_{steel}	Steel strain
ζ	Coefficient of viscous damping
θ	Limit-state function parameter
λ	Annual frequency of exceedance
μ_Δ	Displacement ductility
μ_ϕ	Curvature ductility
v	Mean rate of occurrence
$\rho_{s,long.}$	Steel longitudinal reinforcement ratio (%)
$\rho_{s,trans.}$	Steel transverse reinforcement ratio (%)
σ	PSDM dispersion (randomness only)
$\sigma_{concrete}$	Stress in concrete fiber

$\sigma_{DM|EDP}$	PDM dispersion (randomness only)
$\sigma_{DV|DM}$	PLM dispersion (randomness only)
$\sigma_{EDP|IM}$	PSDM dispersion (randomness only)
σ_{PDM}	PDM dispersion (epistemic only)
σ_{PLM}	PLM dispersion (epistemic only)
σ_{PSDM}	PSDM dispersion (epistemic only)
$\sigma_{T,PDM}$	PDM total dispersion (randomness and epistemic)
$\sigma_{T,PLM}$	PLM total dispersion (randomness and epistemic)
$\sigma_{T,PSDM}$	PSDM total dispersion (randomness and epistemic)
σ_{steel}	Stress in steel fiber
ϕ'	Angle of internal soil friction (degrees)
ϕ_y	Yield curvature

1 Introduction

1.1 DECISION MAKING FOR HIGHWAY BRIDGES

Most decision criteria ultimately assume a monetary decision-making form, even when they include a measure of the loss of life. Therefore, the terms "cost," and "cost due to loss" are used throughout this decision-making discussion. For the case of reinforced-concrete highway overpass bridges in California, there are two principal lines of development that contribute to economic-based decision making. The total expected loss after an earthquake includes not only the cost associated with damage to the structure itself (direct losses), but also the cost associated with the loss of function (indirect losses). Functional loss is particularly relevant in the case of a highway network system because the indirect losses to an urban area might greatly exceed the direct losses. Therefore, in this report, loss is defined as decision making based on cost and loss of function. The actual costs due to the loss of function are not presented here; they are the subjects of transportation network simulations.

Large-scale simulations on urban regions and transportation networks have been the focus of numerous projects, such as HAZUS (HAZUS 1997), REDARS (Werner 2000), and associated PEER highway demonstration research (Moore 2000). The goal of such simulations is to provide an economic impact analysis of damage to a transportation system in an extreme event, such as an earthquake, on an urban area. The economic impact can be defined in terms of damaged and failed links in the transportation network and link costs associated with traffic flow. Identification of critical paths is an important part of post-earthquake emergency response. Economic impact is also defined explicitly in terms of monetary losses. Direct losses to the region include damage to components (bridges) as well as time delays in the damaged network. Indirect losses are due to the interruption of goods and services to those businesses affected by the earthquake.

Highway network risk assessment is performed as a decision-making aid in both the pre-earthquake and post-earthquake settings to make better-informed decisions on the allocation of resources for retrofit, design, and the improved redundancy of a network. Similarly, post-earthquake repair and capacity management are improved by the outcome of network analysis. Bridges can be considered as the critical links in a highway network that are vulnerable to earthquake hazard both in terms of ground shaking and ground deformation. Inputs into such simulations are bridge-level assessments of repair and loss of function. This study focuses solely on individual bridges in the network and on methods for improving the prediction of direct and indirect costs due to damage and loss of function to such bridges treated individually.

As applied to individual highway bridges, there are two categories of decision criteria. First, a bridge functional decision criterion may be defined as the post-earthquake operational state of the bridge. This implies a graded system of performance objectives involving lane closures, reduction in traffic volume, or complete bridge closure that is useful for traffic network modeling. The loss of function can be assessed directly after an earthquake as well as at several stages of repair in the aftermath of the quake. This return to functionality over time plays an important role in the highway network simulations. Second, a bridge repair decision criterion is the time (cost) of bridge repair and restoration. This decision variable is triggered only if the bridge function decision criterion crosses the repair threshold. Therefore, the total cost (due to an individual bridge in the network) for a given earthquake scenario is the sum of the indirect (or operational) costs from the loss of function, and the direct costs to restore previous functionality.

Given the need to assess both the direct and indirect losses to a highway network, and therefore individual bridges in that network, it follows that two parallel lines of development are necessary for applying a performance-based methodology to earthquake engineering of highway bridges. In this report, cases are formulated and presented in this report for each of these lines of development. The first case demonstrates bridge component-level decision making (distinctly different from bridges as components in a network setting), and is therefore applicable to decisions regarding direct losses. The second case demonstrates bridge-level decision making, and is therefore applicable to indirect loss assessment (at the individual bridge level) and decision making. The framework presented provides the background for probabilistic assessments that will be used in larger-scale (i.e., network) loss estimation research in the future. Consequently, no transportation network calibration of the individual loss models (direct and indirect costs) was made in this study.

In the evolving world of performance-based earthquake engineering, engineers are transitioning away from development of deterministic design criteria for site-specific seismic hazard. Describing the resulting structural performance as safe or unsafe is misleading when considering the uncertainty inherent in not only the seismic hazard, but also in structural capacity and function. Therefore, current seismic performance assessment methodologies are tending toward fragility curves as a means of describing the fragility of structures, such as highway bridges, under uncertain input. Fragility curves describe probabilities of exceeding design or performance criteria at different levels of seismic input intensity. These are particularly useful when applied to highway bridges because in a transportation network setting, numerous bridges of the same class may exist in a spatially distributed network with differing expected seismic hazard.

The formulation of bridge fragility curves, sometimes termed vulnerability curves, has historically transitioned from empirical to analytical methods. The development of empirical fragility curves was motivated by the reconnaissance data obtained from, in particular, two recent urban earthquakes, namely the 1994 Northridge and 1995 Hyogo-ken Nanbu events. Basöz and Kiremidjian developed fragility curves (Basöz 1997, 1999a) for different observed damage states from the Northridge (and Loma Prieta) data. Yamazaki developed similar curves using the Kobe event (Yamazaki 1998). Experimental fragility curves suffer from numerous pitfalls, including lack of sample points for all damage states, subjective or unverifiable definitions of damage states, and lack of correlation with bridge geometry and structural properties. However, they have been useful in providing a basic form for highway bridge fragilities and motivating analytical fragility work.

A large array of analytical bridge fragility studies has been undertaken. For example, Mander and Basöz (Basöz 1999b) developed a theoretical approach to developing fragility curves for HAZUS, compatible with categories of bridges from the National Bridge Inventory (NBI) and new proposed subcategories by Basöz (1996). A capacity spectrum method was the basis for these curves, with capacity derived from previous experimental and analytical work. These curves, and associated repair cost information, were compared with the Northridge empirical data. Karim and Yamazaki used simplified analysis and finite element techniques to develop analytical curves that were subsequently compared to the Kobe data (Karim 2001). This study incorporated the use of ground motion time histories in the demand simulation, but made use of ductility and hysteretic energy-based damage states. Elnashai compared Northridge and

Kobe empirical curves to a more rigorous analytical method for reinforced concrete highway bridges (Elnashai 2003). Uncertainty in the ground motions and structural components was included; however, damage was still defined in terms of deformation-based demand quantities.

Analytical work is, for the most part, based on mimicking the damage states obtained from empirical studies. Previous analytical work has neither consistently addressed the uncertainty in both the demand and capacity sides of the problem, nor extended the fragility concept to the decision or loss level. A rigorous probabilistic study by Gardoni (2002) introduced reliability into the prediction of reinforced concrete bridge fragility by updating traditional deterministic predictions of capacity and demand using a Bayesian approach. Sample fragility curves were generated for the one- and two-bent reinforced concrete highway bridges used in this study. Shear and deformation failure limit states were considered for univariate fragility curves, as well as for failure of these limit states in series. The demand was determined from inelastic spectra using variations on multiple degree-of-freedom nonlinear pushover analyses.

Another method of presenting performance-based results is the hazard curve. However, derivation of hazard curves requires site-specific hazard and is therefore not applicable to all bridges in a spatially distributed highway network. Therefore, the remainder of this report will focus primarily on the development of bridge fragility curves. The ultimate goal of a highway bridge decision-making procedure then becomes the generation of the conditional probability of exceeding a loss measure (or decision variable), given the earthquake intensity. Such fragilities may subsequently be utilized by others to make better-informed decisions regarding network loss modeling and loss estimation.

1.2 PEER DECISION-MAKING FRAMEWORK

Recent developments in the design and analysis of structures under seismic loading have led away from traditional code-based, prescriptive design strategies and toward probabilistic strategies. Probabilistic methods allow for the definition of performance acceptance criteria under uncertain hazard levels. The Pacific Earthquake Engineering Research Center (PEER) developed a probabilistic framework for performance-based earthquake engineering (PBEE) in the effort to achieve a consistent reliability-based approach for seismic decision making. Performance objectives are defined in terms of annual frequencies of socio-economic decision

variables (*DV*s) being exceeded in the seismic hazard environment of the urban region and site under consideration. While a general probabilistic model directly relating *DV*s to measures describing the site seismicity is useful to owners, decision makers, and engineers alike, it is too complex to derive directly.

Instead, the PEER performance-based design and evaluation framework utilizes the Total Probability Theorem to disaggregate the problem (Cornell 2000) into several interim probabilistic models that address sources of randomness and uncertainty more rigorously. This disaggregation of the decision-making framework involves global or component damage measures (*DM > dm*), structural engineering demand parameters (*EDP > edp*), and seismic hazard intensity measures (*IM > im*). The limit-state probability of a *DV* related to a structure exceeding a limiting value, *dv*, for a single earthquake event is shown in Equation 1.1. The convention of probabilistic variable names in uppercase text and values of random variables in lowercase text is adopted throughout this report.

$$P(DV > dv) = \int_{dm} \int_{edp} \int_{im} G_{DV|DM}(dv \mid dm) \cdot \left| dG_{DM|EDP}(dm \mid edp) \right| \cdot \left| dG_{EDP|IM}(edp \mid im) \right| \cdot \left| dG_{IM}(im) \right| \tag{1.1}$$

If it is assumed that the arrival of earthquakes follows a Poisson process (with mean rate of occurrence ν), then the annual hazard (of an earthquake intensity *IM* exceeding a value *im*) is equal to $\lambda_{IM}(im) = \nu \cdot P(IM > im)$. However, due to the presence of non-renewing uncertainties in the structure, correlations between events prevent the writing of similar annual hazard relations for *EDP, DM,* and *DV*. The probability of exceeding a limit value *dv* at least once in a year is approximately equal to the mean annual frequency only under assumptions regarding the non-renewing nature of uncertainties (Der Kiureghian 2005). The annual probability approximation always yields a conservative value for conventional structures and is sufficiently accurate for smaller probability values (less than 0.01).

The commonly recognized form of PEER framing equation (Cornell 2000) is shown in Equation 1.2. The term $\lambda_{DV}(dv)$ is the mean annual frequency (MAF) of a *DV* exceeding a limiting value *dv*. This is a robust quantity because Equation 1.2 holds even in the presence of non-renewing uncertainties and non-Poisson renewal models. Therefore, the MAF is implied for the remainder of the report when discussing hazard.

$$\lambda_{DV}(dv) = \int_{dm} \int_{edp} \int_{im} G(dv \mid dm) \cdot \left| dG(dm \mid edp) \right| \cdot \left| dG(edp \mid im) \right| \cdot \left| d\lambda(im) \right| \tag{1.2}$$

The interim probabilistic models in Equations 1.1 and 1.2 are:

- *G(DV|DM)* is a loss or performance model, predicting the complementary cumulative distribution of a *DV* (such as repair cost or traffic capacity reduction), conditioned on a *DM*;

- *G(DM|EDP)* is a capacity or damage model, predicting the complementary cumulative distribution of a *DM* (such as amount of spalling or crack density), conditioned on an *EDP*;

- *G(EDP|IM)* is a demand model, predicting the complementary cumulative distribution of an *EDP* (such as drift ratio or steel rebar stress), conditioned on a seismic hazard *IM*; and

- *G(IM)* is a seismic hazard model, predicting the complementary cumulative distribution of a seismic hazard *IM* (such as peak ground acceleration) in a single earthquake event.

- *λ(IM)* is a seismic hazard model, predicting the MAF (of exceeding) of an *IM* in a particular seismic hazard environment.

The application of the total probability theorem in Equation 1.1 implies that the interim models are mutually exclusive and collectively exhaustive. The intermediate variables (*DM, EDP, IM*) are chosen so that probability conditioning is not carried over from one model to the next, known as "Markovian dependence" for stochastic processes. Additionally, the uncertainties over the full range of model variables are systematically addressed and propagated, making the selection of each interim model critical to the final outcome. Nevertheless, these independent models can be designed separately and used interchangeably, making it easier to develop a general performance-based framework for decision making (Mackie 2003). The disaggregated nature of the framework makes it applicable to a wide range of earthquake engineering problems, not just for highway bridges.

Disaggregation of the decision-making process is depicted in Figure 1.1 for the case of a highway overpass bridge. First, seismic hazards, evaluated using a regional hazard model, are expressed using *IM*s. A demand model, built for this class of bridges, is then used to correlate hazard *IM*s to structural *EDP*s for this bridge. Next, a damage model is used to relate structural *EDP*s to *DM*s. Finally, *DM*s are used to effect the loss in performance, evaluated in terms of *DV*s. Decision variables describe the performance of a typical overpass bridge after an earthquake in terms of its function in a regional traffic network. This includes reduction in load-carrying capacity and assessment of speed limits and traffic capacity, or duration of bridge closure and cost of bridge repair (Mackie 2003).
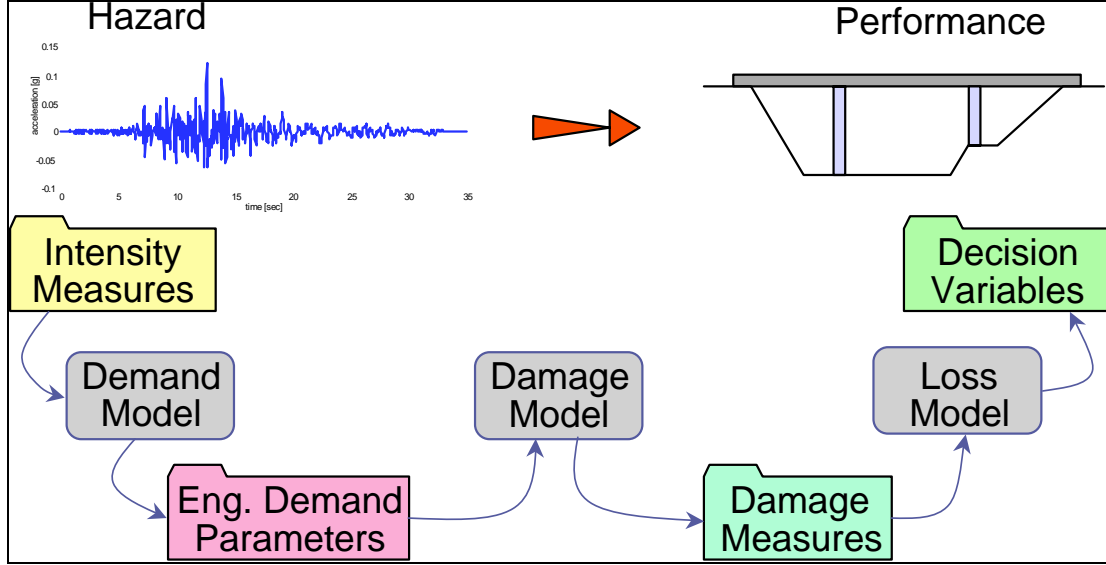
Fig. 1.1 PEER performance-based earthquake engineering framework

The results of a complete performance-based evaluation (Eq. 1.2) of an overpass bridge would be the mean annual frequencies of exceeding decision variable values. In addition, the site hazard need not necessarily be convolved with the loss models. The framing equation also predicts standard fragility curves. Fragility is defined as the conditional probability of exceeding a prescribed limit state, given a level of earthquake intensity. For each limit state, there is a unique cumulative distribution function (CDF) with ground motion intensity measure (*IM*) values on the horizontal axis as an outcome of fragility analysis. If decision variables are conditioned on the earthquake *IM*, the framing equation yields a standard loss- or decision-fragility curve (Eq. 1.3).

$$P(DV > dv \mid IM = im) = \int\limits_{edp} \int\limits_{dm} G_{DV|DM}(dv \mid dm) \cdot \left| dG_{DM|EDP}(dm \mid edp) \right| \cdot \left| dG_{EDP|IM}(edp \mid im) \right| \quad (1.3)$$

However, the power of the PEER framework lies in the ability to disaggregate the total process into interim models. Therefore, at each interim level (demand and damage), it is also possible to cast the framework in either an annual frequency or fragility format. The interim cumulative distribution functions (fragility curves) obtained are also useful for loss modeling and decision making of individual highway bridges.

1.2.1   Demand Model

Demand models are usually formulated using nonlinear dynamic finite-element simulations under multiple ground motions.   This does not preclude the demand models from being generated experimentally; however, the time cost associated with analysis is lower. Each ground motion can be described by one or more *IM*s.   These *IM*s are selected to provide unique characteristic information about the earthquake of interest. The response of a structure subjected to an earthquake motion, characterized by the descriptor *IM*, is designated an engineering demand parameter (*EDP*). In the case of highway overpass bridges, possible *EDP*s are grouped into three categories. Global *EDP*s describe overall bridge behavior, such as maximum column displacement, motion at the abutments, and residual displacements. Intermediate *EDP*s describe performance of bridge structural components, such as maximum column curvature, and shear force in the abutment shear tabs. Finally, local *EDP*s describe material level responses (stress and strain) anywhere of interest in the bridge.

The result of probabilistic seismic demand analysis (PSDA) is a probabilistic seismic demand model (PSDM). The PSDM is the mathematical model that relates *IM*s to *EDP*s. It is possible to use stripe analysis to find a probability distribution of *EDP*s for a single *IM* level. A stripe analysis involves scaling all ground motions to the same intensity level. Several stripe analyses together are termed an "incremental dynamic analysis" (IDA) (Vamvatsikos 2002). Alternatively, PSDA can be performed using a cloud approach.   The cloud describes the selection of earthquakes with variable *IM*s. Both methods can be used to determine the median (or mean) relationship between *EDP* and *IM*, and an associated measure of uncertainty. Parameters of the median relationship and the associated uncertainty completely define the PSDM.

1.2.2   Damage Model

Damage models can be obtained from a variety of sources.   The most common source is experimental tests of structural components, subassemblies, or systems. In this context, damage models are often termed "capacity models."   The response predicted by analytical demand models does not necessarily correlate to physical descriptions of damage, failure, and collapse. Therefore, observed, experimental, or analytical estimates of damage are often incorporated into

the PBEE formulation by determining capacity and damage induced at different levels of structural response. Response is described in terms of *EDP*s and damage in terms of damage measures (*DM*). *DM*s are usually discrete, such as observations of the onset of certain damage states. Examples of damage states of reinforced concrete columns include cracking, spalling, transverse reinforcement fracture, longitudinal reinforcement buckling, and failure. However, it is also possible to determine continuous *DM*s such as loss of lateral load-carrying capacity.

There are numerous sources of uncertainty in experimental results and subjective damage assessments; therefore, the capacity approach is sometimes performed analytically using finite element reliability analysis. This is particularly useful when considering bridge systems rather than individual components because little experimental data are available for large configurations or subassemblies. Reliability analysis also allows development of a mathematical model specifically for the bridge of concern, rather than interpolating between previous experimental geometry and material designs. Reliability analyses introduce epistemic uncertainties related to the finite element model used but may reduce the uncertainties inherent to experimental testing. The uncertainties captured by the two approaches should not necessarily be assumed equal.

Damage states are often individual discrete values, rather than continuous variables. Due to the discrete nature of most *DM*s, or the individual determination of *DM* limit states, it is often difficult to describe a median (or mean) *DM* relationship conditioned on *EDP*, as was done in the demand model case. There is no loss of generality in the method, however, as the damage assessment procedure invariably provides the probability of exceeding a limit state, given an *EDP* level. This CDF can be used without modification in the annual frequency or fragility formulations of Equations 1.2 and 1.3, respectively. In the case of a continuous *DM*, the mathematical model relating *EDP*s to *DM*s is sought. Parameters of the median relationship between *EDP* and *DM* and the associated uncertainty completely define the damage model.

1.2.3 Loss Model

Empirical and analytical sources of loss data for highway overpass bridges (needed to formulate a loss model) are sparse. Loss model, or alternatively decision model, data can be obtained from professional surveys and opinion, reconnaissance data from previous earthquakes, repair data from post-earthquake reconstruction, or inference of policy decisions. Sometimes these data

already exist but were not systematically applied for the purpose of loss estimation. Some loss model data may be obtainable from the research laboratory through repair of experimental specimens or from construction estimates using Means (RS Means 2004) catalogs. The decision criteria does not need to include repair cost or repair time, although previous research has focused largely on these. The return of a highway bridge to differing degrees of functionality in a highway network is also an important loss criterion. Functionality may be measured in terms of lateral load resistance in aftershocks, traffic volume, lane and speed reductions, or access to emergency vehicles.

As with probabilistic damage models, it may not be possible to describe a continuous relationship between *DM*s and *DV*s. This is compounded by the fact that both the *DM* and the *DV* may be discrete variables. Decision quantities are highly likely to be binary in nature. For example, highway bridges might be categorized as either open or closed. Therefore, loss models are often also in the form of probabilities of exceeding explicit discrete decision states given different *DM*s (CDFs). However, when both the *DM* and *DV* are chosen as continuous variables, the median relationship between *DM* and *DV* and the associated uncertainty completely define the loss model.

1.3   HIGHWAY BRIDGE CLASS

The Federal Highway Administration (FHWA) maintains a national bridge inventory (FHWA 2003). Highway bridges are classified according to material type and structure type. From the 2003 census of California bridges, 15670 (66%) bridges were constructed of either concrete or prestressed concrete. The structural types included slab, stringer/multi-beam or girder, box beam or girder, and culvert. A total of 10291 (43%) of the total are either box beam or girder or culvert type. Additionally, from highway network studies specifically on the San Francisco Bay Area (Moore 2000; Kiremidjian 2002), a total of 2640 bridges were further characterized by type, year built, number of spans, etc. Of this subset, 1415 (54%) were reinforced concrete box beam, girder, or culvert. The predominance of these bridge characteristics guided the selection of the bridge type investigated in this study.

Typical new reinforced concrete California highway overpass bridges were selected as the class of structures in this study. A class is defined by geometry, components, and methods of design. Ideally, each of these can be investigated in a parameter sensitivity study using the

resulting PSDMs. The bridges presented in this report were designed according to Caltrans' Seismic Design Criteria (Caltrans 1999) for reinforced concrete bridges. Consistent with the displacement-based design approach used by Caltrans for new bridges, it was assumed that reinforced concrete columns developed plastic hinges in flexure rather than experienced shear failure (Mackie 2003).

Structural configurations for bridges in this class are shown in Figure 1.2. Longitudinal variations include single-span, two-span, and three-span overpasses (including abutments) and stand-alone components of multi-span viaducts divided at expansion joints. In the transverse direction, typical California overpasses have single, two-column, or multi-column bents. Only single-column bents (in the transverse direction) were considered for all of the bridges in this study. At abutments and expansion joints these bridges have varying degrees of restraint.
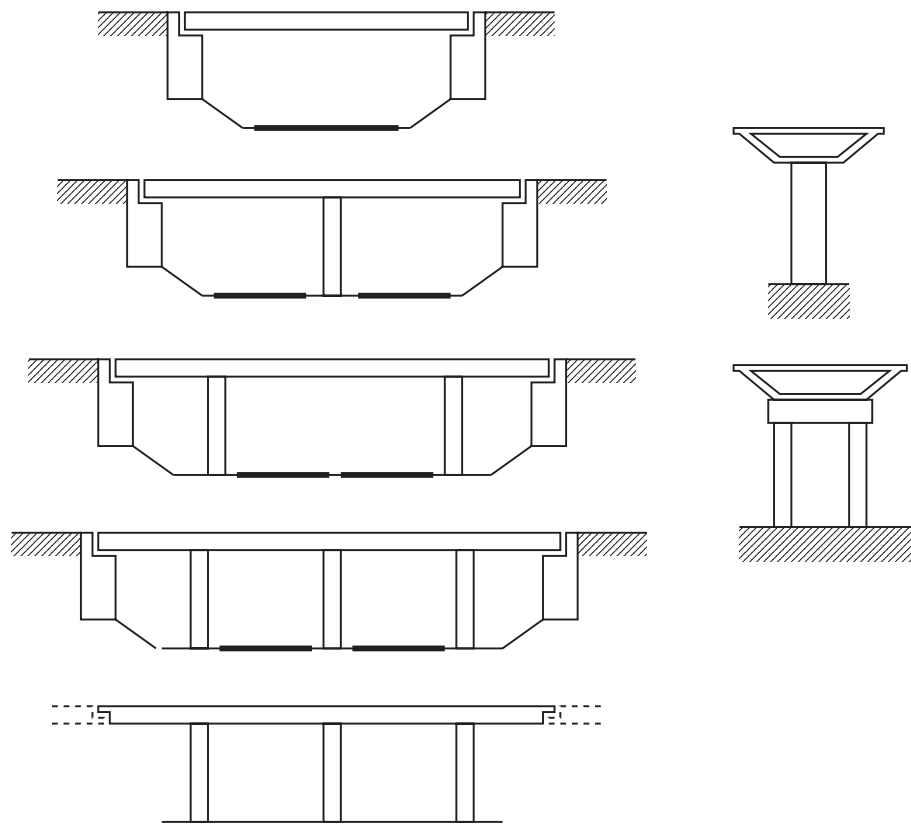
Fig. 1.2 Bridge longitudinal and transverse configurations

Common to all bridge types is a single-column bent with uniform circular cross section over the complete column height above grade, continuing into an integral Type I pile-shaft

11

foundation. All bridges are of reinforced concrete construction, including a continuous reinforced concrete box girder superstructure, as designed by Caltrans (Yashinsky 2000). All bridges in the class were seated on cohesionless sand sites with uniform soil profile properties. The water table was assumed to be below the base of the pile shafts.

Each individual bridge generated for analysis was not intended to correspond directly to any existing bridge design. Rather, a bridge portfolio was developed to represent a class of highway overpass bridges with varying designs. The portfolio would then cover a full range of bridge design possibilities. Starting from a realistic base bridge configuration, the suite of bridges was developed by varying certain design parameters. The spectrum of designs in the bridge portfolio was made possible by the parametric variation of these bridge design parameters, using acceptable engineering ranges for each. Each parameter was varied against the base configuration, not necessarily against all the other parameters. This limited the number of bridges analyzed to a scope acceptable for the rigorous amount of computations required (Mackie 2003). Details of the design strength of the base bridge configuration are contained in Section 2.1.

1.4   ORGANIZATION OF REPORT

The analytical bridge models developed for this study were common to all the PBEE models and their analysis methods. Therefore, they are detailed separately in Chapter 2. The subsequent chapters each address one of the interim models of the PEER decision-making formulation (Eq. 1.2). Consequently, each chapter stands alone as a useful engineering entity but also is integral when building up results in the overall PBEE format. The interim models are addressed in order moving from the right of Equation 1.2 to the left.

The probabilistic demand model is addressed in Chapter 3. This chapter focuses on the nuances of developing a large array of probabilistic seismic demand models for the highway bridges in this study. This includes choice of analysis methods, optimal choice of constituent variables, and sensitivity to different bridge design parameters. Development of a probabilistic damage, or capacity, model is addressed in Chapter 4. The damage models are formulated both analytically and based on results from thousands of experimental studies. These damage models are developed in parallel for the component and bridge level to address the need for direct and indirect losses, respectively. Chapter 5 introduces the specific loss models pertaining to highway

bridges. The decision variables in Chapter 5 are closely related to the two damage variable counterparts in Chapter 4.

Also discussed in each probabilistic model chapter is coupling with previous models to obtain more meaningful loss modeling results. Specifically, fragilities and hazard curves are generated at the end of each chapter. Finally, a general PBEE formulation is presented for the entire decision-making process in Chapter 6. This chapter includes examples with some simplifying assumptions and resulting descriptive equations. Conclusions, future work, and appendices wrap up the report.

2 Analytical Bridge Models

Bridge models were generated for each of the overpass configurations (Fig. 1.2) shown in the highway bridge class. Primary model development took place on single-column-per-bent, single-bent bridges for demand model generation. Such a bridge subclass was then used to further investigate damage and loss models. The single-bent model was subsequently extended to two- and three-bent bridges, but only to investigate demand model validity on different structures in the bridge class.

The PEER OpenSees (McKenna 2000; OpenSees) program was selected as the nonlinear finite element platform for all computational aspects of this study. Particular effort was made to accurately model the nonlinear behavior of all the bridge components contributing to seismic response. A more realistic bridge model allowed higher confidence in the response over other simplified models or analysis methods (elastic analysis, e.g.). Even though the benefits of using a more complex model were not evident in the medians of the demand models, a significant reduction of the modeling (epistemic) uncertainty was achieved. This was reflected directly in the reduction of total dispersions inherent to the demand models and the overall improvement in the confidence afforded by the computed fragility curves.

2.1 SINGLE-BENT BRIDGE

The OpenSees single-bent bridge model was derived from the same single-bent bridge used in previous PEER research (Mackie 2003). More detailed analytical and material model information is contained therein. Only a summary, including modifications for this study, is included here. A reduction in the number of design parameter variations performed was necessary to pursue damage and loss models. More in-depth treatment of design parameter variation in demand models is contained elsewhere (Mackie 2002b, 2003).

2.1.1 Design Parameters

Analyses were performed for nine different design parameters, detailed in Table 2.1 along with the ranges assigned to each of the parameters. Four equally spaced values of each parameter were chosen. The design parameters are shown graphically in Figure 2.1. The span length parameter (L) was applied directly to each of the equal spans. Column height above grade was then obtained from the span-to-column height ratio (L/H). As the span-to-column height ratio (L/H) was varied, the length (L) was held constant, thereby altering only the column height (H). Conversely, as L was varied, the L/H ratio remained constant, thereby making the L design parameter a measure of the overall size of the bridge, not just the span lengths (Mackie 2003).

Table 2.1 Design parameter variation for single-bent overpass bridge

Description	Parameter	Range
Span length	L	18–55 m (60–180 ft)
Span-to-column height ratio	L/H	1.2–3.5
Column-to-superstructure dimension ratio	D_c/D_s	0.67–1.33
Reinforcement nominal yield strength	f_y	470–655 MPa (68–95 ksi)
Concrete nominal strength	f'_c	20–55 MPa (3–8 ksi)
Longitudinal reinforcement ratio	$\rho_{s,long}$	1–4%
Transverse reinforcement ratio	$\rho_{s,trans}$	0.4–1.1%
Foundation soil internal friction angle	ϕ'	20, 27, 35, 42 (°)
Foundation soil dry unit weight	γ	16.5 kN/m^3 (105 pcf), 17.3 (100), 18.1 (115), 21.2 (135)
Additional bridge dead load	Wt	10–75% self-weight
Deck depth	D_s	1.5 m (5 ft)

The column-to-superstructure dimension ratio (D_c/D_s) was used to size the column, given a fixed superstructure deck depth detailed below. The ranges of this parameter were governed by the Caltrans SDC (Caltrans 1999). Material properties were varied for both concrete and reinforcing steel. Steel nominal yield strength (f_y) ranged from f_{ye} in the SDC document to higher values that can be expected for modern reinforcing steel. These steel properties were

applied to the column for both longitudinal ($\rho_{s,l}$) and transverse ($\rho_{s,t}$) reinforcement. The nominal unconfined concrete strength (f'_c) was varied between strengths universally available in modern construction practice.
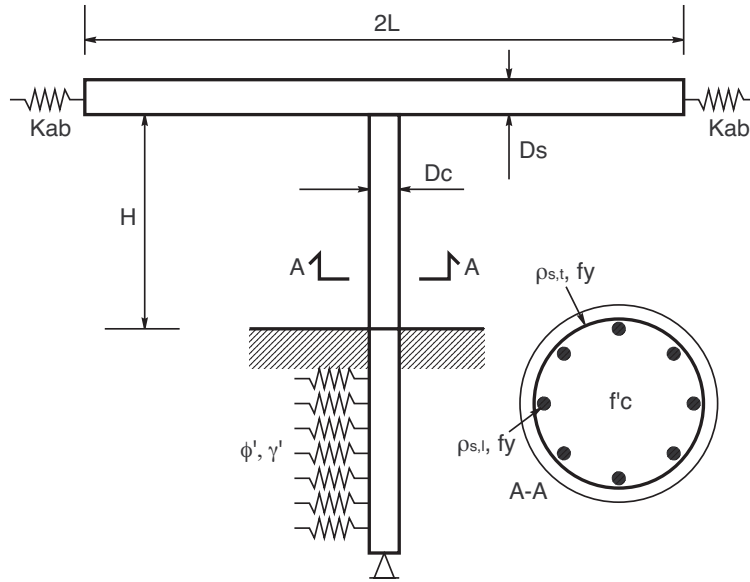
Fig. 2.1 Single-bent bridge design parameters

Different possible site conditions below grade were accounted for through the use of nonlinear soil *p-y* springs acting on the pile shafts. The properties of these springs were developed from values of the internal friction angle (ϕ') and the unit weight (γ') of the assumed continuous soil profile (see Section 2.1.3). The model soil property values were selected to correspond to values in the region of USGS soil groups A, B, C, and D, or their corresponding NEHRP soil groups B, C, D, and E. These soil groups are designated K_{soil} in the remainder of the report. It was not intended to perform a site-specific soil analysis, however, to provide the base of the column with some rotational and displacement flexibility. The flexibility provided more realistic global bridge behavior than did assuming a rigid foundation.

The final two design parameters considered were additional bridge dead load (*Wt*) and the deck depth (D_s). The dead load was applied in percentages of the existing bridge self-weight. The additional load increased the column axial load ratio, reported as a response quantity, and made the column more susceptible to nonlinear geometric effects. While the deck depth was not explicitly varied as a design parameter, it allowed control of the overall stiffness of the bridge

due to the relationship to the column diameter (through D_c/D_s). A value of 1.5 m (5 ft) was selected for all bridge realizations in this study.

A base bridge configuration was derived to simplify comparisons between design parameters. The single-bent base bridge configuration included two 18.3 m (60 ft) spans, a single-column bent 7.6 m high (25 ft), with a 1.6 m (5.25 ft) diameter circular column, 2% longitudinal reinforcement, and 0.7% transverse reinforcement. Roller boundary conditions were assumed for the abutments, and the soil below grade was assumed to have a friction angle of 37° and a unit weight of 18.1 kN/m^3 (115 pcf). The additional deadweight was assumed to be at 25% of the superstructure deadweight to amplify dynamics demands on the bridge. Only one design parameter was varied from the base configuration at a time.

The strength of the base bridge (in terms of the *R*-factor) was 2.1 and 3.9 in the longitudinal direction with respect to the averaged bin spectrum (R_{CS}) and the 2% in 50-year USGS spectrum (R_{USGS}), respectively (see Section 3.2 for definitions). The LMSR bin was selected for the R_{CS} factor, and the USGS spectrum was obtained for a site in Berkeley, California (see Section 6.1). The transverse *R*-factors were 1.5 and 3.6 for R_{CS} and R_{USGS}, respectively. For comparison, using the Caltrans hazard map (*PGA* of 0.6g for Berkeley, California) and ARS curves (Caltrans 1999), the longitudinal and transverse *R*-factors were 2.5 and 2.2, respectively.

A subset of the bridges was used in this study to evaluate such issues as the dependence of demand model efficiency on structural period. The bridges used, their design parameters, and lowest longitudinal and transverse periods are presented in Table 2.2. The periods designated with "pre" refer to the initial elastic periods, while those designated "post" refer to the elastic period after gravity load equilibrium. To be strictly accurate, there is only one fundamental period (the lowest period) per structure; however, the earthquake response of the structure is considered separately in the longitudinal and transverse directions. The mode shapes also exhibit deformation in each direction exclusively. Therefore, the lowest period corresponding to each of those directions is shown in Table 2.2. This notation is adopted, because the longitudinally dominated mode may be mode 1, 2, or 3 in the post–gravity-load analysis case. Post–gravity-load periods are listed only for the bridges utilized in Section 3.4.3.

Table 2.2 Single-bent bridge periods for sample bridge configurations

Structure number	Design parameter	$T_{1,long}$ pre	$T_{1,tran}$ pre	$T_{1,long}$ post	$T_{1,tran}$ post
0001	Base	1.40	1.57	1.45	2.09
0005	$L/H = 3.5$	1.15	1.31	1.19	2.03
0009	$L/H = 1.8$	1.76	1.94	1.82	2.20
0013	$L/H = 1.2$	2.54	2.74	2.64	2.94
0017	$D_c/D_s = 0.67$	1.63	1.77	1.69	2.18
0021	$D_c/D_s = 1.00$	0.98	1.23	1.03	1.98
0025	$D_c/D_s = 1.30$	0.76	1.08	0.78	1.58
0029	$\rho_{s,long} = 0.01$	1.46	1.62	-	-
0033	$\rho_{s,long} = 0.03$	1.36	1.53	-	-
0037	$\rho_{s,long} = 0.04$	1.31	1.50	-	-
0041	$L = 1080$ in.	2.38	2.74	-	-
0045	$L = 1440$ in.	3.57	4.20	-	-
0049	$L = 2160$ in.	6.64	8.01	-	-
0053	$Wt = 0.10$	1.32	1.47	-	-
0057	$Wt = 0.50$	1.53	1.72	-	-
0061	$Wt = 0.75$	1.66	1.85	-	-
0065	$K_{soil} = C$	1.56	1.73	-	-
0069	$K_{soil} = D$	1.75	1.92	-	-
0073	$K_{soil} = A$	1.27	1.44	-	-

2.1.2 Column and Deck

Reinforced, uniformly circular, concrete column cross sections were used throughout. The diameter of the columns was determined from the D_c/D_s design parameter. All columns had perimeter longitudinal reinforcement. Longitudinal bars were all #9 (1.128 in. diameter, 1.0 in.^{2} cross-sectional area), evenly spaced at a radius determined using 3.8 cm (1.5 in.) cover and the

diameter of transverse reinforcement. Transverse spiral reinforcement was used to confine the concrete, consisting of #6 bars (0.750 in. diameter, 0.44 in.^{2} cross-sectional area).

The columns were modeled in OpenSees using three-dimensional, fiber-discretized, nonlinear, beam-column elements (Neuenhofer 1998). Nonlinear geometry was addressed through inclusion of big P-Δ effects for the columns. Constitutive models used for concrete were based on the Kent-Scott-Park stress-strain relation (Kent 1971), as modeled in OpenSees. For this study, the maximum confined concrete stress was determined from the Mander confined concrete model (Mander 1988). The constitutive model used for the steel reinforcement was an elastic-plastic trilinear model with inclusion of the Bauschinger effect. The steel had initial stiffness E = 200000 MPa (29000 ksi), and post-yield hardening stiffness of 1.5% pre-yield stiffness, or 3 MPa (435 ksi). Including the Bauschinger effect gave a more realistic estimate of energy dissipation during cyclic loading. The Bauschinger steel model hardened until a strain of 0.08, after which it softened at a slope of 0.75% (of the elastic modulus) until it reached an ultimate fracture strain of 0.12. While this strain is higher than that prescribed by Caltrans (Caltrans 1999), modern steels can be expected to easily achieve such ultimate strain. Softening was required to achieve a degradation of global bridge strength after ultimate strength was reached and more closely mimics parabolic hardening (and softening) behavior.
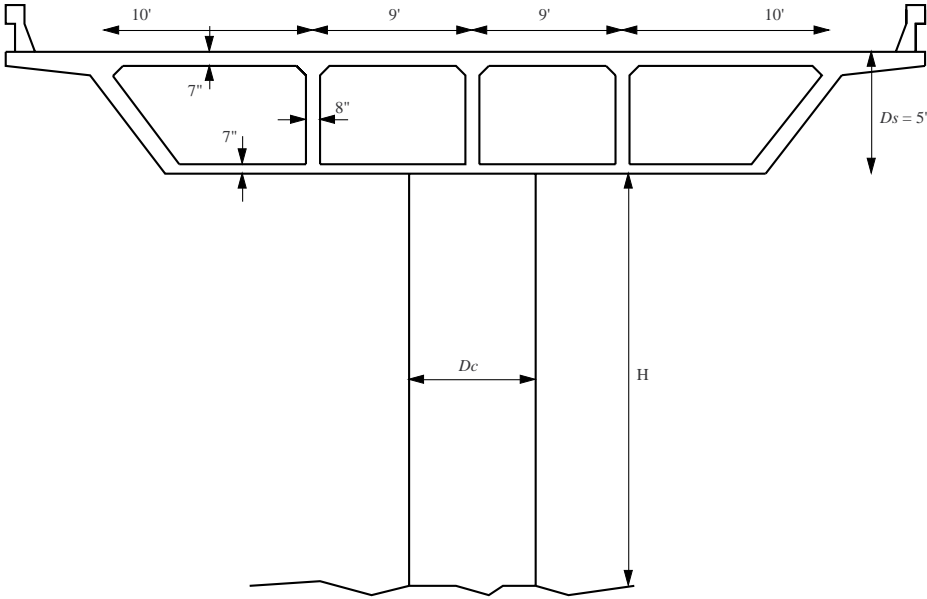
Fig. 2.2 Deck and column dimensions

Shear was included in the model of the column by aggregating a nonlinear shear force-shear strain relationship with each element. The bilinear relationship was defined by a shear strength and stiffness. Caltrans SDC (Caltrans 1999) shear equations for steel and concrete were utilized to determine the strength value. The stiffness was assumed equal to the initial shear modulus of concrete. As initially assumed for all bridges in the class, the shear capacity exceeds the shear demand; therefore, the specification of a shear constitutive relation was unnecessary for the earthquake intensity range employed.

The deck cross section utilized was of reinforced concrete box girder construction. A typical 3 lane (design traffic lane width 3.66 m), four-cell box girder was used, with a width of 10.9 m (36 ft) and a variable depth (D_s). See Figure 2.2 for dimensions. Each bridge deck node had six mass terms, three translational (masses) and three rotational (moment of inertias). The nonlinear deck was discretized into two elements per span with 4 integration points each and a distributed mass (mass/unit length) to achieve the same total mass. Rotational mass terms were lumped at the nodes. Steel reinforcement (the box girder was assumed not to be post-tensioned) was then placed both in the soffit and deck slabs.

2.1.3 Pile Shafts and Soil Springs

The Type I integral pile shafts (Caltrans 1999) used in this study featured a continuous amount of longitudinal reinforcement running through both the column and pile shaft. There was no increase in concrete cover below grade. Any lap splices and discontinuous longitudinal reinforcement were assumed to be located outside of the expected plastic hinge zones. In this configuration, the expected location of plastic hinging was at the column-deck connection and in the pile shaft below grade.

The plastic hinge assumptions were confirmed by plotting a typical maximum moment diagram over the height of the column and pile shaft (Fig. 2.3). The moment and curvature distributions were generated from a longitudinal pushover analysis of the base bridge configuration. The section forces and deformations were sampled at a column tip displacement of 76 cm (30 in., $\mu_\Delta \approx 5.5$) using distributed plasticity elements (the location of the plastic hinges was not assumed apriori). Plastic hinging was concentrated at the top of the column, whereas hinging was distributed below grade (spread-plasticity). The difference between moment values

at a constant curvature value was due to the increase in axial force on elements closer to the base of the pile shaft.

The pile-shaft cross section and reinforcement were identical to that of the column, as described above. Pile-shaft length was arbitrarily assumed to be 1.75 times the length of the column above grade. The pile shafts were discretized into six elements for the express purpose of accommodating 14 (two at each node) soil p-y springs to model the soil stiffness acting on the pile shaft. Mass was assigned to each pile-shaft node based on pile self-weight properties. A spring oriented in both the longitudinal and transverse directions (with the same stiffness properties) was placed at each pile-shaft node. The node at the ground surface was assigned a torsional single-point constraint. The use of a pile shaft and p-y springs allows for some rotation and displacement of the bridge column at ground level. This is more realistic than assuming a fixed-base column.
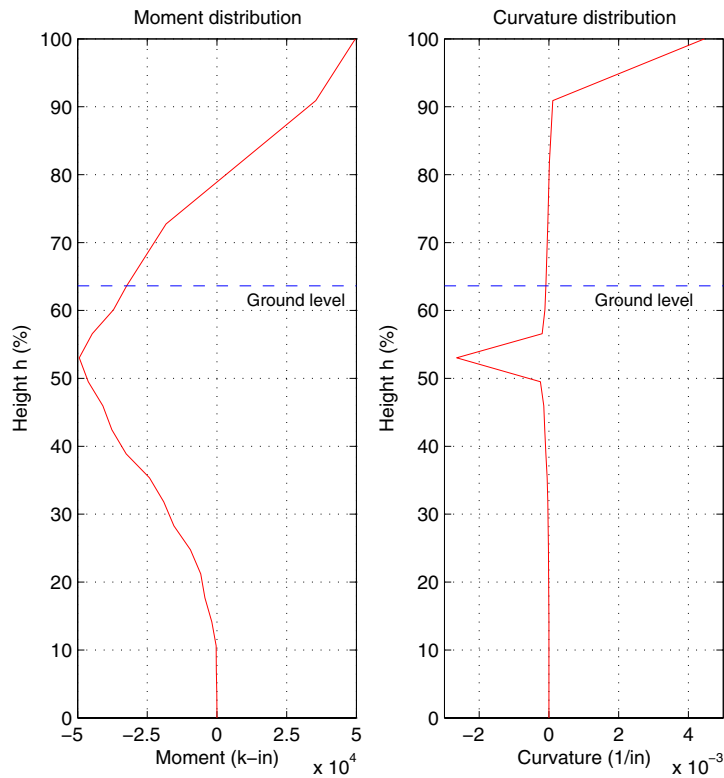
Fig. 2.3 Location of plastic hinges over length of column and pile shaft

22

The material constitutive law used for the *p-y* springs was derived from load-deflection curves for cohesionless soils (Boulanger 1999) and implemented in OpenSees. Parameters to the constitutive model included the ultimate lateral bearing capacity (p_{ult}), the displacement at which 50% of the ultimate strength is mobilized (y_{50}), the drag resistance, and free-field radiation viscous damping. The ultimate bearing capacity was derived using relations for sand in the API code (API 1993), or from simple relations for sand by Brinch-Hansen (Brinch-Hansen 1961) shown in Equation 2.1.

$$p_{ult} = C_p K_p \sigma'_{v0} D_c = \frac{\phi'}{10} \tan^2\left(45° + \frac{\phi'}{2}\right) \sigma'_{v0} D_c \qquad (2.1)$$

The effective stress at the depth of each spring (σ'_{v0}) was determined using the unit weight of soil (γ) input as a design parameter into the model. Similarly, the friction angle (ϕ') was also input directly as a design parameter. The water table was assumed below the site of interest; therefore, the spring stiffnesses will typically be higher than in analyses incorporating the hydrostatic pore water pressure and the excess pore water pressure that is developed as a result of earthquake shaking.

As the API recommendations for initial subgrade modulus were obtained from drained tests at shallow depths, the initial stiffness ($k \cdot x_h$) at large depths is overestimated by the API equation (and hence the y_{50} parameter underestimated) and should be reduced (Boulanger 1999). The variable x_h indicates the depth below grade. Therefore, two reduced approximations of y_{50} were made for comparison. The initial stiffness was obtained from the G_{max} low strain modulus (Seed 1984) for sand. A G/G_{max} ratio of 0.25 was then assumed as per Boulanger (Boulanger 1999). The K_0 coefficient was obtained directly from the friction angle as $K_0 = 1 - \sin\phi'$. Blow-counts (N_{60}) were estimated based on the friction angle input into the model and subsequently corrected for overburden ($N_{1,60}$).

The initial subgrade modulus k was then determined using a simplified form of Vesic's elastic theory (Vesic 1961). The resulting y_{50} value was calculated according to the API equation shown in Equation 2.2.

$$y_{50} = \frac{0.56 p_{ult}}{k x_h} \qquad (2.2)$$

A second value was compared with the y_{50} equation of Matlock (Matlock 1970) for clays merely as a comparison. The parameter y_{50} was estimated as *2.5$\varepsilon_c D_c$*, with ε_c for triaxial tests on

noncohesive soils assumed to be 0.01. At larger depths, the two values coincided. The first method described above was adopted for analysis. It should be noted that by substituting $\sqrt{x_h}$ for x_h in Equation 2.2, the predicted y_{50} values are approximately the same. This is consistent with the notion that the modulus increases roughly in proportion to the square root of the confinement, not linearly. A sample load-deflection relationship (*p-y*) is shown in Figure 2.4, where the soil resistance was multiplied by the pile contributing length to obtain a force.
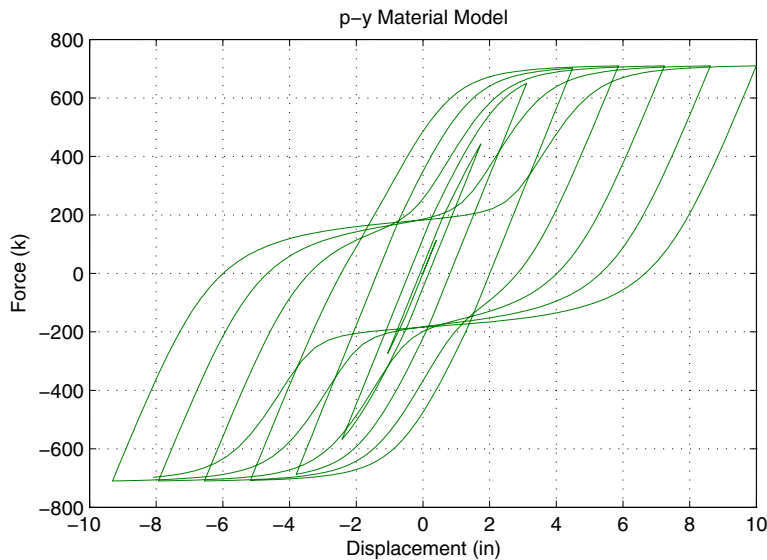
Fig. 2.4 OpenSees material constitutive model PySimple1

2.2   MULTIPLE-BENT BRIDGE

The remainder of the California highway overpass bridge class of structures includes two-, and three-bent (three-, and four-span) configurations (Fig. 1.2). This selection of spans was intended to cover a large range of frames used in stand-alone analyses performed in current design practice. The resulting designs are typical of long overpass bridges with segments separated by expansion joints, where individual frames are expected to perform independently (Caltrans 1999). The base configuration used for the multiple-bent bridges resembled the single-bent bridge base configuration. Specifically, the reinforced concrete bridges featured a single circular column for each bent, integral pile shafts, and continuous box girder superstructures spans that were not necessarily equal. The multiple-bent bridge models used in this report were the same as those used in previous PEER research (Mackie 2003).

The influence of multiple bridge spans on their seismic behavior, such as the effect of higher mode response, was investigated. As bridge designs become more complex (more bents), it becomes less likely they can be expected to respond in single-degree-of-freedom fashion. Of particular interest was whether the optimal PSDMs from single-bent bridges remained optimal for all bridge bent configurations considered. If so, this would imply that the PSDA method was sufficiently general for application to all bridges in the class of structures selected, making it a very powerful tool for risk assessment.

2.2.1   Design Parameters

For each multiple-bent configuration, the bridge design was varied through a series of design parameters. These included the parameters developed for single-bent bridges (Table 2.1), as well as those specific to multi-span bridges. Additional parameters for two- and three-bent bridges are shown in Tables 2.3 and 2.4, respectively. The two-bent base configuration included 27.4–36.6–27.4 m (90–120–90 ft) continuous spans. The columns were 15.2 m (50 ft) high above grade, with 1.7 m (5.6 ft) diameters, 2% longitudinal, and 0.8% transverse reinforcement. Definitions of the design parameters for the two-bent case are shown in Figure 2.5.

When the design parameters were varied, L_1 was always set equal to L_3,;therefore the spans were always symmetric. Irregularity was introduced only when varying L_2, L_2/H_1, and D_{c1}/D_s. Irregularity is defined as the increasing difference in response between bents in the transverse direction. In this study, L_1, L_2, D_{c2}, and H_2 all remained constant throughout. Therefore, the height of the left column (H_1) was determined solely by the values of L_2 and L_2/H_1. Design parameter analyses for the two-bent model were all carried out with an analytical abutment model (a trilinear stiffness material model) at both ends of the bridge. Further details of the abutment model formulation used and sensitivity to abutment model parameters are discussed elsewhere (Mackie 2003).
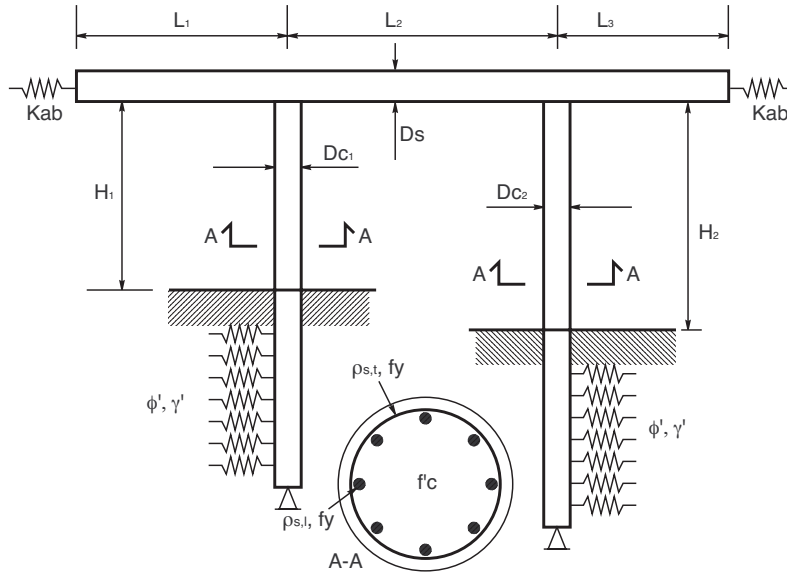
Fig. 2.5 Two-bent bridge design parameters

The three-bent bridge model adopted the same configuration as the two-bent model, with the addition of another 36.6 m (120 ft) interior span. A limited subset of design parameters was selected for analysis; therefore, L_1 was fixed at 27.4 m (90 ft) and L_3 at 36.6 m (120 ft). Similarly, the properties of the left column were fixed at $L_1/H_1 = 1.8$ and $Dc_1/Ds = 0.8$. The right column properties were fixed at $L_1/H_1 = 2.4$ and $Dc_1/Ds = 0.8$. The height of the middle bent in the three-bent model (H_2) was determined solely by the values of L_2 and L_2/H_2. This determination was different from the two-bent bridge case.

Table 2.3 Design parameter variation for two-bent overpass bridge

Description	Parameter	Range
Span length left	L_1	27–64 m (90–210 ft)
Span length right	L_2	27–64 m (90–210 ft)
Span-to-column height ratio	L_2/H_1	1.2–3.5
Column-to-superstructure dimension ratio	D_{c1}/D_s	0.67–1.33
Longitudinal reinforcement ratio	$\rho_{s,long}$	1–4%

Table 2.4 Design parameter variation for three-bent overpass bridge

Description	Parameter	Range
Span length middle	L_2	27–64 m (90–210 ft)
Span-to-column height ratio	L_2/H_2	1.2–3.5
Column-to-superstructure dimension ratio	D_{c2}/D_s	0.67–1.33

All base bridges for both the two-bent and three-bent models were on a USGS class B (NEHRP C) soil site. However, unlike the single-bent bridge, stiff bilinear soil springs were employed, as in Mackie (Mackie 2001, 2003). For the three-bent bridge design parameter study, the abutment boundary conditions were assumed to be rollers. The rollers best mimic a stand-alone bridge configuration that can be strung together in longer chains with expansion joints to form a complete viaduct-type bridge.

For the assumed roller boundary condition at the abutments, the fundamental mode for all three bent types (one-, two-, and three-bent) was in the transverse direction. This mode involved a simple transverse translation of the deck (Fig. 3.5). The second mode was also common to all three bent types, involving a longitudinal translation of the superstructure, coupled with small rotations of the columns and supports (Fig. 3.6). When analytical abutment models were added to any of the bridges, the transverse stiffness increased beyond that of the longitudinal direction. The gap in the longitudinal direction before abutment impact provided the same initial elastic stiffness in the longitudinal direction as the roller boundary condition. Hence the fundamental mode of the bridge with abutment model became longitudinal, and the second mode transverse. The first two periods for the two-bent bridge configurations and three-bent configurations are shown in Tables 2.5 and 2.6, respectively.

Table 2.5 Two-bent bridge periods for sample bridge configurations

Structure number	Design parameter	T_1 (sec)	T_2 (sec)
0001	Base	1.54	1.06
0005	$L_2 = 1080$ in.	0.84	0.45
0009	$L_2 = 2160$ in.	1.34	0.61
0013	$L_2 = 2520$ in.	1.46	0.80
0017	$L_2/H_1 = 1.2$	1.79	1.31
0021	$L_2/H_1 = 1.8$	1.16	0.50
0025	$L_2/H_1 = 3.5$	0.85	0.48
0029	$D_{c1}/D_s = 0.67$	1.14	0.50
0033	$D_{c1}/D_s = 1.00$	0.88	0.49
0037	$D_{c1}/D_s = 1.30$	1.18	0.80
0041	$\rho_{s,long} = 0.01$	1.07	0.50
0045	$\rho_{s,long} = 0.03$	0.99	0.50
0049	$\rho_{s,long} = 0.04$	0.96	0.49

Table 2.6 Three-bent bridge periods for sample bridge configurations

Structure number	Design parameter	T_1 (sec)	T_2 (sec)
0001	Base	1.54	1.06
0005	$L_2 = 1080$ in.	1.46	0.80
0009	$L_2 = 2160$ in.	1.79	1.31
0013	$L_2 = 2520$ in.	1.88	1.40
0017	$L_2/H_2 = 1.2$	1.71	1.27
0021	$L_2/H_2 = 1.8$	1.64	1.16
0025	$L_2/H_2 = 3.5$	1.35	0.90
0029	$D_{c2}/D_s = 0.67$	1.61	1.15
0033	$D_{c2}/D_s = 1.00$	1.03	0.43
0037	$D_{c2}/D_s = 1.30$	1.18	0.80

3   Demand Model

In current practice, probabilistic seismic demand evaluation is routinely done as a part of performance-based design of important structures. In such projects, complex nonlinear structural models are typically subjected to a large number of real and artificial ground motions to estimate the required probabilities of exceeding predetermined values of project-specific demand or decision variables. Such computationally intensive seismic risk assessment approaches are applicable only to unique structures and cannot be used in routine performance-based design (Mackie 2003).

A disaggregated performance-based design framework (Eq. 1.2) is a practical alternative for such nonunique structures. One reason for extensibility in this framework is that probabilistic seismic demand analysis (PSDA) applies to an entire urban region, rather than to a unique location. Second, it applies to an array of possible decision variables rather than a single one. And finally it applies to a class of structures, rather than to a unique structure. Resulting probabilistic seismic demand models (PSDMs) are therefore quite general (Mackie 2003).

The PSDM formulated herein is the outcome from PSDA. PSDA has previously been used (Bazzurro 1998; Shome 1998; and Carballo 2000) to couple probabilistic seismic hazard analysis (PSHA) with demand predictions from nonlinear finite element analysis. This is done to estimate the annual frequency of exceeding a given demand, and results in a structural demand hazard curve (Luco 2001a). Alternatively, PSDA can be used alone to provide probabilities of exceeding demand limit states, given measures of intensity. Such a relationship is termed a "demand fragility curve" in this study.

The procedure (PSDA) used to formulate the PSDMs of interest involves five steps. First, a set of ground motions, representative of regional seismic hazard, is selected or synthesized (Section 3.1). Instrumental in selecting these motions is categorizing them according to computable intensity measures descriptive of their content. Second, the class of structures to be investigated is selected, as defined in Section 1.3. Associated with this class is a

suite of engineering demand parameters (Section 3.2) that can be measured during analysis to assess structural performance under the considered hazard. Third, a nonlinear finite element analysis model is generated to model the class of structures selected, with provisions to vary designs of the class through the use of design parameters. Thus, a portfolio of structures is generated by different realizations of the design parameters. The different finite element models developed for this study are detailed in Chapter 2. Fourth, nonlinear dynamic analyses are performed until all motions and structural model combinations have been exhausted (Section 3.3). Fifth, a demand model is formulated between resulting ground motion *IM*s and structural *EDP*s (Mackie 2003).

3.1   HAZARD AND INTENSITY

The hazard environment for all bridges in this study was formed based on previously recorded earthquakes in California. This section addresses the selection of these earthquake records, how they were grouped and utilized for analysis, and definitions of the ground motion intensity measures used to describe them. Specific details of the individual earthquake records used can be found in the Appendix.

3.1.1   Ground Motions

The PSDA method used herein to formulate the PSDMs involved the ground motion bin approach. It would also be possible to perform the analysis using a standard Monte Carlo simulation (Deodatis 1997; Foutch 1992) involving hundreds or thousands of ground motions, or by generation of synthetic ground motions. Synthetic motions are site specific and include both expected acceleration time histories or motions generated based on design spectra. The bin approach that was proposed and used by Shome and Cornell (Shome 1999) is used to subdivide ground motions into hypothetical bins based on magnitude (M_w), closest distance (R), and local soil type. The use of magnitude and distance allows parallels between standard attenuation relationships and existing PSHA (Mackie 2003).

Advantages of the bin approach include the ability to assess the effect of generalized earthquake characteristics, such as frequency-domain content or duration, on structural demands. For example, bins differentiate between near- and far-field earthquake types, rather than between

individual near- and far-field records. Ground motion intensity can also be abstracted by scaling the earthquakes in a bin to the same level of intensity (otherwise known as "stripe"), such as spectral acceleration at the fundamental period of a structure. This approach is adopted in incremental dynamic analysis (IDA). Second, the use of bins is substantial in limiting the number of ground motions selected for analysis. Shome and Cornell (Shome 1998) show that, assuming a lognormal probability distribution of structural *EDP*s (conditioned on *IM*), the number of ground motions sufficient to yield response quantity statistics that have a required level of confidence is proportional to the square of a measure of dispersion in the demand model. They also show (Shome 1999) that the bin approach, and scaling motions within bins, by itself does not introduce bias into the relation between *EDP*s and ground motion *IM*s (Mackie 2003).

Four bins with 20 ground motions each were obtained from the PEER Strong Motion Database (PEER Strong Motion Catalog). These motions are characteristic of non–near-fault motions ($R > 15$ km) recorded in California. The delineation between small (SM) and large (LM) magnitude bins was at $M_w = 6.5$. Ground motions with closest distance R ranging between 15 and 30 km were grouped into a small distance (SR) bin, while ground motions with $R > 30$ km were in the large distance (LR) bin. All ground motions were recorded on NEHRP soil type D sites. The specific records selected were similar to those used by Krawinkler (Gupta 2000; Medina 2001) in a companion PEER research project related to building structures. The distribution of motions selected within the four bins (in M_w and R space) is shown in Figure 3.1. Details of all the ground motion records used, including earthquake names, sensor location, magnitude, distance, soil type, faulting mechanism, and peak waveform ordinates are provided in the Appendix.

The fifth bin, also containing 20 ground motions (as seen in Fig. 3.1, labeled "Near"), comprised ground motions from Luco's (Luco 2001b) near-field bin. These are high-magnitude earthquakes measured at a distance (R) of less than 15 km. Structural response to earthquakes in this bin was then expected to exhibit some near-field effects such as directivity, fling, and pulse response. The choice of records on medium soil (NEHRP D) provided a conservative approach to evaluating performance because the expected spectral acceleration on firm, dense soil (NEHRP B, C) and rock sites (NEHRP A) for an equivalent earthquake is less likely amplified in the range of periods expected for the fundamental bridge modes under consideration. The structural periods of all bridge types in this study are detailed in Chapter 2.
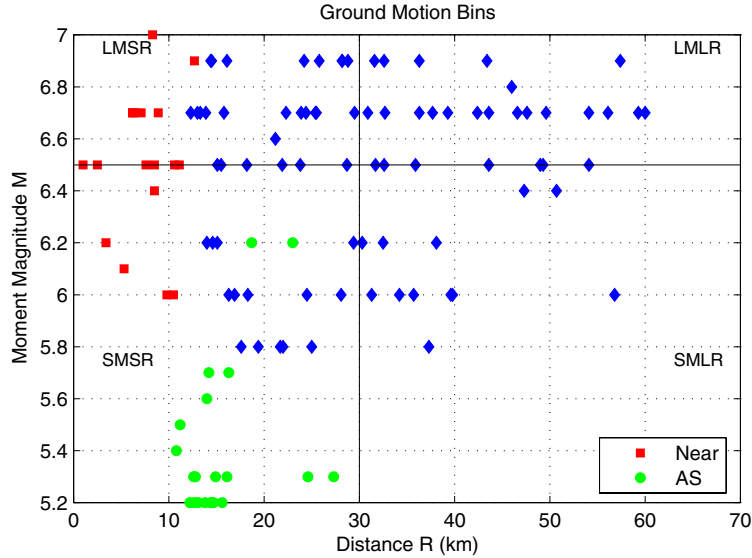
Fig. 3.1 **Distribution of ground motion records in *M_w*-*R* space**

All three orthogonal component accelerograms were utilized for each earthquake selected. This allowed for a fully three-dimensional analysis without the generation of artificial or rotated records. Each component of all the earthquake records was filtered to set all sampling frequencies to 50 Hz (0.02 sec). As the primary bridge modes of vibration occurred at periods higher than 0.02 sec, little higher-mode accuracy was lost in reducing all records to a 0.02 second sampling rate. The magnitude and frequency content of the records used was otherwise unaltered. Due to the absence of very high-magnitude California records, and to ensure nonlinear structural response, especially in the smaller intensity bins, the records were scaled by a factor of two if used as is. Such artificial record amplification was limited to preserve realistic record characteristics as much as possible. The scaling was achieved by a simple amplification of all the acceleration values during any of the probabilistic seismic demand model analyses. During IDA, record intensities required by the method were attained by amplitude scaling as needed.

3.1.2 Intensity Measures

Three classes of intensity measures (*IM*s) are used in current practice. The first class contains traditional *IM*s that describe the earthquake source characteristics and time history record. These *IM*s are predominantly duration, maxima, and energy based. Not included specifically as *IM*s in

this class are the earthquake magnitude (M_w) and distance (R), as they cannot be obtained directly from the accelerogram. The second class includes the *IM*s that describe the time history obtained using a single-degree-of-freedom system filter on the original record. All Class I *IM*s can therefore be calculated directly from this new filtered record. However, there are numerous *IM*s in the literature specific to Class II, so they are included directly. Among these are the traditional spectral quantities, such as spectral acceleration. The third class extends the filter concept to *IM*s that result from applying an arbitrary filter to the original time history.

3.1.2.1 Class I Intensity Measures

Class I intensity measures are defined as those that can be generated directly from the recorded earthquake time history (from time $t = 0$ to time $t = D_f$, the record duration). Time history information is usually presented in acceleration units; therefore, integration of the time history to obtain velocity and displacement histories may also be necessary. In this study, 17 Class I *IM*s were considered. These are summarized in Table 3.1, with their associated *IM* number in this study. Note that not all *IM* numbers in forthcoming tables are consecutive. The range of *IM* numbers is enumerated within each *IM* class.

Table 3.1 Class I intensity measures

IM number	*IM* name	Definition	Units
1	Strong motion duration	$T_D = t(0.95 I_A) - t(0.05 I_A)$	s
2	Peak ground acceleration	$PGA = \max\|\ddot{u}_g(t)\|$	g
3	Peak ground velocity	$PGV = \max\|\dot{u}_g(t)\|$	cm/s
4	Peak ground displacement	$PGD = \max\|u_g(t)\|$	cm
5	Arias intensity (Arias 1970)	$I_A = \dfrac{\pi}{2g} \int\limits_0^{D_f} [\ddot{u}_g(t)]^2\, dt$	cm/s
6	Velocity intensity	$I_V = \dfrac{1}{PGV} \int\limits_0^{D_f} [\dot{u}_g(t)]^2\, dt$	cm
7	Displacement intensity	$I_D = \dfrac{1}{PGD} \int\limits_0^{D_f} [u_g(t)]^2$	cm-s
8	Cumulative absolute velocity	$CAV = \int\limits_0^{D_f} \|\ddot{u}_g(t)\|$	cm/s
9	Cumulative absolute displacement	$CAD = \int\limits_0^{D_f} \|\dot{u}_g(t)\|$	cm
10	Cumulative absolute impulse	$CAI = \int\limits_0^{D_f} \|u_g(t)\|$	cm-s
11	Root mean square acceleration	$A_{rms} = \sqrt{\dfrac{1}{T_D} \int\limits_0^{D_f} [\ddot{u}_g(t)]^2\, dt}$	cm/s^2
12	Root mean square velocity	$V_{rms} = \sqrt{\dfrac{1}{T_D} \int\limits_0^{D_f} [\dot{u}_g(t)]^2\, dt}$	cm/s
13	Root mean square displacement	$D_{rms} = \sqrt{\dfrac{1}{T_D} \int\limits_0^{D_f} [u_g(t)]^2\, dt}$	cm

Table 3.1 — *continued*

14	Characteristic intensity	$I_C = A_{rms}^{1.5} T_D^{0.5}$	$cm^{1.5}/s^{2.5}$
15	Frequency ratio 1	$FR_1 = \dfrac{PGV}{PGA}$	s
16	Frequency ratio 2	$FR_2 = \dfrac{PGD}{PGV}$	s
17	Medium period *IM* (Fajfar 1990)	$I = PGV\left(T_D^{0.25}\right)$	$cm/s^{0.75}$

3.1.2.2 Class II Intensity Measures

Class II and Class III intensity measures are both defined as Class I *IM*s acting on earthquake time histories that have been filtered using different processes. Therefore, the definitions in Table 3.1 are still valid except u_g (ground motion) has been replaced by u_f (filtered ground motion). Class II *IM*s are the special case of a single-degree-of-freedom (SDOF) system used as the filter. This is the origin of the traditional spectral quantity *Sd* (spectral displacement). *Sd* is simply the maximum of $u_f(t)$, as defined for *PGD* in Table 3.1, hence the new notation ^{SDOF}PGD. As there is a large body of research on *IM*s using this type of filter, there are numerous SDOF specific *IM*s that are included in this class of *IM*s in addition to Table 3.1. These are summarized in Table 3.2. Note once again that the *IM* numbers are not consecutive between Tables 3.1 and 3.2, but are enumerated following Table 3.2.

Table 3.2 Class II intensity measures

IM number	*IM* name	Definition	Units
35	Pseudo-spectral velocity	$PSv(T_i) = \omega_i Sd(T_i)$	cm/s
36	Pseudo-spectral acceleration	$PSa(T_i) = \omega_i^2 Sd(T_i)$	g
54	Luco 1st mode predictor (Luco 2003)	$IM_{1I} = \left\| PF_1^{[1]} \right\| Sd^I = \dfrac{Sd^I(T_1, \zeta, d_y)}{Sd(T_1, \zeta)} Sa(T_1, \zeta)$	cm/s^2
55	Cordova predictor (Cordova 2000)	$IM_{1eff} = Sa(T_1, \zeta) \left[\dfrac{Sa(cT_1, \zeta)}{Sa(T_1, \zeta)} \right]^{\alpha}, c = 2, \alpha = \tfrac{1}{2}$	cm/s^2
56	Effective peak acceleration (ATC 1978)	$EPA = \dfrac{Sa_{avg}(T_i, \zeta)\big|_{0.1}^{0.5=T_i}}{2.5}$	g
57	Effective peak velocity	$EPV = \dfrac{Sv_{avg}(T_i, \zeta)\big|_{0.7}^{2.0=T_i}}{2.5}$	cm/s
58	Effective peak displacement	$EPD = \dfrac{Sd_{avg}(T_i, \zeta)\big|_{2.5}^{4.0=T_i}}{2.5}$	cm
59	Acceleration response intensity (Von Thun 1988)	$ASI = \displaystyle\int_{0.1}^{0.5} Sa(T, \zeta = 0.05)dT$	g
60	Velocity response intensity	$VSI = \displaystyle\int_{0.7}^{2.0} Sv(T, \zeta = 0.05)dT$	cm/s
61	Displacement response intensity	$DSI = \displaystyle\int_{2.5}^{4.0} Sd(T, \zeta = 0.05)dT$	cm
62	Response spectrum intensity (Housner 1959)	$SI = \displaystyle\int_{0.1}^{2.5} Sv(T, \zeta = 0.05)dT$	cm
63	Average spectral acceleration	$Sa_{avg} = \displaystyle\sum_{T_1}^{T_n} \dfrac{Sa(T_i, \zeta)}{n}$	g

Table 3.2 — *continued*

64	Average spectral velocity	$Sv_{avg} = \sum\limits_{T_1}^{T_n} \dfrac{Sv(T_i,\zeta)}{n}$	cm/s
65	Average spectral displacement	$Sd_{avg} = \sum\limits_{T_1}^{T_n} \dfrac{Sd(T_i,\zeta)}{n}$	cm

Intermediate *IM* values not listed, for example 18 to 34, are simply Class I *IM*s from Table 3.1 acting on the SDOF filtered record. Specifically, 18 to 34 are elastic SDOF systems at T_1 and 5% viscous damping, and 37 to 53 are inelastic SDOF systems at T_1, 5% viscous damping, yield strength f_y of the structure, and 1% strain hardening. *IM* numbers 63 to 65 (average spectral quantities) are repeated 7 times, each for different period bands about T_1. These are summarized in Table 3.3.

Table 3.3 Averaged spectral combination Class II *IM*s

IM number(s)	Name	T_{lower}	T_{upper}
63–65	Band 1	$0.5\ T_1$	$2\ T_1$
66–68	Band 2	$4/7\ T_1$	$7/4\ T_1$
69–71	Band 3	$8/13\ T_1$	$13/8\ T_1$
72–74	Band 4	$2/3\ T_1$	$3/2\ T_1$
75–77	Band 5	$8/11\ T_1$	$11/8\ T_1$
78–80	Band 6	$4/5\ T_1$	$5/4\ T_1$
81–83	Band 7	$8/9\ T_1$	$9/8\ T_1$

3.1.2.3 Class III Intensity Measures

Like Class II *IM*s, Class III *IM*s are Class I *IM*s acting on filtered time history records. This is a completely general method for viewing *IM*s, as soon as one realizes the choice of filter is arbitrary and not limited to a SDOF system. This section attempts to introduce several other types of filters that can be used to obtain more efficient demand models. Two filters were used.

One is structure-specific (a two-degree-of-freedom system), and the other is a common signal-processing concept: the bandpass filter.

For a structure with response dominated by more than just the fundamental mode, it may be beneficial to introduce more information about the second mode into the demand model computation. This can be achieved using a lumped mass and stiffness, two-degree-of-freedom (2DOF) system (Fig. 3.2). For simplicity, it was assumed that each mass in the model is excited equally by the ground motion, and the first mass (m_1) and stiffness values (k_1) are normalized to unity. The remainder of the 2DOF system can be determined with the input of the first- and second-mode periods, T_1 and T_2. The resulting values for m_2 and k_2 are shown in Equations 3.1 and 3.2, respectively.
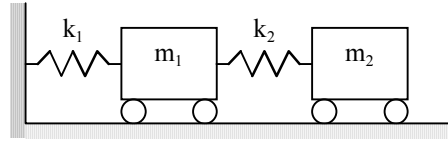
Fig. 3.2 Two-degree-of-freedom system *IM* filter

$$m_2 = \frac{-1}{16\pi^4}\left(4\pi^2 - T_1^2\right)\left(4\pi^2 - T_2^2\right) \tag{3.1}$$

$$k_2 = \frac{1}{T_1^2 T_2^2}\left(-4\pi^2 + T_1^2\right)\left(4\pi^2 - T_2^2\right) \tag{3.2}$$

In the case of this study, the 2DOF filter was elastic with four input parameters: T_1, T_2, ζ, and u_1 or u_2. The final argument specified which output record to use as u_f in the subsequent Class I *IM*s. The damping matrix was formulated using a superposition of modal damping matrices with each of the two modes having damping ratio ζ.

A large amount of computation was required to average spectral quantities from Class II *IM*s over a range of periods. As demonstrated later, these may be more efficient than spectral quantities at specific periods; therefore, an alternative method of achieving these results is desirable. In signal processing, the bandpass filter is often used to isolate or separate out a range of frequency components from the original source. For this study, a fourth-order Butterworth bandpass filter was used with bandwidth B. The bandwidth is the frequency separation between

the upper and lower half-power points. A sample filter magnitude plot is shown in Figure 3.3 for cutoff frequencies corresponding to periods of 1.25 and 1.50 sec.
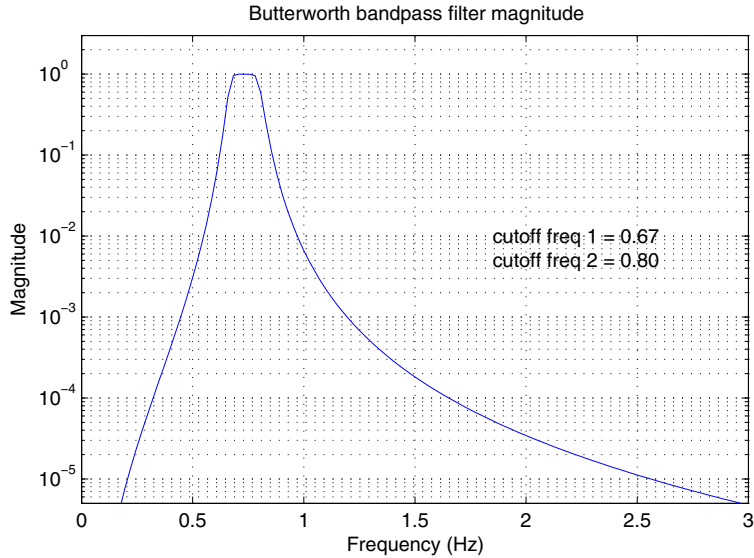
Fig. 3.3 Sample Butterworth bandpass filter with 0.25 sec bandwidth

Time history records can be efficiently filtered using signal processing enabled programs, such as Matlab. The resulting filtered record (e.g., Fig. 3.4) was then used as u_f in calculating subsequent Class I *IM*s. Both records were scaled to the original record's *PGA*; however, the magnitude of ^{BP}PGA is generally not the same. Similar to the 2DOF system filter, it is possible to design digital filters of arbitrary cutoff frequencies and frequency bands. Therefore, if desirable, a filter with two or more pass bands could also be used to generate further Class III *IM*s. This method is considerably more general than developing specific multiple-degree-of-freedom (MDOF) structural models.   There are also considerable computational speed advantages over performing numerical solutions of the equations of motion.
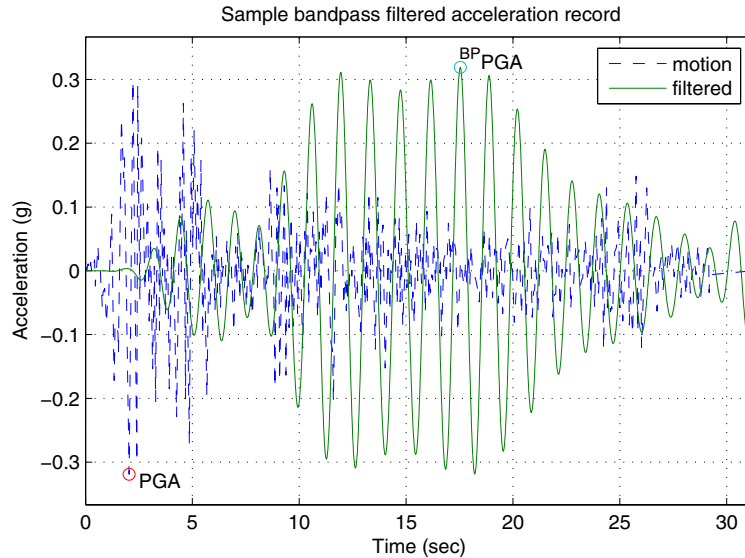
Fig. 3.4 Sample bandpass filtered acceleration record

3.1.3 Probabilistic Seismic Hazard Analysis

Probabilistic seismic hazard analysis (PSHA) has existed since the 1960s (Cornell 1968). As opposed to deterministic hazard analysis, PSHA provides a probabilistic means for predicting the rate of exceeding different *IM* values at a particular site. Therefore, inherent in the method is a treatment of uncertainty that accompanies the inception of earthquakes. Specifically, the uncertainty accompanies the site's proximity to known faults, or the seismic source model, and the prediction of intensity given the source model.

While highway network or basic urban post-earthquake assessment requires a spatial distribution of earthquake intensities, it suffices for a single integral (Eq. 1.1) evaluation to consider only site-specific hazard. Determination of the seismic source model includes detailing known faults, their magnitude, proximity to the site, and rate of occurrence. Also included are background seismicity, blind faults, or any regional or local hazard described by a recurrence versus magnitude relation. The prediction of intensity follows from the source according to pre-derived attenuation relationships. Attenuation relationships provide a probability distribution of a particular *IM* (usually *PGA* or *Sa*), conditioned on distance, magnitude, fault mechanism, soil type, etc. The probabilities of exceeding a specified *IM* value are integrated over the range of all these variables and weighted by the rate of each constituent event. The total rate of exceedance is then the summation over all sources of seismicity affecting the site (Eq. 3.3).

$$P(IM > im, t = 1) \approx \lambda_{IM}(im) = \sum_{i=1}^{N} v_i \cdot \iint G_{IM|M,R}(im \mid m_i, r_i) dG_{M,R}(m_i, r_i) dm_i \cdot dr_i \quad (3.3)$$

The mean rate of exceeding different *IM* values (assuming a Poisson process) is then termed a hazard curve. An equal hazard spectrum (e.g., spectral acceleration versus period) can be obtained from an *IM* with equal probabilities of exceedance. It is also possible to disaggregate each *IM* at a probability of exceedance level into contributing magnitude (M_w) and distance (*R*). The issue of residual independence of response on M_w and *R* is termed sufficiency (Section 3.4). However, for the purposes of the hazard model used in this study, a form of the hazard curve alone is required.

For small probabilities of exceedance, the hazard curve can be written in closed form as Equation 3.4. The constants need to be derived for each site and each *IM* using PSHA. Rarely is the full domain of *im* values covered by PSHA. For example, often only three discrete levels of hazard are specified: 2% in 50 years, 10% in 50 years, and 50% in 50 years. Therefore it is helpful to write Equation 3.4 in log format (Eq. 3.5). This form lends itself to least-squares determination of the coefficients.

$$\lambda_{IM}(im) = k_0(im)^{-k} \quad (3.4)$$

$$\ln(\lambda_{IM}(im)) = \ln(k_0) - k \ln(im) \quad (3.5)$$

3.1.4 Aftershocks

The same methodology applied to the generation of PSDMs for first-shock earthquake scenarios was applied to aftershocks in this study. The only extension involved the selection of bins, aftershocks bins, and the sequence of first-shock and aftershock events. To maintain continuity, the same first-shock bins were employed. After each first shock, the structure was allowed to come to rest before randomly selecting an aftershock record from one of five different aftershock bins. A single bin of specific recorded aftershock time histories was selected from the PEER ground motion catalog (PEER Strong Motion Catalog). Details of individual records in this bin are contained in the Appendix, and plotted with the first-shock bins in Figure 3.1, labeled "AS" for "aftershock."

The aftershock records were scaled up by a factor of two to ensure that damage in the structure occurred. The remaining four bins were identical to the first-shock bins, but with intensity scaled by a factor of a half. Each first-shock bin was paired with each aftershock bin, creating a total of 20 bins for analysis. Therefore, for every structure, the required computations increased by a factor of 5. The *IM* of the first-shock is maintained throughout the aftershock analysis and used in the prediction of the ultimate *EDP* value. The first-shock (FS) *IM* was termed $IM_{FS} = IM_1$, while the aftershock (AS) *IM* was termed $IM_{AS} = IM_2$.

3.2   ENGINEERING DEMAND PARAMETERS

The bridge *EDP*s were originally chosen from the database of experimental results for concrete bridge components (Hose 2000, PEER Capacity Catalog). The database detailed specific discrete limit states for each of the *EDP*s considered, complete with visual depictions at each of five different limit states. By mirroring the component database, it would be possible to directly evaluate damage in a bridge, given the analysis demands. However, this database was not used in subsequent damage model derivations (Chapter 4) because the damage was only quantified into arbitrary (numbered) damage limit states. The *EDP*s adopted for this study ranged from global parameters, such as drift ratio, to intermediate parameters, such as cross-sectional curvature, to local parameters, such as material strains.

Several other descriptive measures were also added to assess the loading (axial load ratio) and relative strength of the bridge (*R*-factors). The axial load ratios ranged from 3.3%–29.5% and the longitudinal R_{CS} and R_{USGS}-factors ranged from 1–3.2 and 1–10.4, respectively. The transverse R_{CS} and R_{USGS}-factors ranged from 1–2.4 and 1–10.2, respectively. All the *EDP*s in this study are shown in Table 3.4. For the equations defining the strength reduction factors, *m* was the total mass of the bridge column and superstructure. F_y' was the yield force. V_b was the base shear at the column of interest.

Table 3.4 Engineering demand parameters

Name	Formula	Units
Axial load ratio	$ALR = \dfrac{N}{f_c' A_g}$	%
Yield displacement	u_y	in.
Yield curvature	ϕ_y	1/in.
Yield energy	$E_y = \displaystyle\int_0^{u(\max(F))} F(u)\,du$	k-in.
Maximum displacement	$u_{\max} = \max(|u(t)|)$	in.
Drift ratio	$\Delta = \dfrac{u_{\max}}{H}$	%
Maximum curvature	$\phi_{\max} = \max(|\phi(t)|)$	1/in.
Maximum moment	$M_{\max} = \max(|M(t)|)$	k-in.
Maximum shear force	$V_{\max} = \max(|V(t)|)$	k
Maximum steel strain	$\varepsilon_{s,\max} = \max(|\varepsilon_s(t)|)$	%
Maximum steel stress	$\sigma_{s,\max} = \max(|\sigma_s(t)|)$	ksi
Maximum concrete strain	$\varepsilon_{c,\max} = \max(|\varepsilon_c(t)|)$	%
Maximum concrete stress	$\sigma_{c,\max} = \max(|\sigma_c(t)|)$	ksi
Residual displacement	$u_{resid} = |u(t_{\max})|$	in.
Residual displacement index	$RDI = \dfrac{u_{resid}}{u_y}$	%
Hysteretic energy	$HE = \displaystyle\oint_\theta M(\theta)\,d\theta$ or $HE = \displaystyle\oint_u P(u)\,du$	k-in.
Normalized hysteretic energy	$NHE = \dfrac{HE}{E_y}$	%
Peak strength	$P_{\max} = \max\{abs(V_b)\}$	k
R-factor (capacity spectrum)	$R_{CS} = \dfrac{m \cdot Sa_{avg,bin}(T)}{F_y'}$	-

Table 3.4 — *continued*

R-factor (USGS)	$R_{USGS} = \dfrac{m \cdot Sa_{2\%-50year}(T)}{F'_y}$	-
Displacement ductility	$\mu_\Delta = \dfrac{u_{max}}{u_y}$	-
Curvature ductility	$\mu_\phi = \dfrac{\phi_{max}}{\phi_y}$	-
Plastic rotation	$\theta_{pl} = \dfrac{u_{max} - u_y}{H}$	rad

3.3   PSDA PROCEDURE

The PSDMs in this study were formulated using two analysis methods, probabilistic seismic demand analysis (PSDA) and Incremental Dynamic Analysis (IDA). The first method attempts to represent seismicity through a wide selection of many ground motions, grouped into bins. The latter method achieves the same by stepwise incrementation of a select few ground motion records. The procedure referred to as PSDA in this study is otherwise known as the "cloud" analysis method. This is due to the use of the ground motion bins described above without any prior scaling within or between bins. Therefore, there are a cloud of data points within the M_w-R space of earthquakes (Fig. 3.1). The alternative approach (IDA) is to scale ground motions within bins to a common value (or an intensity "stripe"). The basic formulation for the two analysis methods remains the same, however. The procedures common to both methods are presented first.

3.3.1   Single Earthquake Analysis Procedure

Nonlinear models were generated for each of the bridge configurations and analyzed for each ground motion. Each routine involved a static pushover analysis to determine yield values, a modal analysis to determine natural frequency and mode shape information, and a dynamic time history analysis to determine demand. Static pushover analyses included separate routines for the bridge longitudinal direction, transverse direction, and also the vertical direction (executed

separately). For the case of a single-bent bridge, lateral pushover analysis was performed by incrementing the lateral load at the top of the column and monitoring displacement until failure. As would be expected, for the case of the single-column, single-bent bridge, the pushover diagrams were quite similar in the longitudinal and transverse directions. The vertical pushover, otherwise termed a "pushunder" analysis, was performed by incrementing the vertical load on the column and monitoring vertical displacement until failure. Residual lateral displacements impacted the pushunder ultimate capacity due to geometric nonlinearities.

While single-bent bridges used standard static pushover techniques for both longitudinal and transverse directions, multiple-bent bridges required a modification of the procedure in the transverse direction. Similar to the modal pushover procedure for buildings (Chopra 2001) and the pushover analysis in the N2 method (Fajfar 1997), the distribution of lateral forces was determined from the shape of the fundamental transverse mode, weighted by tributary mass. This method was also employed by Gardoni (Gardoni 2002). Displacements at column tips were then monitored along with shear forces induced in the columns, such as base shear in buildings. This allowed for irregular bridges to be accurately analyzed as well, producing separate yield data for different bents. Irregularity frequently occurs when the properties of each bent are varied from each other.

Modal analysis was performed before each analysis (elastic stiffness), as well as after each analysis, to assess the change in natural frequencies at the onset of damage in the bridge. For the assumed roller boundary condition at the abutments, the fundamental mode for all three bent types (one-, two-, and three-bent bridges) was in the transverse direction. This mode involved a simple transverse translation of the deck (Fig. 3.5). The second mode involved a longitudinal translation of the superstructure, coupled with small rotations of the columns and supports (Fig. 3.6). As mentioned previously, when abutment models were added, the transverse stiffness (from the abutments) became dominant (over the longitudinal stiffness) due to the gap. Hence the fundamental mode of the bridge shifts to the longitudinal mode described above, and the second mode becomes transverse.

Sample period information for various single-bent bridge configurations was listed in Table 2.2. The fundamental period values ranged from 1.08 for short bridges to 2.74 for long-span bridges. Second-mode periods varied similarly from 0.76 to 2.54. Similar period information was also presented for two-bent bridges (Table 2.5) and three-bent bridges (Table 2.6). The time history analyses were performed for all ground motions and bridge instantiations.

A static analysis was performed first to allow application of the gravity loads. Following this, the constant average acceleration Newmark numerical integrator was used with 2.5% Rayleigh damping to perform the dynamic time steps. Numerous quantities were monitored and then passed to the data extraction routines to extract maximum dynamic quantities, such as stress, strain, moment, displacements, etc.
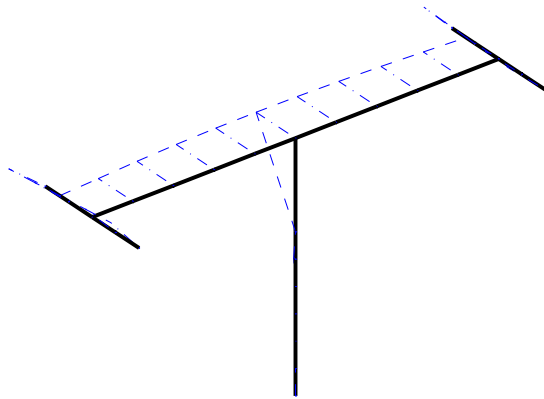
Fig. 3.5 Single-bent 1st mode trans.   **Fig. 3.6 Single-bent 2nd mode long.**
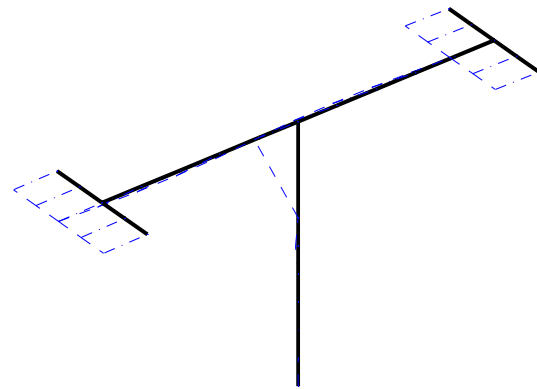
3.3.2   PSDA "Cloud" Results

PSDA uses a bin approach, where a portfolio of ground motions was chosen to represent the seismicity of an urban region. The single earthquake procedure (Section 3.3.1) was repeated for each of the 20 ground motions in a bin. As mentioned previously, first-shock records were scaled by a common factor of two to ensure nonlinear structural response, especially in the small-magnitude and long distance bins. Any number of bins can be analyzed in this manner, but the primary four bins are shown here. Similarly, the entire procedure can be repeated any number of times for an arbitrary number of bridge designs obtained from varying the different bridge design parameters. A single example is shown below for the single-bent bridge base configuration. Figure 3.7 shows the resulting demand model using the cloud approach, plotted in linear space. For comparison, Figure 3.8 shows the same data plotted in (natural) log space.

All of the demand models formulated and presented in later chapters were generated using this PSDA, or "cloud" procedure. Hence, these terms are used synonymously from this

point on. Other researchers have selected the IDA method (Jalayer 2003; Krawinkler 2002), particularly for research related to steel frame buildings. For the case of reinforced concrete highway overpass bridges, a comparison of the two methods was performed to assess the equivalency of the ensuing PSDMs (Mackie 2002c). It was shown that for similar computational effort (i.e., 8 ground motions incremented 10 times each, or 10 ground motions incremented 8 times each), there is good agreement between the first and second moments (see Section 3.3.4) obtained from mathematical models using the PSDA and IDA procedures (Mackie 2002c).
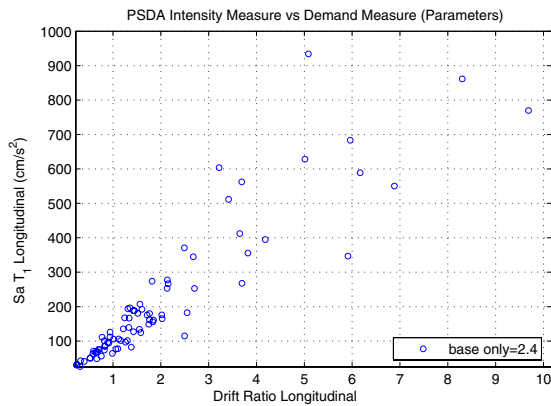
Fig. 3.7 Sample PSDM using cloud method, *Sa(T₁)-Δ*, linear space
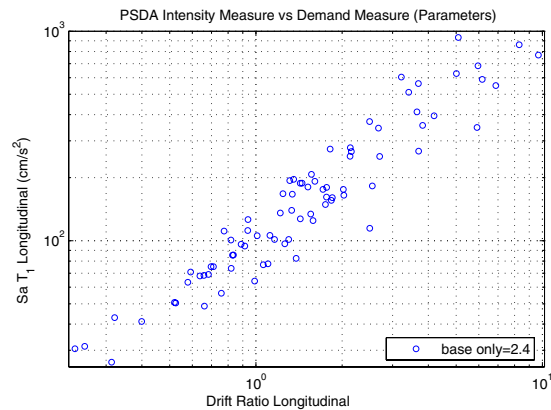
Fig. 3.8 Sample PSDM using cloud method, *Sa(T₁)-Δ*, log space

3.3.3   IDA Results

IDA is the dynamic equivalent to a familiar static pushover analysis. Given a structure and a ground motion, IDA is done by conducting a series of nonlinear time history analyses. The intensity of the ground motion, measured using an , is incrementally increased in each analysis. An *EDP*, such as global drift ratio, is monitored during each analysis. The extreme values of an *EDP* are plotted against the corresponding value of the ground motion *IM* for each intensity level to produce a dynamic pushover curve for the structure and the chosen earthquake record. To achieve comparison with an equivalent PSDA cloud, several motions are required, and IDA intensities must cover a similar range. Stripe analysis is simply a special case of IDA. A single *IM* level is selected and *EDP* data are obtained, providing a one-dimensional "stripe" of response data.

The only variance between the two analysis tools (PSDA, IDA) was in the first step described in the PSDA analysis method (Chapter 3). The PSDA and IDA were conducted using the same portfolio of recorded ground motions; however, IDA used a smaller subset of these. The theory behind IDA lies in the ability to take a small subset of ground motions from a larger catalog or series of bins and reuse the same motion to mimic variable intensities. This variation in intensity is achieved by incrementally increasing the amplitude of the ground motion record (Vamvatsikos 2002). Careful selection of PSDA bins described above ensured that intensity values were clustered at approximately the same values as the increments used in IDA, allowing comparable demand results. Ideally, a ground motion could be scaled until the structure collapses, generating a dynamic pushover plot.

Example IDA curves are shown in Figure 3.9. Usually plotted in linear scale, each curve depicts one ground motion as it was incremented. The *PGA* of each record was scaled individually in each increment, not the spectral acceleration. To see "stripes" in the analysis results, all records in the bins utilized would need to be scaled to the same $Sa(T_1)$ increment at each analysis step. A seamless transition to PSDMs was obtained when plotting the data points in log-space (Fig. 3.10) with $Sa(T_1)$ as the *IM*. All of the above figures were obtained using an IDA comprising 8 ground motions scaled 10 times each on the single-bent bridge base configuration. Therefore, they are comparable to Figure 3.8 of the cloud approach.

Of primary interest when using IDAs is the evolution of the median values (effectiveness), and dispersion (efficiency) surrounding functional fits to the data (see Section 3.4.4). Previous research showed as the number of ground motions used in IDA was increased from 4 to 8 and beyond, the first and second PSDM moments were in good agreement (Mackie 2002c). Using too few (4 or less) IDA ground motions led to the underprediction of the true model dispersion and introduction of model bias due to the ground motions selected. As mentioned previously, since the computational effort between PSDA and IDA is the same, PSDA "cloud" analysis was selected for all remaining demand model computations in this study.
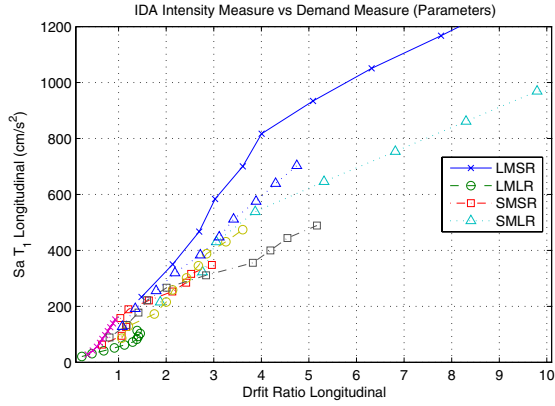
Fig. 3.9 Sample PSDM using IDA curves, **Fig. 3.10 Sample PSDM using IDA method,**
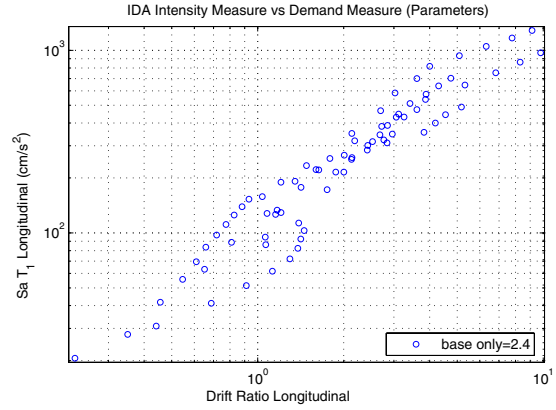
Sa(T₁)-Δ, **linear space**   *Sa(T₁)-Δ,* **log space**

3.3.4 PSDM Formulation

With the complete database of *IM*s and *EDP*s generated from either analysis method, it was then possible to generate an arbitrary PSDM by selecting a single variable from each group. In each subsequent PSDM, the data were plotted in (natural) log scale, with the demand measure (*EDP*) on the abscissa and the intensity measure on the ordinate. This is a standard method for plotting any *IM-EDP* relationship even though the demand measure is regarded as the dependent variable in all the models. Each demand model was constructed in the longitudinal and the transverse direction independently.   Where applicable, the demand model was also generated for the vertical direction, although these were not the focus of attention for developing optimal models.

Each PSDM was analyzed separately to determine the form of the mathematical model. The functional form in Equation 3.6 was fitted to the data.

$$\ln(EDP) = \ln(\hat{EDP}) + \sigma\varepsilon \tag{3.6}$$

The best estimate of the resulting model, $\hat{EDP}$, was defined as the median, or the mean of the natural log of the *n* data points (Eq. 3.7). The error term, ε, was assumed to be a normally distributed (standard normal) random variable with N(0, 1). As is commonly assumed (Gardoni 2002), the standard deviation of the model error (σ) was assumed to be independent of the independent variable (*IM*). This assumption may not be valid at higher intensities, but sufficed for the range of *IM*s considered in this study. The standard deviation of the model error (Eq. 3.8)

is termed "dispersion" in this study, as in Shome (Shome 1999). The dispersion is dependent on the number of parameters (*df*) being estimated in a linear regression on the *EDP* data.

$$\ln(\hat{EDP}) = \frac{1}{n}\left(\sum_{i=1}^{n}\ln(EDP_i)\right) \tag{3.7}$$

$$\sigma = \sqrt{\frac{\sum_{i=1}^{n}\left(\ln(EDP_i) - \ln(\hat{EDP})\right)^2}{n - df}} \tag{3.8}$$

Due to the presentation of PSDMs in log space, if the *EDP*s follow a power-law relationship, the *IM-EDP* relationship will appear customarily linear. Additionally, it is often assumed the conditional distribution of *EDP* on *IM* is lognormal. The lognormality assumption for *EDP*s has been observed by numerous researchers (Shome 1999; Gardoni 2002; Mackie 2003). Due to the lognormal form of the model, the coefficient of variation of the *EDP*s was approximately equal to σ (for small values of σ). The assumed (normal) simple form for the median *EDP* ($\hat{EDP}$) relationship in log space is shown in Equation 3.9 and linear space in Equation 3.10.

$$\ln(\hat{EDP}) = A + B\ln(IM) \tag{3.9}$$

$$\hat{EDP} = a(IM)^b \tag{3.10}$$

The parameters determined from linear least-squares regression are *A* and *B* (i.e., *df* = 2). The two equations are equivalent if $A = \ln(a)$ and $B = b$. A single linear fit was applied to the PSDMs obtained from PSDA and IDA in Figures 3.8 and 3.10, respectively. The resulting coefficients obtained from least-squares regression are A = -4.287 and B = 0.932 (cloud approach). The dispersion was 0.25. A comparison of the resulting fits (PSDA and IDA) is shown together in Figure 3.11.
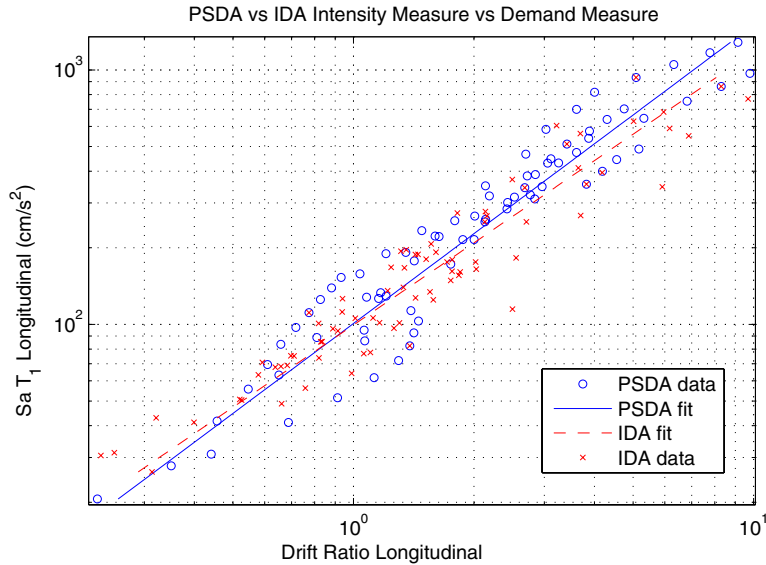
Fig. 3.11 Comparison of PSDM obtained from PSDA and IDA methods

While the linear fit is customarily made over the complete domain of the data, it is also possible to make piecewise linear fits in situations where a single fit does not describe the behavior being modeled. For the purposes of this study, bilinear and trilinear least-squares regressions were also performed on the data to reduce the model dispersion. Only the aleatory uncertainty due to the inherent randomness nature of earthquake input was considered in all PSDMs of this chapter. A treatment of epistemic and total uncertainty is included in Sections 3.9, 4.3, and 5.3.

3.4   OPTIMAL DEMAND MODELS

This section addresses the search for an optimal PSDM amongst the possible *IM* (Tables 3.1 and 3.2) and *EDP* (Table 3.4) combinations. Optimal was defined in Mackie (Mackie 2002a; Mackie 2003) as being practical, sufficient, effective, efficient, and robust. In summary, an *IM-EDP* pair is practical if it has some direct correlation to known engineering quantities and makes engineering sense. Specifically, *IM*s derived from known ground motion parameters are practical. *EDP*s obtained from subsequent nonlinear analyses are practical. The correlation between analytical models and experimental data lends further practicality to the *EDP*s of the demand model. A further criterion for evaluating practicality is whether the *IM* is readily described by available attenuation relationships or other sources of hazard data.

As discussed in Equation 1.2, the PEER performance-based design framework achieves disaggregation of the hazard and demand model if and only if the *IM-EDP* pair does not have a statistical dependence on ground motion characteristics, such as magnitude and distance. Such demand models with no conditional dependence are termed "sufficient" (Luco 2003). The effectiveness of a demand model is determined by the ability to evaluate Equation 1.2 in a closed form. For this to be accomplished, it was assumed that the *EDP*s followed a power-law relationship (Shome 1999). Thus an equation describing the demand model can be written as Equation 3.10 to which a linear, or piecewise-linear, regression in log-log space can be applied to determine the coefficients (Eq. 3.9). Demand models lending themselves to this form allow closed-form integration of Equation 1.2 and casting the entire framework in an LRFD type format (Lee 2002). An example of such an implementation is the SAC project (Cornell 2002; FEMA 2000b) for steel moment frames that proved to be crucial for wide adoption of probabilistic performance-based design in practice.

Efficiency is the amount of variability of an *EDP* given an *IM*. The measure used to evaluate efficiency is the dispersion (Eq. 3.8). An efficient demand model requires a smaller number of nonlinear time history analyses to achieve a desired level of confidence. In general, dispersion is a measure of randomness, or aleatory uncertainty, but is not the only source of uncertainty. Epistemic uncertainty, derived from such issues as modeling, nonlinearity, approximate analysis methods, and limited number of ground motions considered (Cornell 2002), is considered in Section 3.9. As mentioned previously, bilinear and trilinear fits were made to some PSDMs to reduce the calculated dispersion (increase efficiency).

Robustness describes the efficiency trends of an *IM-EDP* pair across different structures (and therefore fundamental period) ranges. Many of the Class I *IM*s used on unfiltered ground motion records produced nonrobust PSDMs. For example, *PGA* is practical, but only efficient for stiff (low-period) structures as it is a measure of the ground (zero-period structure) response. Similarly, *PGD* is only efficient for flexible (long-period) structures as it is a measure of the deformation of an infinitely flexible structure. A robust *IM* would approximately satisfy the relation in Equation 3.11.

$$\frac{\partial \sigma_{EDP|IM}}{\partial T_1} \approx 0 \qquad (3.11)$$

A number of *IM-EDP* pairs presented in the literature in recent years have been aimed at performance-based design of buildings (FEMA 2000b). Thus, a principal milestone in the development of a PSDM for highway overpass bridges is the search for an optimal intensity and demand measure pair for this class of structures. Several important distinctions should be made regarding the choice of *IM*s in the optimal PSDMs. First, efficiency is not the only measure for evaluation of optimality. Therefore, while some models exhibit lower dispersions than others, this alone does not make them optimal. Careful attention should be paid to practicality, effectiveness, and sufficiency. Second, among the models that are deemed optimal (specifically, they are practical, effective, and efficient), dispersion then becomes the measure of which PSDM is considered the "best." PSDMs with dispersions on the order of 0.20–0.30 are considered superior. However, the final PSDM selected not only exhibits all of these characteristics, but also does so for PSDMs generated for structures across a wide range of periods (robustness).

3.4.1   Existing *IM*s

Due to the prevalence of certain *IM*s currently adopted by both researchers and practitioners in the earthquake engineering field today, it was beneficial to develop optimal PSDMs from among these *IM*s only. The group of *IM*s under consideration was therefore *IM*s #1–5, 8, 11, and 14 from Table 3.1 and *IM*s #35–36, and 55 from Table 3.2. These *IM*s describe maximum quantities (e.g., *PGA* or *Sa*(T_1)), energy based quantities (e.g., Arias intensity or *CAV*), or duration quantities (e.g., strong motion duration). The common feature between all the *IM*s is that they are either described by an attenuation relationship, are used in site-specific hazard analysis, or are combinations of the other *IM*s selected. It should be noted that *Sa*, *Sv*, and *Sd* are used interchangeably in this section. As *Sa* and *Sv* are pseudo-spectral quantities (related to *Sd* by a constant factor of *T*), the resulting PSDMs in log-space all showed the same dispersion.

Presented below is a small subset of the entire parametric study performed, focusing on the parameters that produced an optimal demand model. All of the design parameters presented are in reference to the single-bent base bridge configuration. Design parameters referenced in this section were limited to the column-to-superstructure depth ratio (D_c/D_s), and the span-to-column height ratio (*L/H*). The R_{CS} factors for the base bridge (LMSR bin) are 2.1 and 1.5 for the longitudinal and transverse directions, respectively. For the SMLR bin, the R_{CS} factors dropped to unity (earthquakes do not produce inelastic behavior). The R_{USGS} factors for the base

bridge were 3.9 and 3.6 for the longitudinal and transverse directions, respectively. For each design parameter shown in subsequent PSDM plots, the corresponding dispersion value is displayed in the upper-left of the figure. Dispersions less than 0.3 are considered superior.

Given the varying engineering usefulness of each of the *EDP*s calculated (Table 3.4), an optimal demand model for each was developed. Several of the *EDP*s were mutually dependent and therefore produced a demand model with the same dispersion. For example, maximum displacement, displacement ductility, and drift ratio are related by constants (height and yield displacement). This is also true of maximum curvature and curvature ductility. Residual displacements, hysteretic energy, and plastic rotations yielded poor *IM-EDP* relationships and were therefore neglected in this section. The remaining *EDP*s considered can be categorized as either local, intermediate, or global.

3.4.1.1 Local Engineering Demand Parameters

Local demand quantities, such as material stress in the column, proved to be good performance indicators. Peak stress values in both steel and concrete materials were computed at the critical column cross section (location of maximum response). These values were obtained from monitoring the stress and strain directly in each fiber of the cross section. A PSDM for steel stress (σ_{steel}) was first developed showing *L/H* as the design parameter of variation. Four design parameters (four bridges) are shown on the same plot in order to assess the robustness of the chosen *IM*s across different bridge fundamental periods. Using first-mode spectral displacement, the resulting PSDM (Fig. 3.12) produced very efficient fits, largely due to the stress-plateau behavior at high stress levels. The bilinear PSDM fits reflect a bilinear material stress-strain envelope when the strain is thought of as a function of earthquake intensity.
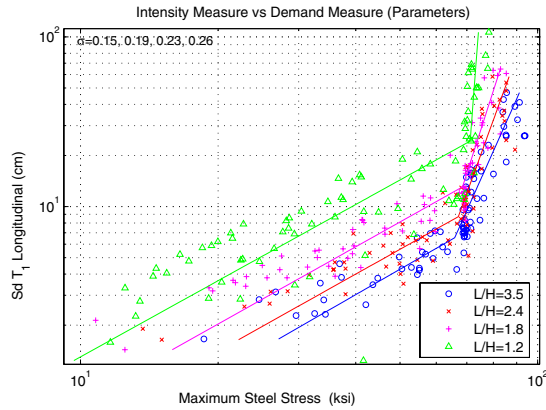
Fig. 3.12 *Sd(T₁)-σ_steel, L/H* **sensitivity longitudinal**
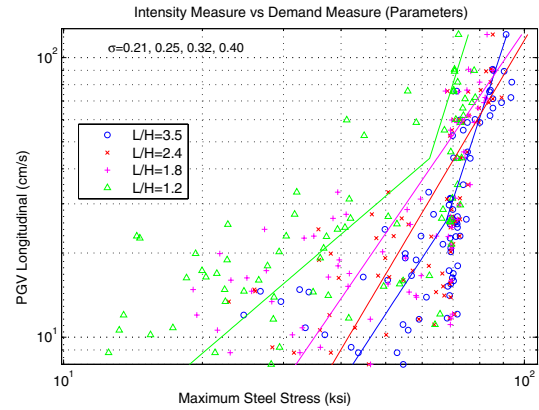
Fig. 3.13 *PGV-σ_steel, L/H* **sensitivity longitudinal**

The use of *Sd* can be confusing since changing design parameters also modifies the bridge period (e.g., stiffness in the *L/H* case, Fig. 3.12). The result is lack of commonality between the PSDMs shown in the same plot. If a single earthquake scenario is selected, then the *IM*s will be different for each bridge. Hence, there is no way to draw a single line of constant intensity across the PSDM plot to assess changes in performance. This became particularly important when considering design parameter sensitivities (Section 3.5). Therefore, an *IM* was sought which was necessarily independent of the bridge period, but still exhibited properties of an optimal PSDM. Results indicated the use of Arias intensity or PGV as period-independent *IM*s yielded models with dispersions approximately 50% higher than *Sd*. In the *PGV* case (Fig. 3.13), a line of constant intensity can be drawn across the plot to determine performance.

A PSDM was also developed for concrete stress (not shown here) using the same design parameter variation and *IM*s as the steel stress above. The bilinear PSDM fits were both efficient and effective. However, PSDMs involving concrete stress exhibited interesting behavior, as the separate maxima from unconfined and confined concrete could be discerned. Unlike steel, which continues to harden until high strains, concrete begins to soften post-peak at strains less of than 0.01. Therefore, each value of *f'_c* (for each separate bridge design) depicted two plateau regions in the results. As with steel, the stronger designs attracted more stress.
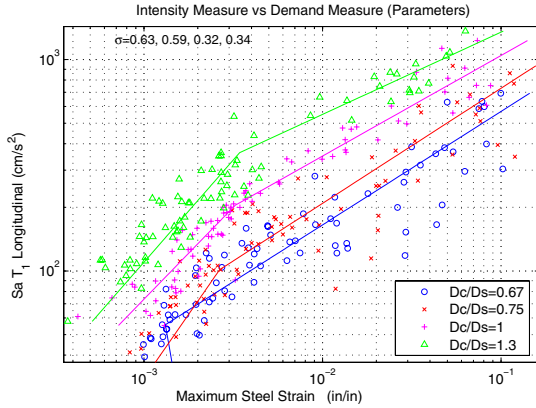
Fig. 3.14 $Sa(T_1)$-ε_{steel}, D_c/D_s sensitivity longitudinal
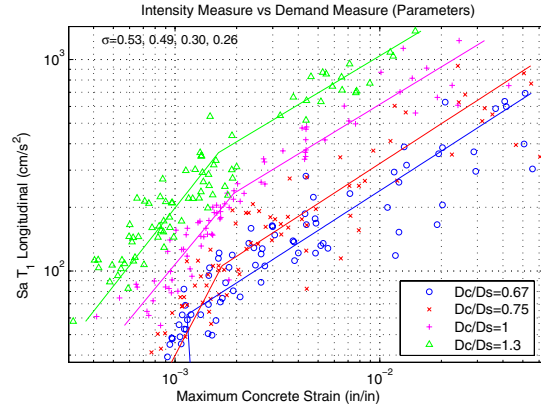
Fig. 3.15 $Sa(T_1)$-$\varepsilon_{concrete}$, D_c/D_s sensitivity longitudinal

While all of the local stress-based PSDMs developed show good qualities in terms of effectiveness and efficiency, none are practical from an engineering testing standpoint. At a local level, the only measure quantifiable during experimentation is strain. Deriving stress from this quantity would require analytical material models. Therefore, PSDMs using local material strains were also investigated, but suffered from a lack of efficiency. The steel strain model (Fig. 3.14) dispersion ranged between design parameters, even when using $Sa(T_1)$. The use of the period-independent *IM*s *PGV* and Arias Intensity resulted in dispersions approximately 50% higher. The steel model showed stiffer designs reduced demand, while the concrete strain model (Fig. 3.15) showed a similar trend for stronger designs. The increase in dispersion when using strain-based PSDMs (on the order of 100%) over stress-based PSDMs was enough to direct attention to the intermediate and global engineering demand parameters.

3.4.1.2 Intermediate Engineering Demand Parameters

The intermediate *EDP*s were obtained from the same critical column cross section used for the local *EDP*s. Figure 3.16 shows the ensuing PSDM for maximum moment in the longitudinal direction. The optimal *IM* for parametric variation of column diameter-to-superstructure depth ratio (D_c/D_s) was first-mode spectral acceleration. Spectral displacement provided an adequate extension of this relationship to the transverse direction (Fig. 3.17). It should be noted that T_1

56

and T_2 can be used interchangeably in the transverse direction and still maintain efficiency. The determination of optimal period is investigated in Section 3.4.3.
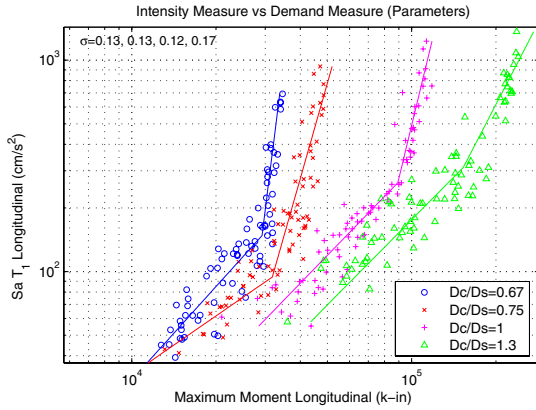
Fig. 3.16 $Sa(T_1)$-M_{max}, D_c/D_s sensitivity longitudinal
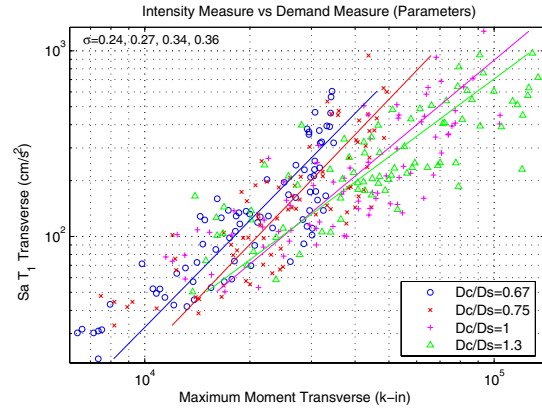
Fig. 3.17 $Sa(T_1)$-M_{max}, D_c/D_s sensitivity transverse

As would be expected, the stiffer the column was made, the more force it attracted. More flexible structures resulted in higher dispersions. Results indicated the use of Arias intensity or *PGV* yielded models with dispersions approximately 40% higher than $Sa(T_1)$. In addition, *PGV* and Arias intensity demand models exhibited higher dispersions for stiffer structures, indicating unpredictable behavior of these *IM*s except in the extreme low-period regime ($T < 0.3$ sec).

The most efficient and effective fits for column curvature ductilities were once more obtained by using $Sa(T_1)$ as the *IM*. The PSDM varying D_c/D_s for curvature ductility is shown in Figure 3.18. The large period dependence of the dispersions in this model should be noted, as was the case with local steel and concrete strain quantities. Therefore, for optimal demand models, the force-based quantities were more efficient than the deformation-based quantities (at the element level). As discussed earlier, it may be useful for the designer to consider period-independent parameters. Therefore, to eliminate Sd intensity shifts due to variation in T_1, the use of Arias intensity, characteristic intensity, or *PGV* as an *IM* increased dispersions by approximately 30% over $Sa(T_1)$. This dispersion increase resulted in very high dispersions (0.70–0.80) for some longer-period structures. Therefore, the curvature ductility demand model was not considered optimal.

3.4.1.3 Global Engineering Demand Parameters

The final PSDM developed was for drift ratio (or drift angle) of the column. Due to the relative rigidity of the deck, this response quantity also described the longitudinal movement of the deck at the abutments. The optimal model was obtained by varying D_c/D_s and again using $Sa(T_1)$ as the *IM* (Fig. 3.19). Other possibilities included incorporating Arias Intensity, *CAV*, or inelastic spectral displacement of the first mode as the *IM*. These options increased dispersions by approximately 33%–40% from using $Sa(T_1)$. Spectral acceleration and drift ratio exhibited all of the qualities of an optimal PSDM. Specifically detailed here are its extremely high efficiency (dispersion on the order of 0.20–0.30), and therefore ability to fit a single linear model to the data (effectiveness). Sufficiency is explored in the next section.
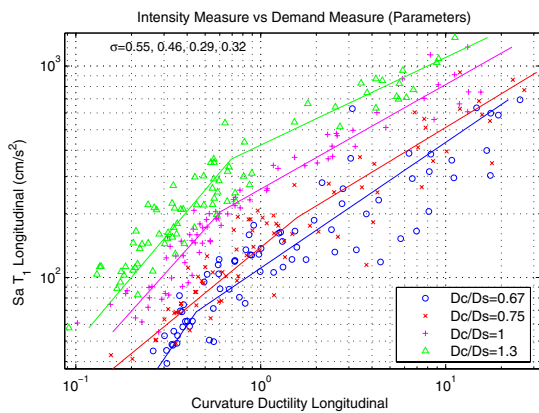
Fig. 3.18 $Sa(T_1)$-μ_ϕ, D_c/D_s sensitivity longitudinal
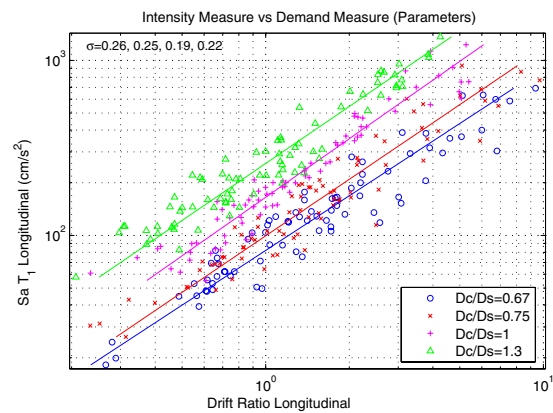
Fig. 3.19 $Sa(T_1)$-Δ, D_c/D_s sensitivity longitudinal

The PSDM for $Sa(T_1)$ and drift ratio was also constructed in the transverse direction. This PSDM exhibited slightly higher dispersions, on the order of 0.30–0.40. Therefore, in order to produce a PSDM with efficiency roughly equivalent to the longitudinal direction, IM_{1eff} (Cordova 2000) was employed. This *IM* incorporates more period information and is more efficient in predicting the transverse drift behavior (Fig. 3.20). If it is desired to use only the spectral quantities alone, *Sa* should be used for the transverse direction at the optimal transverse period (see Section 3.4.3.1).
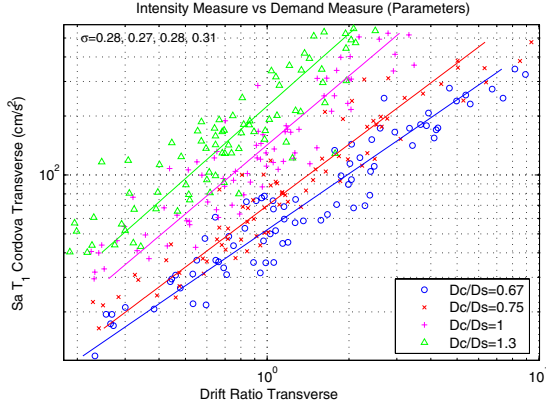
Fig. 3.20 IM_{1eff}-Δ, D_c/D_s sensitivity transverse
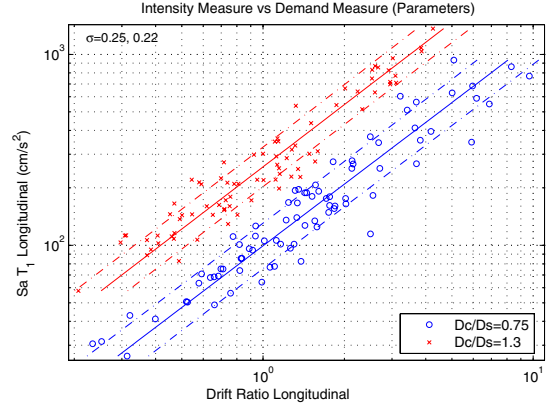
Fig. 3.21 $Sa(T_1)$-$\Delta \pm 1\sigma$ stripes, D_c/D_s sensitivity longitudinal

3.4.2   Verification of Optimality Conditions

From the previously discussed models, the relationship between $Sa(T_1)$ and longitudinal drift ratio for the column diameter (D_c/D_s) parameter variation (Fig. 3.8) was selected as the best existing IM optimal demand model based on efficiency and effectiveness. Therefore, it was investigated here for other demand model properties. As with any of the models, it is possible to generate not only the median fitted relationship (Eq. 3.9), but also the $\pm$ 1σ (16th and 84th percentile) distribution stripes. These stripes were calculated using the standardized residual form (Vardeman 1994) rather than simply adding the dispersion to the fitted EDP values (Eq. 3.12). The sample size is (for each structure and each PSDM of interest) once again n.

$$EDP_{\pm 1\sigma, j} = \sigma_{EDP|IM} \sqrt{1 + \frac{1}{n} + \frac{(IM_j - \mu_{IM})^2}{\sum_{i=1}^{n}(IM_i - \mu_{IM})^2}} \tag{3.12}$$

This probability distribution is shown in Figure 3.21 for the optimal PSDM.

Efficiency and effectiveness have already been established; however, sufficiency and practicality remain to be confirmed. The classification of practicality is, unfortunately, a subjective exercise. If the perception of the EDP is of holding a particular definition in the engineering sense, maximum material stress is then also practical. However, in terms of instrumentation and physical test specimens, stress by itself is an indeterminable physical quantity. A clearly practical EDP is the global drift ratio.

59

Sufficiency is required to determine whether the total probability theorem can be used to disaggregate the various components of the PEER framework equation. This cannot be done if there are any residual dependencies on M_w, R, etc. Equation 3.13 can be used with the form of the hazard curve in Equation 3.4 if the demand model is statistically independent (of M_w, R). Otherwise, Equation 3.3 must be utilized, necessarily complicating evaluation of Equation 1.2. Equation 3.13 describes the MAF of exceeding a demand limit state.

$$\lambda_{EDP}(edp) = \int G_{EDP|IM}(edp \mid im) \left| \frac{d\lambda_{IM}(im)}{dim} \right| dim \qquad (3.13)$$

To assess this sufficiency, regression on the *IM-EDP* pair residuals was performed, conditioned on M_w, R. The same formulation can also be applied to assess dependence on strong motion duration, D, even though this is usually not included in PSHA. The resulting sufficiency plots for the PSDM of interest are shown in Figure 3.22 for M_w, Figure 3.23 for R, and Figure 3.24 for D. The first takes moment magnitude (M_w) from the database of *IM*s and plots it versus the residual of the chosen *IM-EDP* fit. Similarly, the second plots residual versus closest distance (R), etc. The slopes of the linear regression lines in the plot are shown at the top of each of the plots. Small slope values for all parameters indicate that these demand models have the sufficiency required to neglect the conditional probability as described above.
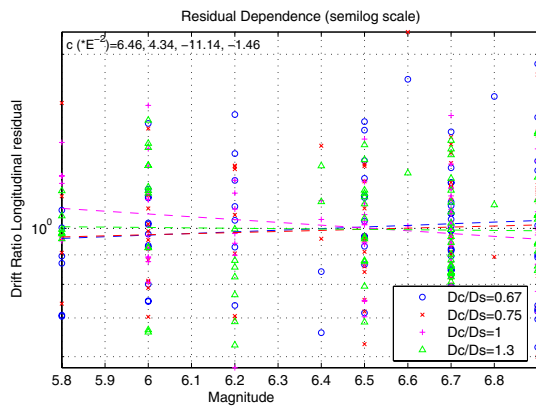
**Fig. 3.22 *Sa(T₁)-Δ Mₓ* dependence, *D_c/D_s*
sensitivity longitudinal**
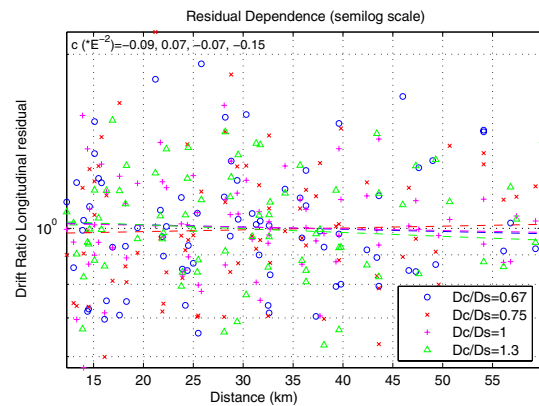
**Fig. 3.23 *Sa(T₁)-Δ R* dependence, *D_c/D_s*
sensitivity longitudinal**

60

A more rigorous definition of sufficiency can also be used when the regression lines described above are ambiguous. Fitting of residual data is equivalent to the multivariate linear regression of Equation 3.14. In attenuation relationships, R is often treated in log form; therefore $\ln(R)$ could also be used in Equation 3.14, if desired.

$$\ln(EDP) = A + B\ln(IM) + C_M(M) + C_R(R) + C_D(D) + \varepsilon \qquad (3.14)$$

While median coefficient values are shown in the plots, it is also possible to obtain statistics for an arbitrary confidence interval. If there is no residual dependence on M_w, R, and D, the coefficients C_M, C_R, and C_D are zero somewhere within the defined confidence interval. For purposes of this study, no residual dependence on a 90% confidence interval is termed sufficient. The optimal PSDM of interest does not exhibit any residual dependence on these quantities, as shown.

The final requirement for an *IM* to be classified as optimal is its usefulness across a large range of periods common to design. This implicit assumption is in large part the cause for rejection of such *IM*s as *PGA* or *CAV*. While these *IM*s may give efficient correlations for low-period structures (stiff), they lose efficiency in the longer periods. Given the practicality, efficiency, effectiveness, and sufficiency of $Sa(T_1)$, this *IM* is selected to investigate robustness across design parameters. The method used to evaluate robustness is the dispersion of the drift ratio and M_{max} PSDMs, given the *IM* and a set of bridges with specific design parameters varied (see Mackie 2003).

Four parameter groups were chosen (L/H, D_c/D_s, L, and Wt) because changing these parameters also alters the period of the bridge. The period values were normalized with respect to the period of the base bridge configuration and the dispersions were normalized with respect to the PSDM for the base bridge configuration. These normalized quantities facilitated comparisons between not only different *IM*s (and consequently different efficiencies) but also between different choices of the *EDP* (Δ and M_{max} are considered here) used in the PSDM. *Sa* efficiency improved in the long- and short-period ranges. In contrast, *PGA* rapidly lost robustness at longer periods. This phenomenon was in addition to *PGA*'s lack of overall efficiency.

To simplify the robustness trends, a linear regression across all the design parameter values (periods) was performed (according to Eq. 3.11). Figure 3.25 shows the robustness $Sa(T_1)$, *PGA*, and *CAV*. As with *PGA*, *CAV* continued to lose efficiency at longer periods, albeit

a somewhat more effective measure than *PGA*. Spectral acceleration even showed somewhat of a decrease in dispersion at longer periods (in the range of periods considered). Therefore, the previous conclusion regarding $Sa(T_1)$ being the optimal *IM* remains true when robustness in the presence of different design parameters is considered.
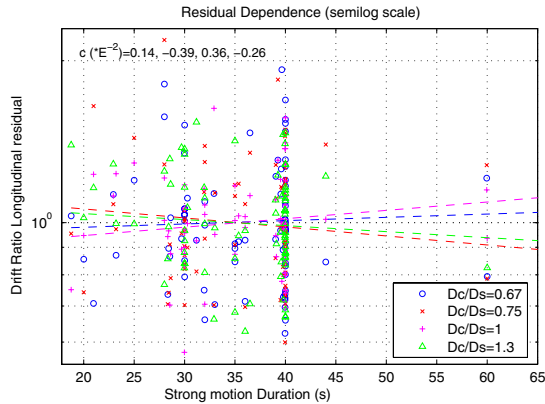
Fig. 3.24 *$Sa(T_1)$-Δ D dependence, D_c/D_s sensitivity longitudinal*
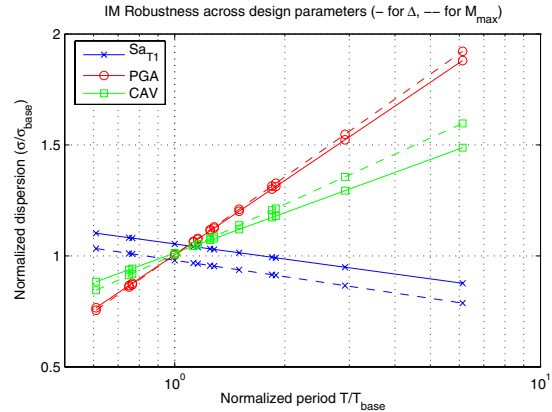
Fig. 3.25 Comparison of robustness for different *IM*s

In summary, it was found that first-mode spectral displacement ($Sd(T_1)$) was the optimal existing *IM* when coupled with a variety of *EDP*s. These *EDP*s included local measures (maximum material stresses), intermediate measures (maximum column moment), and global measures (drift ratio). Regardless of the fundamental vibration mode shape, T_1 remained the optimal period at which to sample the spectral quantities. This was useful for avoiding confusion over whether the longitudinal or transverse bridge response was being considered. With a sometimes large trade-off in efficiency, the use of period-independent Arias intensity or *PGV* as the *IM* was also acceptable as an optimal *IM*. Advantages to using period-independent *IM*s become readily apparent when varying bridge design parameters (Section 3.5).

Of the *EDP*s considered, the most efficient demand model was the relationship between $Sa(T_1)$ and drift ratio. This was also verified to be effective, sufficient, practical, and robust. The spectral values can be considered as superior *IM* quantities as they not only incorporate measures of the motion frequency content, but also are directly related to modal response of the given structure. Arias intensity does not include this structure-dependent information, but does include the cumulative effect of energy input from the ground motion. There are several practical reasons to utilize Arias intensity though, given that it can be used to compare structures

at constant intensity levels, and has been recently described by an attenuation relationship (Travasarou 2003).

As described after the definition of an optimal PSDM, this section does not address the issue of finding the lowest dispersion only. Further increases in efficiency of the demand models, beyond the basic spectral quantities used here, was possible and is pursued further in later sections using various spectral combinations (Section 3.4.3). These are not included here as they are only effective and efficient on a case-by-case basis. Also, they are not currently described by attenuation relationships, and are possibly difficult to scale to the same intensity level, making them an impractical general choice.

3.4.3   Highly Efficient *IM*s

While Section 3.4.1 covered the search for optimal PSDMs among *IM*s commonly used in research and practice today (for example, *PGA* and spectral acceleration), this section concentrates on the issue of finding extremely efficient PSDMs at the expense of familiarity with the resulting *IM*s. This section addresses improvement in PSDMs through selection of input parameters to the second class of *IM*s and the use of new filters to the third class. An efficient demand model requires a smaller number of nonlinear time history analyses to achieve a desired level of confidence. Therefore by minimizing the dispersion, tighter confidence bands on resulting demand, and ultimately decision, performance objectives can be achieved. For example, lowering the dispersion by a factor of two would require four times fewer ground motion records (Luco 2003) to achieve the same confidence interval.

There are two primary caveats to using the cloud procedure here as opposed to stripe analysis. First, the dispersion includes not only the randomness inherent in ground motions, but also a contribution from the error due to the choice of regression form over an *IM* range. Therefore, the total error might be overestimated due to this model error. Second, the dispersion is assumed constant over the entire *IM* range, an assumption that is often false at high intensities. However, for the purposes of this study, the standard PSDA approach is acceptable, as the *IM* range does not include extremely high intensities and a treatment of collapse. Additionally, as mentioned above, highly efficient models are implicitly effective, and as the dispersion is reduced, so is the model error. The dispersion was used solely as a means for comparing multiple *IM*s, therefore determining the proportion of model error in each was less important.

As an initial baseline, the efficiency of all Class I (Table 3.1) *IM*s are plotted in Figure 3.26 for several choices of structural period. In this medium-period range, the *IM*s exhibiting best efficiency are *PGV*, *PGD*, *CAD*, V_{rms}, and *I*. The *IM* number on the horizontal axis corresponds to the number in Table 3.1. It would be expected that many Class I *IM*s are largely period dependent. For example, *PGA* (*IM* #2) exhibited higher efficiency for stiff structures.
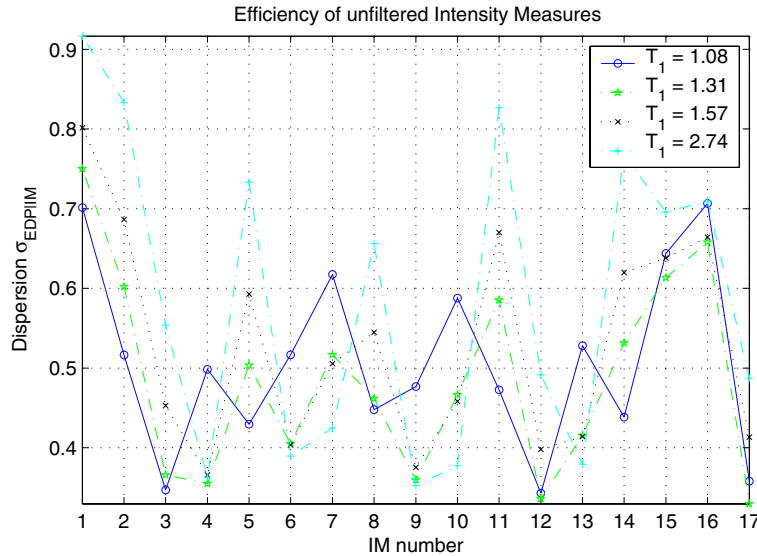
Fig. 3.26 Efficiency of Class I *IM*s

The period dependence is confirmed by the robustness plot in Figure 3.27. Only *PGD* (*IM* #4) showed improved efficiency at higher periods. This would be expected as the maximum displacement approaches the *PGD* in the long-period range. The period-dependent phenomenon, however, made any of the Class I *IM*s a poor choice for an arbitrary structure. Therefore, structure-specific quantities were pursued in the next two series of *IM*s.

The efficiency of all Class II (Table 3.2) *IM*s is plotted in Figure 3.28. The *IM* number on the horizontal axis corresponds to those listed in Table 3.2. Intermediate values not listed, for example 18–34, are simply Class I *IM*s from Table 3.1 acting on the SDOF filtered record. Specifically, 18–34 are elastic SDOF systems at T_1 and 5% viscous damping, and 37–53 are inelastic SDOF systems at T_1, 5% viscous damping, yield strength f_y of the structure, and 1% strain hardening. *IM* numbers 63–65 (average spectral quantities) are repeated seven times, each for different period bands about T_1. These are summarized in Table 3.3.
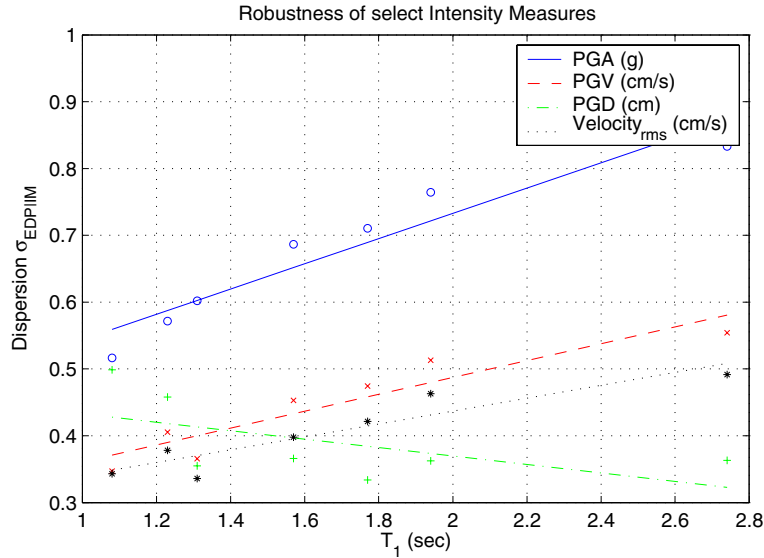
Fig. 3.27 Robustness of Class I *IM*s

The most efficient *IM*s in this class were (filtered SDOF records) elastic ^{SDOF}PGA (*IM* #19), elastic pseudo ^{SDOF}PGA (*IM* #36), inelastic ^{SDOF}PGD (*IM* #40), Luco first-mode predictor (*IM* #54), *EPD* (*IM* #58), *DSI* (*IM* #61), and the averaged spectral combinations from Table 3.3. While DSI exhibited the lowest dispersion of any *IM*s for several periods, it was not pursued further due to the large-period dependency. It should be considered, however, for long-period structures ($T_1 > 2.5$ sec).
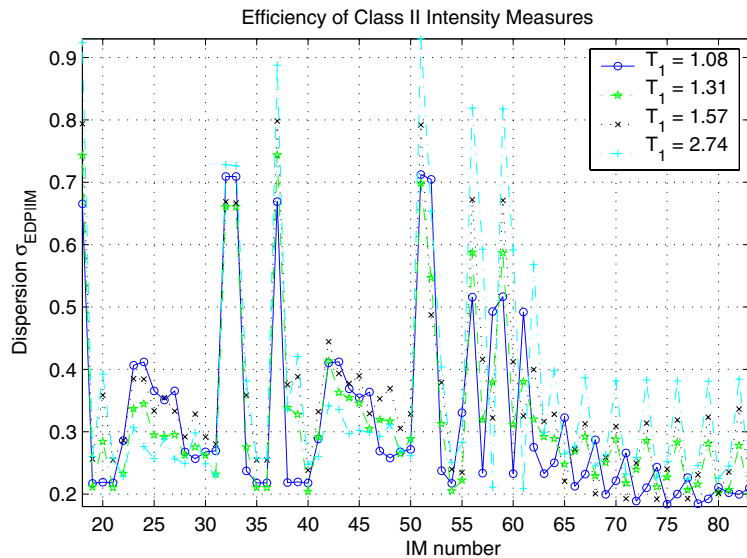
Fig. 3.28 Efficiency of Class II *IM*s

In most current demand analyses, $Sa(T_1)$ is used as the *IM*. This is in fact usually the pseudo-spectral acceleration (*IM* #36), not the actual maximum obtained from differentiating the time history displacement response twice. However, at the low levels of damping considered in this study, and for bridges in general, these quantities are essentially equivalent and only the ^{SDOF}PGA as defined in Table 3.2 will be used henceforth (this is the true spectral acceleration).

Given the traditional ^{SDOF}PGA as a benchmark, it can be seen from Figure 3.29 that inelastic ^{SDOF}PGD and averaging *Sa* offered improved efficiency. By narrowing the band around the period of interest, the efficiency of the results continued to improve. However, above band 6, the change in efficiency became negligible until it increased back to the level of ^{SDOF}PGA. It should be noticed that all of the *IM*s from Figure 3.29 were relatively insensitive to changes in the period. This made them appealing for use in any structural system. In practical application, the slight improvement in efficiency from using averaged spectral quantities is offset by the large amount of computation required to determine SDOF filtered records at all the intermediate periods. A single inelastic SDOF filtered record achieved similar results and requires only a single analysis.
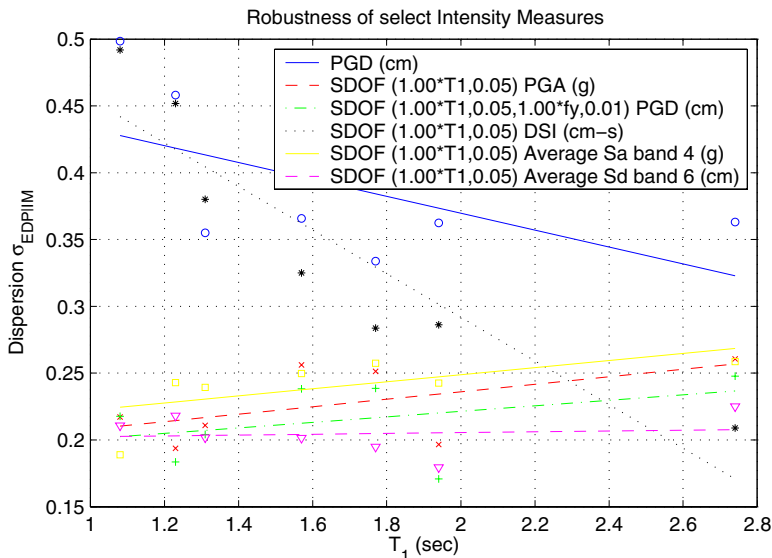
Fig. 3.29 Robustness of Class II *IM*s

Although not shown here, the same trends above were true in the transverse direction. However, it should be noted that there was slight negative correlation between period and efficiency in the transverse spectral quantities. This implies shorter-period structures (T < 1 sec

66

in this case) would be less efficient; however, this was found not to be the general trend (Mackie 2003).

Class III efficiency and robustness results are shown in Figures 3.30 and 3.31, respectively. The *IM*s with numbers 84–100 are Class I *IM*s acting on the u_1 2DOF filtered record; 101–117 acting on u_2. Promising 2DOF filtered *IM*s included ^{2DOF}PGD (*IM* #87), $^{2DOF}A_{rms}$ (*IM* #94), $^{2DOF}I_C$ (*IM* #97), and ^{2DOF}I (*IM* #100). The most robust choice was once again ^{2DOF}PGD.

A large amount of computation was required to average spectral quantities from Class II *IM*s over a range of periods. As shown above, these may be more efficient than spectral quantities at specific periods; therefore, an alternative method of achieving these results is desirable. The efficiency of Class I *IM*s acting on bandpass filtered records is shown in Figure 3.30 (*IM* numbers 120–134). Interestingly, for the bandpass filter, the same *IM*s were efficient as for the 2DOF filter. The highest efficiency was generated by $^{BP}I_C$ (*IM* #131) and $^{BP}I_A$ (*IM* #122); however, this was for the long-period range only. The best choice of *IM* was ^{BP}PGA (*IM* #119) for efficiency and robustness. ^{BP}I (*IM* #134) was also robust with slightly higher dispersion.
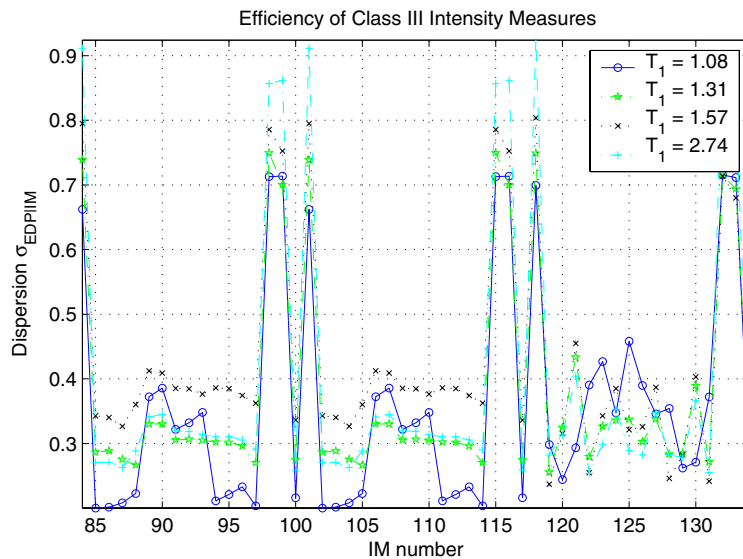
Fig. 3.30 Efficiency of Class III *IM*s
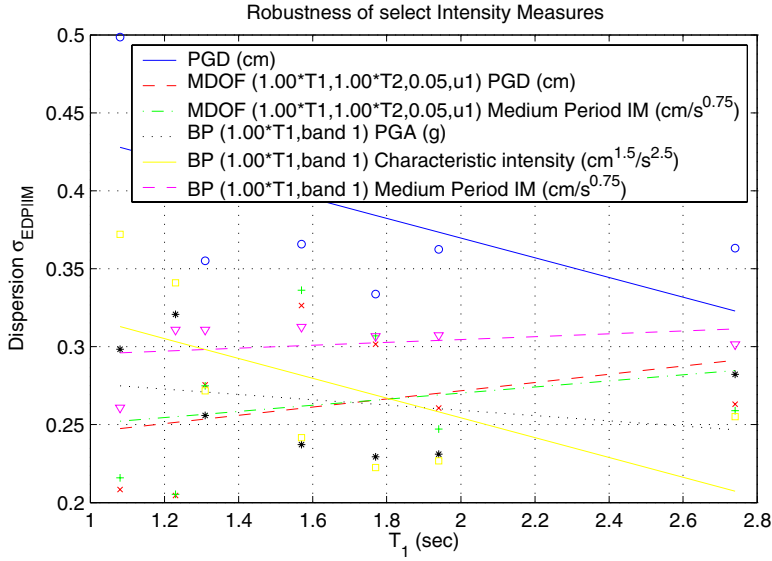
Fig. 3.31 Robustness of Class III *IM*s

3.4.3.1   IM Filter Parameter Sensitivity Study

With the introduction of filters described for Class II or III *IM*s comes a choice of filter parameters. All of the filters attempted to improve the predictive qualities of the resulting *IM*s by incorporating some knowledge of the structure, mainly through structural period. However, numerous other parameters exist and can be tuned to obtain more efficient results.   The parameters for Class II are rigorously investigated in the subsection below. Some insight gained is then applied to Class III in the subsequent subsection.

3.4.3.1.1 Class II Parameter Sensitivity

The SDOF system filter has two possible parameters for elastic systems and four possible parameters for inelastic systems. The common arguments are period, T, and viscous damping ratio, ζ. The inelastic bilinear system behavior was governed by the yield strength, f_y, and the hardening ratio, α_h. A parametric study of each is explored below.

Selection of the fundamental structural period, T_1, is an uncertain proposition by itself. Therefore, basing all Class II and III *IM*s on this quantity is imposing a lack of knowledge limitation on the resulting PSDMs. The elastic period was largely dependent on the selection of materials and elements in a finite element model or the choice of data sets in empirical period

predictions. The elastic period also changed after a structure had experienced inelastic excursions during earthquake excitation. Therefore, this parametric study focuses on the trends in the data to help rationally select a modification factor for filter periods. ^{SDOF}PGD was selected as the single *IM* on which to vary parameters, as it showed consistently high efficiency.

The sensitivity to period is shown in Figure 3.32 for the longitudinal direction for the case of three separate structures. The elastic SDOF filter (blue) is contrasted with the inelastic SDOF filter (green) on the same plot. The structures can be identified by the period at the minima from the entries in Table 3.5. A similar sensitivity plot is shown in Figure 3.33 for the transverse direction. The selection of a single period at which to develop a SDOF filter appeared as a clear minimization problem. Both Figures 3.32 and 3.33 were plotted with a fraction of the fundamental period T_1 on the horizontal axis. It was necessary to correct the period ratio based on the actual lowest period in the direction of interest. This was accomplished (see Table 3.5) using the pre– and post–gravity-load analysis periods in Table 2.2 and the locations of minima from the above plots (L_{fac} and T_{fac}, or longitudinal factor and transverse factor, respectively).
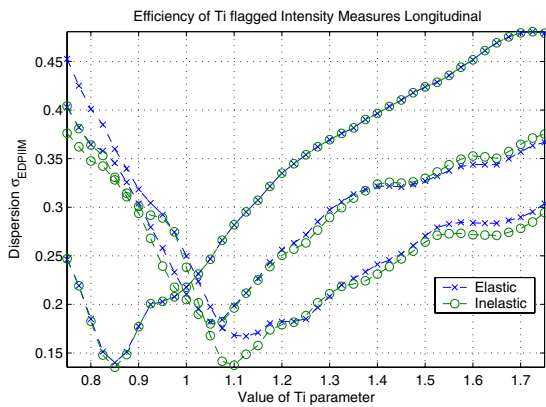
Fig. 3.32 Longitudinal period sensitivity   **Fig. 3.33 Transverse period sensitivity**
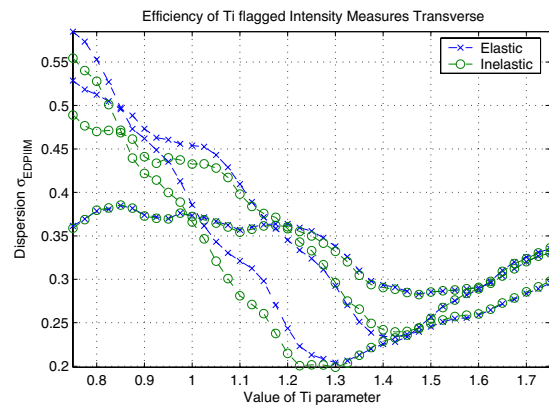
The results indicated the optimal transverse period was $T_T \approx 1.36(T_1)$ and the optimal longitudinal period was $T_L \approx 1.20(T_2)$. T_1 and T_2 in this case referred to the initial elastic periods in the transverse and longitudinal directions, respectively. Clearly, by choosing the initial elastic period, the single selection of T_1 for Class II *IM*s does not yield optimal results. It was therefore attempted to relate these period shifts to the loaded condition (post-gravity), a partially damaged condition (post-earthquake), and the complete post-earthquake event (displacement ductility *EDP*).

Table 3.5 Class II IM period modification factors

Structure number	T_{fac} (xT_1)	L_{fac} (xT_1)	L_{fac} (xT_{long})	Post-gravity		Post-earthquake	
				ΔT_{fac}	ΔL_{fac}	ΔT_{fac}	ΔL_{fac}
0001*	1.40	1.12	1.25	0.07	0.21	0.08	0.08
0005*	1.43	1.05	1.20	0.12	0.17	0.07	0.08
0009*	1.23	1.02	1.12	0.10	0.09	0.05	0.27
0013	1.20	1.10	1.19	0.13	0.15	0.04	0.15
0017*	1.30	1.10	1.20	0.07	0.16	0.09	0.09
0021	1.45	0.97	1.22	0.16	0.17	0.16	0.15
0025	1.48	0.85	1.21	0.02	0.18	0.01	0.18

The condition labeled post-earthquake was a low-level (elastic) earthquake simulation using the Covina-West Badillo Northridge earthquake record. By applying a ductility demand on the order of 0.5–0.8, cracking and nonlinear concrete behavior was induced, thereby somewhat elongating the period values. Table 3.5 shows the difference (ΔT_{fac} and ΔL_{fac}) between the observed minima and the post-gravity and post-earthquake normalized periods.

For the transverse direction, three predictive equations are proposed for estimating T_{fac} (relative to original T_1, initial elastic period) a priori (Eq. 3.15). The residuals are assumed to be normally distributed with a standard deviation indicated at the end of each equation. The response in the transverse direction was well described by the period after gravity-load analysis has been performed. Only to refine the estimate of T_{fac} (designated T_{fac}*) would it be necessary to incorporate information about the expected displacement ductility demand. The post-gravity ($T_{fac,gravity} = T_{post-gravity}/T_1$) and post-earthquake ($T_{fac,eqk} = T_{post-eqk}/T_1$) period factors should be determined for the bridge of interest prior to predicting the optimal transverse period with Equation 3.15.

$$T_{fac}^* = \begin{cases} T_{fac,gravity} & \sigma = 0.11 \\ T_{fac,eqk} & \sigma = 0.09 \\ 0.325\sqrt{\mu_\Delta} + 0.741T_{fac,gravity} & \sigma = 0.07 \end{cases} \qquad (3.15)$$

For the longitudinal direction, the results differed somewhat. The post–gravity-load-analysis period gave a poor estimate of L_{fac} (relative to original T_2, initial elastic period);

however, the expected displacement ductility demand and post-earthquake period were better predictors (Eq. 3.16). To reduce the scatter in the prediction, the post–gravity-load factor was combined with the average displacement ductility demand to better estimate L_{fac} (designated $L_{fac}{}^*$). Similarly, the post-gravity ($L_{fac,gravity} = L_{post-gravity}/T_2$) and post-earthquake ($L_{fac,eqk} = L_{post-eqk}/T_2$) period factors should be determined prior to predicting the optimal longitudinal period with Equation 3.16.

$$L_{fac}^* = \begin{cases} \sqrt{\mu_\Delta} & \sigma = 0.20 \\ L_{fac,eqk} & \sigma = 0.17 \\ \sqrt{\mu_{\Delta,mean}}\, L_{fac,gravity} & \sigma = 0.04 \end{cases} \tag{3.16}$$

The displacement ductility demands (μ_Δ) used in the analyses were the mean plus half standard deviation for each given structure, unless otherwise noted.

Almost all spectral analyses done today use a damping coefficient of 5% of critical. This may not agree with the damping in any of the actual structural modes under consideration. The finite element model of the bridge used Rayleigh damping calculated for the first two modes. The specified damping ratio was 2.5% of critical. Using the calculated α_1 and β_2 parameters (mass and stiffness proportional damping), the effective damping ratio in each of the modes was back calculated. For both the longitudinal and transverse directions, this value was 2.6% for both pre- and post-gravity-load analyses. These values were then also verified by free-vibration tests on the structure in each of these directions. Free-vibration tests indicated whether other modes were present in the two primary directions. The results yielded similar damping values, 2.3% for the longitudinal direction, and 3.1% for the transverse direction. Transverse free vibration included a small contribution from the third mode, especially for structures 0021 and 0025.
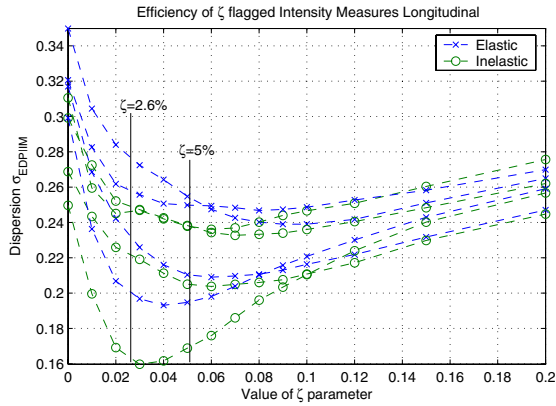
Fig. 3.34 Longitudinal damping ratio (ζ) sensitivity
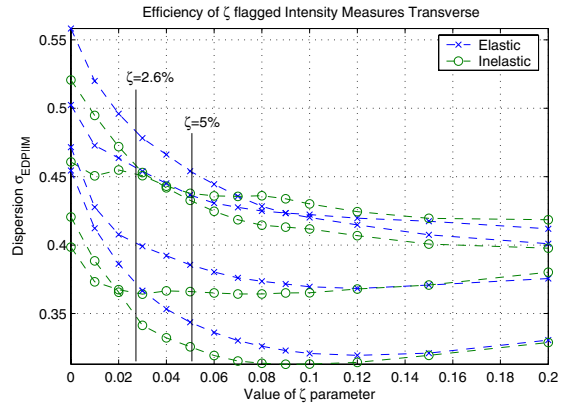
Fig. 3.35 Transverse damping ratio (ζ) sensitivity

Figure 3.34 shows the sensitivity to damping ratio in the longitudinal direction, Figure 3.35 in the transverse direction for structures marked with an asterisk in Table 3.5. There were no apparent trends in either direction that suggested an improved value of the damping ratio to use in SDOF filters. While not the optimal value, the use of 5% damping in each case yielded better results than using the system damping ratio.

For the case of the inelastic SDOF filter, the yield strength of the system needed to be specified as an additional parameter. A bilinear fit to the nonlinear force-displacement pushover response of the structure was made. The yield strength was chosen to minimize the area between the pushover curve and bilinear approximation (FEMA 2000a). Yield strength sensitivity in the longitudinal direction is shown in Figure 3.36 and the transverse direction in Figure 3.37.
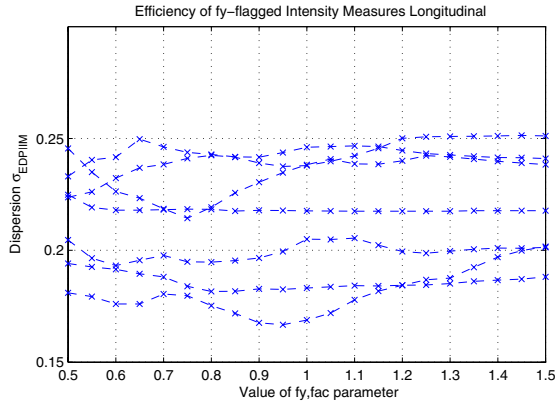
Fig. 3.36 Longitudinal yield strength (f_y) sensitivity
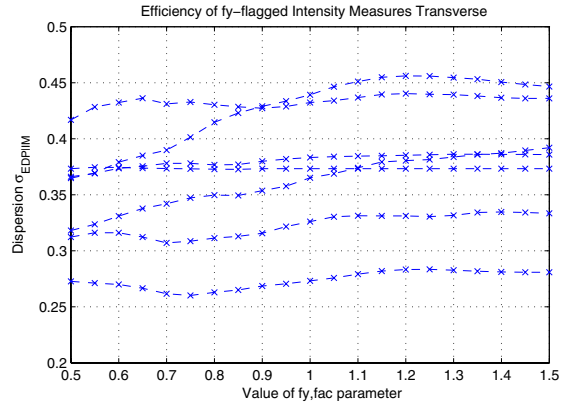
Fig. 3.37 Transverse yield strength (f_y) sensitivity

While there appeared to be some benefit to allowing the onset of hysteretic behavior (lower f_y), there was no definitive optimal choice of this parameter. The values on the abscissa were normalized with respect to the selected yield strength of the system. It should also be noted that selection of f_y from a nonlinear pushover is not exact, but given the bounds on the f_y parameter in this study, it would suggest the exact value chosen is unimportant.

The hardening ratio can be determined from the bilinear fit made to the pushover of the structure. Only the sensitivity to the hardening ratio in the longitudinal direction is shown (Fig. 3.38). The value was varied widely and had little impact on the model efficiency. A value of 0.02 is recommended for use with inelastic SDOF filters. It should be noted that the value used for steel strain hardening in the finite element model was 1.5%. The transverse results were comparable but not shown here.

3.4.3.1.2 Class III Parameter Sensitivity

Focusing on the 2DOF filter introduced earlier, the individual values of T_1 and T_2 were varied neither explicitly nor with respect to each other. However, the relationships developed for the SDOF filter periods ($T_{fac}*$ and $L_{fac}*$ in Eqs. 3.16 and 3.15, respectively) were applied to the 2DOF filter to determine if this was beneficial to the efficiency of the 2DOF filter as well. Compared to the values for the basic MDOF filter in Figure 3.30, the selection of optimal SDOF periods also slightly improved the overall performance for the 2DOF filter.

Focusing on the bandpass filter, a parameter study was performed using the same procedure as for the SDOF filter. It was assumed that the optimal single period, and therefore the central frequency, was determined using Equations 3.15 and 3.16. The only parameter that was varied was then the bandwidth B of the filter. The same values were used as in Table 3.3 to facilitate comparison. A comparison of results is shown for the bandpass filter and the corresponding averaged spectral combinations in Figure 3.39. As with the average spectral quantities from Table 3.3, choosing a bandwidth between bands 5 and 6 produced optimal results.
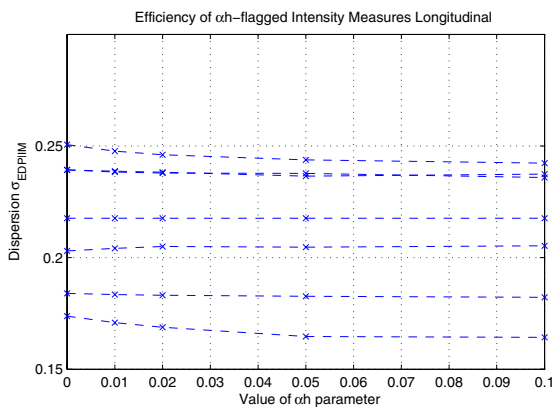
Fig. 3.38 Longitudinal hardening ratio (α_h) sensitivity
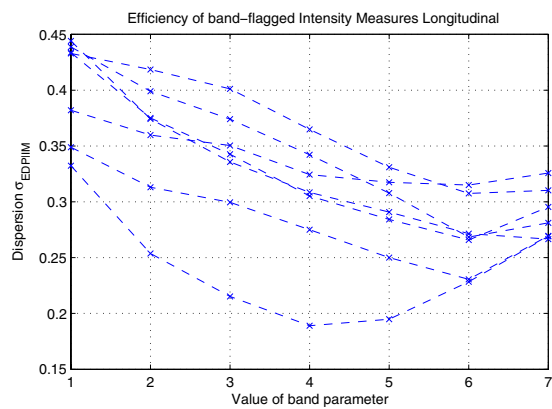
Fig. 3.39 Longitudinal band sensitivity

Several thousand existing and new *IM*s were considered in this exhaustive study. The goal was to develop a PSDM that exhibited a higher level of efficiency than conventional *IM*s (Section 3.4.1). This allows a higher level of confidence in achieving performance objectives, both at the demand level, and as part of the complete PBEE framework. It was not intended to achieve increased efficiency by developing spectral or other combinations with calibrated structure-specific constants. Rather, from the existing pool of *IM* knowledge, it was intended to isolate the input parameters that make *IM*s better predictors in PSDMs. By choosing a medium- and long-period range of bridge structures with which to generate these models, the period dependence (lack of robustness) of Class I (unfiltered) *IM*s was revealed. This facilitated the optimal selection of parameters for Class II (SDOF filtered) *IM*s and possible future development of new Class III (arbitrary filter) *IM*s.

While current use of $Sa(T_1)$ as the *IM* in seismic performance assessment provides better efficiency than previously used *IM*s such as *PGA*, $Sa(T_1)$ is neither the best *IM* choice, nor is T_1 the best period choice. It was determined that inelastic ^{SDOF}PGD outperforms elastic ^{SDOF}PGD (standard spectral displacement) for a large period range. Depending on the direction of concern (longitudinal or transverse), a modified period value outperforms the initial elastic period. By performing gravity-load analysis, or low-level static or dynamic analysis on the structure, the resulting period is a better predictor for post-earthquake response. It is also possible to modify the initial elastic period by the expected displacement ductility demand on the structure during the earthquake. Equations 3.16 and 3.15 can be used to accomplish this period modification. For the inelastic SDOF filter, the yield strength obtained from the nonlinear pushover response should be used. The hardening ratio corresponding to the global structural hardening ratio should be employed, and a damping ratio of 5% of critical selected.

If improved efficiency above ^{SDOF}PGD is desired, this quantity should be averaged over a narrow band (0.8–1.25 times period) around the filter's structural period. To be more computationally efficient, this procedure can also be accomplished using a bandpass filter with the same frequency band. For a structure with earthquake response in several modes, the concept of a MDOF or multiple pass-band Class III filter can be investigated. The use of the bandpass filter for the Class III *IM*s was more computationally efficient than solving the equations of motion. All of the *IM*s were evaluated with respect to a PSDM containing drift ratio as the *EDP*. It was also found that the optimal choice of *IM* and selection of T_1 using Equations 3.16 and 3.15 were applicable to PSDMs containing maximum column moment, displacement ductility, and residual displacement. PSDMs featuring cumulative *EDP*s, such as normalized hysteretic energy, were optimal with inelastic $^{SDOF}I_C$ and inelastic $^{SDOF}I_A$ *IM*s. The best results were once again obtained when modifying the period using Equations 3.16 and 3.15.

3.5   DESIGN PARAMETER VARIATION

This section addresses the trends evident in PSDMs obtained from varying various bridge design parameters, and development of methods employing PSDMs to predict bridge response without coupling to the complete PBEE framework. All of the design parameters presented are in reference to the same single-bent base bridge configuration. Once again, the variation of design

parameters from this base configuration (Table 2.1) was intended to cover the complete spectrum of possible bridge designs, even if independent values were uncommon in design practice.

In the parametric study of this section, the *IM*s were limited to the spectral quantities, *PGV*, *PGD*, and *CAD* only. First-mode spectral displacement $Sd(T_1)$, $Sa(T_1)$, and $Sv(T_1)$ were used interchangeably, as the dispersions in the PSDMs were independent of the choice of spectral quantity. Of the total possible *EDP* combinations, only a few were selected for the design parameter study, as based on their previously determined optimal properties. Two global *EDP*s, used in current bridge design practice, are the column drift ratio (Δ) and displacement ductility (μ_Δ). These are two kinematically dependent measures that can be used interchangeably in the PSDMs. The other *EDP*s that yielded optimal PSDMs were maximum column moment (M_{max}) and curvature ductility demand (μ_ϕ), intermediate *EDP*s, and concrete material strain (ε_{conc}), a local *EDP*.

The consequence of choosing spectral quantities for the demand model is the period dependence of the *IM*. Since the initial elastic stiffness was used to compute the measure of $Sa(T_1)$, design parameters that vary the stiffness of the bridge system will cause intensity shifts in the demand models for a given earthquake. Alternative *IM*s, which introduced more dispersion, were *PGV*, *PGD*, and *CAD*. To alleviate the *IM* period dependence, these *IM*s can be used when comparing *EDP*s. In this case, the result is a single line of constant *IM* value parallel to the *EDP* axis that aids direct evaluation of varying design parameters on performance.

Given the trends due to design parameter variation described by period-independent *IM*s, a set of design equations can be written. A single design equation for each design parameter was generated for each *IM-EDP* combination. The equation can be used explicitly by designers without coupling to Equation 1.1. This was done at the expense of efficiency, albeit eliminating *T* as a design variable. The general form of a design equation was found to follow Equation 3.17.

$$
\begin{aligned}
\ln(E\hat{D}P) &= \left(A_i x^2 + A_j x + A_k\right) + \left(B_i x^2 + B_j x + B_k\right)\ln(IM) \\
&= A(x) + B(x)\ln(IM)
\end{aligned}
\tag{3.17}
$$

This form was not suitable for all *IM-EDP* combinations, but in general, for any PSDM that was both effective and efficient, Equation 3.17 provided a good estimate of the median response (σ_{fit} < 0.05). An estimate of the model dispersion to use for a PSDM obtained from this equation is suggested in Section 3.8.1.

Specifically, the design parameters considered in this section were D_c/D_s, L/H, $\rho_{s,long}$, and L. The three geometric design parameters were marked by varying bridge stiffnesses, evident in the period differences within parameter groups (Table 2.2). The initial stiffness of the bridge was only minimally influenced by the amount of reinforcement (longitudinal and transverse) in the reinforced concrete column section. The only parameter that altered the mass, and accordingly the spectral values, was the additional deadweight, Wt. In order to understand the effect of design parameters, constant intensity lines (black dashed lines) have been added to the figures below. This was performed regardless of the period dependence of the IM selected in each PSDM.

As a demonstration of the pitfalls of selecting $Sa(T_1)$ as the IM of choice for design parameter comparison, two optimal models (local and intermediate EDPs, respectively) for the column diameter parameter (D_c/D_s) sensitivity are shown in Figures 3.40 and 3.41, respectively. Also shown on the figures are sample design trends when evaluating performance by varying the column diameter. Variation of column-to-superstructure dimension ratio (D_c/D_s) was based on varying the column diameter as the superstructure depth and other properties were held fixed throughout. By increasing the diameter, the bridge stiffness increased and there was a resulting decrease in the maximum concrete strain demand in the column (Fig. 3.40). Similarly, as the diameter increased, the maximum curvature ductility demand was also reduced (Fig. 3.41). Lines of constant intensity were included for the case of the Sunnyvale-Colton Avenue (Table A.1) earthquake scenario. Assessing trends is an iterative process in this case as the period needs to be calculated for each bridge design parameter value selected.
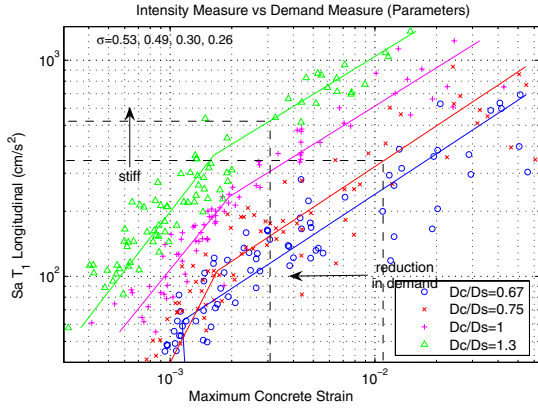
Fig. 3.40 $Sa(T_1)$-$\varepsilon_{concrete}$, D_c/D_s sensitivity longitudinal
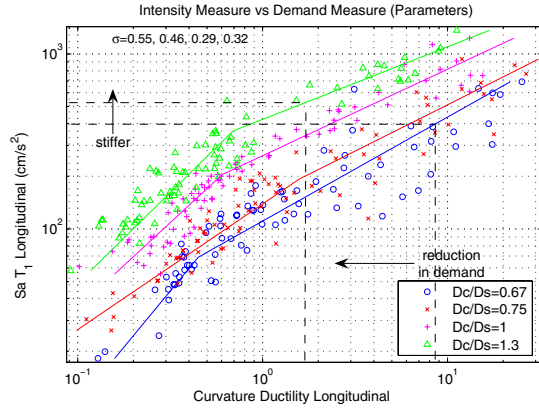
Fig. 3.41 $Sa(T_1)$-μ_ϕ, D_c/D_s sensitivity longitudinal
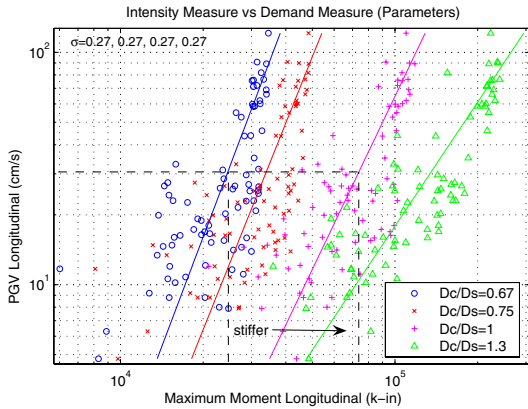
Fig. 3.42 PGV-M_{max}, D_c/D_s sensitivity longitudinal
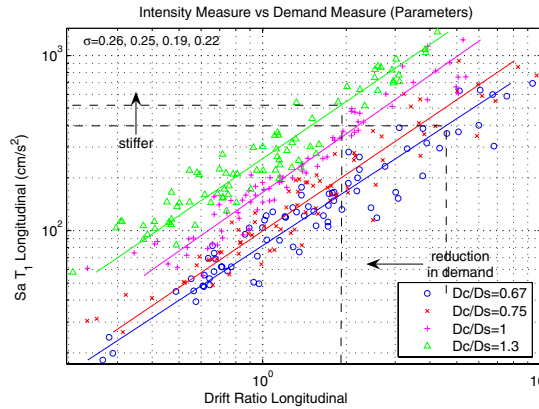
Fig. 3.43 $Sa(T_1)$-Δ, D_c/D_s sensitivity longitudinal

A desirable property of design parameter PSDMs is therefore to include a period-independent *IM* and also to be effective (described by a single linear fit in log-space). Any PSDM of this form lends itself to the uncomplicated determination of a design equation (Eq. 3.17). For example, using *PGV* and the maximum column moment, a desirable PSDM was formed (Fig. 3.42). As the column diameter was increased, the stiffness and strength of the column were also increased and more force (moment) was attracted. The slope of the fits corresponded directly to the rate of change of performance (demand). Steep slopes resulted in minimal demand changes, while shallow slopes produced large demand reductions for small

variations in design parameter values. The design equation for Figure 3.42 is shown in Equation 3.18.

$$\ln(M_{\max}, long.) = \left(-3.59x^2 + 8.45x + 4.96\right) +$$
$$\left(0.435x^2 - 0.474x + 0.445\right)\ln(PGV, long.) \tag{3.18}$$
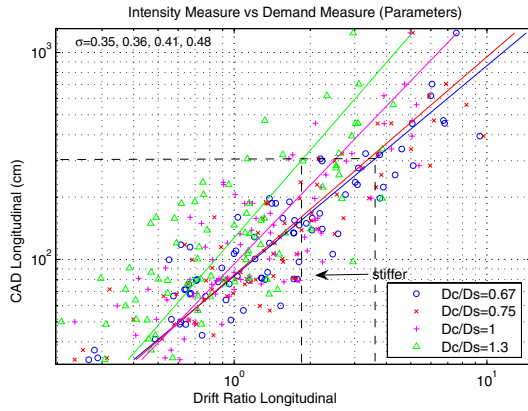
Fig. 3.44 *CAD-Δ, D_c/D_s sensitivity longitudinal*
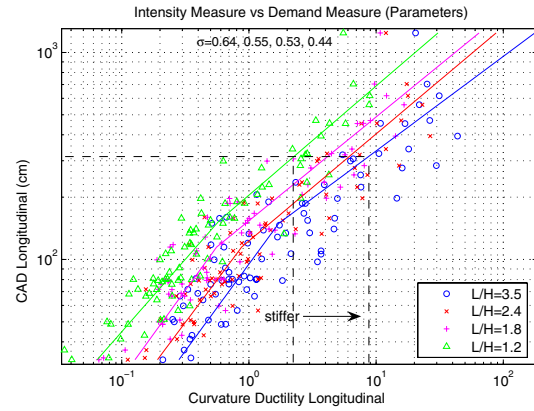
Fig. 3.45 *CAD-μ_ϕ, L/H sensitivity longitudinal*

Maintaining D_c/D_s as the design parameter, the design parameter (and thus period) dependent change in dispersions between a period-dependent ($Sa(T_1)$) and period-independent (*CAD*) *IM* was assessed directly. The optimal global *EDP* (Δ) PSDM was selected for comparison. The PSDM formed with $Sa(T_1)$ is shown in Figure 3.43, including trends showing the decrease in drift ratio as the column stiffness was increased. Figure 3.43 is typical of how shallow slopes show larger performance differences. The corresponding period-independent PSDM is shown in Figure 3.44, formed with *CAD*. The drawbacks of period-independent *IM*s are immediately evident, as efficiency values dropped by 35–100%. The continuously efficient *IM* across the complete design parameter period range was noticeably absent, as Class I *IM*s are not robust (Section 3.4.3). Therefore, confidence in the PSDMs used for design parameter variation was lower; however, they provided the best means to investigate the effect of design parameter variation. The design equation stemming from Figure 3.44 is shown in Equation 3.19.

$$\ln(\Delta, long.) = \left(-2.70x^2 + 6.81x - 7.74\right) +$$
$$\left(0.490x^2 - 1.41x + 1.72\right)\ln(CAD, long.) \tag{3.19}$$

The drop in efficiency using period-independent *IM*s is not always as pronounced as the case above. For example, the PSDM formed between $Sa(T_1)$ and curvature ductility demand already exhibited higher dispersions (Fig. 3.18). Therefore, the introduction of *CAD* in Figure 3.45 had little impact on the model efficiency. Therefore, *CAD-μ_ϕ* was used to illustrate trends in performance due to variation of the span-to-column height ratio design parameter (*L/H*). The span length was held fixed while the value of *L/H* determined the column height. Therefore, as *L/H* was increased, the bridge became stiffer (more squat). A single line of constant intensity shows the increase in curvature ductility demand as the column becomes shorter (stiffer). While it was possible to write a design equation for this PSDM and *L/H* sensitivity, the use of a piecewise linear median fit to reduce the model dispersion introduced the need for two design equations and *IM* limits for usage. The intersection of the bilinear fit varied based on the value of the design parameter; therefore, it is easier to solve both equations and select the larger response value if the fits are concave, and the smaller value if the fits are convex (as viewed from the origin). The two design equations for Figure 3.45 are shown in Equation 3.20.

$$\ln\left(\mu_\phi, long.\right) = \max_{convex} \begin{cases} \left(-0.610\,x^2 + 3.81x - 11.3\right) + \left(0.101\,x^2 - 0.564\,x + 1.94\right) \cdot \\ \qquad\qquad\qquad\qquad\qquad\qquad\qquad \ln\left(CAD, long.\right) \\ \left(-0.552\,x^2 + 2.53\,x - 12.5\right) + \left(0.0556\,x^2 - 0.149\,x + 2.02\right) \cdot \\ \qquad\qquad\qquad\qquad\qquad\qquad\qquad \ln\left(CAD, long.\right) \end{cases} \quad (3.20)$$
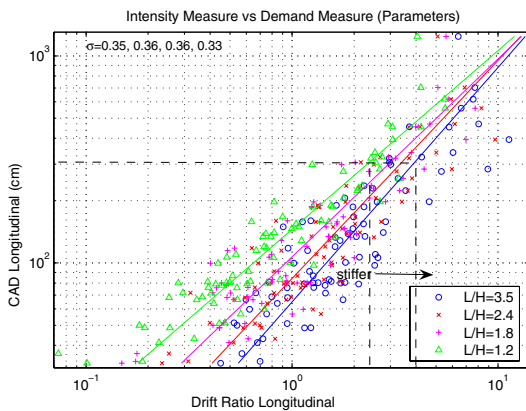
Fig. 3.46 *CAD-Δ, L/H* sensitivity longitudinal
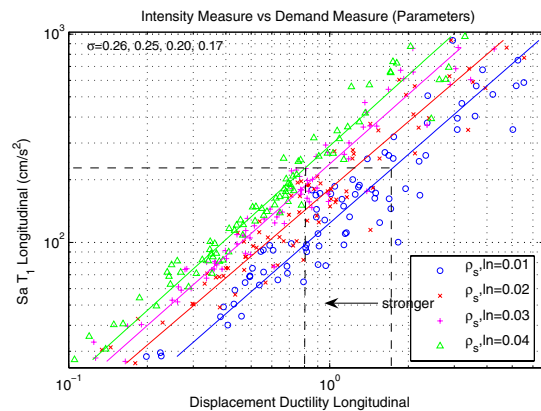
Fig. 3.47 *Sa(T₁)-μ_Δ, ρ_{s,long}* sensitivity longitudinal

Similar to the variation of D_c/D_s, the period-independent PSDM for *L/H* was formed with *CAD* and a single linear median fit (Fig. 3.46). As *L/H* was increased (column is shorter), the

drift ratio actually increased. While this may seem counterintuitive, it should be realized that the maximum displacement (u_{max}) was decreasing with increased stiffness; however, drift ratio is a normalized quantity. Therefore, the change in column height was larger than the change in u_{max} between design parameter values. The design equation for Figure 3.46 is shown in Equation 3.21.

$$\ln(\Delta, long.) = \left(-0.350x^2 + 2.55x - 8.34\right) + $$
$$\left(0.0466x^2 - 0.340x + 1.50\right)\ln(CAD, long.)$$

(3.21)

The steel reinforcement ratio ($\rho_{s,long}$) was one of the parameters not causing large intensity shifts in PSDMs formed with spectral quantities. Using $Sa(T_1)$, the reduction in displacement ductility demand was immediately correlated to the design strength (Fig. 3.47). A linear increase in reinforcement did not correspond to a linear decrease in demand, however. The sensitivity of performance at lower reinforcing ratios was more pronounced. Similarly for forces, increasing the reinforcing amount had a drastic effect on the amount of moment attracted to the column (Fig. 3.48). This PSDM used CAD instead of $Sa(T_1)$, as the dispersions remained low. Evident are two linear regimes for each design parameter, as may be expected of an idealized bilinear moment-curvature relation of the column cross section. A design equation is only shown (Eq. 3.22) for the single linear fit of Figure 3.47.

$$\ln(\mu_\Delta, long.) = \left(884x^2 - 63.5x + 0.894\right) + $$
$$\left(-87.1x^2 + 3.18x + 0.894\right)\ln(Sa(T_1), long.)$$

(3.22)
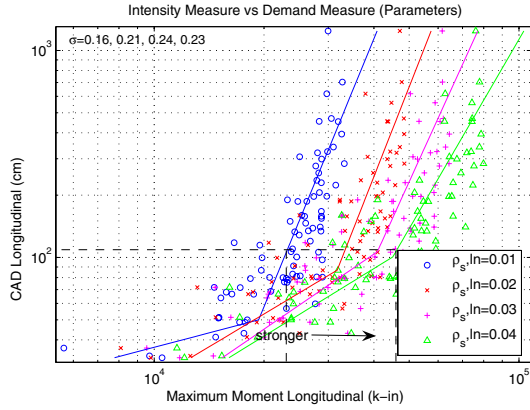
Fig. 3.48 *CAD-M$_{max}$, $\rho_{s,long}$* sensitivity longitudinal
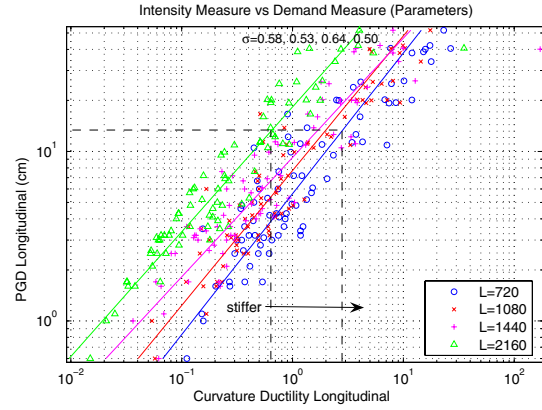
Fig. 3.49 *PGD-μ_ϕ, L* sensitivity longitudinal

The *L* design parameter effects the overall size of the bridge, as the column height grows according to a constant *L/H* ratio. Therefore, as *L* was increased, overall flexibility increased. Performance trends due to varying *L* are shown for curvature ductility and drift ratio in Figures 3.49 and 3.50, respectively. The large values of *L* resulted in bridge periods beyond 2 sec; hence the period-independent *IM PGD* became more efficient. For stiffer bridges (small *L*), the curvature ductility demand increased. The corresponding design equation is shown in Equation 3.23. Similar to the *L/H* variation, the drift ratio actually increased for stiffer structures (small *L*). However, the maximum displacement was increasing for larger values of *L*. The drift ratio response for *L* can be described by Equation 3.24.

$$
\ln\left(\mu_\phi, long.\right) = \left(2.07e^{-7}x^2 - 0.00191x - 0.793\right) +
$$
$$
\left(-2.04e^{-7}x^2 + 7.14e^{-4}x + 0.776\right)\ln\left(PGD, long.\right)
$$
(3.23)

$$
\ln\left(\Delta, long.\right) = \left(1.94e^{-7}x^2 - 0.0019x + 0.349\right) +
$$
$$
\left(-1.33e^{-7}x^2 + 6.94e^{-4}x + 0.241\right)\ln\left(PGD, long.\right)
$$
(3.24)

As seen in Table 2.1, the small change in period attributed to bridge mass resulted in a similarly small moment demand reduction. However, when a large mass was considered (150%), significant P-Δ effects caused an increase in moment demand (not shown here). In the context of the response spectrum, larger mass can be equated with a flexible structure, or longer period. Therefore, dispersions increased with longer-period design parameter models when

using period-independent *IM*s such as *PGA* and I_A. However, for a *Wt* of 150%, the period was akin to larger bridges from varying the *L* parameter; hence *PGD* and *CAD* became more efficient. The lack of a single period-independent *IM* for the *Wt* parameter led to its exclusion from a design parameter equation.
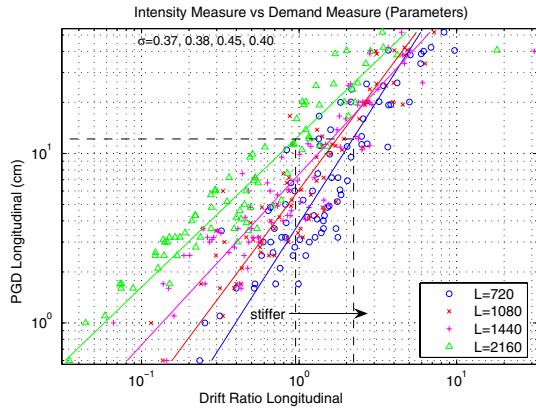
Fig. 3.50 *PGD-Δ, L* sensitivity longitudinal
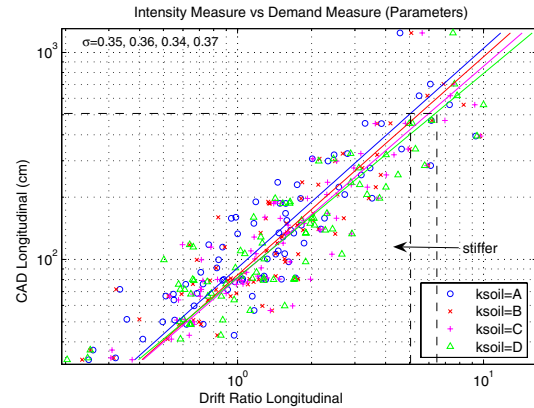
Fig. 3.51 *CAD-Δ, K_soil* sensitivity longitudinal

Figure 3.51 shows the relationships for variation of soil properties, K_{soil}. The variable K_{soil} assumed values of the USGS soil groups in the figure legend. The particular effect on bridge modeling was described by the unit weight (γ) and internal friction angle (ϕ') in Table 2.1. While there was a reduction in demand when considering either a rock or soft soil site, the difference between a USGS B or C site was small. However, the presence of soil springs was effective in elongating the fundamental period of the bridges to a more realistic value. The high stiffness bilinear soil springs used in previous studies (Mackie 2003) were more closely analogous to a fixed-base column end condition.

This section described the derivation of design equations given the trends due to design parameter variation. The design parameters varied were D_c/D_s, L/H, $\rho_{s,long}$, and *L*. Only period-independent *IM*s (e.g., *PGV*) were used and a single design equation for each design parameter was generated for each *IM-EDP* combination. The design equations (Eq. 3.17 general form) can be used explicitly by designers without coupling to Equation 1.1. This was done at the expense of efficiency but eliminated the natural period of the structure as a design variable.

3.6   MULTIPLE-BENT HIGHWAY BRIDGES

The PSDA approach was subsequently applied to the remainder of the bridges in the California reinforced concrete bridge class. This included the commonality of optimal demand models between different bent configurations in the class as well as design parameter studies akin to the single-bent variations. The multiple-bent bridges used in analysis were detailed in Section 2.2 and in Mackie (Mackie 2003). The base bridge configurations for all three bent types (one-, two-, and three-bent) shared the same column heights and cross-sectional details. Therefore, it was possible to assess trends in performance between the bridge designs. As would be expected, adding bents increased the longitudinal stiffness and therefore reduced deformations. However, the transverse direction remained similar to the single-bent case (stiffness and deformation-wise) as the bents were added in longitudinal series, not in the transverse direction. Nevertheless, to demonstrate the applicability of the PSDA method to bridges with and without analytical abutment models, the two-bent bridge was selected for abutment modeling.
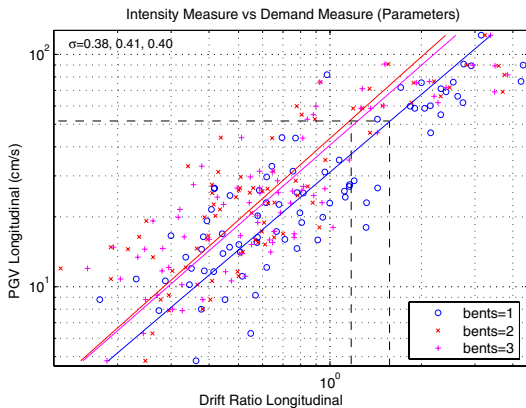
| Fig. 3.52 *PGV-Δ*, bent comparison longitudinal | Fig. 3.53 *PGV-Δ*, bent comparison transverse |
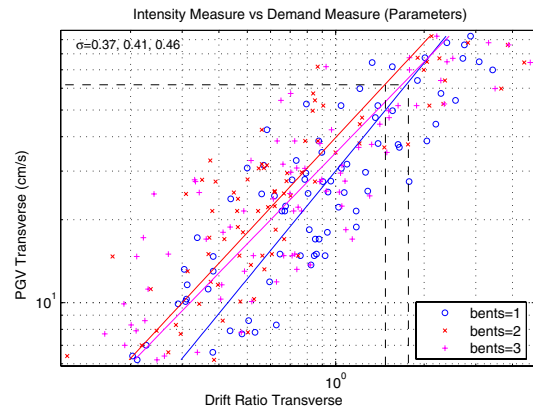
Comparisons of the bent types were achieved using a period independent *IM*, *PGV*, with drift ratio (*Δ*) as the *EDP*. The added stiffness resulted in the two- and three-bent bridges having similar longitudinal stiffness (Fig. 3.52). In the transverse direction, only the two-bent bridge with abutments exhibited reduced deformations. From the single-bent bridge study, optimal candidate PSDMs using existing *IM*s were *Sa-Δ*, *Sa-M_{max}*, and *Sa-σ*. The same PSDMs were evaluated in terms of efficiency, effectiveness, and sufficiency for multi-bent bridges. Some

other PSDMs formulated using local and intermediate *EDP*s were also included to show the similarity with single-bent PSDMs, even though the efficiency of the models was lower. The local *EDP* PSDM between $Sa(T_1)$ and maximum steel stress (σ_{steel}) is shown in Figure 3.54. As with the single-bent counterpart (Fig. 3.12), the efficient bilinear fit resembles the bilinear steel-strain constitutive model. However, because steel stress is not a practical *EDP*, this PSDM was not considered optimal. The PSDMs utilizing material strains demonstrated lower efficiency but were otherwise optimal. Such a PSDM is shown for concrete strain and $Sa(T_1)$ in Figure 3.55.
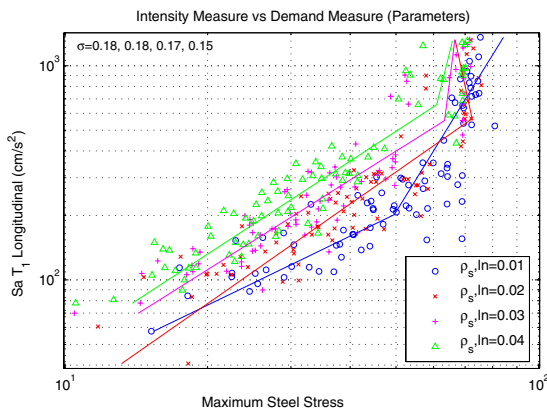
Fig. 3.54 $Sa(T_1)$-σ_{steel}, **2 bent** $\rho_{s,long}$ **sensitivity longitudinal**
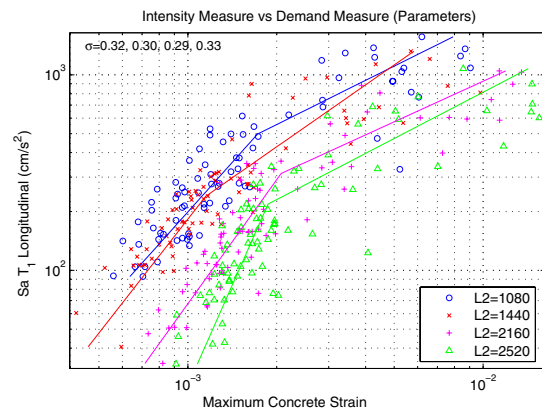
Fig. 3.55 $Sa(T_1)$-$\varepsilon_{concrete}$, **2 bent** L_2 **sensitivity longitudinal**

As with the single-bent PSDMs, maximum column moment (maximum is obtained from observing critical cross section of both bents) yielded a highly efficient PSDM when paired with any of the spectral quantities (Fig. 3.56). An alternative intermediate *EDP* can be used at the expense of a significant dispersion increase. The PSDM between column curvature ductility (μ_ϕ) and $Sa(T_1)$ is shown in Figure 3.57. The same two PSDMs were formulated in the transverse direction with similar results; however, the dispersions were 50% higher.
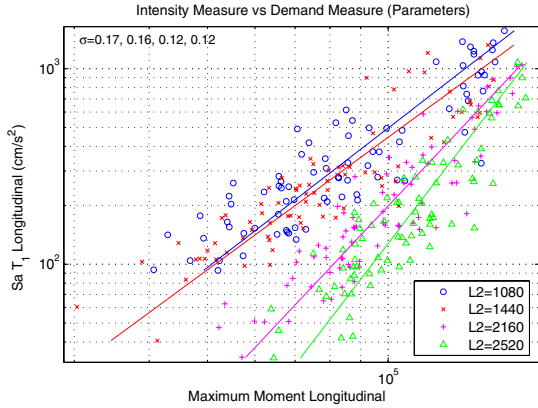
Fig. 3.56 *Sa(T₁)-M$_{max}$*, **2 bent *L₂* sensitivity longitudinal**
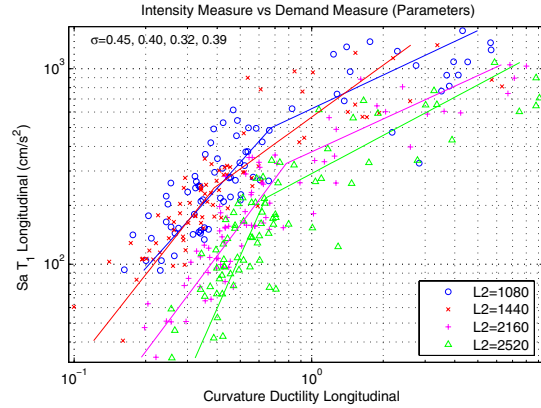
Fig. 3.57 *Sa(T₁)-μ$_\phi$*, **2 bent *L₂* sensitivity longitudinal**

While drift ratio was used as the global *EDP* in the single-bent PSDMs (e.g., Fig. 3.19), displacement ductility is presented in the two-bent PSDMs. As mentioned previously, these two *EDP*s are related kinematically through constants (u_y and H); therefore, they produced the same dispersions when PSDMs were formulated in log-space. Displacement ductility was used here as the parameter variation trends were more apparent for the variation of L_2. The global *EDP* (μ_Δ) shown in Figure 3.58 was once again the best choice for practicality, effectiveness, efficiency, and robustness. The only caveat for the two-bent bridges was the extension of the PSDMs to the transverse direction. Figure 3.59 shows the increase in dispersion in the transverse direction over the longitudinal direction for the same *IM-EDP* pair. However, it should be noted that the increased stiffness provided by the abutments reduced the transverse ductility demands to the elastic range for most of the ground motions considered. As shown later for the three-bent model with no abutments, the presence of the abutment is the main contributor to increased dispersion in the transverse direction.
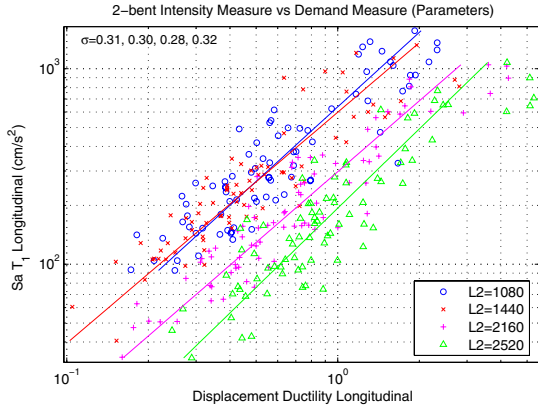
Fig. 3.58 *Sa(T₁)-μ_Δ, 2 bent L₂ sensitivity longitudinal*
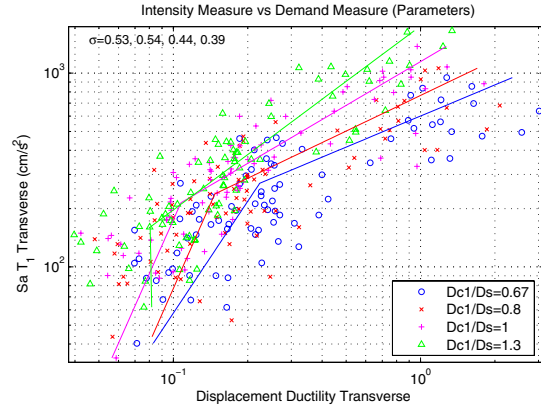
Fig. 3.59 *Sa(T₁)-μ_Δ, 2 bent D_{c1}/D_s sensitivity transverse*

The final condition for optimality requires the PSDMs also be sufficient. Sufficiency was verified for the global *EDP* PSDM shown in Figure 3.58. The residuals in log space were regressed against moment magnitude (M_w), closest distance (R), and strong motion duration (D). There was a slight positive correlation between the residuals and magnitude. However, according to Equation 3.14, the conditional dependence on magnitude could be neglected. No conditional dependence on closest distance was evident. Once again, not explicitly required for the hazard analysis, conditional dependence on strong motion duration was also assessed. There was slight correlation with D; however, the C_D coefficient was zero somewhere in the 90% confidence intervals. All residual dependence plots are contained in Mackie (Mackie 2004). Therefore, sufficiency was verified, and the same PSDMs deemed optimal for single-bent bridges were similarly optimal for two-bent bridges in the structural class.

Design parameter sensitivity studies were performed for the two-bent bridge configuration specific design parameters from Table 2.3. As with the single-bent case, variations in the fundamental period of the different structures obtained from design parameter variation made it desirable to use a period-independent *IM*. *PGV* was selected as the *IM* as it produced the lowest dispersion of the period-independent *IM*s analyzed for the two-bent bridges. Arias intensity and *CAV* can also be used, but dispersions were approximately 30–40% higher than those with *PGV*. Figure 3.60 shows the sensitivity of ductility demand to L_2. As L_2 was increased, H_1 also increased (the bridge became larger on the left side); therefore the structure became more flexible. As indicated, more flexible realizations resulted in increased demand at all intensity levels.
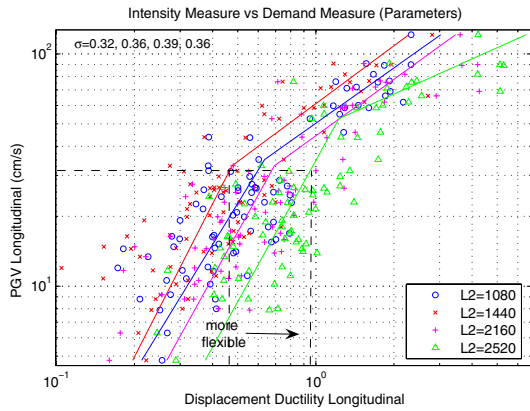
Fig. 3.60 *PGV-μ_Δ*, 2 bent *L_2* sensitivity longitudinal
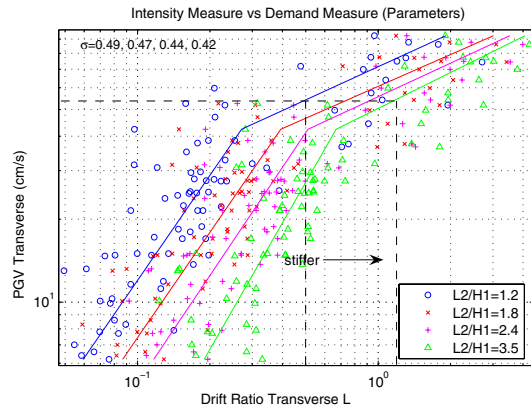
Fig. 3.61 *PGV-Δ_L*, 2 bent *L_2/H_1* sensitivity transverse

While changing *L_2* altered the overall size of the bridge (span length and column height), *L_2/H_1* effected only the left column height (*H_1*). As *L_2/H_1* was increased, *H_1* decreased thereby making the two-bent bridge stiffer. The increased stiffness and corresponding decrease in displacement was best viewed at the left bent level where the column height changes occurred. Figure 3.61 shows the sensitivity of drift ratio of the left column (*Δ_L*) to changes in *L_2/H_1* in the transverse direction. While there was a slight reduction in overall bridge longitudinal displacement (not shown here) with increasing stiffness, there was an increase in drift ratio due to the reduced column size. Similarly, in the transverse direction, the abutment contribution prevented large transverse displacement as the column became more flexible. Therefore, the drift ratio also increased as the column height was reduced (stiffer configuration), even though this is counterintuitive.
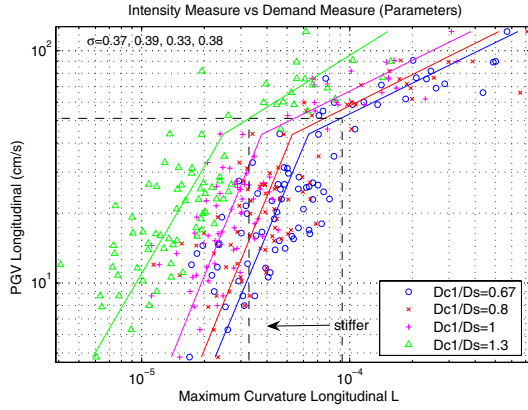
Fig. 3.62 *PGV-$\phi_{max,L}$*, 2 bent *D_{c1}/D_s* sensitivity longitudinal
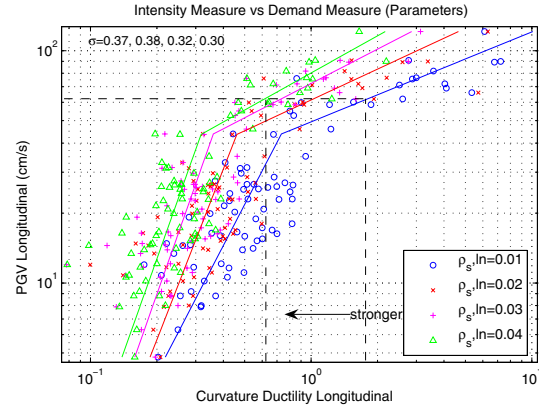
Fig. 3.63 *PGV-μ_ϕ*, 2 bent *$\rho_{s,long}$* sensitivity longitudinal

Performance changes from varying the column cross section were best viewed with intermediate *EDP*s. As the column diameter was increased (D_{c1}/D_s), the longitudinal curvature demand (Fig. 3.62) on the left column was reduced. Similarly, adding strength by increasing the amount of longitudinal column reinforcement resulted in a decrease in curvature ductility demand (Fig. 3.63). However, both increased stiffness (D_{c1}/D_s) and strength ($\rho_{s,long}$) attracted more force into the column. Figure 3.64 shows the increase in the left column maximum moment ($M_{max,L}$) as the section was made stronger. While it is possible to write design equations for piece-wise linear period-independent PSDMs, it was easier when a simple linear fit was used. For the case of $Sa(T_1)$-$M_{max,L}$, the resulting design equations are shown in Equation 3.25. The design parameter value selected was $x = \rho_{s,long}$. It was possible to use Sa as the amount of longitudinal reinforcement did not alter the initial elastic period of the structure.

$$
\begin{aligned}
\ln(M_{max,L}, long.) = &\left(302x^2 - 26.7x + 9.21\right) + \\
&\left(-129x^2 + 11.5x + 0.262\right)\ln(Sa(T_1), long.)
\end{aligned}
$$
(3.25)

A similar procedure to assess optimal PSDMs and design parameter sensitivity was followed with the three-bent, stand-alone, type configuration (with no abutments). No new *IM-EDP* pairs were introduced; however, the extension of existing optimal *IM*s to the three-bent configuration was explored. To maintain brevity, optimal models with local *EDP*s are not shown here. However, as with one- and two-bent models, material stress PSDMs were highly efficient (e.g., Fig. 3.12) but not necessarily practical. Material strain PSDMs lost efficiency (e.g., Fig.

3.14) but were more comparable to observable phenomenon. At the intermediate *EDP* level, maximum column moment (with a spectral *IM*) was the most efficient PSDM (Fig. 3.65). Additionally, curvature ductility also provided a low dispersion alternative (Fig. 3.66), as compared to its single-bent (Fig. 3.18) and two-bent (Fig. 3.57) counterparts.
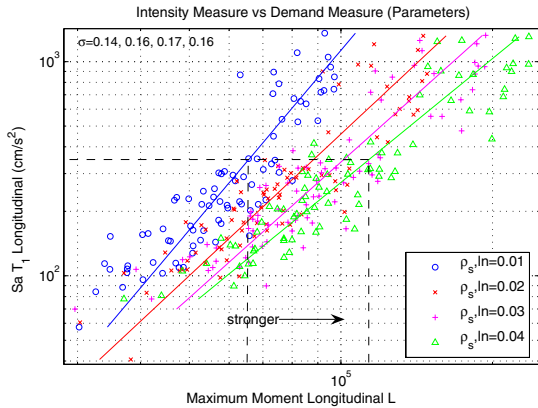
Fig. 3.64 $Sa(T_1)$-$M_{max,L}$, 2 bent $\rho_{s,long}$ sensitivity longitudinal
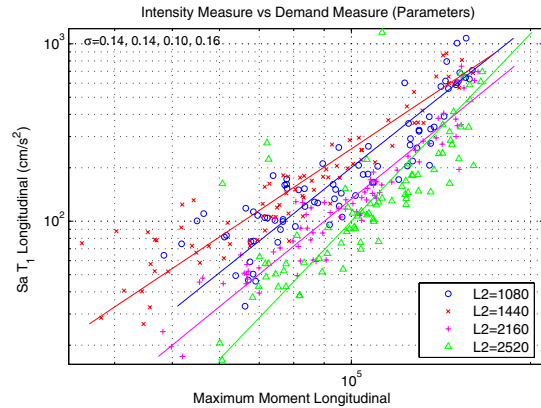
Fig. 3.65 $Sa(T_1)$-M_{max}, 3 bent L_2 sensitivity longitudinal
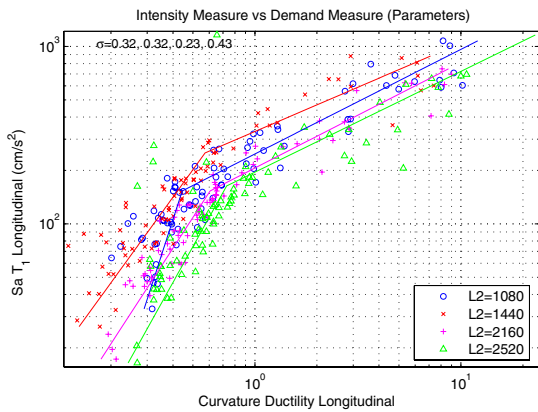
Fig. 3.66 $Sa(T_1)$-μ_ϕ, 3 bent L_2 sensitivity longitudinal
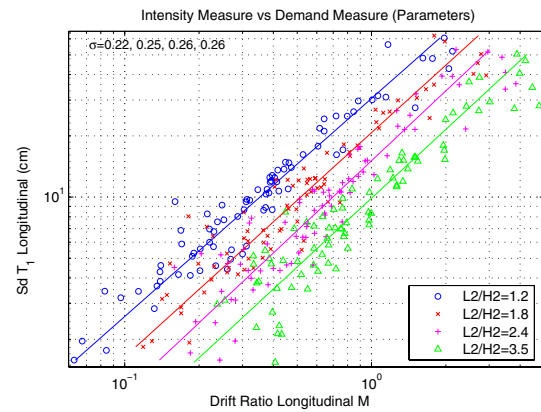
Fig. 3.67 $Sd(T_1)$-Δ_M, 3 bent L_2/H_2 sensitivity longitudinal

Continuing previous trends, it was the global *EDP* PSDM formed from drift ratio or displacement ductility (Fig. 3.67) that provided the most robust and effective (single linear fit) PSDM. In Figure 3.67, the design parameter used to illustrate robustness was L_2/H_2. As mentioned in Section 2.2, the spans were held constant while only the middle column height (H_2)

was changed. This resulted in locally stiffer behavior that did not effect the overall longitudinal deck displacement, but was important for deflections in the transverse direction. Therefore, the drift ratio of the middle bent (Δ_M) was used in the longitudinal (Fig. 3.67) and transverse (Fig. 3.68) PSDMs. Comparable to previous models, the transverse PSDM was not as efficient as the longitudinal PSDM, but still exhibited optimal characteristics. Sufficiency of the $Sd(T_1)$-Δ_M PSDM was investigated, but not shown here. There was no conditional dependence on either magnitude (M_w), distance (R), or duration (D).
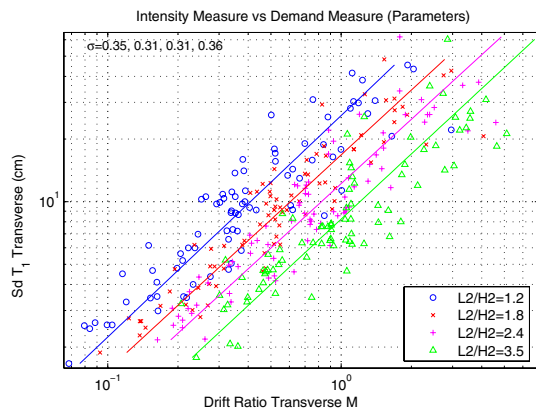
Fig. 3.68 *$Sd(T_1)$-Δ_M,* **3 bent *L_2/H_2* sensitivity transverse**
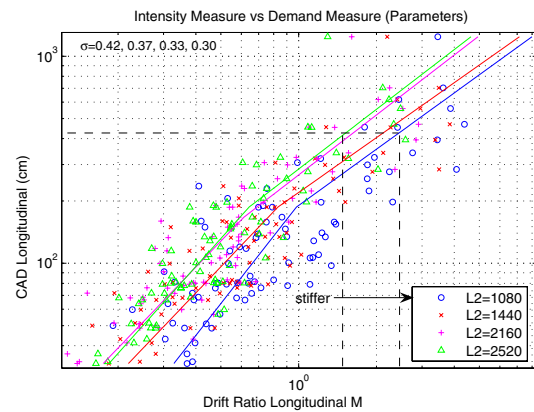
Fig. 3.69 *CAD-Δ_M,* **3 bent *L_2* sensitivity longitudinal**

As with the two-bent bridge configuration, only the design parameters specific to the three-bent model (Table 2.4) were varied here. The period-independent *IM* chosen to allow lines of constant intensity in the PSDMs was *CAD*. Alternatively, *PGV* or *CAV* could have been used, but exhibited dispersions 10–20% higher than *CAD*. The *L_2* design parameter effected the overall size of the bridge as both the span length and column height (H_2) increased with increasing *L_2*. As *L_2* was increased, displacements increase slightly in the longitudinal direction, but the overall drift ratio of the middle column (Δ_M) decreased (Fig. 3.69). Transverse displacements increased minimally as well, reproducing the increase in drift ratio in the transverse direction (Fig. 3.70).
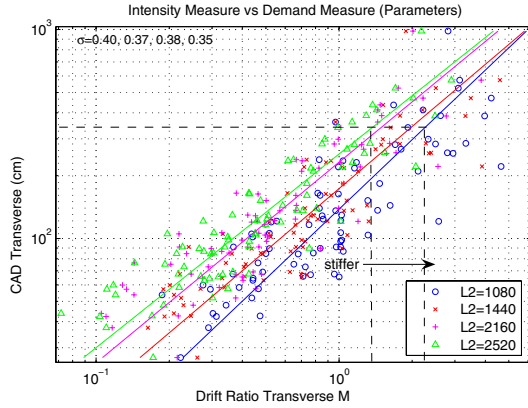
Fig. 3.70 *CAD-Δ_M*, **3 bent L_2 sensitivity transverse**
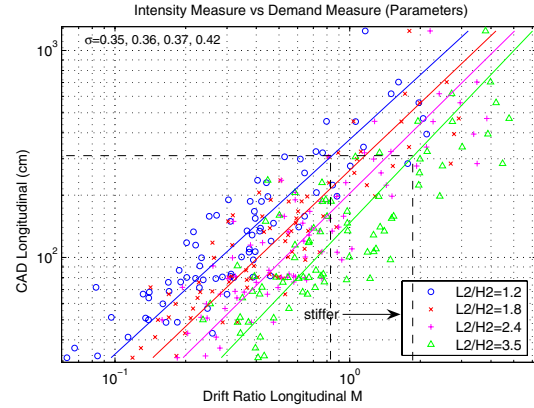
Fig. 3.71 *CAD-Δ_M*, **3 bent L_2/H_2 sensitivity longitudinal**

To isolate the effect of disparate column heights within a multiple-bent bridge, the middle column height (H_2) was altered according to L_2/H_2. As the design parameter increased, H_2 decreased. The resulting increase in stiffness decreased the overall displacement slightly; however, the drift ratios increased. This behavior was true in both the longitudinal (Fig. 3.71) and transverse (Fig. 3.72) directions when examining the drift demand at the center column. Both of these PSDMs lent themselves toward a single linear design equation. The resulting design equation for the longitudinal direction is shown in Equation 3.26, and the transverse direction in Equation 3.27. The design parameter value selected was $x = L_2/H_2$.

$$\ln(\Delta_M, long.) = \left(-0.127x^2 + 1.25x - 7.02\right) + \left(0.00414x^2 - 0.0733x + 1.05\right)\ln(CAD, long.) \tag{3.26}$$

$$\ln(\Delta_M, tran.) = \left(0.0105x^2 + 0.610x - 6.72\right) + \left(-0.0245x^2 + 0.0649x + 0.993x\right)\ln(CAD, tran.) \tag{3.27}$$
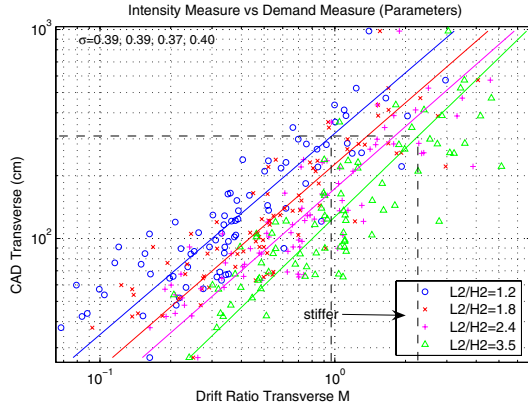
Fig. 3.72 *CAD-Δ_M, 3 bent L_2/H_2 sensitivity transverse*
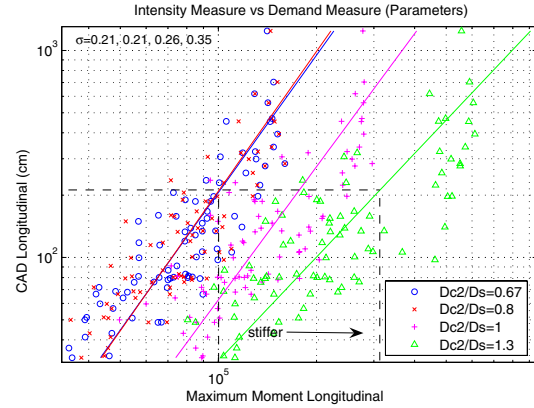
Fig. 3.73 *CAD-M_{max}, 3 bent D_{c2}/D_s sensitivity longitudinal*

Finally, the diameter of the center column was varied through the D_{c2}/D_s design parameter with a constant deck depth. As would be expected for a stiffer column, the displacements were reduced while the force demands were higher. Figure 3.73 shows the PSDM between *CAD* and maximum column moment (all columns considered). For the case of $D_{c2}/D_s = 0.67$, the diameter of the other two columns dominated the moment demand (the other two columns remained at $D_c/D_s = 0.80$); therefore, the lowest two design parameter values were equivalent.

In summary, when applied to multiple-span highway bridges, the criteria required for disaggregation were maintained in the resulting PSDMs, thus allowing seamless integration into the PEER framework. More importantly, the same *IM-EDP* pairs derived as optimal for single-bent bridges were also optimal for multiple-bent bridges. The wide use of spectral acceleration in current practice makes it a useful property for bridges. As tools for designers, the PSDMs for multiple span bridges were especially useful, as they were not subject to deterioration of effectiveness or sufficiency due to bridge irregularity. Optimality of *IM-EDP* pairs was maintained across a broad range of irregular configurations. This standardization allows designers to evaluate bridge response without an initial requirement that a bridge design qualify as an "ordinary standard bridge" (Caltrans 1999).

While only California reinforced concrete highway overpasses were investigated in this section, the optimal selection of a spectral *IM* (such as spectral acceleration or spectral displacement) and a global *EDP*, such as drift ratio, appear to be insensitive to the choice of structure. Prudent choice of the natural period for use in the spectral *IM* was important, but

followed directly from the primary mode of deformation expected for the structure, regardless of whether it fell at the lowest period or not. This optimal *IM-EDP* combination also appeared optimal over a variety of design parameter variations, making it a good choice for assessing performance trends in demand models.

3.7   AFTERSHOCK PSDMS

Due to computational power constraints, a comprehensive PSDM study was not attempted for the inclusion of aftershocks. However, results were computed for two values of the *L/H* design parameter for the single-bent configuration (*L/H* = 2.4 and 3.5). Keeping track of both the first-shock intensity (IM_{FS}) and aftershock intensity (IM_{AS}), a PSDM was constructed in three dimensions with the post-aftershock response being conditioned on both *IM*s. For simplicity, the same *IM* was used for both IM_{FS} and IM_{AS}.

   As a simple extension of Equation 3.9, a best-fit plane was sought to describe the response, given the intensities (Eq. 3.28). The same selection of feasible *EDP* and *IM* combinations were possible as with the single-bent bridge first-shock case. A sample PSDM is shown in Figure 3.74 for *L/H* = 2.4, $Sd(T_1)$ as the *IM*, and drift ratio in the longitudinal direction as the *EDP*. The corresponding coefficients were *A* = -1.49, B_{FS} = 0.0744, B_{AS} = 0.728, and a dispersion of 0.28. For better visualization, the *L/H* = 3.5 case was excluded from the plot; its dispersion was 0.34.

$$\ln\left(E\hat{D}P\right) = A + B_{FS}\ln\left(IM_{FS}\right) + B_{AS}\ln\left(IM_{AS}\right) \qquad (3.28)$$

   Given the sensitivity of PSDM efficiency to period in the spectral quantities (Section 3.4.3.1.1), it would suggest the choice of the initial elastic period was an especially poor choice in the aftershock scenario. The softening due to cycling from two ground motion events would suggest an elongated period would have been a better choice. For computational reasons, this sensitivity was not performed.
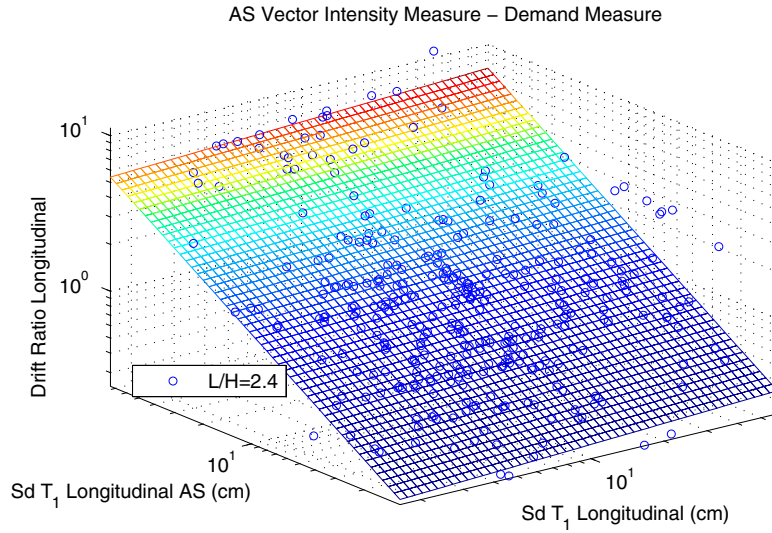
Fig. 3.74 *Sd(T₁)-Δ* **aftershock PSDM,** *L/H* **= 2.4 longitudinal**

However, as an alternative, a period-independent *IM* good at describing such elongated period motions was an efficient choice. It was determined the best Class I *IM* for the design parameter values selected was *PGD*. The PSDM formed using *PGD* and longitudinal drift ratio is shown in Figure 3.75 for *L/H* = 3.5. The resulting dispersions for both *L/H* values were 0.35 and 0.37, respectively.
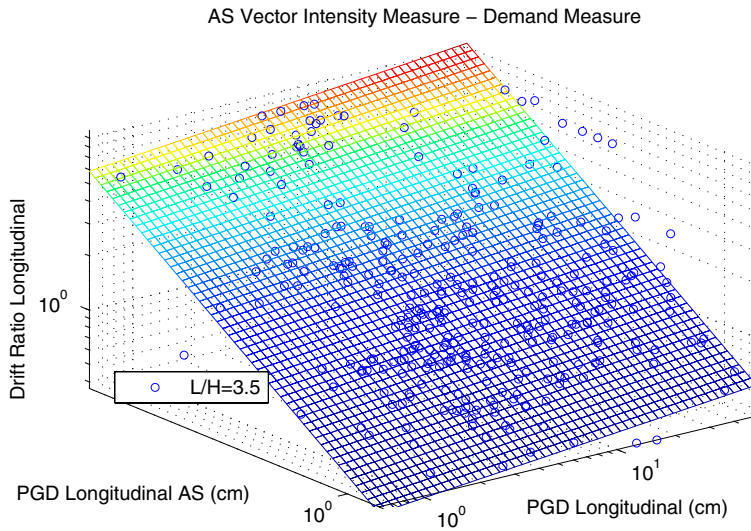
Fig. 3.75 *PGD-Δ* **aftershock PSDM,** *L/H* **= 3.5 longitudinal**

3.8   ALTERNATIVE DEMAND FORMATS

The PSDM is the building block of all subsequent demand outputs.   However, there are numerous other methods of presenting the data.   These include plotting the PSDM directly as a probability distribution, rather than simply the data points and best fit, and convolving the PSDM with site-specific hazard to create a demand hazard curve.

3.8.1   Demand Fragility

The most intuitive of the alternative formats is to plot a demand cumulative distribution function (CDF). This is accomplished by selecting a demand limit state (edp^{LS}), such as 1.5% drift ratio. The probability of exceeding a specific value of the demand limit state can then be calculated for each intensity value considered in the PSDM. Owing to the definition of a fragility curve, such a conditional distribution is termed a demand fragility curve. The CDF, or fragility, plot can be obtained directly from a vertical stripe of EDP data, or from the (assumed) lognormal distribution and associated distribution parameters ($\hat{EDP}$ and σ). Given the parameters A, B, and σ from PSDA simulation, the demand fragility form becomes Equation 3.29.

$$P\left[EDP < edp^{LS}\middle|IM = im\right] = \int_0^{edp^{LS}} \frac{1}{\sigma_{EDP|IM}\sqrt{2\pi}edp}\exp\left[-\frac{1}{2}\left(\frac{\ln edp - A - B\ln(im)}{\sigma_{EDP|IM}}\right)^2\right]dedp \quad (3.29)$$

A plot of single (complementary CDF) demand limit-state fragility curves ($edp^{LS} > 3\%$) is shown in Figure 3.76 for D_c/D_s parameter variation. The PSDM used to derive the fragility curve was shown in Figure 3.19. This form of presenting demand models is particularly useful for designers and engineers to quantify performance changes due to design parameter variation probabilistically. However, for demand fragility curves using period-dependent IMs, lines of constant intensity are not vertical. As an example, using Gilroy Array #3 as the design scenario earthquake, the probability of exceeding a 3% drift demand was 0.99 for $D_c/D_s = 0.75$ but only 0.3 for $D_c/D_s = 1.0$. The period-independent alternative is illustrated in Figure 3.77 for CAD as the IM and L/H design parameter sensitivity. In this case, direct assessment was possible by the single vertical constant intensity line.
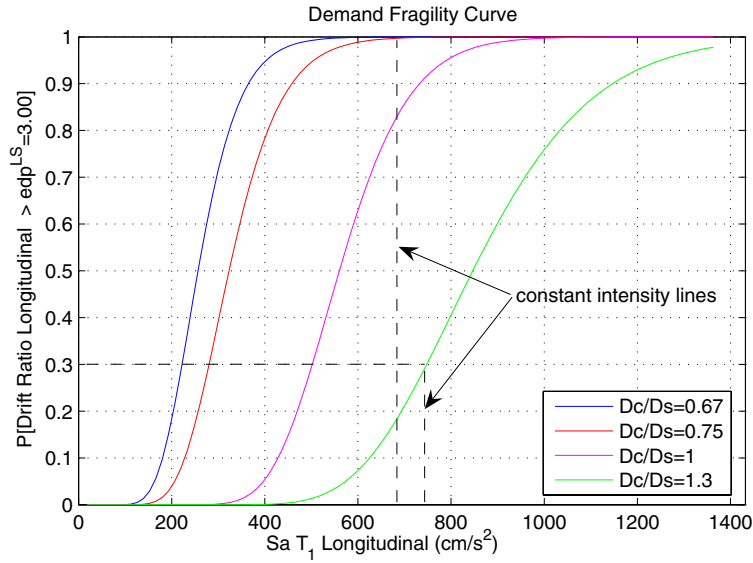
Fig. 3.76 *Sa(T₁)-Δ* demand fragility, *Dc/Ds* sensitivity longitudinal
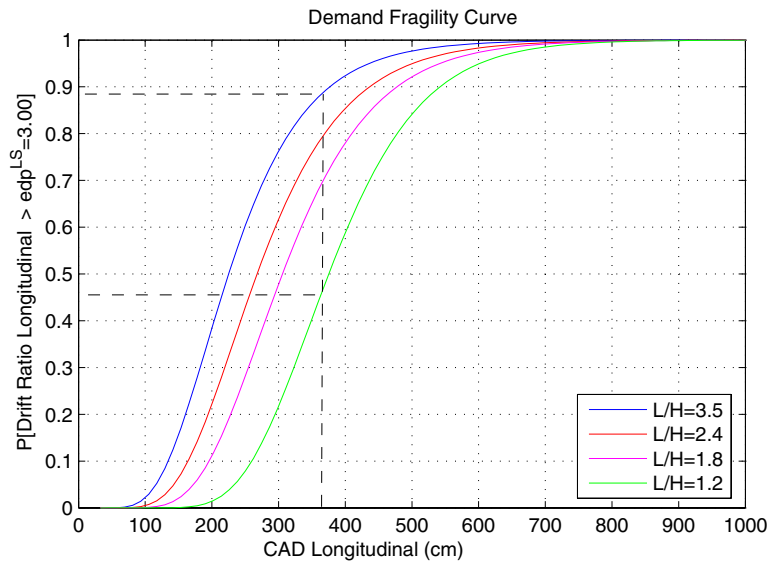
Fig. 3.77 *CAD-Δ* demand fragility, *L/H* sensitivity

The two-dimensional demand fragility presentation of Figure 3.76 is useful when discrete known design parameter values and limit-state values (or simply a single demand fragility curve) are desired. However, to assess overall trends, an entire series of demand fragility curves can be plotted together as a demand fragility surface. Numerous fragility curves for different limit-state values (edp^{LS}) for a single bridge realization ($D_c/D_s = 0.75$) can be conveniently visualized as a

97

fragility surface (Fig. 3.78). Each black line on the demand fragility surface is a traditional demand fragility curve at a specific limit-state value. Given an array of fragility curves corresponding to different values of the same limit state, it is possible to assess the effect of earthquake intensity on structural fragilities (i.e., Fig. 3.78). This format is compatible with all possible *IM*s, as only one structure is considered in each surface.
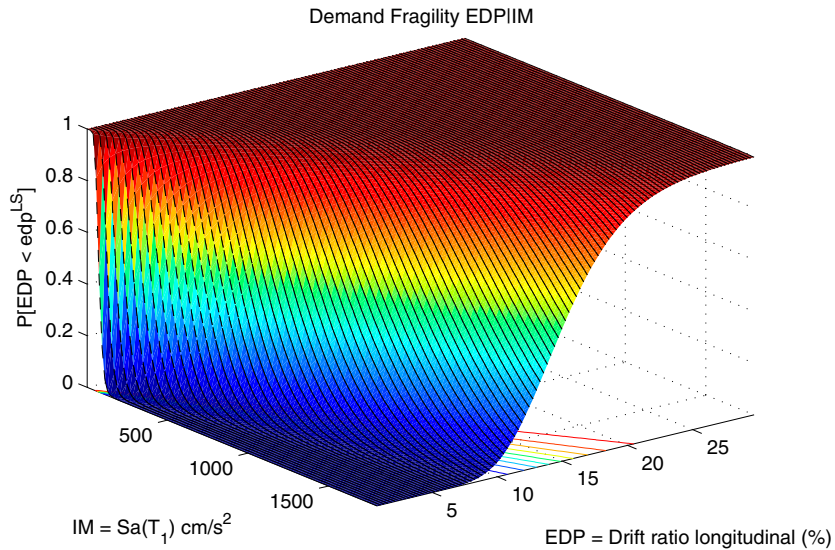
Fig. 3.78 *Sa(T₁)-Δ* demand fragility surface, *Δ* limit states

Alternatively, given an array of fragility curves corresponding to different bridge designs (or design parameters) at the same value of the limit state, it is possible to assess the effect of different designs on the probability of exceeding set performance levels (limit states). This approach also produces a three-dimensional demand fragility surface. However, trends between design parameter values need to be determined, and thereby, the design parameter becomes another independent variable. As mentioned in the design parameter section (Section 3.5), design equations utilizing period-dependent *IM*s (such as $Sa(T_1)$) are not useful as they do not account for implicit period dependence. While it may be possible to solve Equation 3.17 using iterative techniques, this requires determination of the fundamental period for numerous intermediate structures.

For illustration of three-dimensional demand fragility, the (period-independent) PSDM between *CAD* and drift ratio was adopted for *L/H* sensitivity. First, the design equation from design parameter variation during PSDA was obtained. The general form of the design equation

was shown in Equation 3.17. To further simplify the subsequent probability computations, the standard deviation of the assumed lognormal distribution was calculated from the dispersions obtained during PSDA and was assumed constant. A value equal to the mean plus one-half standard deviation of these dispersions was adopted due to the introduction of model error in determining the coefficients A_i to B_k. With this information, the demand fragility surface with design parameter variation can be described exactly by Equation 3.30. The median EDP value ($\hat{EDP}$) is dependent on the design parameter value x as in Equation 3.17. This term is therefore dependent on both the intensity and the design parameter; hence Equation 3.30 describes a complete surface of values.

$$P\left(EDP < edp^{LS} \mid IM = im, X = x\right) = \Phi\left[\frac{\ln\left(edp^{LS}\right) - \ln\left(\hat{EDP}(im,x)\right)}{\sigma}\right] \qquad (3.30)$$

Equation 3.30 is the best estimate of the demand fragility surface given a constant standard deviation (σ). As a practical form, however, it may be difficult to use; therefore, a nonlinear regression was performed on the data. The functional form fit to the data is indicated in Equation 3.31.

$$P\left(EDP > edp^{LS} \mid IM = im, X = x\right) = \frac{1}{1 + \exp\left(A_f + B_f(im)^{\beta_1} + C_f(x)^{\beta_2}\right)} \qquad (3.31)$$

Therefore, for each PSDM generated, it was possible to obtain not only a design equation (Eq. 3.17) for demand values, but also a design equation for a demand fragility surface (Eq. 3.31).

The results of the sample demand fragility surface are presented in Figure 3.79. The regression coefficients in Equation 3.31 were $A_f = -16.74$, $B_f = -2.435$, $\beta_1 = 0.3182$, $C_f = 33.25$, and $\beta_2 = -0.0757$. For verification purposes, the fragility surface described by Equation 3.30 was plotted in the figure as the transparent grey surface. The surface in full color is the fragility surface described by Equation 3.31 with the aforementioned coefficients. The largest (probability) discrepancy was 0.08 at small values of the design parameter and IM.
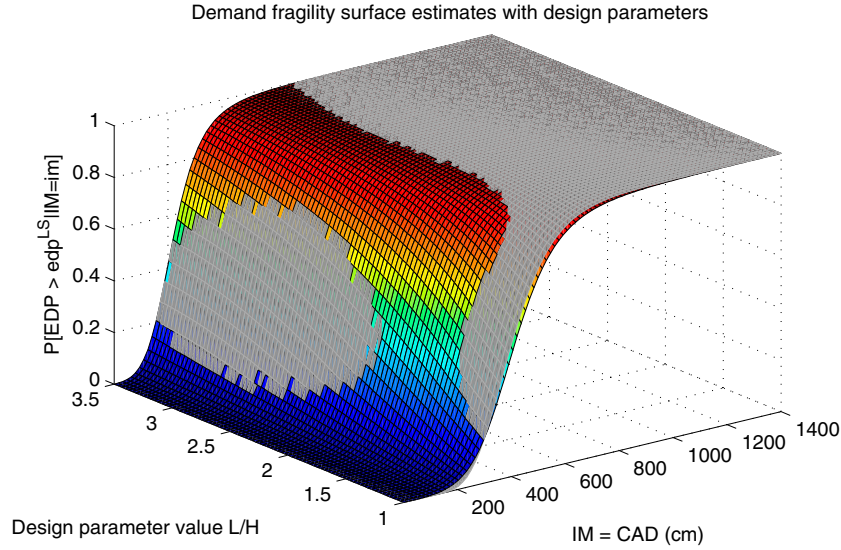
Fig. 3.79 *CAD-Δ* **demand fragility surface,** *L/H* **sensitivity**

If the array of ground motions chosen completely described the expected hazard at the site of interest, then the limit-state probability of exceeding each *EDP* value in the demand model could also be calculated. This can be achieved in two ways. The first method takes the distribution of *IM* data input into the demand analysis method (*f_IM*) and integrates with the PSDM, as shown in Equation 3.32.

$$P(EDP < edp) = \int P_{EDP|IM}(edp \mid im) f_{IM}(im) dim \qquad (3.32)$$

Since *IM* values can be related to *EDP*s through Equation 3.9, it is not necessary to actually perform the integration in Equation 3.32. Instead only the distribution of response (*f_EDP*) data need be integrated (Eq. 3.33).

$$P(EDP < edp) = \int f_{EDP}(edp) dedp \qquad (3.33)$$

3.8.2 Demand Hazard Curves

The hazard curve can be extended to the demand model by integrating the median hazard (Eq. 3.4) and the PSDM (Eq. 3.10). The result is still an annual hazard curve; however, it shows the mean annual frequency of exceeding a demand limit state according to Equation 3.13. This effectively removes the dependence of the demand model on the intensity. Integrating a PSDM

that relates $Sa(T_1)$ to drift ratio (Fig. 3.19), for a variation of the column diameter design parameter, with the hazard curve derived in Section 6.1 produced the structural demand hazard curve (SDHC) shown in Figure 3.80.
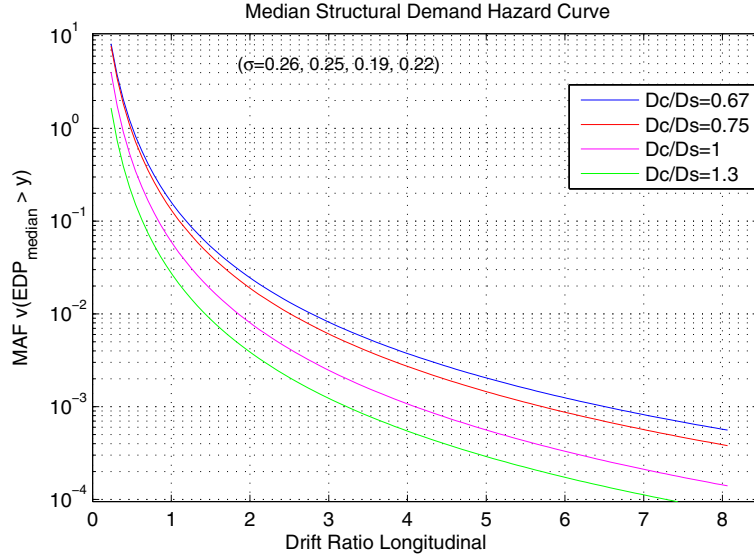
Fig. 3.80 $Sa(T_1)$-Δ structural demand hazard curve, D_c/D_s sensitivity

This integration can be performed numerically with the demand model data, or can be evaluated in closed form using the coefficients of the linear fit to the demand model (Eqs. 3.10 and 3.9). Details of the integration by parts are demonstrated by other researchers (Jalayer 2003). The resulting closed-form SDHC is shown in Equation 3.34. To be strictly accurate, Equation 3.34 does not include epistemic uncertainty or the uncertainty from the hazard curve. The uncertainty from the hazard curve can be included explicitly in Equation 3.34, or it can be included by using the mean hazard curve (rather than the median). The inclusion of epistemic uncertainty is detailed further in the following section.

$$\lambda_{EDP}(edp) = k_0 \left[\left(\frac{edp}{a} \right)^{\frac{1}{b}} \right]^{-k} \exp\left(\frac{k^2}{2b^2} \sigma^2_{EDP|IM} \right) \tag{3.34}$$

3.9   UNCERTAINTY

Until this point, all the PSDMs were constructed considering only the variability inherent in the random processes of earthquake records. In the case of nonoptimal models, the total uncertainty in the problem was largely dominated by this aleatory uncertainty, so only including randomness remained a good assumption. However, in the case of highly efficient PSDMs (low aleatory dispersion), additional epistemic uncertainties may have a more pronounced affect on the overall uncertainty. Such epistemic uncertainty can nevertheless be included in any demand model by introducing an additional dispersion term in each subsequent analysis.

The total uncertainty in the demand model can be estimated by the square root of the sum of squares (SRSS) of the aleatory and epistemic contributions (Cornell 2002; Jalayer 2003), as shown in Equation 3.35.

$$\sigma_{T,PSDM} = \sqrt{\sigma_{EDP|IM}^2 + \sigma_{PSDM}^2} \qquad (3.35)$$

The epistemic term (σ_{PSDM}) can be estimated based on professional opinion or simulation studies. It can be introduced as a penalty for bias introduced by approximate analysis methods or poor modeling assumptions. For buildings, the SAC project sought to quantify this uncertainty (Lee 2002); however for bridges little information is currently available on appropriate values.

A complex nonlinear time history analysis was performed for each bridge in the PSDA procedure in this study; therefore, it was assumed that a relatively low level of epistemic uncertainty was present. A value of $\sigma_{PSDM} = 0.15$ was assumed for the remainder of this report. The resulting total uncertainty can be used without modification by substituting $\sigma_{T,PSDM}$ for $\sigma_{EDP|IM}$ in either Equation 3.29 or 3.34 for demand fragilities and demand hazard curves, respectively. The net result would be the prediction of a mean structural hazard curve (mean MAF) in Figure 3.80, as the MAF also becomes a lognormally distributed random variable. Due to the relatively low dispersions considered, the mean hazard curve was not plotted separately here.

However, it is instructive to consider different forms of the demand fragility curve. The median fragility curves are shown in Figure 3.76, considering only the aleatory portion. As an example, the base bridge fragility curve was selected ($D_c/D_s = 0.75$). Equation 3.30 was modified to include the epistemic uncertainty separated from the aleatory portion, as shown in Equation 3.36 (Bazzurro 2004).

$$P\left(EDP < edp^{LS} \mid IM = im, Y = y\right) = \Phi\left[\frac{\ln\left(edp^{LS}\right) - \ln\left(E\hat{D}P(im)\right) - y\sigma_{PSDM}}{\sigma_{EDP|IM}}\right] \quad (3.36)$$

The variable y is the standard normal value corresponding to the desired probability band. For example, for the 84th percentile, $y = 1$. Three values of y (0, -1, and 1) are plotted with the mean fragility curve in Figure 3.81. The same approach can be applied to any of the demand fragility curves created in this chapter.
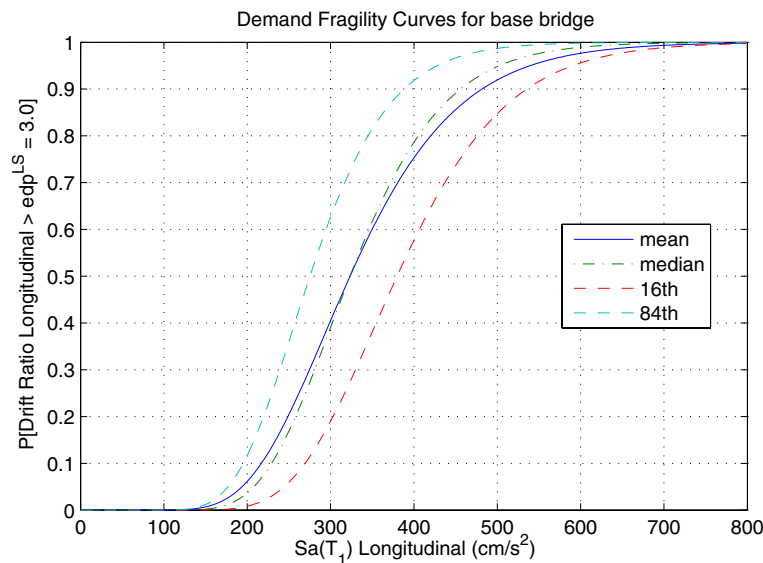
Fig. 3.81 *Sa(T₁)-Δ* **demand fragility percentiles, base bridge longitudinal**

Another means of quantifying the uncertainty surrounding least-squares parameter fitting in the demand model was to examine confidence intervals on the mean (or median) *EDP-IM* fit. Traditional two-sided intervals were derived for each set of data at varying levels of confidence. In this case, the 90% confidence level was selected for illustration. This confidence interval brackets the selection of the median in approximately 90% of repeated applications and is indicative of the amount of scatter (aleatory) in the model.

The base bridge configuration was once again selected, and four more parameters estimated (A and B for each side of the interval). It was assumed the median and each interval exhibited the same dispersion; however this is not strictly true. For the purposes of this section though, it allowed plotting of confidence intervals in a demand fragility format, as shown in Figure 3.82 (50% intervals also included).
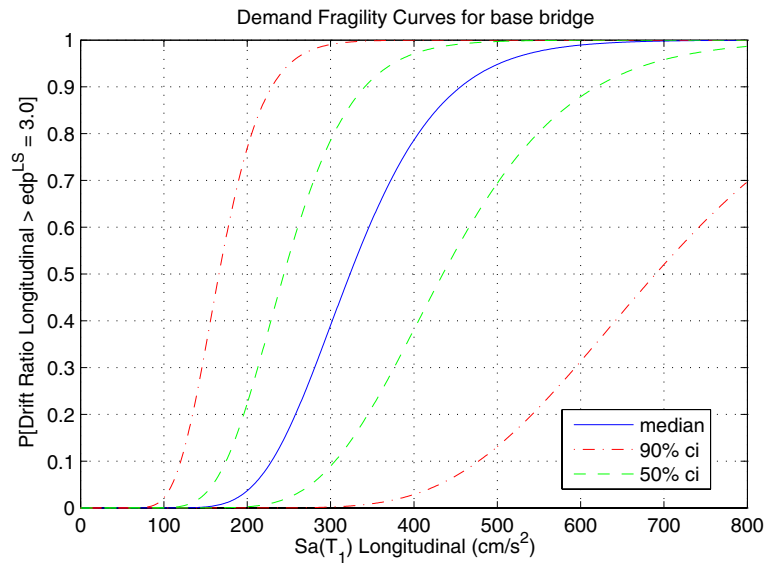
Figure 3.82 *Sa*(*T₁*)-*Δ* demand fragility confidence intervals, base bridge long

No particular probability levels are associated with the confidence intervals in Figure 3.82; however, they are illustrative of the level of confidence in the median demand model. The optimal demand models in this chapter were fairly certain and therefore the 50% intervals were quite narrow; but it will be demonstrated in later chapters that even the 50% intervals were large for functional *EDP*s and *DM*s.

4 Damage Model

Demand and damage are often used interchangeably. However, this is not technically accurate, as demand simulations performed using finite element analysis are usually unable to completely capture complex natural phenomena such as global and local buckling, cracking, rebar buckling, and the onset of collapse. Such phenomena are identified as structural damage. Therefore, to perform any seismic risk assessment on bridges, it is necessary to introduce the capacity of bridge components and/or the complete bridge system, and subsequently make comparisons with the expected levels of demand. Another grey area is the use of demand limit states to define different levels of damage. This study will not rely on these deterministic demand limit states in the damage model formulation; rather, complete demand and damage analyses will be performed separately. For the purposes of this study, the terms "capacity model" and "damage model" are used interchangeably.

Discussion of appropriate damage measures (*DM*) for use in damage models should not be separated from the underlying needs of calculating losses for individual highway bridges. Specifically, this chapter is divided into two sections that correspond directly to the two paths constituting total losses to a highway network in an earthquake scenario. The first section (Section 4.1) focuses on the *DM*s corresponding to direct costs associated with bridge repair and restoration. The second section (Section 4.2) focuses on post-earthquake bridge function, or loss thereof, that results in indirect losses. Quantifying damage is pursued at the individual bridge level only.

The *DM*s required for each of the two types of losses must be realistic. Realistic *DM*s address relevant damage states that can be related to dollar losses, function losses, or collapse, and include treatment of bridge system as well as component damage. At the component level, localized damage models involving observable damage and loss of capacity are obtained. The corresponding *DV*s relate to repair and restoration of function. At the bridge system level, functional damage models involving loss of lateral and vertical load-carrying capacity are

obtained. Resulting *DV*s lend themselves to evaluation of traffic capacity and safety factors for an earthquake scenario.

Further insight into post-earthquake decision-making may be gained from the introduction of the probability of collapse during aftershocks. Barring collapse, the subsequent decrease in performance as compared to the initial performance goals may also be of interest. Aftershock residual capacity can be seen as another method of determining post-earthquake capacity, such as the lateral load-carrying capacity described above. Due to the different sources of damage data, and the different possible outcomes in terms of *DM*s, there is no single procedure that defines probabilistic damage analysis (such as was the case for demand). Therefore, probabilistic damage model (PDM) formulation is covered explicitly with each *DM* considered in this chapter.

The ultimate goal of generating individual demand and damage models is to combine them for a meaningful result. One method of visualizing damage probability is the fragility curve. The formulation for damage fragility using the PEER framework is shown in Equation 4.1. The damage fragility shows the conditional probability of exceeding a damage limit state given an *IM*. This necessarily includes demand model information beyond the PDMs of this chapter. Unless otherwise noted, the demand models used in the damage fragilities of this study were presented in Chapter 3.

$$P\left(DM < dm^{LS}\middle|IM = im\right) = \int_{edp} P_{DM|EDP}\left(dm^{LS} \mid edp\right) \cdot dP_{EDP|IM}\left(edp \mid im\right) \qquad (4.1)$$

The first term in Equation 4.1 is the CDF obtained directly from the PDMs of this chapter. The second term is the derivative of Equation 3.29, or simply the PDF of the demand model at the specified *IM* level. The resulting damage fragility curve is also a CDF for a single damage limit state (dm^{LS}) with intensity on the horizontal axis.

The chapter concludes with results from an experimental study to validate analytical predictions of the loss of axial load-carrying capacity of reinforced concrete specimens. By developing an experimentally verified two-step analytical process, it will be possible to better predict the load capacity loss of more complex bridge structures. The experimental procedure involved lateral excitation using displacement histories with prescribed maximum ductility demands, followed by axial compression until failure. The analytical procedure involved developing a relationship between the loss of axial capacity and the maximum lateral ductility demand. Such experimental or analytical curves can be used as displacement-based damage

models in the framework of Equation 4.1, with the added benefit of lower dispersions than the bridge-level analytical methods derived in Section 4.2.3.

4.1   COMPONENT LEVEL

This section is by no means a comprehensive assessment of component-level damage critical to highway bridges. It concerns only damage to the column of the single-column reinforced concrete highway bridge configuration. This excludes discussion of other classes of highway bridges, as well as other critical components in a highway overpass bridge system. Component-level damage would be anticipated at any number of locations in this class of highway bridges. These include abutment embankment and backfill slumping, abutment wing wall and bridge shear key failure, damage to the bearings, pile cap and pile damage below grade, deck-column joint damage, and offsets or damage at expansion joints. Therefore, the total direct losses to the bridge are the sum over all bridge components. However, there are currently experimental data available for columns to form a comprehensive framework study, whereas other essential bridge elements are lacking in currently available research. Therefore, only the column losses were included in this study.

The bridge under consideration in this section is the single-bent base bridge configuration detailed in Section 2.1. In summary, it contains two equal spans, a single-column bent, and roller abutment supports. Where applicable, several design parameters have been varied. These were limited to the span length-to-column height ratio (L/H) and the column diameter-to-superstructure depth ratio (D_c/D_s). These design parameters were chosen because they directly induce geometric changes in the column. Design parameters involving the material properties of the column, such as reinforcement ratio and concrete strength, were not varied in this study (and remained constant), although they can also be correlated with experimental column damage research.

4.1.1   Component Damage Measures

Large databases of experimental results exist (PEER SPD, CEB 2003) that are a collation of experimental tests on reinforced concrete columns performed by numerous researchers and organizations. These tests included pseudo-static, pseudo-dynamic, and fully dynamic uniaxial

bending tests of columns in different geometric and material configurations. Measurements of response were usually deformation-based and included strains, curvatures, drift ratios, or displacements. Numerous tests also included observations of damage and response levels corresponding to each observation. This implies a whole family of component *DM* values such as spalling and cracking that can be related directly to *EDP* values.

For the purposes of this study, the *DM* can be thought of as component damage with specific values ranging from spalling to failure. This discrete *DM* variable has numerous interim values, including yielding, the onset of longitudinal bar buckling, longitudinal bar fracture, transverse reinforcement fracture, and loss of axial-load capacity. An important distinction with this selection of damage states is that the *DM* becomes a discrete variable and there fails to exist a mathematical PDM that relates *DM*s to *EDP*s. The loss of axial-load capacity refers to the loss of the ability to support the initial gravity load, not the state of zero axial-load capacity. Failure does not necessarily imply the collapse of the specimens; rather a significant drop in the post-peak lateral force, or the first observation of any bar fracture or buckling. Each of these *DM* values was defined at a specific *EDP* level at the first sign of occurrence.

4.1.2   Experimental Damage Models

Collations of numerous experimental studies on reinforced concrete columns have been performed. The PEER Center developed one such database of experimental results expanded from past NIST results (Berry 2004). The resulting Structural Performance Database (PEER SPD) can be used for columns described by numerous design parameters and for several different damage states. Data exist in the form of force-displacement time histories as well as observations of damage at given demand levels (*EDP*). Specifically, the *EDP* derived for immediate use from the database is drift ratio. Damage observations include all those in Section 4.1.1, except for yielding.

The specification of column properties, for example rebar yield strength and column aspect ratio, lends itself to regression of damage states with respect to these properties. Given enough experimental data points, this can be performed using simple linear regression for any of the damage states above. The resulting equation can be used to predict the mean (or median) *EDP* at which the damage observation occurred. With an estimate of the variation of the data,

CDFs can be developed that describe the probability of exceeding a damage state (*DM*), given a demand level (*EDP*). These CDFs completely describe the PDM for the case of a discrete *DM*.

The procedure is illustrated for the bar buckling limit state and the design parameter values for the single-bent bridge (Table 2.1) in Equation 4.2. The H and D_c column-level variables were derived from the L/H and D_c/D_s bridge-level variables, respectively. A plot of the predicted damage model CDFs is shown in Figure 4.1 for the D_c/D_s design parameter. The reinforcement ratios ($\rho_{s,long}$, $\rho_{s,trans}$) are in units of percent (not decimal). To be consistent with the demand models, it was assumed that the conditional probability distributions of *DM* on *EDP* were lognormal. The coefficient of variation associated with this linear model was 0.37. The median values predicted by Equation 4.2 for variation of the D_c/D_s design parameter were 5.40, 5.43, 4.80, and 3.45 (%), respectively.

$$\Delta_{b.b.} = -1.58 + 0.0222H - 0.101D_c + 0.0361f'_c + 0.0707f_y + 1.71\rho_{s,long} + 2.56\rho_{s,trans} - 20.6\frac{N}{A_g f'_c} \tag{4.2}$$

Alternatively, parameterized regressions may yield more suitable equations for describing the mean relationship between demand and damage. Such equations exist (Berry 2003) for bar buckling (Eq. 4.3) and cover concrete spalling (Eq. 4.4) for circular concrete columns. These equations reduce uncertainty in the prediction of damage because they are derived using the principles of mechanics and, therefore, incorporate the variables that describe the relevant properties of the column.
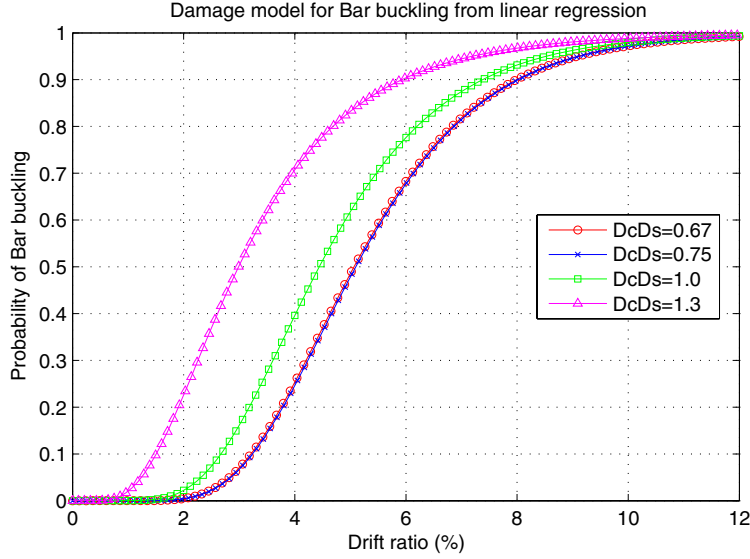
Fig. 4.1 Bar buckling component PDM from linear regression, D_c/D_s sensitivity

$$\Delta_{b.b.} = 3.25 \left(1 + 150 \rho_{s,trans} \frac{f_y}{f_c'} \frac{d_b}{D_c} \right) \left(1 - \frac{N}{A_g f_c'} \right) \left(1 + \frac{H}{10 D_c} \right) \qquad (4.3)$$

$$\Delta_{sp.} = 1.6 \left(1 - \frac{N}{A_g f_c'} \right) \left(1 + \frac{H}{10 D_c} \right) \qquad (4.4)$$

The associated measures of uncertainty (coefficients of variation) for the above two equations are 0.25 and 0.33, respectively. These formulas and coefficients of variation are valid only for the case of spirally reinforced circular concrete columns. See Eberhard and Berry (Berry 2003) for more recent and general equations describing these damage limit states.

The drift measurements (Δ) are all in units of percent. The steel reinforcement properties include the yield strength (f_y), diameter of longitudinal bars (d_b), and percent of transverse reinforcement ($\rho_{s,trans}$). The term containing the axial load (N) is simply the axial load ratio of the column. The remaining variables are concrete strength (f'_c), the effective cantilever height (H) and column diameter (D_c). Parameterization in this manner is important because the variables correspond in large part to the design parameters employed throughout this study.
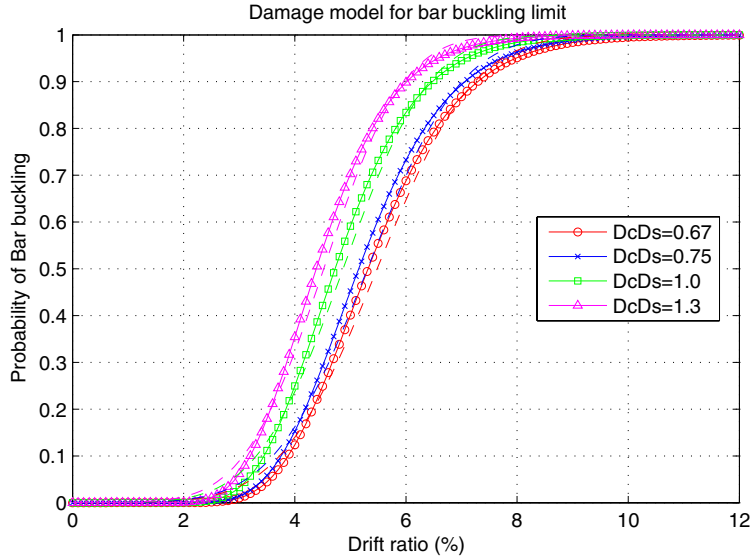
Fig. 4.2 **Bar buckling component PDM from Eq. 4.3, D_c/D_s sensitivity**

Equation 4.3 was used to predict drift ratio at bar buckling. The median values were 5.48, 5.31, 4.87, and 4.52 (%) for D_c/D_s sensitivity. The column height was halved for the effective cantilever length because the bridge column was in double curvature in the longitudinal direction. Two distributions were assumed and plotted together in Figure 4.2. For consistency with other probabilistic models in this study, the lognormal assumption is shown in solid lines while the normal distribution is dashed. This form of the bar buckling model was superior to the one obtained using linear regression (Fig. 4.1) in both the median and variance.

Focusing on the base bridge configuration, the lognormal CDF for bar buckling is shown in Figure 4.3, along with the CDFs derived for spalling and failure. The spalling CDF was derived from Equation 4.4, while the failure CDF was derived from linear regression mentioned above. While the normal distribution shown in bold lines is appropriate for a numerical integration of the PEER integral, to make some simplifying assumptions and develop closed-form solutions, a lognormal distribution is required. A comparison of the two distributions is included in the figure. As can be seen, the tails vary only minimally for the calculated standard deviation values.

Given the damage model derived above, it was possible to convolve it with intensity to obtain two useful outcomes. The first was a traditional damage fragility curve (Eq. 4.1) that shows the probability of exceeding a damage limit state as a function of *IM*. This damage fragility is shown (Fig. 4.4) for the three *DM* limit states from the damage model in Figure 4.3.

The second outcome incorporated the expected site hazard to obtain the annual frequency of exceeding each of the three *DM* limit states. The specific hazard is detailed in Section 6.1. This damage hazard curve is shown in Figure 4.5 for the numerical case (discrete), as well as an approximate continuous curve fitted through the points. The continuous curve was obtained by assuming that the value of the *DM* variable is in fact the median drift ratio for each limit state. This made it possible to provide a smooth curve with numerical values on the abscissa.
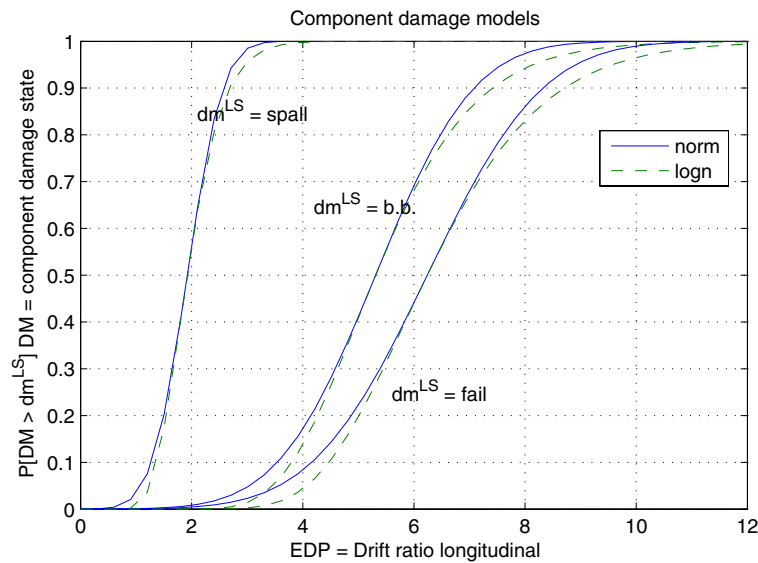
Fig. 4.3 Component damage models

Useful information can be gleaned from the *DM* fragility curves in Figure 4.4. For a given earthquake event with an expected intensity (*IM*) of $Sa(T_1) = 800$ cm/s^2, the probability of spalling is 1.0 (100%), but the probability of bar buckling is only 0.80. Similarly, the probability of failure is slightly less at 0.65. This information is general within the limits of analyzed bridge types and earthquake scenarios typical for California, and within these limits it can be applied to any earthquake scenario for a given bridge. It is also possible to draw vertical lines of constant intensity with the period-dependent *IM Sa(T_1)* in this case, as no structural parameter variations were performed.
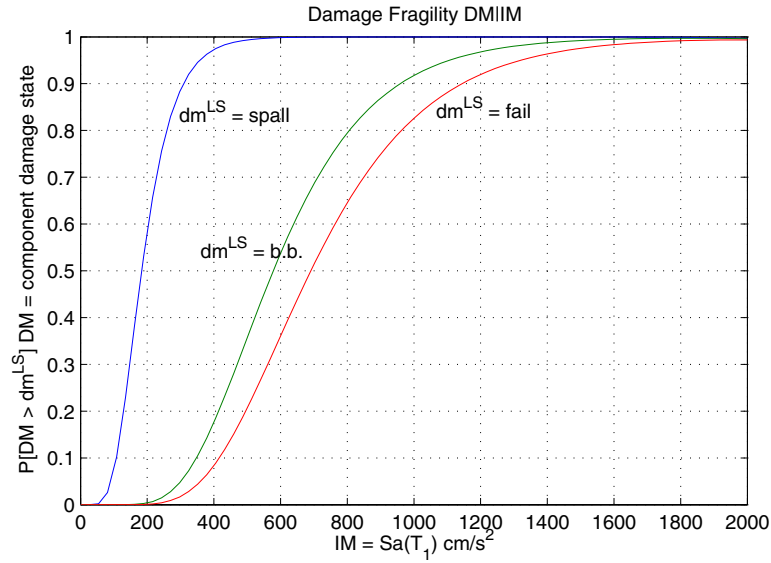
Fig. 4.4 Component damage fragility curves
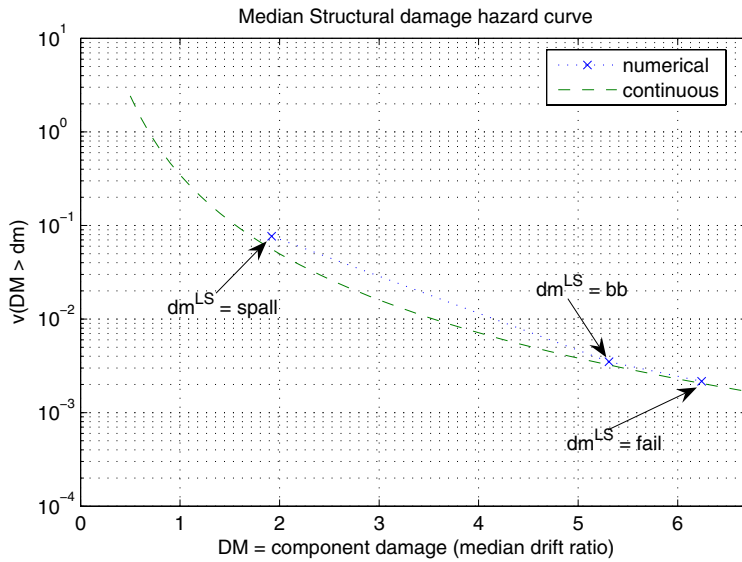
Fig. 4.5 Component damage hazard curve

In a similar manner, the ultimate chord rotation (equivalent to drift ratio in this case) for reinforced concrete members was predicted using nonlinear regression models based on an experimental database developed by Panagiotakis (Panagiotakis 2001) and improved in the *fib* report (CEB 2003). For a similar spiral reinforced column as utilized for spalling (Eq. 4.4) and bar buckling (Eq. 4.3), the mean prediction of ultimate displacement was made using Equation

4.5 (CEB 2003). Quantities not relevant to the columns in this bridge class were removed from the equation. For the purposes of this study, it was assumed that bar buckling is a failure mechanism, and therefore the ultimate displacement limit state and bar buckling were comparable between the two databases.

$$\Delta u = 1.5(1 - 0.38 a_{cyc})(0.3^{ALR})(f_c'^{0.2})\left(\frac{H}{D_c}\right)^{0.425} 25^{\left(1 - \frac{s'}{2D_c'}\right)\rho_{s,trans}\frac{f_y}{f'_c}} \qquad (4.5)$$

The drift measurements are in units of percent. The coefficient of variation is 0.47. All stress quantities are in MPa units. The a_{cyc} constant describes the loading history by assuming a value of 0 for monotonic loading and 1 for cyclic. The variables with apostrophes indicate clear distances (e.g., s') between transverse reinforcement. The confinement effectiveness term was introduced into the equation according to Mander (Mander 1988) for spirally reinforced columns. As a comparison with Equation 4.3, the base bridge configuration ultimate chord rotation was 6.04 for monotonic loading and 3.74 for cyclic loading. The average of these values (4.89%) is in close agreement with Equation 4.3.

4.1.3 Analytical Damage Models

Calibrated equations (Eqs. 4.3, 4.4, and 4.5) are useful, as they have been simplified for general usage and are applicable to a wide range of columns with input parameters in the range of data points considered. However, in the scenario of a nontypical column, a bridge system as a whole, or a structural component behaving in a manner different than a column (beam for example), it is beneficial to generate damage data specific to the structure or component of concern. Additionally, a damage state other than that described by the equations may be sought, particularly when a continuum of damage measure values is required (see Section 4.2.1). On the other hand, reliability analysis is applicable to any configuration or damage state, and it is faster than performing an experimental proof test of a particular component/system. Therefore, an attempt was made to analytically simulate a specific damage state using a reliability approach.

Numerous uncertainties are present in the drift predictions made with Equations 4.3, 4.4, and 4.5. Measurement error may lead to large bias in the prediction of the mean (or median). This error includes equipment, calibration, instrument fidelity, placement of displacement

monitoring devices, and most important, the observations of the onset of damage. Model error associated with Equations 4.3, 4.4, and 4.5 includes unknown variables and incorrect mathematical form. Finally, statistical error is also largely due to the insufficient number of tests for a given geometry and material property case. The form of the predictive probability distribution is also assumed. However, the main caveat of analytical models is the (possibly unknown) magnitude of the error (depending on the damage state) introduced due to the finite element approximation utilized. Additionally, a single reliability analysis is applicable only to the specimen at hand, making rapid evaluation of design choices more difficult. Consequently, to validate an analytical procedure for predicting damage, the case for which experimental column data (and predictive equations) were available for comparison was chosen.

A reinforced concrete column in a cantilever (single curvature) configuration was adopted for an analytical reliability-based study to mimic the results generated through the experimental databases. For simplicity, a circular cross section was chosen with spiral (transverse) reinforcement. The column was modeled using OpenSees (http://opensees.berkeley.edu/) in the same manner as the bridge columns of the reinforced concrete bridge class. OpenSees contains a set of reliability tools; incorporated by Haukaas and Der Kiureghian (Haukaas 2003), to supplement its finite element capabilities. A nonlinear force-formulated element with a fiberized cross section was used in the analysis. The cover and core concrete constitutive models followed the Kent-Park-Scott relationships for concrete. The longitudinal reinforcing steel used a linear strain-hardening constitutive model with no discontinuities in the loading tangent stiffness.

For the purposes of this study, only a single loading condition was applied to the column. The loading condition employed was a static linearly increasing displacement history. This simulated the static backbone response of the column. For this loading case, displacements (and strains) were monotonically increasing; therefore, the peak strain always occurred at the final displacement demand imposed on the column. Future publications by the authors will address the issue of cyclic displacements and further intricacies surrounding the choice of limit-state functions.

During loading, three different response quantities were monitored, namely drift ratio (Δ), hysteretic energy (*HE*), and column base shear *(P)*. These three response quantities were monitored until one of three damage limit states was reached. The first damage state considered in this study was the ultimate column lateral strength (P_{max}). The second damage state

considered was buckling of the longitudinal reinforcement. The final damage state considered was spalling of the cover concrete. The ultimate column strength was defined in terms of the force response quantity only. The bar buckling and spalling states were defined in terms of both drift and HE response quantities. For example, the drift ratio at buckling ($\Delta_{b.b.}$) is defined as the maximum drift ratio response before the onset of bar buckling. Similarly, $HE_{b.b.}$ is a cumulative measure up to the onset of damage, obtained by integration of the base-shear, tip-displacement diagram.

4.1.3.1 Limit-State Functions

To perform reliability analysis of the column, it was necessary to specify the limit-state functions corresponding to each damage state. While not comparable to the database equations, the lateral strength of the column was also included as a damage state. The limit-state function (Eq. 4.6) did not depend on time as long as the test was run long enough to attain the maximum force. The vector of random variables is **x**. P_θ is the parametric demand, varied to produce different values on the fragility curve.

$$g_1(\mathbf{x}, \theta) = P_{max} - P_\theta \qquad (4.6)$$

The onset of bar buckling was determined using longitudinal reinforcement strain histories. However, buckling is usually formulated in force or stress space. For an elastic system, the critical buckling load or stress is proportional to the modulus of elasticity and the inverse of the square of the unsupported length. For nonlinear problems, this critical load can be determined by iterations using the tangent stiffness. However, nonlinear constitutive material relationships prevented reaching the elastic critical stress. Therefore, the secant stiffness was used and the corresponding strain was determined from the steel stress-strain relationship. The strain at bar buckling was also a function of the random variables, including the volume of transverse reinforcement (s = spacing) and the size of reinforcing (d_b) bars used. A closed-form expression for the critical buckling strain is shown in Equation 4.7. The end condition constant was taken as 0.75. This is midway between the constant expected for pinned and fixed-end conditions.

The end condition constant (k_{bb}) was verified using an analytical study on individual reinforcing bars. Bars of varying diameter (#3 to #8) and center-to-center spacing (3.5–8.5 in., or 8.9–21.6 cm) were used in a fixed-fixed condition. An axial load was applied to each bar with a small lateral perturbation in the center of the bar. By using a large displacement geometric transformation (corotational formulation), the strain corresponding to a stress 25% of the peak strength was measured. Comparisons to Equation 4.7 were made to determine a suitable value of k_{bb}. Results indicated an average of 0.75 and a standard deviation of 0.05.

$$\varepsilon_{cr,b.b.}(\mathbf{x}) = \frac{\pi^2 d_b^2}{16 k_{bb}^2 s^2} \tag{4.7}$$

The limit-state function for bar buckling was then written in strain space as Equation 4.8. It is in the traditional format of capacity less demand, implying that failure occurs when demand exceeds capacity. Strain was monitored only in the extreme steel fiber in the direction of loading. A maximum compressive strain up to time t_f is used. Time indicates only the termination of the test, not to imply a time-dependent problem. Strictly speaking, Equation 4.8 is not differentiable as written (due to the *max* function); therefore, care should be exercised when using reliability methods that require limit-state function gradients.

$$g_{b.b.}(\mathbf{x}, t_f) = \varepsilon_{cr,b.b.}(\mathbf{x}) - \max_{t=0:t_f} \left(\varepsilon_{sc,i}(t) \right) \tag{4.8}$$

To generate fragility curves in displacement (or drift) space, it was necessary to rewrite the limit-state function as Equation 4.9. The time at bar buckling ($t_{@b.b.}$) was generated from the solution of $g_{b.b.}(x, t_{@b.b.}) = 0$. The parametric demand (Δ_θ) remained constant for each reliability analysis. While this formulation appears cumbersome, it was employed because it allowed arbitrary specification of the response quantity for use in the fragility functions.

$$g_2(\mathbf{x}, \theta) = \Delta(t_{@b.b.}) - \Delta_\theta \tag{4.9}$$

Similarly, it was necessary to rewrite the limit-state function in hysteretic energy space. The result is Equation 4.10.

$$g_3(\mathbf{x}, \theta) = HE(t_{@b.b.}) - HE_\theta \tag{4.10}$$

The concrete spalling limit state was simpler to measure, as the spalling strain used in the concrete constitutive model was a random variable by itself. In the mean, at a strain of 0.005, the cover concrete was assumed to lose strength as cover concrete is lost. It was assumed zero strength was reached in the cover by a strain of 0.006. The resulting strain limit-state function is Equation 4.11. As with bar buckling, only the compressive strain in the extreme fiber was considered, and Equation 4.11 is not differentiable as written.

$$g_{sp.}(\mathbf{x}, t_f) = \varepsilon_{sp} - \max_{t=0:t_f} (\varepsilon_{c,i}(t)) \qquad (4.11)$$

Once again, the time at spalling ($t_{@sp.}$), or design point time, was generated from the solution of $g_{sp.}(x, t_{@sp.}) = 0$. The limit functions in drift and hysteretic energy space then became Equations 4.12 and 4.13, respectively.

$$g_4(\mathbf{x}, \theta) = \Delta(t_{@sp.}) - \Delta_\theta \qquad (4.12)$$

$$g_5(\mathbf{x}, \theta) = HE(t_{@sp.}) - HE_\theta \qquad (4.13)$$

The static backbone curve (pushover curve) was produced through a displacement control scheme. Displacements were incremented in the lateral direction in steps of 0.001 inches until a maximum load was reached and the strength subsequently decayed to zero. To reduce the number of finite element computations, only 12 random variables were used to describe the problem. A description of the random variables, along with their means and standard deviations, is shown in Table 4.1 for the first column analyzed. The reduction in random variables was accomplished by inserting the same material random variables into the finite element model at each integration point rather than assigning a separate variable to each material parameter at each point. This strategy also made it possible to utilize finite elements for which response quantity sensitivity gradients do not exist. All of the different analysis combinations are summarized in Table 4.2.

118

Table 4.1 Analytical component damage model random variables

Name	Description	Type	Mean	Std. Dev.
H	Column height	Normal	7.6 m (300 in.)	5 cm (2 in.)
Lat	Lateral eccentricity	Normal	0.03 cm (0.01in.)	0.64 cm (0.25 in.)
E_f	Steel elastic modulus	Lognormal	2e5 MPa (29000 ksi)	3450 MPa (500 ksi)
f_y	Steel yield strength	Lognormal	470 MPa (68 ksi)	41 MPa (6 ksi)
f'_c	Concrete Unconfined strength	Lognormal	34.5 MPa (5 ksi)	8.6 MPa (1.25 ksi)
$\rho_{s,long}$	Percent longitudinal reinforcement	Normal	2%	0.1%
D_c	Column diameter	Normal	114 cm (45 in.)	1.9 cm (0.75 in.)
Wt	Axial load ratio	Normal	10%	2%
$\rho_{s,trans}$	Percent transverse reinforcement	Normal	0.7%	0.075%
ε_0	Strain at unconfined peak stress	Lognormal	0.002	0.0005
ε_{sp}	Spalling strain	Lognormal	0.006	0.00075
k_{bb}	Buckling length constant	Normal	0.70	0.05

Table 4.2 Analytical component damage model analyses

Analysis #	Displacement profile	Response quantity	Limit-state function
1	Linear	P_{max}	g_1
2	Linear	$\Delta_{b.b.}$	g_2
3	Linear	$HE_{b.b.}$	g_3
4	Linear	$\Delta_{sp.}$	g_4
5	Linear	$HE_{sp.}$	g_5

A mean value, first-order, second-moment analysis (MVFOSM) was performed for each limit-state function to determine the mean and standard deviation of each of the response quantities. This was followed by parametric first-order reliability method (FORM) analysis to determine the probability of failure over a range of each response quantity. Due to the extensive computational demands of performing finite element reliability analysis, random variable reduction was performed to allow refinement to the finite element solutions. This was achieved by removing the unimportant random variables (importance measure less than 5%). Therefore, parametric FORM analysis was consequently performed only with the reduced random variable set. This reduced set is detailed for each limit state and displacement history below.

4.1.3.2 Linear Displacement Profile (LDP) Results

MVFOSM analysis was performed by a first-order approximation of the limit-state functions expanded around the mean point. The gradients were determined from finite difference perturbations of all random variables. Response quantity first and second moments are reported in Table 4.3. These quantities were used as bounds on the parametric FORM analyses. The gradients computed were also used to generate approximate importance measures ($\tilde{\alpha}$) by multiplying by the standard deviation ($\nabla_{\mathbf{x}}g \cdot \sigma / \|\nabla_{\mathbf{x}}g \cdot \sigma\|$). These importance measures are reported in Table 4.4.

Table 4.3 Analytical component damage LDP first and second moments

	Before random variable reduction		After random variable reduction	
Analysis	μ_{MVFOSM}	σ_{MVFOSM}	μ_{MVFOSM}	σ_{MVFOSM}
1	134.53 k	12.395	134.53	12.304
2	6.759 %	1.546	6.7593	1.546
3	2293.8 k-in.	559.88	2293.8	558.66
4	1.857 %	0.1751	1.8574	0.1737
5	537.8 k-in.	82.948	537.8	80.952

FORM analysis was then performed to obtain a first-order estimate of the failure probability for several response quantity (θ) values. As well as the failure probability,

information at the end of the analysis was used to determine the correlated importance measure, $\hat{\gamma}$. This is reported with the MVFOSM importance measures in Table 4.4. The least important random variables were eliminated from the set of random variables. Retained random variables are indicated in bold in Table 4.4.

Table 4.4 Analytical component damage LDP importance measures

		1	2	3	4	5
1	$\tilde{\alpha}_{full}$	-8.00e-2	5.83e-2	1.47e-2	1.51e-1	4.45e-2
	$\hat{\gamma}_{reduced}$	-8.26e-2	5.89e-2		1.42e-1	
2	$\tilde{\alpha}_{full}$	-4.89e-2	1.53e-3	-2.18e-2	-1.13e-3	-4.43e-2
	$\hat{\gamma}_{reduced}$					
3	$\tilde{\alpha}_{full}$	2.07e-2	-5.34e-3	5.59e-3	-7.58e-2	-2.94e-2
	$\hat{\gamma}_{reduced}$				-8.54e-2	
4	$\tilde{\alpha}_{full}$	5.90e-1	9.54e-2	3.70e-1	5.43e-1	6.00e-1
	$\hat{\gamma}_{reduced}$	5.92e-1	7.71e-2	3.91e-1	5.53e-1	5.91e-1
5	$\tilde{\alpha}_{full}$	6.06e-1	-1.06e-1	9.62e-3	-1.81e-1	4.34e-1
	$\hat{\gamma}_{reduced}$	6.03e-1	-8.73e-2		-1.65e-1	4.46e-1
6	$\tilde{\alpha}_{full}$	3.48e-1	1.75e-1	3.08e-1	4.53e-2	2.13e-1
	$\hat{\gamma}_{reduced}$	3.47e-1	1.72e-1	3.17e-1		1.99e-1
7	$\tilde{\alpha}_{full}$	3.20e-1	5.83e-2	1.81e-1	-1.81e-1	1.11e-1
	$\hat{\gamma}_{reduced}$	3.23e-1	6.35e-2	1.88e-1	-1.85e-1	1.22e-1
8	$\tilde{\alpha}_{full}$	1.45e-1	-1.06e-1	-1.32e-1	-2.86e-1	-4.45e-2
	$\hat{\gamma}_{reduced}$	1.64e-1	-1.18e-1	-1.81e-1	-2.70e-1	
9	$\tilde{\alpha}_{full}$	-1.93e-2	8.00e-1	7.05e-1	1.47e-2	-8.63e-3
	$\hat{\gamma}_{reduced}$		7.74e-1	6.65e-1		
10	$\tilde{\alpha}_{full}$	-1.48e-1	2.17e-1	2.03e-1	1.51e-1	-1.50e-1
	$\hat{\gamma}_{reduced}$	-1.36e-1	2.14e-1	2.03e-1	1.39e-1	-1.62e-1
11	$\tilde{\alpha}_{full}$	9.78e-2	0.00e+0	5.58e-3	7.10e-1	6.05e-1
	$\hat{\gamma}_{reduced}$	9.51e-2			7.16e-1	6.09e-1

Table 4.4 — *continued*

12	$\tilde{\alpha}_{full}$	0.00e+0	-4.93e-1	-4.24e-1	0.00e+0	0.00e+0
	$\hat{\gamma}_{reduced}$		-5.39e-1	-4.41-1		

Complete parametric FORM analysis was performed for Equation 4.6 under both the complete and reduced random variable sets. The resulting fragility (CDF) curve and distribution (PDF) are shown in Figure 4.6. It is ostensible from the figure that the parametric FORM results coincide well with the distributions fitted to the MVFOSM data. The lognormal fit is particularly good at capturing the distribution tail behavior.
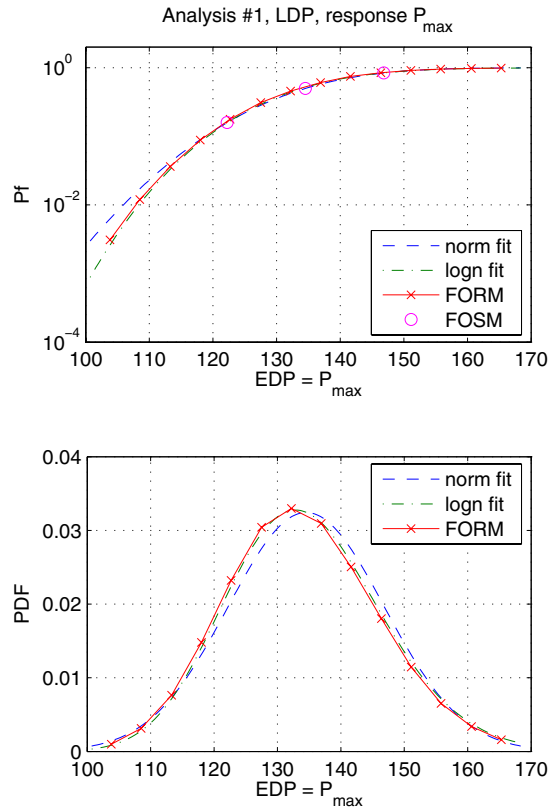
Fig. 4.6 Analytical component damage P_{max} LDP parametric FORM results

The limit-state function in Equation 4.9 was solved using both the complete and reduced sets for bar buckling (both drift and energy response quantities). The resulting CDF and PDF for drift at bar buckling are shown in Figure 4.7. For this analysis, the iHLRF algorithm failed to

converge for two of the parametric drift ratio demands. This is due to the trade-off between numerical accuracy of the finite element results, the perturbation factor used to calculated numerical gradients, and the size of the displacement-controlled static increment. To lower computation time, the displacement increment was increased to 0.00125 in. The perturbation factor (actual perturbation is scaled by random variable standard deviation) was selected as 25. This factor was selected to effect a quantifiable difference in response for each random variable so that the importance measures were unique for each variable considered. For this reason, the displacement increment and perturbation factor were selected separately for each analysis to optimize the calculation of the complete parametric curve. For the points where convergence failed, the CDF value was interpolated from neighboring values (and the PDF estimated from the derivative of these values).

Results for hysteretic energy at bar buckling (Eq. 4.10) were very similar to drift. The fragility curve and PDF are shown in Figure 4.8. In order to aid comparison with different column configurations, it is possible to normalize the abscissa by the hysteretic energy in a single cycle or hysteretic energy under P_{max}; however, this was not performed in this study. As would be expected from the LDP case, the coefficient of variation of the drift ratio and hysteretic energy response values at bar buckling are roughly equivalent. Once again, the lognormal fit through the MVFOSM data was a good predictor of tail behavior.
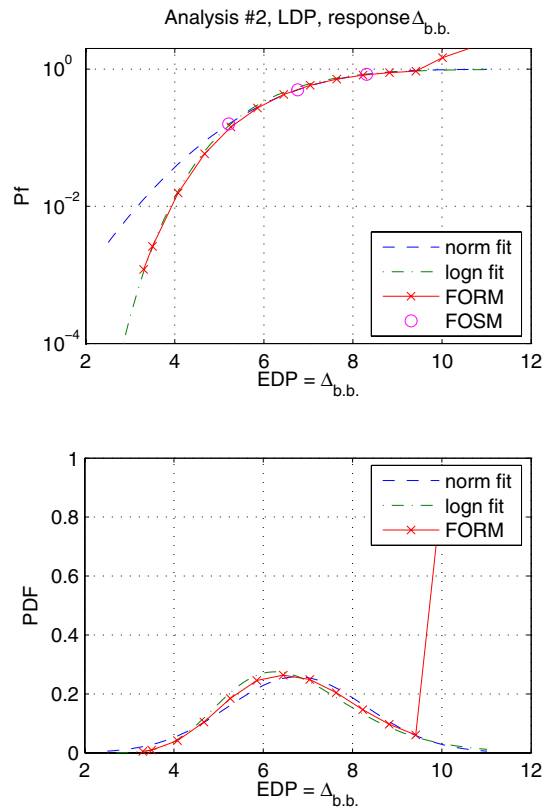
Fig. 4.7 Analytical component damage $\Delta_{b.b.}$ LDP parametric FORM results
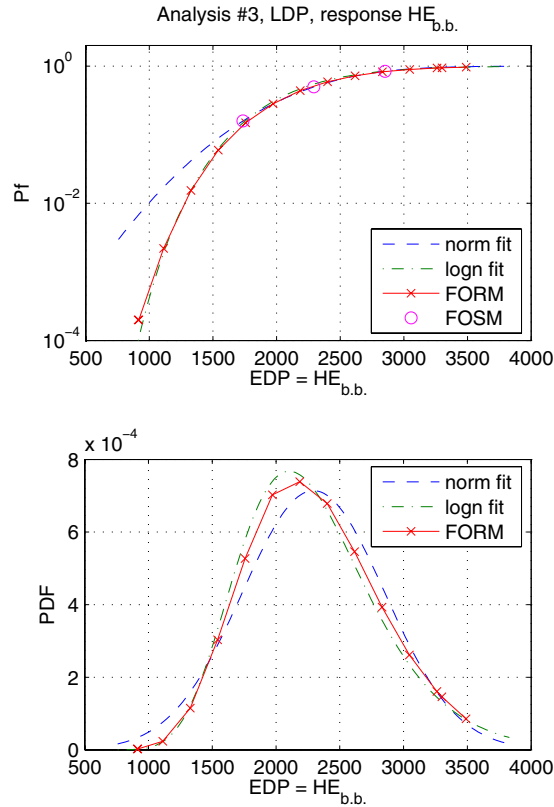
Fig. 4.8 **Analytical component damage *HE_{b.b.}* LDP parametric FORM results**

The onset of spalling occurs at low drift ratios; therefore, the resolution of finite element results needed to be increased at these lower displacements. The results shown here were derived using a displacement increment of 0.0005 in. The fragility curve for drift ratio at spalling, shown in Figure 4.13, exhibited low standard deviation. The coefficient of variation is 9.4% as compared to the bar buckling limit states that had values of 23 and 24%, respectively. The standard deviations will be compared with experimental values in the next section; however, from the outset it is apparent that this value is low.

Hysteretic energy is a cumulative quantity and the resulting finite element limit-state surface is usually smoother. The fragility curve derived using the reduced random variable set is shown in Figure 4.10. Interestingly enough, the coefficient of variation for hysteretic energy at spalling is higher (15%) than that for drift ratio. The same trend was evident with the cyclic displacement profiles (see below) and is due to the sensitivity of hysteretic energy to the force

(as well as displacement) in the response. At spalling especially, many specimens exhibit a plateau or slight strength decrease before strain hardening.
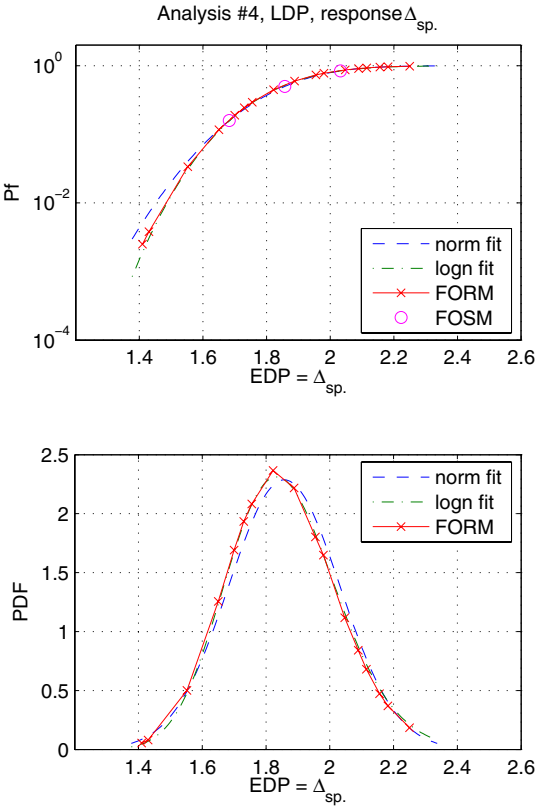
Fig. 4.9 Analytical component damage $\Delta_{sp.}$ LDP parametric FORM results
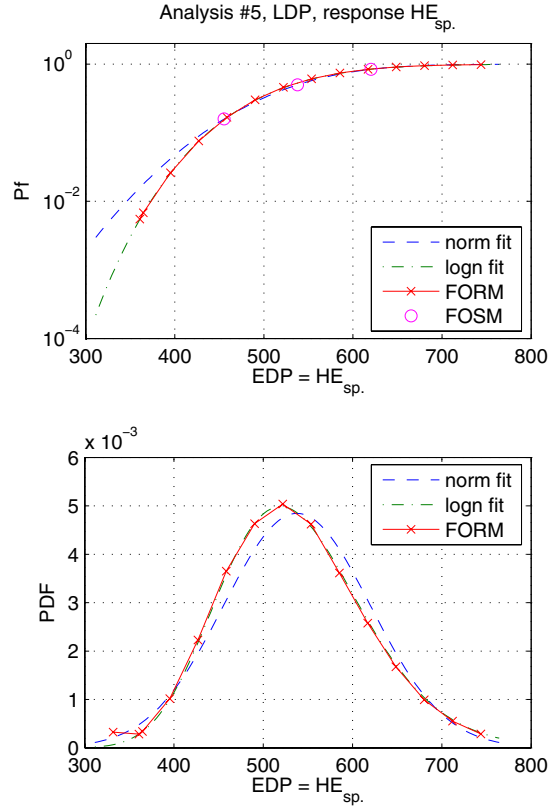
Fig. 4.10 Analytical component damage *HE$_{sp.}$* LDP parametric FORM results

4.1.3.3 System Analysis

Each column could be considered a critical link in an individual bridge system if bar buckling occurred or the shear demand exceeded the peak strength. Therefore, a column with several failure modes can be modeled as a series system with N components. The generalized system failure probability can be approximated as Equation 4.14.

$$p_{f,series} \approx 1 - \Phi_N(\mathbf{B}, \mathbf{R}) \qquad (4.14)$$

B is simply a vector of reliability index values for each column component, and R is a correlation matrix derived from the dot product of $\hat{\alpha}$ importance vectors.

It was then possible to derive the bivariate fragility surface for each column. For $N = 2$, the series failure probability can be evaluated in closed form from Equation 4.15. The constant ρ refers to the correlation coefficient. The two limit states used in the bivariate fragilities are the peak strength and drift ratio at bar buckling.

127

$$p_{f,series} = 1 - \Phi(\beta_1)\Phi(\beta_2) + \int_0^{\rho} \varphi_2(\beta_1, \beta_2, r)\, dr \qquad (4.15)$$

For each column individually, the bivariate CDF or fragility surface was derived with known correlation between the limit-state functions. A correlation coefficient of $\rho = -0.082$ was derived from the $\tilde{\alpha}$ values in Table 4.4. The resulting bivariate CDF is shown in Figure 4.11.
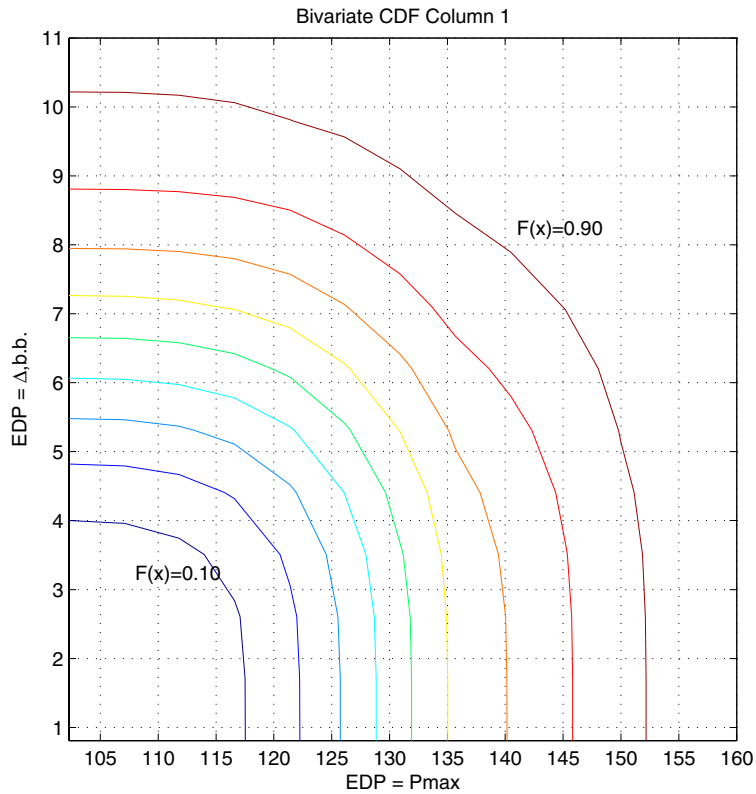
Fig. 4.11 Analytical component damage bivariate CDF

4.1.3.4 Experimental Comparison

To facilitate comparison with experimental results, a second column with different aspect ratio and properties was also analyzed. The values of the random variables for each column are shown in Table 4.5. Column 1 is equivalent to the column used for all of the preceding analyses. Properties for Column 2 were selected to keep the transverse bar spacing constant. Limit-state functions 1 (Eq. 4.6) and 2 (Eq. 4.9) were used in the computation of the fragility curves.

Table 4.5 Component damage column 1 and 2 properties

	RC column 1	RC column 2
H mean	7.6 m (300 in.)	9.1 m (360 in.)
f_y mean	470 MPa (68 ksi)	470 MPa (68 ksi)
f'_c mean	34.5 MPa (5 ksi)	34.5 MPa (5 ksi)
D_c mean	114 cm (45 in.)	182 cm (72 in.)
Wt mean	0.10	0.04
$\rho_{s,trans}$ mean	0.7 %	0.43 %
P_{max} mean (LDP)	593 kN (133.30 k)	2128 kN (478.41 k)
$\Delta_{b.b.}$ mean (LDP)	6.626 %	5.559 %

Using the results for both RC columns 1 and 2, it was possible to compare the experimental predictions (Eqs. 4.3, 4.4, and 4.5) with the reliability analysis in this section. Table 4.6 summarizes all of the mean and standard deviation drift quantities (in units of percent) for both column configurations. The ultimate drift (Eq. 4.5) tends toward a higher value than the bar buckling drift (Eq. 4.3). This phenomenon would be expected, as the onset of bar buckling does not necessarily indicate the ultimate displacement capacity of a column. However, the average of the monotonic and cyclic values for Equation 4.5 is roughly equivalent to the predictions from Equation 4.3.

For the bar buckling limit state, the reliability method captures not only the mean, but also the overall uncertainty very well (between methods). While difficult to quantify the sources of uncertainty individually from the experimental equations, the summation of uncertainties was captured well by the choice of random variables in the analytical method. In particular, the buckling length constant, k_{bb}, was sufficient to capture the required uncertainty in the finite element analysis prediction of the bar buckling phenomenon without employing a more complex model.

In contrast, the analytical prediction of spalling provided a much lower coefficient of variation (0.094) than the database equation. As mentioned, this is lower than the experimental predictor as the drift at the onset of spalling is not subject to observation/measurement error. It may also often be the case that spalling initiated before any visible deterioration of the cover concrete occurred. The net result is the analytical prediction should always underestimate the

experimental value (mean), and the spalling limit state is a discrete point in simulation time for analysis but tends toward a continuum of values based on the first observation experimentally.

Table 4.6 Component damage analytical and experimental comparison

	Column 1 drift (%)		Column 2 drift (%)	
	Experimental	Analytical LDP	Experimental	Analytical LDP
$\Delta_{b.b.}$ mean	6.6	6.8	5.3	5.56
$\Delta_{b.b.}$ σ	1.7	1.5	1.2	3.19
$\Delta_{sp.}$ mean	2.4	1.9	2.3	1.60
$\Delta_{sp.}$ σ	0.79	0.18	0.76	0.10
Δ_u mono.	8.1	6.8	6.9	5.56
Δ_u cyclic	5.0	-	4.3	-
Δ_u avg.	6.6	6.8	5.6	5.56
Δ_u σ	3.1	1.5	2.6	3.19

This section discussed a rigorous analytical reliability-based technique for deriving *EDP-DM* fragilities for circular reinforced concrete columns. Five limit states were considered under a linear displacement profile: peak strength, drift ratio at bar buckling, hysteretic energy at bar buckling, drift ratio at spalling, and hysteretic energy at spalling. Twelve random variables were used; however, these were reduced based on importance measures to allow faster computations. Fragility curves were generated for the limit states using parametric FORM analysis over a range of response values. The first and second moments were then compared with experimentally based predictive equations for spalling and bar buckling.

The purpose of analytically modeling fragilities was to provide an alternative procedure to the existing experimental database founded predictive equations. The reliability procedure allows for the description of material, property, and geometric uncertainties without suffering from the measurement, model (incorrect form and missing variables), and statistical errors of the experimentally based predictive equations. However, the analytical procedure does suffer from model error due to the choice of finite element modeling capabilities and ability to reproduce a

complex phenomenon such as bar buckling. The analytical method also introduces statistical error due to first-order failure probability approximations, and the assumed input probability distributions. Additionally, it should be recognized that the limit-state functions are not applicable to the case of a cyclically applied load. However, overall analysis is advantageous because it can be applied to particular geometries and material properties of interest, with quicker production of results than an experimental program. The analytical procedure is applied to bridge systems in the next section.

4.2 BRIDGE LEVEL

Using the familiar single-bent base bridge configuration, a damage evaluation of the complete (entire) structural system was performed here considering possible structural system, or bridge-level, variables. In PEER meetings with the California Department of Transportation (Porter 2002), several bridge-level outcomes had been discussed. The bridge-level variables all related to a graded system of bridge performance levels such those in ATC-49 (ATC 2001). These are discrete tables with traditional language such as "immediately operational," "emergency traffic only," and "closed." The goal was to provide rational criteria for selection of these performance levels by first defining appropriate damage models.

Currently, Caltrans decision makers use information from post-earthquake bridge inspections to determine whether certain transportation links remain open or closed. Data entering the decision-making process are observed damage to the roadway, settlement, permanent deformation, cracking, fracture, and buckling. Largely subjective decisions are then made on whether the bridge can support live load, and whether it has enough lateral load capacity to withstand an aftershock. This information may be supplemented by pictorial databases (Hose 2000) relating types of observable damage with expected post-earthquake performance. However, on a more rational basis, quantified data on loss of the vertical and lateral load-carrying capacity can be used to distinguish different performance levels of a bridge. These need not only be open and closed, and can include a continuous distribution based on traffic load-carrying capacity relative to the initial or design value. Therefore, the bridge-level *DM*s to be developed must include information on the degradation of a bridge's load-carrying capacity. The issue of structural safety also arises when considering subsequent earthquake

shocks. The decision to assign a damaged bridge to a certain performance level may be more influenced by this safety consideration, rather than its immediate load-carrying capacity.

4.2.1 Bridge Damage Measures

A category of *EDP*s not previously addressed in Chapter 3 is the functional *EDP*. These are more explicitly related to the bridge structural system performance. Specifically, the functional *EDP*s considered in this study are the post-earthquake residual load-carrying capacity of the bridge. The residual load-carrying capacity can be determined in both lateral directions (longitudinal and transverse), as well as the vertical direction. The value of the *EDP* was determined from a static nonlinear pushover of the structure in the lateral directions and a pushunder in the vertical direction. A pushunder is analogous to a pushover, except that the load is applied vertically downward, and the vertical displacement (at the top of the column) is monitored. Results of a pushunder may be interpreted in terms of a gravity load safety factor (Mehanny 2001).

These functional *EDP*s became measures of demand, as they were executed after a dynamic time history analysis. Therefore, the residual load-carrying capacity of a bridge was expected to degrade as the intensity of an earthquake event increased. To facilitate simpler demand model computations, the *EDP* (in force units) was defined relative to the load-carrying capacity at *IM* = 0 (Eq. 4.16). The functional demand parameter was thus termed the "loss of load-carrying capacity" (in force space), but should not be confused with the variability inherent in the capacity of the bridge system in the absence of earthquake loading. The resulting PSDMs, once again using $Sd(T_1)$, for the loss of longitudinal and vertical load-carrying capacities are shown in Figures 4.12 and 4.13, respectively.

$$EDP = EDP_{IM=0} - EDP_i \qquad (4.16)$$
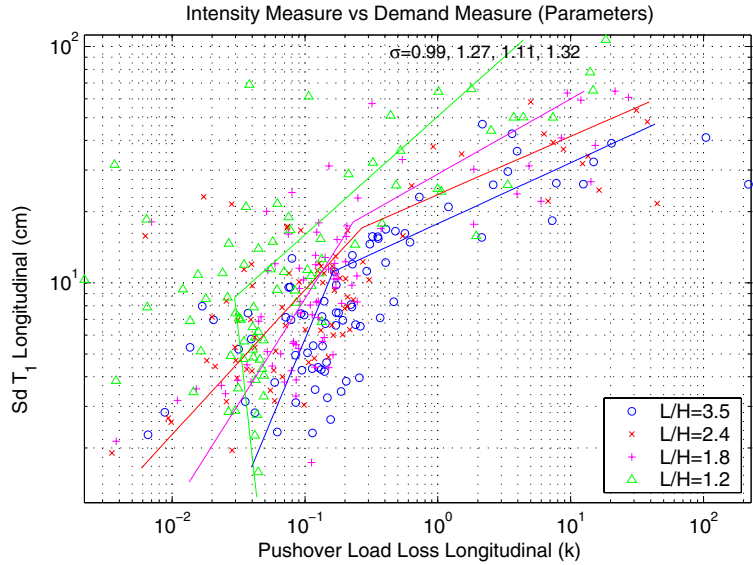
Fig. 4.12 PSDM $Sd(T_1)$-capacity loss, L/H sensitivity longitudinal

Unlike Figure 3.19, for example, these functional *EDP*s cannot be described effectively by a single linear fit (in log space). They exhibited two regimes of behavior that required separate fitting. The low intensity response of bridges was primarily linear; hence there was little or no degradation in the residual load-carrying capacity. This regime is shown in Figure 4.12 as the nearly vertical lines in log-space (and truly vertical lines in linear space) at small *IM* values. The second regime defined the range of intensities that damaged the bridge structure and decreased its ability to carry post-earthquake loads according to Equation 3.10.

The vertical axis on Figure 4.13 is a geometric combination of earthquake *IM*s, $Sa(T_1)$, in the longitudinal and transverse directions, and does not include a spectral *IM* in the vertical direction. However, to maintain commonality with the fragility formulation in this study, only the lateral *IM*s were included. As seen by the large scatter, however, the lateral intensities may not be the best predictors of the residual vertical load capacity. The ability to capture strength and stiffness degradation post-earthquake is also highly dependent on the finite element platform and material models selected.
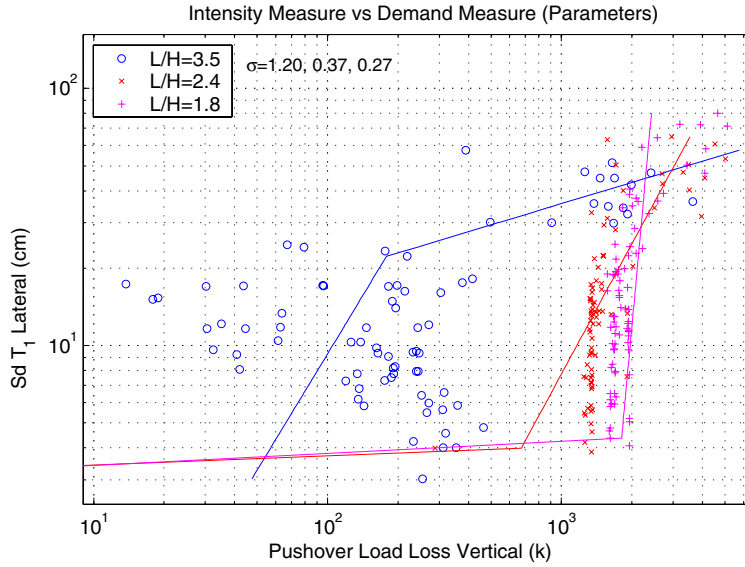
Fig. 4.13 PSDM *Sd*(*T₁*)-capacity loss, *L/H* sensitivity vertical

The wide amount of scatter in the degrading regime lowered the confidence in using these demand models directly, as the selection of the median fit was highly uncertain. Not only was confidence in the median low, but there were also large dispersion values associated with the model fit. As an illustration, demand fragility curves created from the median, 50%, and 90% confidence intervals are shown in Figure 4.14.
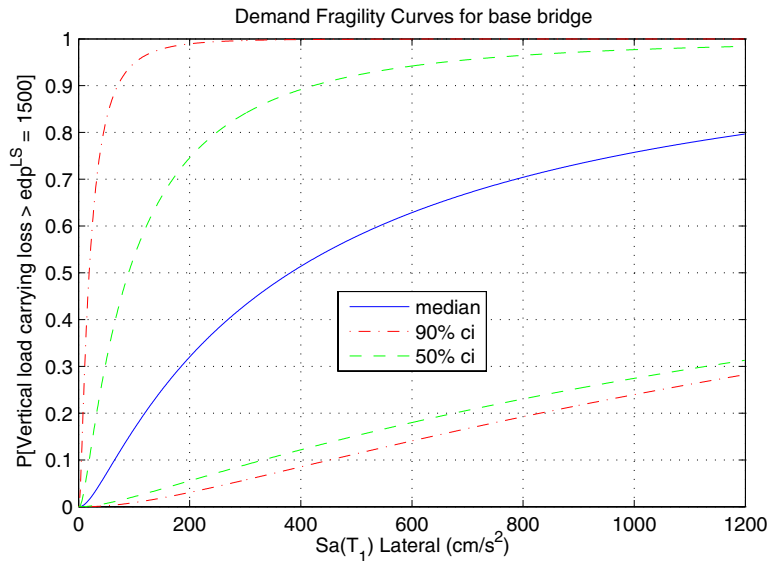
Fig. 4.14 *Sa*(*T₁*)-capacity loss demand fragility confidence intervals, base bridge vertical

Compared to Figure 3.82 where the component-level confidence intervals were shown, it is evident that not only is the dispersion huge, so are both the 50% and 90% confidence intervals. The principal distinction between the two figures is the small discrepancy between the 50% and 90% confidence intervals in Figure 4.14 (hence lack of confidence at all levels). Therefore, methods to improve the prediction of capacity loss through reduction in model uncertainty were investigated and are in Section 4.2.3.

Given the bridge system functionality implied by the *EDP* (loss of load-carrying capacity), it was necessary to extend the *EDP*s to *DM*s at the bridge level as well. The corresponding *DM* was the loss of lateral or vertical load-carrying capacity (as a percent of the original). This *DM* value was produced by introducing a prediction of pre-earthquake load-carrying capacity and then comparing to the residual load-carrying capacity in a demand/capacity evaluation. The pre-earthquake load-carrying capacity was determined using a nonlinear static pushover or pushunder in the same manner as the demand model. However, to incorporate uncertainty in the pre-earthquake capacity, a structural reliability approach was adopted.

4.2.2   Reliability-Based Damage Models

The introduction of capacity at the bridge level is a difficult proposition using experimental results. Not only are there numerous components constituting the structural system, but they may also interact in nonlinear ways. Experimental tests on the (structural) system level are few (Pantelides 2002; Eberhard 1997), especially when specifying a bridge using arbitrary design parameter values. Therefore, this study incorporated uncertainty in the capacity domain by reliability analysis, as was performed for the component-level case in Section 4.1.3. This was achieved using reliability tools integrated into finite element analysis in OpenSees (Haukaas 2003). Using this approach, the variability or uncertainty of the geometry, materials, and loads was accounted for by assigning probability distributions to the input variables in the finite element analysis.

This approach, however, did not include uncertainty from model error or lack of knowledge, as the same finite element model was used for both demand and damage assessments. Subsequent use of this method should therefore be penalized by a larger epistemic uncertainty term in fragility or hazard analyses incorporating the achievement of designated levels of confidence.

Structural reliability methods were employed to estimate the probability of exceeding values of specified limit-state functions. As a convention, the limit-state function is usually denoted as $g(\mathbf{x})$, where $\mathbf{x}$ is the vector of random variables considered in the problem, and $g(\mathbf{x}) \leq 0$ usually defines the failure domain (e.g., when demand exceeds capacity). The problem was simplified by using only ten random variables. These random variables were assumed to have a normal or log-normal distribution as shown in Table 4.7.

While it was possible to insert individual random variables at every element for each material property, the same material random variables were assigned to every element throughout the structure to facilitate reasonable computation time. The limit-state function was defined in terms of the pre-earthquake lateral load-carrying capacity from longitudinal pushover analysis (Eq. 4.17) at different levels of demand (EDP_i). For the bridge level, bar buckling and spalling were not considered as damage limit states.

$$g(\mathbf{x}) = P_{@DM=dm^{LS},long}(\mathbf{x}) - EDP_i \qquad (4.17)$$

Table 4.7 Bridge-level single-bent random variables

Rv num	Variable	Type	Mean	Std. dev.
1	L	Normal	18.3 m (720 in.)	7.6 cm (3 in.)
2	L/H	Normal	2.4	0.05
3	E_f	Normal	2e5 MPa (29000 ksi)	4800 MPa (700 ksi)
4	f_y	Lognormal	470 MPa (68 ksi)	55 MPa (8 ksi)
5	f'_c	Lognormal	34.5 MPa (5 ksi)	6.9 MPa (1 ksi)
6	D_c/D_s	Normal	0.75	0.02
7	ϕ'	Normal	35°	6°
8	γ	Normal	18.1 kN/m³ (115 pcf)	1.6 kN/m³ (10 pcf)
9	$\rho_{s,trans}$	Normal	0.007	0.0015
10	Wt	Normal	0.25	0.1

The probability of failure was estimated using FORM analysis at each level of demand. FORM uses a linearization of the limit-state function at the design point to determine the failure probability. The design point is the most likely failure point in the failure domain. For the limit state $DM = 0$ (no loss of load-carrying capacity), the results of FORM analysis are shown for longitudinal load and vertical load in Figures 4.15 and 4.16, respectively. The estimated PDF for the damage model is shown in the bottom pane of each plot. These damage models are analogous to the P_{max} component damage models obtained in Section 4.1.3.
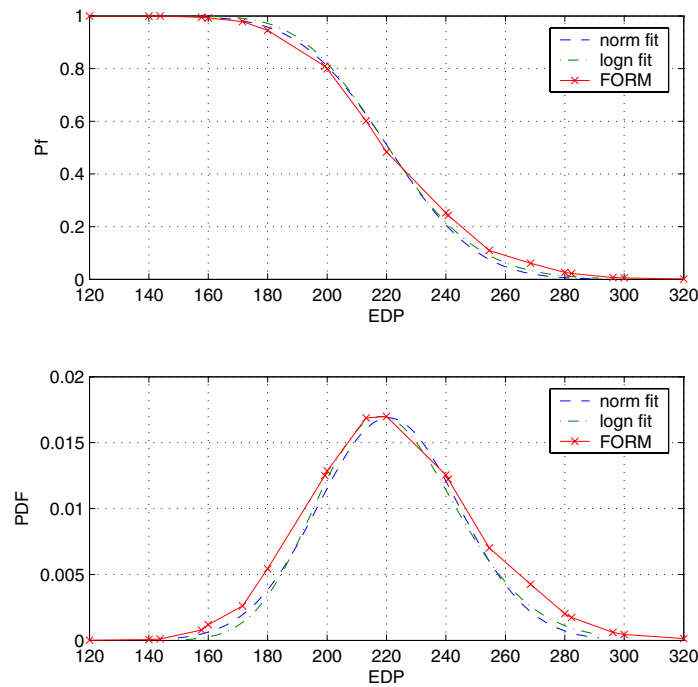
Fig. 4.15 Bridge damage model longitudinal, $dm^{LS} = 0$

Each point on the CDF curves corresponded to a FORM analysis at a given *EDP* level (EDP_i). Each curve represented one value of the damage limit state (dm^{LS}). To facilitate computations with the damage models shown, normal and lognormal distributions were fit to the data points to facilitate closed-form solutions. The lognormal fit was used in subsequent damage models rather than the first-order approximation points.
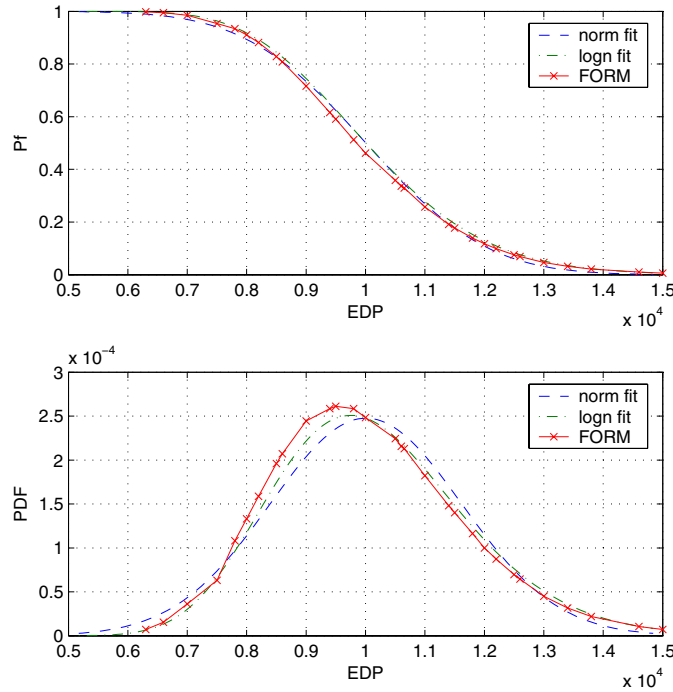
Fig. 4.16 Bridge damage model vertical, $dm^{LS} = 0$

Similar damage models were obtained for a limited number of other values of dm^{LS} (Fig. 4.17).   In between the computed dm^{LS} values, interpolation was carried out by scaling the lognormal distributions according to a constant coefficient of variation. The damage limit state was incorporated into Equation 4.17 as the force at the location on the pushover curve where 1-dm^{LS} (%) of ultimate load existed, consistent with the *DM* definition in Section 4.2.1.

The damage models were then integrated with the demand models to produce the damage fragility curves in Figure 4.18. Alternatively, numerous fragility curves can be plotted as a fragility surface, as shown in Figure 4.20. As determined by the demand model, an extremely large earthquake intensity would be required to cause more than 60% loss of load-carrying capacity. This is reflected in the damage fragility surface by the shelf at higher *DM* values. Confidence in finite element results diminish as the structure softens and becomes highly damaged or close to collapse. Consequently, caution should be exercised when utilizing damage fragilities at these high *DM* values.
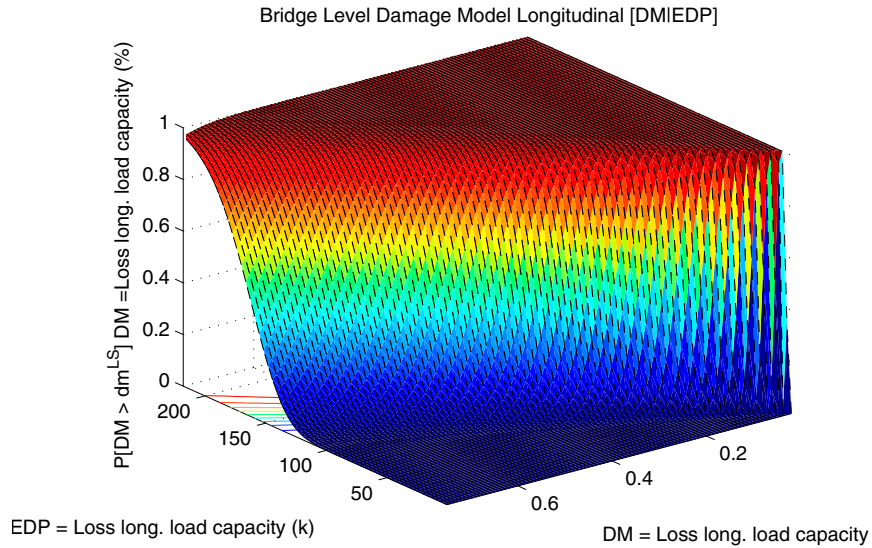
Fig. 4.17 Bridge-level damage model longitudinal
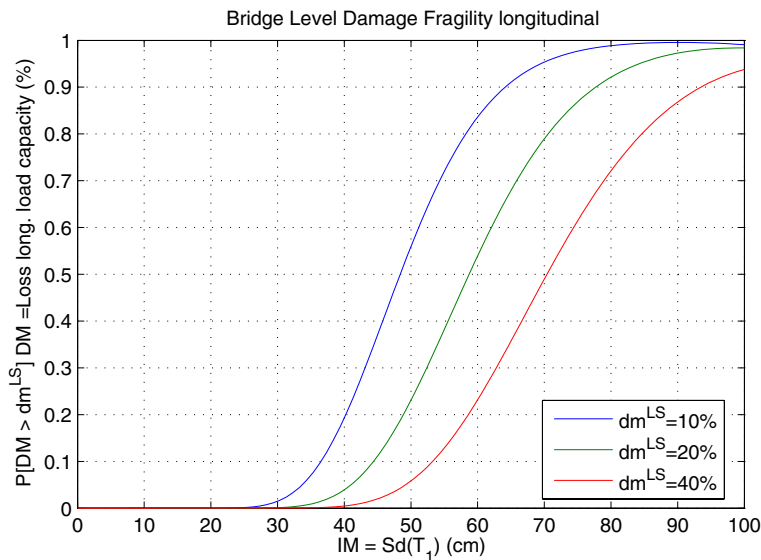
Fig. 4.18 Bridge-level damage fragility longitudinal

Finally, the inclusion of hazard into a damage hazard curve was significantly simpler than the component-level case (see Fig. 4.5) due to the continuous lognormal form of the damage model (as opposed to a discrete-valued damage model for components). For the case of vertical load-carrying capacity as the *DM*, the resulting damage hazard curve using data from Section 6.1 is shown in Figure 4.19. The closed-form solution is discussed in more detail in Section 6.3;

however, the numerical solution was obtained simply from the damage model and the numerical derivative of the demand hazard curve according to Equation 4.18.

$$\lambda_{DM}(dm) = \int P(DM > dm \mid EDP = edp) \cdot d\lambda_{EDP}(edp) \qquad (4.18)$$
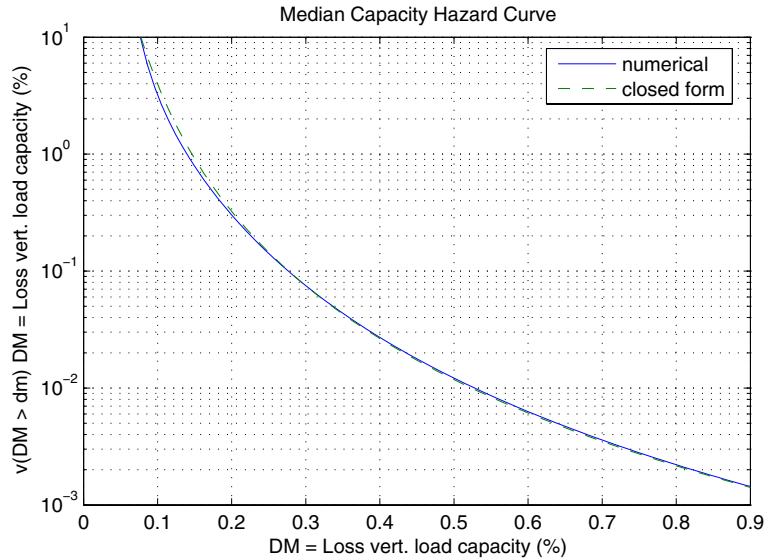
Fig. 4.19 Bridge-level damage hazard curve vertical

4.2.3   Improved Methods for Post-Earthquake Capacity

While it was possible to directly assess the post-earthquake capacity using the traditional PEER formulation, the large uncertainty in this method necessitated development of better methods of prediction. The alternative formulations were also important when determining the aftershock load-carrying capacity of the bridge. The large amount of computation required to develop post-earthquake residual load-carrying capacity curves was multiplied when developing curves for aftershock scenarios. The direct method (formulation used in Section 4.2.2) was addressed as Method A below, followed by three alternative methods for better predicting damage fragility in terms of loss of load-carrying capacity.

4.2.3.1 Method A — Direct Method

This method was a specific application of Equation 4.1 to the PSDMs involving residual load-carrying capacity shown in Figures 4.12 and 4.13. The resulting damage fragilities showing the loss of lateral and vertical load-carrying capacity are shown in Figures 4.20 and 4.21, respectively. To reduce the scope of this study, only the vertical load-carrying results are presented from this point on.
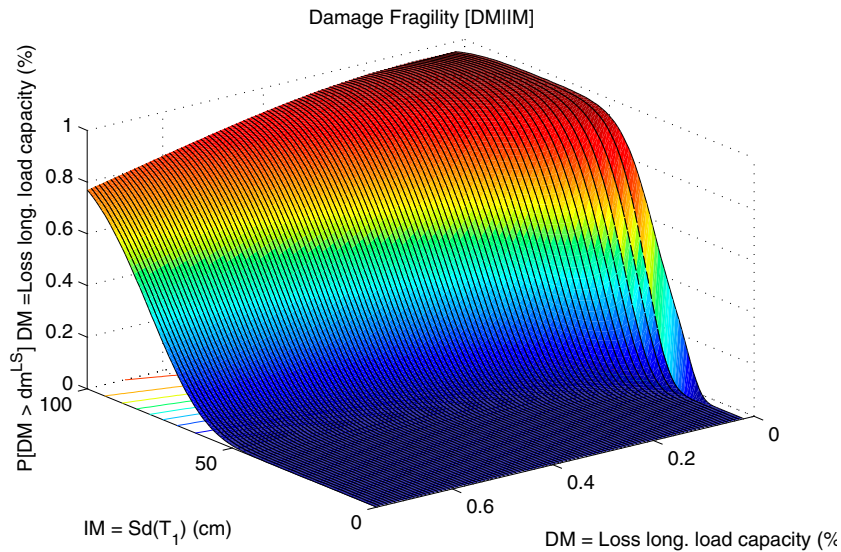
Fig. 4.20 Bridge damage fragility Method A longitudinal

While Method A appeared to generate effective results, the selection of the median PSDM for a first-shock post-earthquake became more and more uncertain with increasing first-shock intensity. The dispersion value used to generate the PSDMs was artificially low due to the lack of dispersion in the linear regime of bridge behavior. The difference in low intensity behavior became apparent when comparing all of the subsequent methods. Nonetheless, the dispersion in the nonlinear range of response was large, creating an inordinately long tail of the PDF. The magnitude of the *IM* axis was curtailed at $Sd(T_1) = 150$ cm (corresponds to a spectral acceleration of 2.4g). The net result was a probability of 1.0 not being obtained for all but the smallest *DM* values. Method A is compared with the other improved methods in Section 4.2.5.
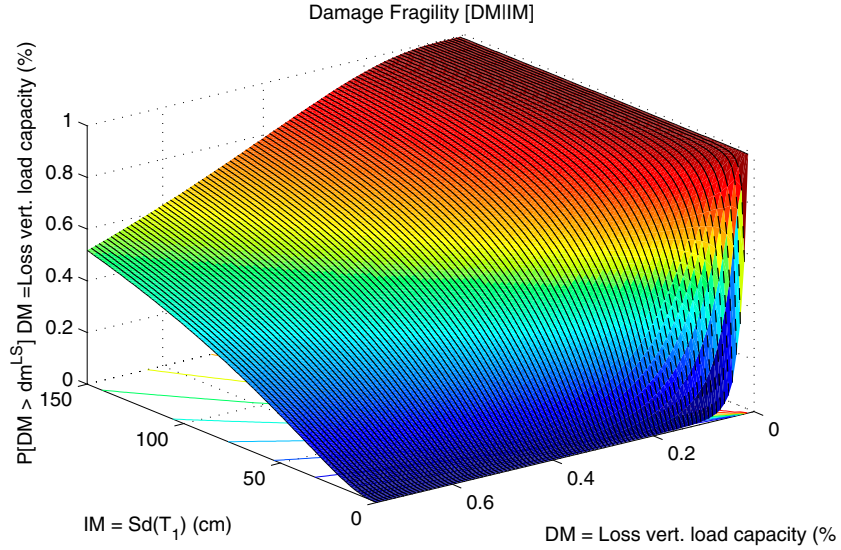
Fig. 4.21 Bridge damage fragility Method A vertical

4.2.3.2 Method B — MDOF Residual Displacement Method

This method introduces the importance of the correlation between post-earthquake capacity and residual displacement. An intermediate variable, post-earthquake residual displacement (u_{res}), was introduced between the *EDP* and *IM* variables. The resulting formulation is shown in Equation 4.19. This method was beneficial because the relationship between residual displacement and earthquake intensity was already developed during previous PSDM studies (Chapter 3). The PS*DM* employed for this method is shown in Figure 4.22, with *L/H* sensitivity. However, there was large uncertainty in predicting residual displacement, especially given a spectral *IM* such as *Sd* or *Sa*. A better *IM* for predicting u_{res} for this bridge was *PGD*. But to maintain consistency between examples, $Sd(T_1)$ was used.

$$P\!\left(DM < dm^{LS} \mid IM = im\right) = \iint P_{DM|EDP}\!\left(dm^{LS} \mid edp\right) \cdot dP_{EDP|U_{res}}\!\left(edp \mid u_{res}\right) \cdot \\ dP_{U_{res}|IM}\!\left(u_{res} \mid im\right) dedp \cdot du_{res} \tag{4.19}$$
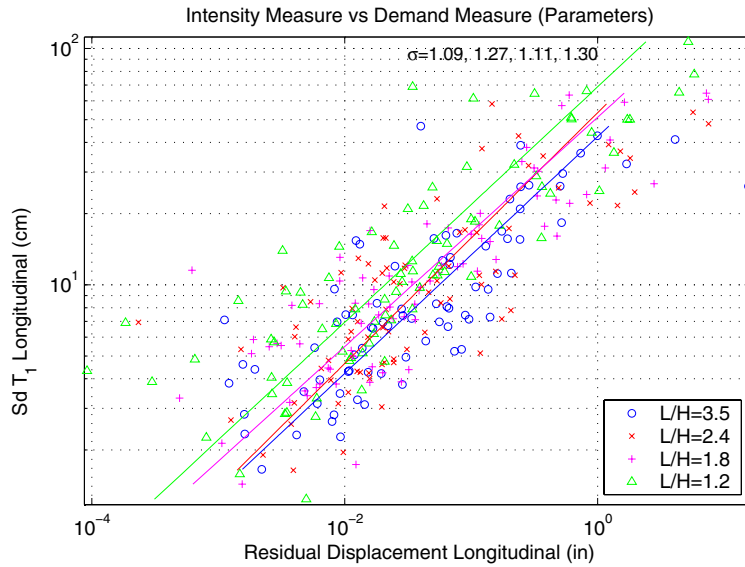
Fig. 4.22 PSDM $Sd(T_1)$-u_{res}, L/H sensitivity longitudinal

In order to utilize Method B, a relationship between residual displacement and loss of capacity needed to be developed. This is shown in Figure 4.23 for the vertical direction. The loss of capacity was due to not only the degradation of stiffness and strength, but also the presence of P-Δ effects for large residual displacements. A linear fit was made to the residual displacement values larger than 5.1 cm (2 in.) and extended to the origin to provide a smooth transition to earthquake intensities. This prevented an unrealistic jump in load-carrying capacity loss around zero intensity (and therefore zero residual displacement).

The resulting damage fragility surface showing the probability of exceeding different levels of vertical load-carrying capacity loss is shown in Figure 4.24. Due to the large intensity required to obtain large residual displacements (Fig. 4.23), the probabilities of exceeding large load losses were small. Not only this, but the method suffered from the same large dispersion problem as Method A, this time due to the uncertainty in the residual displacement PSDM. Once again, all methods are compared in Section 4.2.5.
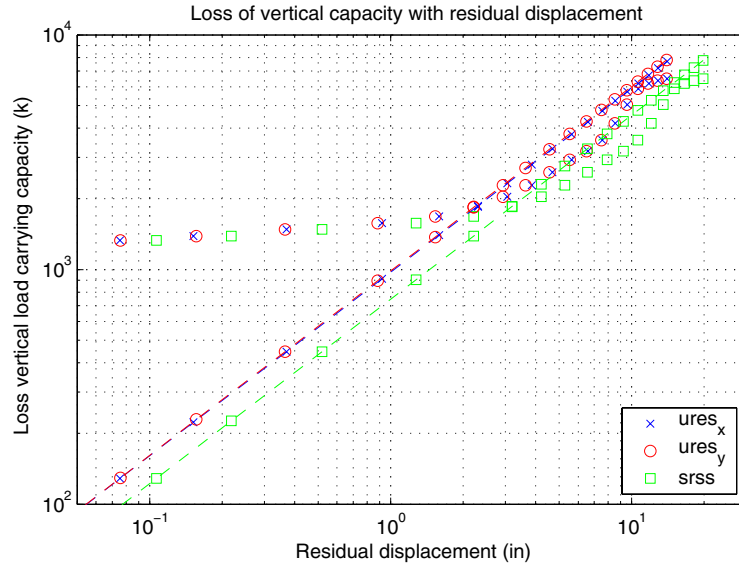
Fig. 4.23 u_{res}-capacity loss vertical
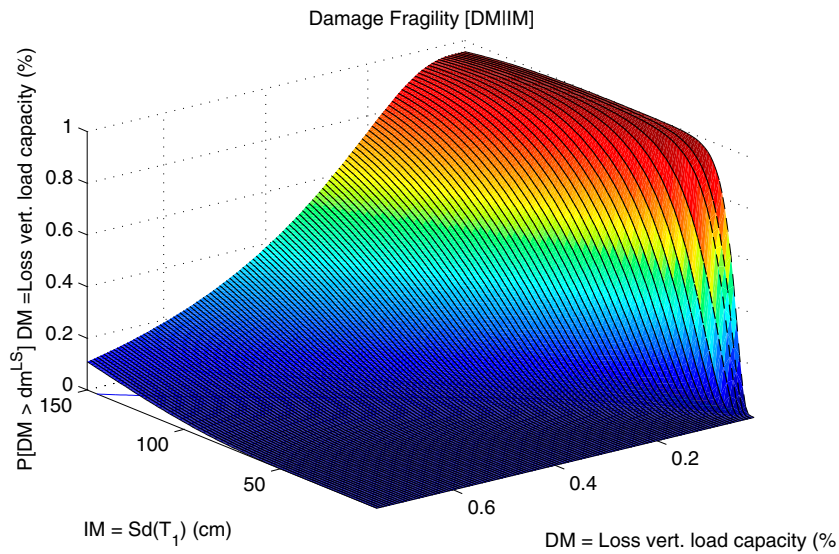
Fig. 4.24 Bridge damage fragility Method B vertical

4.2.3.3 Method C — SDOF Residual Displacement Method

Methods B and C utilize the same formulation (Eq. 4.19) involving residual displacements. The difference with this method is the assumption that residual displacements can be derived using a residual displacement spectrum from equivalent single-degree-of-freedom (SDOF) systems. The

large uncertainty in the PSDM term in Method B motivated a better method for predicting u_{res}. Residual displacement spectra have been examined previously (Kawashima 1998). Sensitivity to earthquake intensity was only examined for measures such as magnitude and distance. In this study, the residual displacement of single-degree-of-freedom oscillators was regressed against all measures of earthquake intensity (*IM*) in Section 3.4.1. This made the procedure analogous to PSDA for more complex structures (Section 3.3).

The inelastic SDOF oscillator employed in this method had the same initial elastic period of the bridge (T_1). The entire spectrum was not generated for each ground motion, i.e., only the residual displacement at T_1 was calculated. The inelastic oscillator's yield strength was taken from the nonlinear pushover of the bridge in the longitudinal and transverse directions. Previous analyses had shown the *R*-factor for this bridge configuration with respect to the USGS 2% in 50-year hazard spectrum was 3.6 for T_1 (transverse direction) and 3.9 for T_2 (longitudinal direction). A value of $R = 4$ and a hardening ratio of 1.5% for the bilinear SDOF oscillator were therefore assumed. The resulting residual displacements can be plotted in a manner consistent with PSDMs, as shown in Figure 4.25. Note the relatively large dispersion.
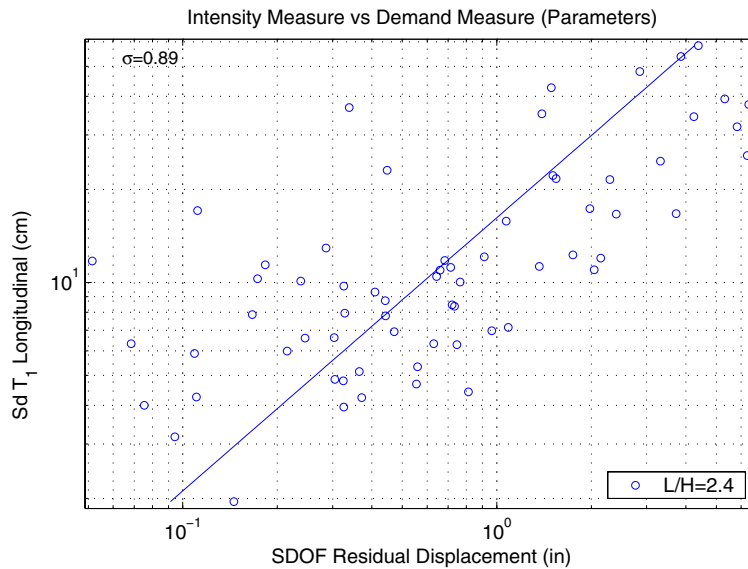
Fig. 4.25 PSDM $Sd(T_1)$-u_{res}, SDOF

The intent of Method C was to reduce the dispersion in the PSDM term used in Method B. As evidenced in Figure 4.25, SDOF oscillators also have a large amount of uncertainty in predicting residual displacements (with *Sd*). Therefore, the results are similar for Methods B and

C, with the slight discrepancy arising from the residual displacement values predicted with either SDOF or MDOF systems and the resulting loss in capacity from Figure 4.23. The advantage of this method was avoiding PSDA on a complex bridge structure and using SDOF data instead. The disadvantage of using this method was the selection of T_1 for the SDOF oscillator. More complex finite element models captured the softening of the fundamental period with accumulation of damage (Method B), but the period of the SDOF system remained fixed.

4.2.3.4 Method D — EDP Correlation Method

This method attempted to eliminate the dependence on interim models that have low efficiency. To accomplish this, the maximum displacement was introduced and correlated with residual displacement. The PSDM involving maximum displacement (or drift ratio) was known to be highly efficient (Section 3.4.1). By introducing yet another interim variable, u_{max}, it was attempted to improve the prediction of vertical loss in load-carrying capacity. The form of the framing equation becomes Equation 4.20.

$$P\left(DM < dm^{LS} \mid IM = im\right) = \iiint P_{DM|EDP}\left(dm^{LS} \mid edp\right) \cdot dP_{EDP|U_{res}}\left(edp \mid u_{res}\right) \cdot$$
$$dP_{U_{res}|U_{max}}\left(u_{res} \mid u_{max}\right) \cdot dP_{U_{max}|IM}\left(u_{max} \mid im\right) dedp \cdot du_{res} \cdot du_{max} \tag{4.20}$$

The only relationship not yet formulated in this method is that between maximum displacement and residual displacement. These data were also obtained from previous PSDM studies for this bridge. Even though the residual displacement was plotted on the ordinate, the power-law fits were made with maximum displacement as the dependent variable (this is opposite to the other PSDMs presented). The resulting plots for the longitudinal and transverse directions are shown in Figures 4.26 and 4.27, respectively.

Employing PSDM data for all of the u_{max}, u_{res}, and IM data may violate the mutual exclusivity criteria required for use of the total probability rule. Therefore, future models relating u_{max} and u_{res} should be derived from bridge stiffness and material relationships. For example, the maximum possible residual displacement can be related to the maximum displacement through the softened global unloading stiffness of the bridge. However, such approximations are not included in this study, as this section was merely illustrative of the method.
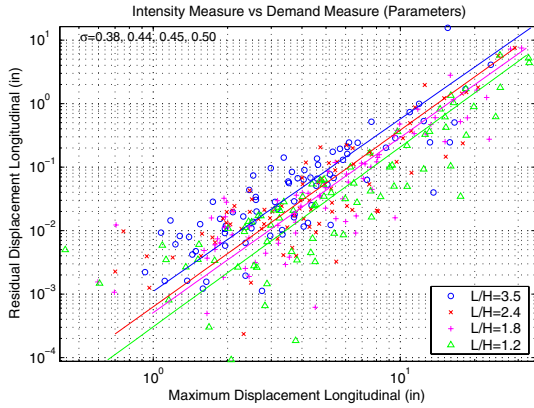
Fig. 4.26 u_{max}-u_{res}, L/H sensitivity longitudinal
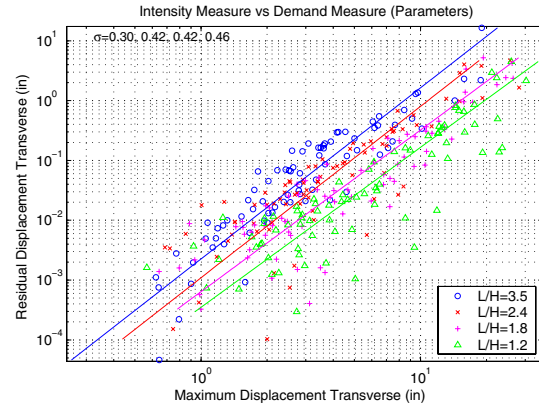
Fig. 4.27 u_{max}-u_{res}, L/H sensitivity transverse

A further option is to eliminate residual displacement altogether and develop an interim determinate or probabilistic analytical model between maximum displacement and loss of load-carrying capacity only that features parameters such as initial and post-peak stiffness. The benefit of such a method would be the efficient demand models associated with maximum displacement as opposed to residual displacement.
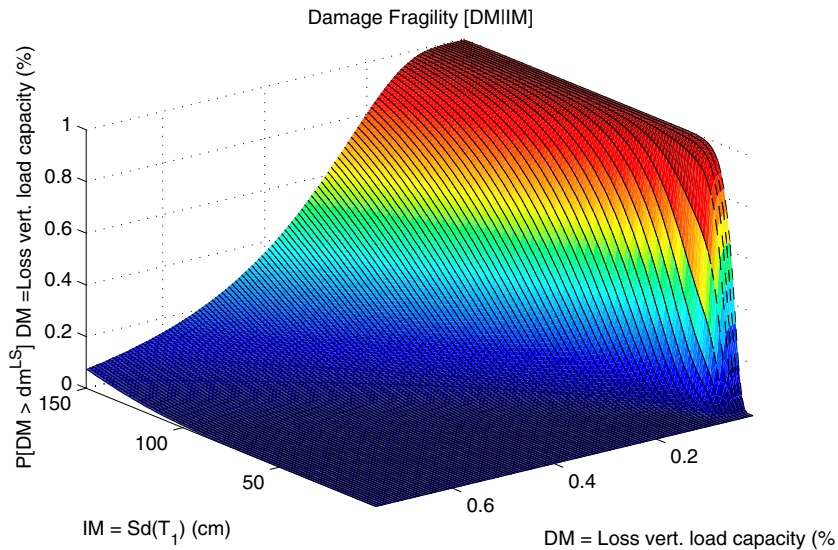
Fig. 4.28 Bridge damage fragility Method D vertical

Integrating all of the interim models together provided a final form for the loss of vertical capacity (Fig. 4.28).   The form was very similar to all of the previous methods but had the advantage of higher confidence in the results due to the lower dispersions of the interim models. However, it suffered from the number of parameters required to fully describe all the models, and the model error associated with each of these.

4.2.4 Improved Methods for Post-Aftershock Capacity

Several of the methods above were applied directly to the performance of highway bridges during aftershock scenarios. This was accomplished by using the PSDM planes presented in Section 3.7 that describe the *EDP* in terms of two *IM*s, one for the intensity of the first shock, the other for the intensity of an aftershock. Response to aftershock events was conditioned on the intensity of the first-shock by using response functions involving both intensities (joint probabilities).   As an example in this section, a first-shock intensity of $Sd(T_1)$ = 40 cm (corresponding to a spectral acceleration of 0.65g) was selected.

4.2.4.1 Method A — Direct Method

The direct method is presented only as it was useful for benchmark comparisons of the other methods. Otherwise, the computational power required to generate the aftershock PSDMs was too intensive to justify the lack of efficiency in the results. A best-fit plane was not the best form of a PSDM model to describe the capacity loss behavior (nor was a higher-order surface). Therefore, any values predicted using this linear equation (Eq. 3.28) are necessarily biased. The benefit, however, was the more accurate calculation of degraded strength due to both the first-shock and aftershock. The resulting cumulative damage fragility curve for aftershocks is shown in Figure 4.29.
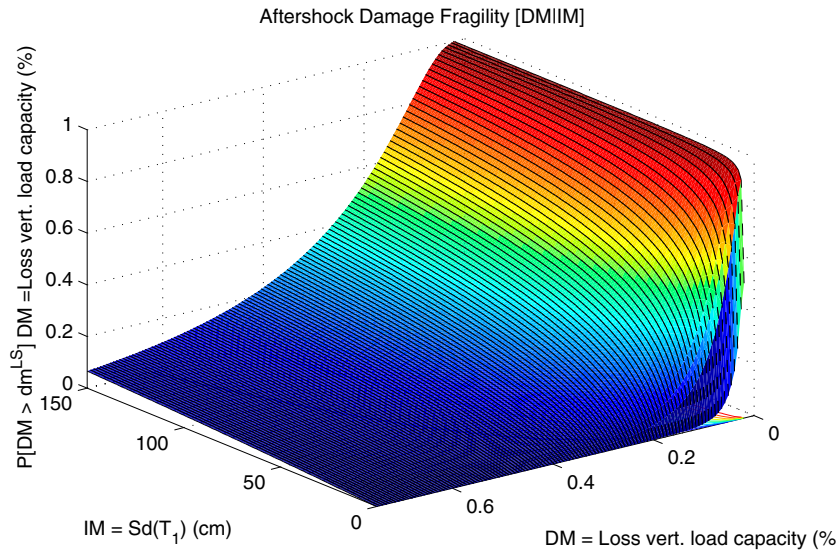
Fig. 4.29 Bridge damage fragility Model A aftershock vertical

4.2.4.2 Method B — MDOF Residual Displacement Method

The same methodology was applied in the aftershock scenario as for the Method B first-shock case. The third term in Equation 4.19 was the only modification, containing data from the aftershock PSDM conditioned on IM_1 (the first-shock intensity). This aftershock PSDM for residual displacement is shown in Figure 4.30. As with the first-shock case (e.g., Fig. 4.22), the dispersions about the best-fit plane were also high.

The resulting fragility surface is shown in Figure 4.34. In this figure, the *IM* axis now describes the intensity of the aftershock, once again using $Sd(T_1)$. It should be noted that this may not be the best choice of *IM* for an aftershock scenario as the fundamental period of the structure would have shifted due to the first-shock. However, to maintain commonality between methods, it was necessary to keep the same T_1 value. A better solution would be to determine the optimal non–structure-dependent *IM* for this bridge, allowing objective comparisons between arbitrary events. Structure-independent *IM*s were discussed in Section 3.4.1.
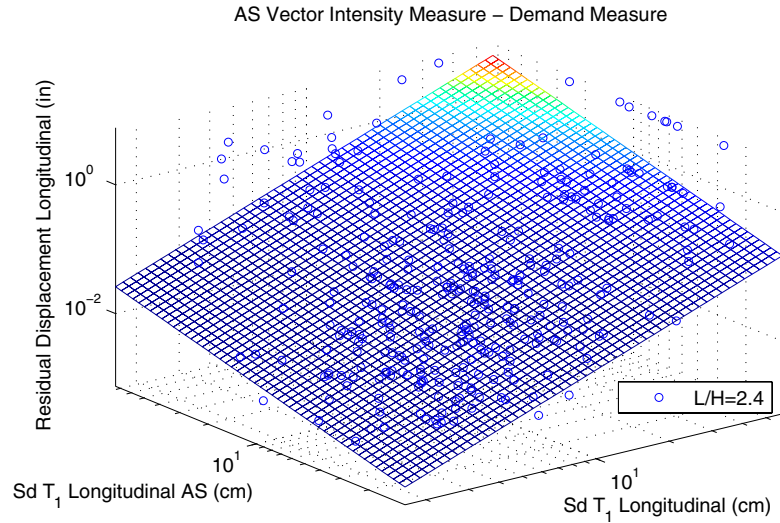
Fig. 4.30 $Sd(T_1)$-u_{res} aftershock PSDM, $L/H = 2.4$ longitudinal
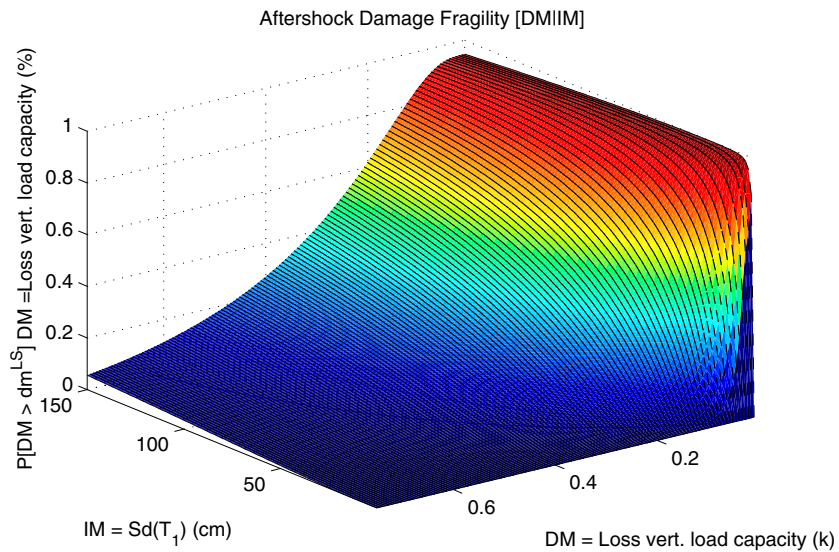
Fig. 4.31 Bridge damage fragility Method B aftershock vertical

A further distinction involving the response from the aftershock scenario is also required. The PSDMs of Figures 3.74 and 4.30 provided a relationship between global displacement response due to an aftershock intensity IM_2, conditioned on a first-shock intensity IM_1. However, loss of load-carrying capacity is obtained separately, independent of both intensities. Therefore, the vertical load-carrying capacity loss surface does not describe the cumulative effect

of both the first-shock and the aftershock. An estimate of the total fragility for the aftershock was made in the next section.

4.2.4.3 Method D — EDP Correlation Method

Similarly, Equation 4.20 was applied as for Method D in the first-shock case. The fourth term in the equation now contained data from the aftershock PSDM for u_{max}. The aftershock PSDM for drift ratio (Fig. 3.74) can be used if modified by a constant (H). As mentioned previously, the dispersions were the same for any two kinematically dependent EDPs. The resulting damage fragility surface is shown in Figure 4.32.
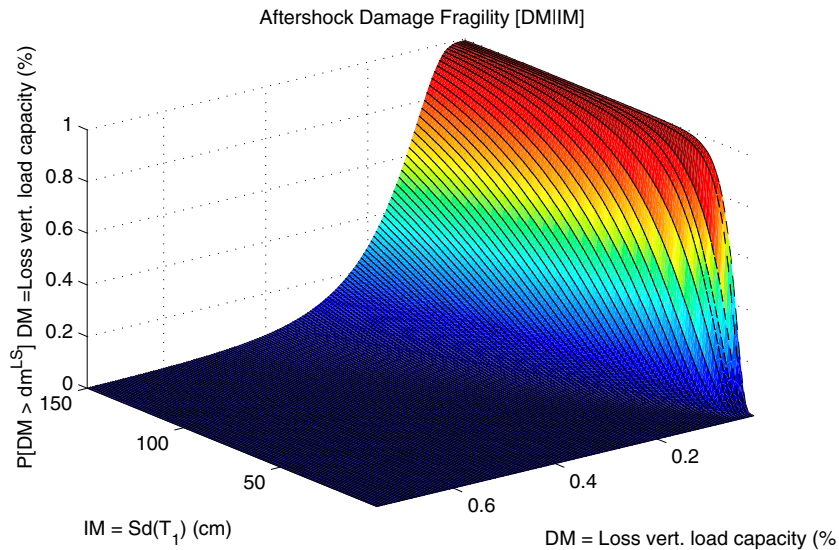
Fig. 4.32 Bridge damage fragility Method D aftershock vertical

Once again, the lowest dispersion is associated with Method D; therefore, it appeared to be the best choice. However, as with the first-shock case, the increased number of interim models increased the likelihood of the introduction of model error. In addition, in the aftershock case, the maximum displacement after the aftershock was a function primarily of the aftershock intensity (IM_{AS}). As mentioned in Method B, the total loss of capacity also included a contribution from the first-shock. Therefore, an estimate of the total capacity loss (due to first-shock and aftershock) was made in the following section.

4.2.5   Method Comparison

All of the proposed methods are compared here for two limit-state values: 10% and 25% loss of the vertical load-carrying capacity. These are now plotted as single fragility curves (Fig. 4.33 for $dm^{LS} = 10\%$ and Figure 4.34 for $dm^{LS} = 25\%$), obtained directly from the fragility surfaces in the preceding figures. The average of all the methods was also included for comparison. It is ostensible from Figure 4.33 that methods B, C, and D give different results from the single step Method A. This was to be expected given the lack of confidence in the median relationship between *IM* and *EDP* in Figure 4.13. In the vertical direction, Method A did not exhibit a linear regime of behavior at low intensities. This resulted in an immediate increase in damage, even for low-intensity events. The immediate onset of damage was not realistic; the curve should be shifted to the right. Therefore, Method A gave a conservative upper bound.
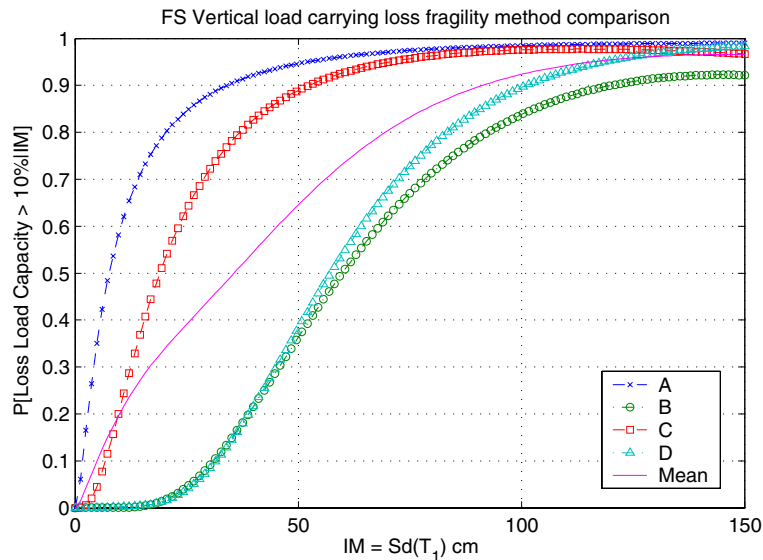
Fig. 4.33 Bridge first-shock method comparison, $dm^{LS} = 10\%$

Of interest when comparing the different methods was the value of the *IM* at the mean and the standard deviation of the fragility curve. Methods B and D had a similar mean. This would be expected given that the PSDM data for all interim models came from the same finite element analysis. Method C had the same form as Method B due to its formulation; however, the mean was shifted because the SDOF system was not modified by a modal participation factor in this analysis and did not account for more complex system interaction. All of the methods

except D exhibited large dispersion in the final fragility. This was due to the large uncertainty in the interim models and results in inaccurate probability distribution tails.
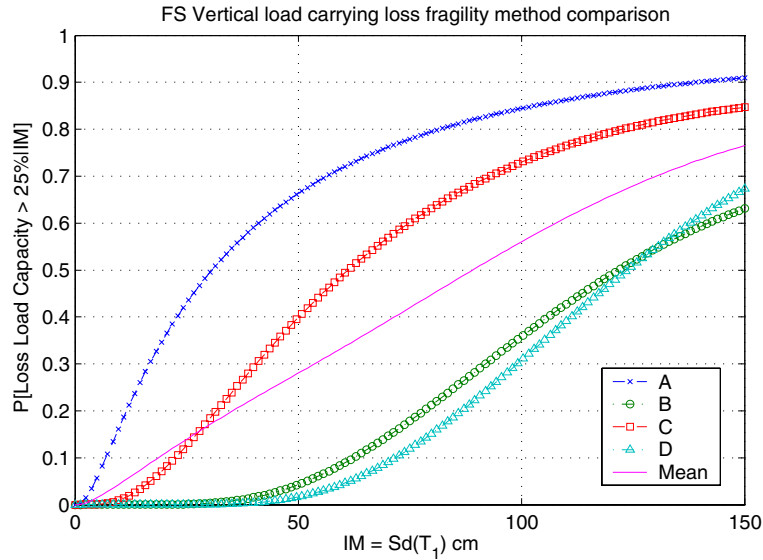
Fig. 4.34 Bridge first-shock method comparison, $dm^{LS} = 25\%$

Of the multiple step methods (B, C, and D), they all correctly predicted a threshold intensity value, below which there is no damage. As mentioned, the SDOF mean was shifted but could be corrected based on the modal participation factor even though the problem was not strictly linear (for modal superposition analysis). Of the individual methods, method D appeared the best single method (based on dispersion) for prediction of the loss of vertical load-carrying capacity. Several other methods are possible but were not investigated in this study.

While only four methods were presented in this section, there are numerous other possibilities for improving the final outcome. Based on the results of Method D, a method that relates loss of vertical load-carrying capacity directly to maximum displacement might prove more efficient than Method D. Also, seamless normalization (by H or u_y) to the u_{res} and u_{max} probabilistic models would allow comparison of the methods between different bridge design parameters. This modification is simple because the slope of the demand models does not change (for example the slope B).

The methods were also compared using data from the aftershock fragilities. Due to the large amount of computation required and the lack of a best-fit plane, Method A was shown to be a poor prediction tool when considering aftershocks. For comparison, the aftershock curve from

Method A was included in Figure 4.35 for the $dm^{LS} = 10\%$ example. This curve was obtained from the series probability of the original fragility curves predicted for the first-shock and aftershock scenarios. The correlation between the two scenarios was obtained from the slope (angle between) of the PSDMs ($\rho_A = 0.32$). The three fragility curves (A, B, D) for both the first-shocks alone and cumulative effect of the aftershocks are shown in Figure 4.35.

Since residual displacement and maximum displacement were functions of the aftershock intensity (IM_2), they were not good reflectors of cumulative damage during multiple events. This was indicated by aftershock Method D's fragility curve closely mimicking the behavior of its first-shock counterpart (not shown here). To estimate the cumulative aftershock effect, the probability of exceeding the damage limit state at an aftershock $IM_2 = 0$ was assumed equal to the probability of exceeding the first-shock limit state at $Sd(T_1) = 40$ cm (the postulated first-shock intensity). Given the first-shock probabilities from Figure 4.33, as well as the adjusted aftershock probabilities of IM_2 conditioned on IM_1, it was possible to find the cumulative probability by the union of the events.
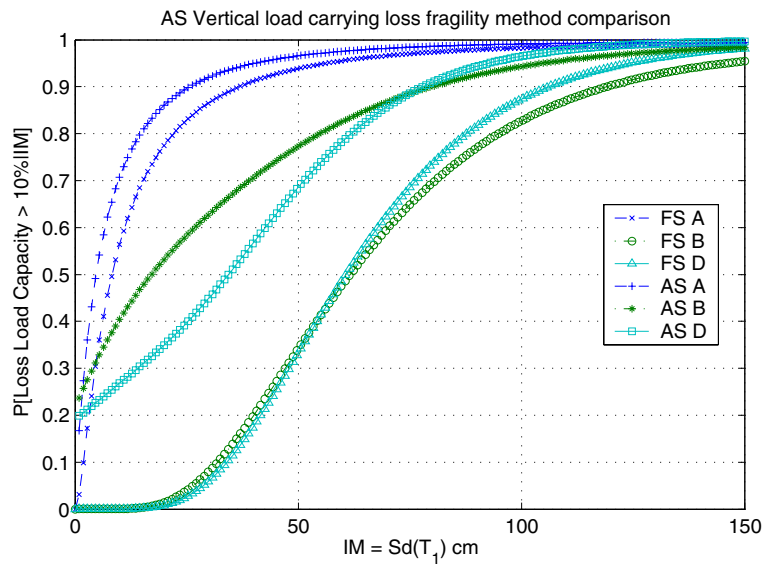
Fig. 4.35 Bridge aftershock method comparison, $dm^{LS} = 10\%$

Correlations for methods B and D were obtained from the slope of their respective PSDMs ($\rho_B = 43$, $\rho_D = 0.12$). This cumulative fragility curve is also shown in Figure 4.35 (for methods B and D), and reflects the likely probability of exceeding 10% loss in vertical load-carrying capacity with an aftershock of intensity IM_2 on the abscissa. Similar to the first-shock

scenario (Fig. 4.33), Method A was a conservative upper bound with bias in the median relationship. Methods B and D were comparable, with Method D providing the lower dispersion. Figure 4.35 cannot be used to directly compare an arbitrary IM_1 and IM_2 as the aftershock fragilities were derived conditionally on $IM_1 = 40$. The first-shock fragilities were included to show the increase in the probability of exceeding the given limit state in an aftershock scenario.

4.2.5.1 Simplified Reconnaissance Tool

The primary use of post-earthquake load-carrying capacity is envisioned as a decision-making tool for engineers and policy makers in a highway network environment. Proposed decision states based on the loss of load-carrying capacity are presented in Table 4.8. Using such a table, calibrated by the institution evaluating the highway bridges, and a simplified method for determining the residual load-carrying capacity of a bridge, it would be possible to effect a more rational performance-based decision-making process.

In a pre-earthquake design or emergency response analysis, it may be possible to predict earthquake intensities at individual geographically distributed sites. However, a more useful tool in the hands of a field engineer would be a rational basis for decision making that is based on criteria that do not require the input earthquake intensity at the bridge site. While the methods developed in Sections 4.2.3 and 4.2.4 were only preliminary indications that residual displacement provides a useful pathway for prediction of loss of load-carrying capacity, residual displacement has long been used in practice as a means for evaluating a bridge post-earthquake.

Table 4.8 Proposed performance levels using bridge-level DVs

Objective name	Traffic capacity remaining (volume)	Loss of lateral load-carrying capacity	Loss of vertical load-carrying capacity
Immediate access	100%	< 2%	< 5%
Weight restriction	75%	< 2%	< 10%
One lane open only	50%	< 5%	< 25%
Emergency access only	25%	< 20%	< 50%
Closed	0%	> 20%	> 50%

With the frameworks presented in this chapter, it was possible to develop such a tool by integrating only the first two terms of Equation 4.19 (Method B). The resulting formulation is shown in Equation 4.21.

$$P\left(DM < dm^{LS} \mid IM = u_{res}\right) = \int P_{DM|EDP}\left(dm^{LS} \mid edp\right)dP_{EDP|U_{res}}\left(edp \mid u_{res}\right)dedp \quad (4.21)$$

By using the same interim models as Method B, Equation 4.21 was evaluated for different limit states of interest. Fragility curves for three limit states are plotted versus residual drift (residual displacement divided by column height) in Figure 4.36 for the loss of vertical load-carrying capacity. This form of the reconnaissance tool allowed direct comparison with other bridge designs by using a dimensionless abscissa. *RDI* (defined in Section 3.2) could be used as an alternative dimensionless quantity. Conceptually, this simplified tool could also be generated using the first three terms of Equation 4.20 (from Method D) to reduce the dispersion. A similar plot can be generated for the loss of lateral load-carrying capacity but is not shown here.
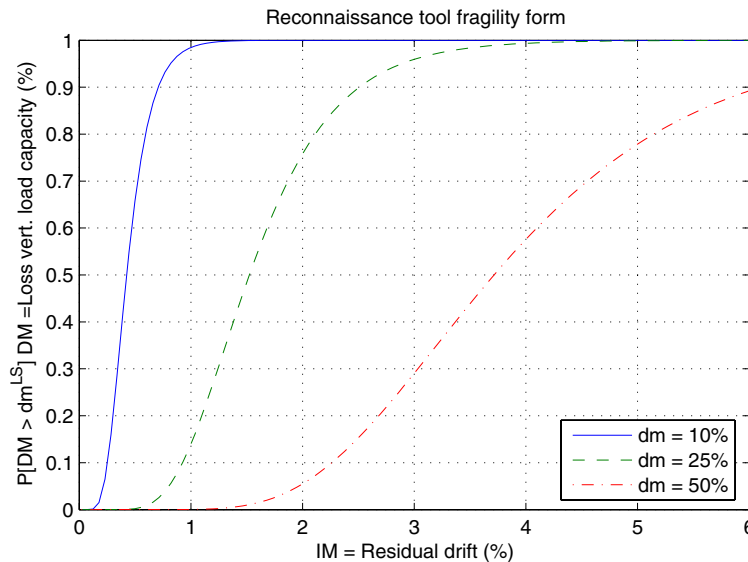
Fig. 4.36 Bridge reconnaissance tool

For example, Table 4.8 and Figure 4.36 can be used to assess the post-earthquake performance of a bridge within a highway network. A rejection (acceptance) criterion for each performance objective in the table must be selected. For example, a bridge weight restriction criteria may be a 75% probability that greater than 10% of the vertical load-carrying capacity has been lost. Conversely, the same criteria may be stated as 25% probability that less than 10%

vertical load-carrying capacity remained. A field engineer can then assess the condition of the bridge according to its residual displacement. If the residual displacement was determined to be 2 in. (0.67% drift ratio), then from Figure 4.36, the probability of exceeding a 10% loss of capacity is 0.87 and the probability of exceeding a 25% loss of capacity is 0.02. The 87% probability of exceedance surpasses the 75% threshold; therefore weight restrictions should be issued. The 2% probability of exceeding 25% loss does not exceed the next performance threshold, so no lane closures are required. The performance thresholds and acceptance criteria are merely examples, to be modified based on practitioner input.

These improved methods provided a proof of concept for more rational and quantifiable decision-making criteria for reinforced concrete highway bridges and are extended further in the next chapter. The criteria selected to evaluate functionality of bridges after a first-shock or aftershock scenario were the loss of bridge lateral and vertical load-carrying capacities. While current decisions to limit traffic or to completely close a bridge in a highway network system rely on inspection data, these can be supplemented by the use of the reconnaissance tool and a sample set of graded performance criteria proposed in this section. The specific values of load-carrying capacity loss at different performance levels remain to be finalized; however, the methods utilized in this paper can be generalized to any such values.

Four methods of obtaining the loss of load-carrying capacity were investigated. The methods introduced post-earthquake residual displacement as a better proxy for capacity loss rather than measures of earthquake intensity. To reduce the dispersions inherent in each interim model, subsequent methods attempted to further disaggregate the problem until more efficient models existed. In this manner, Method D was shown to be the best single method for determining vertical capacity loss, expressed in the form of a damage fragility surface. This method correlated two *EDP*s (maximum displacement and residual displacement) and capacity loss through a series of models obtained from PSDA and finite element simulation. The methods were also applied to aftershock post-earthquake capacity, although more work is needed on damage dependence for aftershocks.

Residual displacement gave a prediction of loss of load-carrying capacity, as desired, but it was still not the best correlation between *IM* and loss of capacity. Dispersions were still large and, while some sources are aleatory, most epistemic sources still need to be more precisely defined. For example, there may be a bias in computing residual displacement introduced by the hysteretic model used in finite element analysis. The power of using Method B, C, or D is that

each interim model can be optimized to reduce dispersion. For example, a better *IM* predictor of residual displacement can be used to greatly enhance the overall prediction of load-carrying capacity loss. Even the highly efficient *IM*s (Section 3.4.3) were unable to properly capture the residual displacement response.

4.2.6 Residual Axial Load-Carrying Capacity

Current knowledge of the post-earthquake load-carrying capacity of reinforced concrete columns is limited. During earthquake excitation, ductile reinforced concrete columns lose strength and stiffness as they accumulate damage. The primary question remaining after an earthquake scenario is what level of residual load-carrying capacity exists for columns, both laterally and axially. This residual strength is particularly important for highway bridges where post-earthquake decision making hinges on functionality of the primary nonredundant load-carrying elements, namely the columns.

This section specifically addresses the experimental and analytical program to test the residual axial load-carrying capacity of small-scale rectangular reinforced concrete column specimens. These cantilever specimens were tested in two separate phases. The first phase involved lateral cycling using a prescribed displacement history. Phase two involved crushing the specimen axially to determine the residual axial force versus axial deformation relationship. Specimens were tested to varying maximum displacement ductility levels to facilitate development of axial loss versus ductility demand curves. The specimens had less confinement in the plastic hinge region to localize the failure mechanism.

By developing an analytical model that mimics axial strength and stiffness degradation, this knowledge was applied directly to the computation of decision criteria for reinforced concrete highway bridges in a PBEE context, such as Section 4.2. Specifically, rational decision-making criteria can be developed for engineers and inspectors to evaluate the load-carrying capacity of a bridge after an earthquake, and therefore its functionality in a highway network system.

Recent seismic codes have made progress toward preventing brittle failure modes in columns. Unless complete failure occurs, columns subjected to earthquake excitation have some level of residual strength remaining. Quantifying this level of residual strength has seen little treatment in current research. Numerous researchers (e.g., Elwood 2002) have looked at the

158

issue of axial failure, defined as the lateral demand at which a column fails to carry its prescribed dead load. Testing setups included constant axial loads applied during lateral excitation (Kato 2002; Yoshimura 2002), as well as several axial load control strategies based on levels of lateral deformation (Tasai 1999). However, the explicit force-deformation characterization in the axial direction post-excitation has largely been ignored. Tasai conducted an experimental and analytical program to investigate this; however, the axial capacity envelope was based largely on sectional analysis (Tasai 1999). The analytical results showed little or no axial degradation under low axial loads during the lateral testing.

Rather than observing loss of axial-carrying capacity of a prescribed level, the specimens were tested to prescribed lateral levels and subsequently evaluated for residual axial strength-axial deformation behavior. The remainder of this chapter investigates whether the analytical model can mimic the strength degradation observed in these tests. These analytical models can then be applied with more confidence to more complex structures in damage model simulations.

4.2.6.1 Experimental Approach

Four T-shape reinforced concrete column-footing assemblages were constructed for testing. Specimen geometry and dimensions are detailed in Figure 4.37. These specimens were intended to be quarter-scale columns similar to those in the Van Nuys building. The reinforced concrete details were obtained from similar cyclic tests conducted at Berkeley by Shin and Moehle (Shin 2002). The more lightly reinforced vertical member is henceforth designated the column. Rebar layout is also shown for the beam, or footing, although this portion was intentionally overdesigned.

The specified unconfined compressive strength of the concrete was 20.7 MPa (3 ksi). Grade 60 steel was used for the longitudinal reinforcement. Four longitudinal reinforcing bars (#3 designation) were placed at the corners of the column. Transverse steel reinforcement was purposely reduced in the plastic hinge zone in order to generate a failure mechanism at the base of the column. The first two hoops (2.38 mm diameter, 135 degree hooks) were placed at 11.4 cm (4.5 in.) on center, while the remainder of the column height had hoops at 2.5 cm (1 in.) on center. The cover was 12.7 mm (0.5 in.) all around. Unconfined cylinder tests (15.2 cm diameter) showed an average compressive strength of 26.4 MPa (3.83 ksi) after approximately 28 days. The average steel yield stress was 483 MPa (70 ksi).
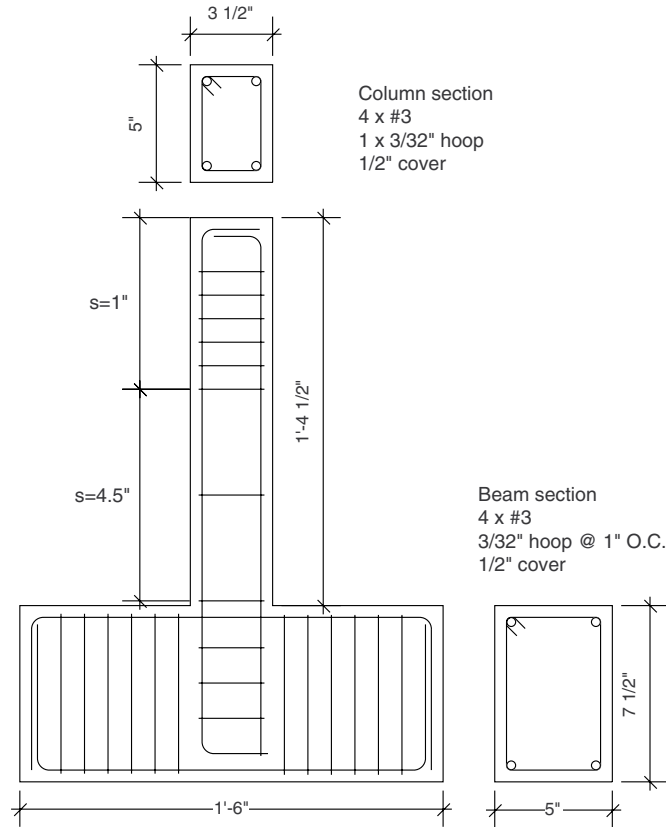
Fig. 4.37 Reinforced concrete specimen dimensions and reinforcement layout

It was initially intended to test one specimen only in the axial direction, in order to determine undamaged load-carrying capacity, followed by three specimens both laterally and axially. The initial axial test on the undamaged specimen (Fig. 4.38) exposed an important flaw in the design of the specimens for the desired testing scheme. Due to termination of the confinement where the longitudinal bars were hooked (90 degrees) at the top of the column, there were large disparities in the compressive strength along the specimen length. Therefore, when axial load was applied, an end condition failure developed at the actuator head where the unconfined concrete was crushed without transferring any load to the longitudinal bars or confined concrete core.

Fig. 4.38 Pre-retrofitted specimen

Fig. 4.39 Retrofitted specimen
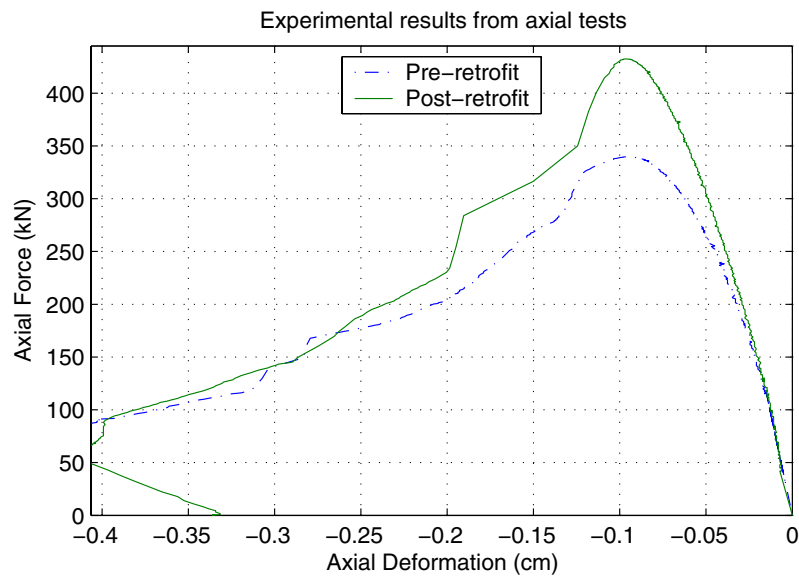
Fig. 4.40 Axial test results for pre- and post-retrofit specimens

A retrofit of all the specimens was then undertaken to resolve this end failure mechanism. Steel pipe sections (20.3 cm nominal diameter) 15.2 cm (6 in.) in length were grouted to the top of the specimens using Hydrostone nonshrink, high-strength grout. Due to the damage to the top of the initial specimen tested, an additional 5.1 cm (2 in.) of grout-filled pipe was added to the top to reproduce the initial column length. This retrofitted specimen (Fig. 4.39) was then

retested using the same axial setup until failure occurred. During this test, the longitudinal bars buckled and the core concrete was crushed in the plastic hinge zone, as expected. A comparison of the force-displacement behavior of the pre- and post-retrofit specimen is shown in Figure 4.40. Due to some initial damage to the specimen during the pre-retrofitted tests, the axial load-carrying capacity of the specimen was estimated to be 489 kN (110 k).

The lateral load testing setup involved a unidirectional lateral actuator, with no applied axial load. The 44.5 kN (10 k) capacity actuator was used to measure force at a centerline distance of 40.6 cm (16 in.) from the base of the column. DCDTs (direct current displacement transducers) were used to monitor column deflection and base slip from a reference frame. The specimens were bolted to the test frame by means of a 5.1 cm (2 in.) thick steel base plate and two 2.5 cm (1 in.) thick plates threaded to the base plate by four 12.7 mm (0.5 in.) diameter rods. This setup fixed the footing to the frame, preventing translation or rotation in any degree of freedom (Fig. 4.42).

The loading protocol involved applying a cyclic displacement pattern to the specimens. Incremental displacement levels were used with 3 cycles each. The displacement levels were incremented in steps of $0.25*u_y$, or ductility increments of 0.25, until a ductility of 1, and in steps of $0.5*u_y$ to the maximum desired displacement level. Maximum ductility levels prescribed for the four specimens were 0 (virgin specimen), 1.5 (Specimen 1), 3.0 (Specimen 2) and 4.5 (Specimen 3). Approximate values of u_y were determined prior to testing as approximately 0.61 cm (0.24 in.). Experimental results yielded an approximate yield displacement of 0.79 cm (0.31 in.).

Lateral force-displacement results are shown in Figure 4.41. All three specimens that were tested laterally exhibited an area of soft response at small displacement demands. The full column lateral stiffness was engaged only at a displacement of approximately 0.25 cm (0.1 in.). The cause of this behavior was likely shear slip at the column-footing interface. Visible damage to the specimens during lateral testing was limited except for the fourth. The shear crack at the column-footing interface continued to develop with displacement demands in all specimens.

Numerous insufficiencies were exposed with the lateral experimental tests. The slipping behavior resulted primarily in a more ductile system than would have been expected based on the initial specimen details. At displacement ductilities on the order of 1 to 2, the specimens exhibited recentering behavior and decreased energy dissipation. At higher ductilities, the specimen behaved more like a shear critical column with force pinching of the hysteretic loops.

Another issue was the lack of symmetry of the forces. This was due to lack of symmetry in the rebar placement during construction as well as electronic (instrument) drift during testing between amplitude cycles. The net result was a relatively poor representation of the true hysteretic behavior. Therefore, only the axial comparisons were emphasized in the analytical section.
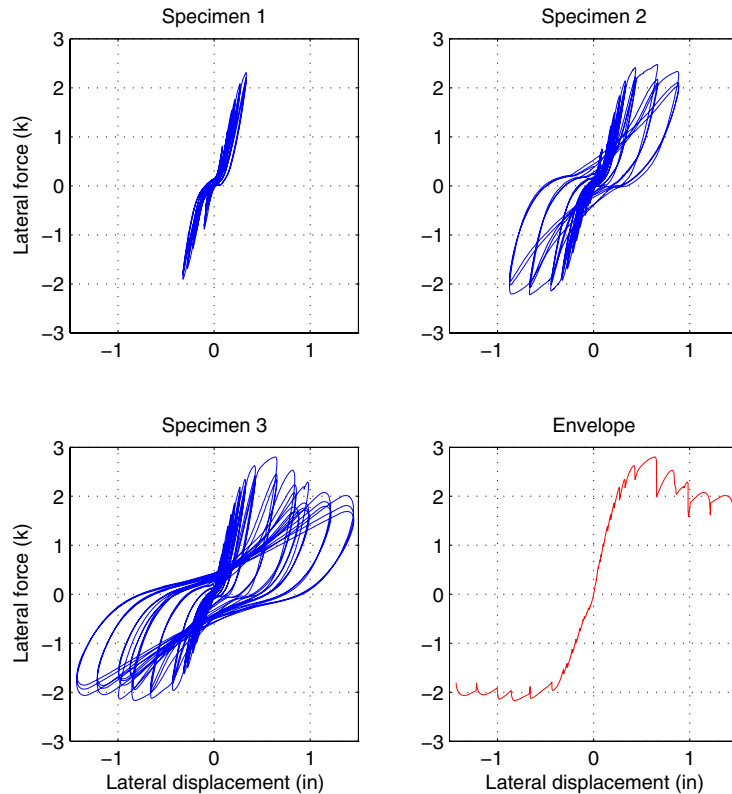
Fig. 4.41 Experimental lateral force-displacement results

After a zero load condition was achieved in the lateral load test setup, the specimens were removed from the test frame and moved to a uniaxial compression setup. This 1330 kN (300 k) capacity compression machine with a spherical head was used to measure the force-displacement characteristics of the specimens in the axial direction. Applied force measurements came from the actuator head (virgin specimen) and load cell (other specimens), while tip displacement was monitored using two separate DCDTs. The DCDTs were attached to the footing and steel plate

at the tip, respectively. During subsequent tests with the retrofitted specimen, the top steel plate was replaced by the grouted steel pipe.

Fig. 4.42 Experimental lateral setup

Fig. 4.43 Specimen 4 after axial crushing

An axial load was applied at a rate of 4.45 kN/sec (1 k/sec) until failure occurred. Post-peak force-displacement response was also measured to help determine loss of capacity. Due to the lack of confinement in the plastic hinge zone, a compressive failure mode was expected to develop at the base of the column. This was confirmed after crushing all the specimens. For example, Specimen 3 is shown (Fig. 4.43) after being removed from the axial setup. A comparison of the experimental axial force-displacement data obtained for the undamaged and three lateral specimens is shown in Figure 4.44. Due to the small amounts of damage induced in the concrete during the first test on the virgin specimen, Specimen 1 actually obtained a higher axial strength. However, the degradation of axial strength with increasing displacement demand is evident.
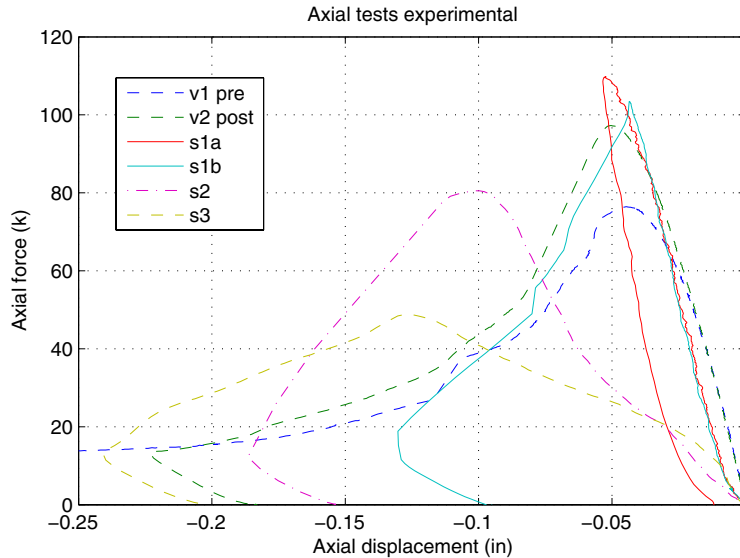
Fig. 4.44 Experimental axial force-displacement results

Specimen 1 was loaded axially to its peak strength (s1a), then immediately unloaded and reloaded again (s1b) until failure. The second loading shows decreased capacity due to damage during the first loading, as would be expected. The value of 489 kN (110 k) from the first test on Specimen 2 was used as the axial capacity of the specimens in subsequent analysis.

4.2.6.2 Analytical Approach

While experimental results were too sparse to develop a well-defined relationship between maximum deformation levels and loss of axial load-carrying capacity, Figure 4.44 does show a quantifiable drop in axial load-carrying capacity after a structure is cycled. This section describes more succinctly the analytical method of predicting this loss. The analytical modeling was performed in large part to verify the use of analytical models in predicting the loss of vertical load-carrying capacity used at the bridge level in Section 4.2. Analytical modeling was once again performed using OpenSees with the same basic set of material models mentioned in Section 2.1.

A finite element model of the column was developed using displacement-formulated, fiberized, beam-column elements in two dimensions. Material models employed for the fibers included a strain-hardening steel model and a Kent-Scott-Park concrete model with no tensile strength. The steel model has a yield strength of 483 MPa (70 ksi), a strain-hardening ratio of

1.5%, and a negative stiffness once an ultimate strength of 655 MPa (95 ksi) is reached at a strain of 0.09. There were no discontinuities in the tangent stiffness of this model. The concrete model included an unconfined stress-strain relation with zero strength after spalling at a strain of 0.006. Due to the amount of transverse reinforcement, the confined strength was only minimally higher than that of the unconfined, but the confined model was included for the upper portion of the column where transverse reinforcement was spaced at 2.5 cm (1 in.) on center.

To simulate the area of low stiffness (shear slip) and approximate recentering behavior at small ductility demands, a prestressed tendon was added to the analytical model only. The tendon was a tension only member with steel hysteretic properties and an area roughly equivalent to the longitudinal reinforcement in the original section. A prestress of three quarters of the yield stress was applied. The peak lateral strengths with this model overpredicted the experimental values, and were therefore normalized during analysis. The initial slip area, initial stiffness, and ultimate force backbone are predicted accurately with the analytical model. However, the pinching at higher ductility demands was not captured adequately. As mentioned previously though, the focus was on determination of the subsequent axial strength, not matching the lateral hysteresis.

The analytically modeled specimens were subjected to the same displacement history as the specimen in the test setup, except increments of $0.25*u_y$ were used throughout. They were then cycled at amplitude to reduce the equilibrium force to a specified tolerance. In the absence of lateral loads, the analytical specimens were then crushed axially to mimic the axial load test. It was not the goal of this research to tweak the analytical model in order to match the experimental and analytical hystereses. It was the goal, however, to validate the prediction of axial load loss due to the accumulation of damage.

The subsequent analytical axial load test results for a single case ($\mu = 3.0$) are shown in Figure 4.48 (anyt. 3.0 in figure) along with the experimental axial results (expt. s3). Also included in this figure are the analytical axial strength envelope of an undamaged specimen (virgin anyt.) and the corresponding experimental results (expt. s1a). The ultimate strengths predicted by analysis were not exactly equal to the experimental values; however, this had as much to do with the uncertainty in the input parameters in the analytical model as the inaccuracy in the analytical procedure itself. To eliminate the disparity, all results were normalized with respect to the maximum resistance. As can be seen, there was good agreement between the experimental and analytical predictions of the damaged specimen axial capacity. This was

especially important in light of the deterministic input values selected for the analytical model, the uncertainty in determination of both the analytical and experimental yield displacements (and ductilities), and the measurement errors associated with the lateral and axial tests.
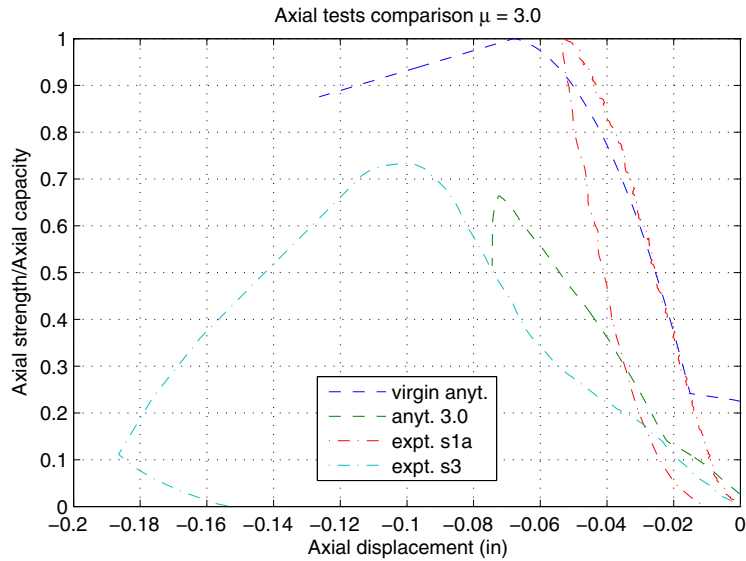
Fig. 4.45 Comparison of analytical and experimental axial results for $\mu = 3.0$

With the analytical model, it was then possible to generate a complete axial degradation plot at different ductility demand levels. Figure 4.46 shows the resulting curves, including both the analytical and experimental results. The data points available from experimental results are plotted as squares in the figure. Also included in the figure is the Total Capacity Model (TCM) prediction adapted from ACI 318 and Elwood (Elwood 2002). The classical shear friction model was modified by Elwood to include information only about the transverse reinforcement. This was then added to the expected strength obtained from the longitudinal reinforcement. The relation was inverted (with $\theta = 65°$) to predict the axial loss at a given displacement demand rather than its original casting as a displacement capacity at prescribed load level (Eq. 4.22).

$$P_{loss} = \frac{A_{sv} f_{yv} d_c}{s}\left(\frac{0.48}{\Delta} - 4.6\right) + \frac{4 A_{sl} d_b f_{yl}}{4 d_b + 3\pi H \Delta} \tag{4.22}$$

Degradation of axial strength with lateral ductility demand
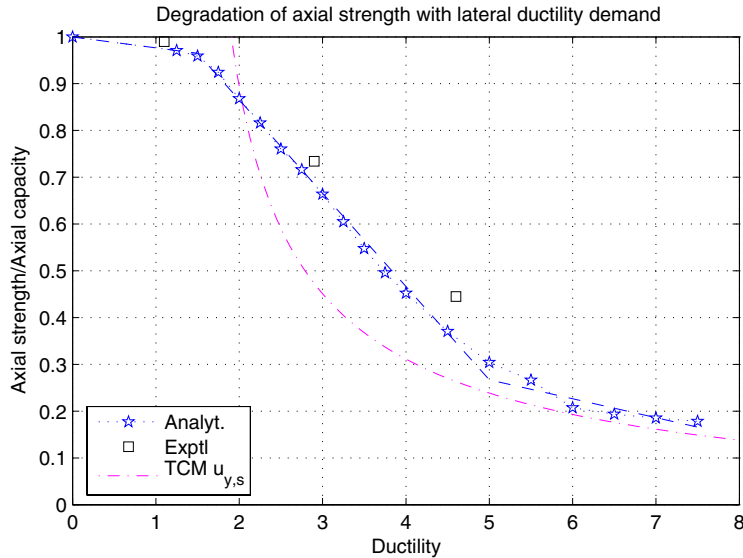
Fig. 4.46 Degradation of axial load-carrying capacity

The TCM method was modified to incorporate the shear slip effect seen in the lateral tests. A constant term corresponding to the slip displacement (0.1 in.) was added, in relation to the expected yield displacement of a corresponding nonslipping system (0.08 in). Therefore, the curve was shifted to the right by a ductility of 1.25. This modified curve agrees more closely with both the experimental and analytical results. A similar approach to the TCM using the truss analogy for residual axial capacity was employed by Tasai (2000). However, this approach requires knowledge of the stresses in the truss mechanism at some deteriorated capacity, making the TCM prediction more attractive.

While the findings and methods presented herein have been addressed before, the true value of the data is when cast in a performance-based earthquake engineering context. The horizontal axis can be viewed as the demand, or *EDP*. The vertical axis can be viewed as the damage induced in the structure, or *DM*. A mathematical relationship (linear, piecewise-linear, or exponential) can be assigned to the *EDP-DM* relationship, together with a measure of uncertainty, thereby completely defining a PDM. In the case of Figure 4.46, an exponential fit was made similar to the TCM.

The exponential fit from Figure 4.46 was then integrated with pre-existing demand models from Section 3.4. The result was a collection of bridge damage fragilities derived from global displacement demands. These are conveniently displayed in a fragility surface, as in Figure 4.47, showing the variation of fragility with both intensity (*IM*) and different limit-state

values (*DM*). As with previous fragility surfaces, families of traditional fragility curves are shown as black lines on the fragility surface. The displacement-based PDM was an alternative method to using residual load-carrying capacity as the *EDP*. As discussed in Section 4.2.3, producing more efficient damage fragilities through better interim models is necessary.

The damage fragilities in Figure 4.47 are compared directly to those obtained using methods A and D (Section 4.2.3) in Figure 4.48. However, caution should be used in such a comparison because the PDM in this section was derived for small-scale rectangular columns with poor confinement. The use of dimensionless quantities on the abscissa of Figure 4.46 does not necessarily make the curves universally applicable. Specifically, there may be scale effects for large diameter specimens, there may be differences between PDMs for circular and rectangular columns, and the decrease in axial strength is directly related to the ductility capacity of the column.
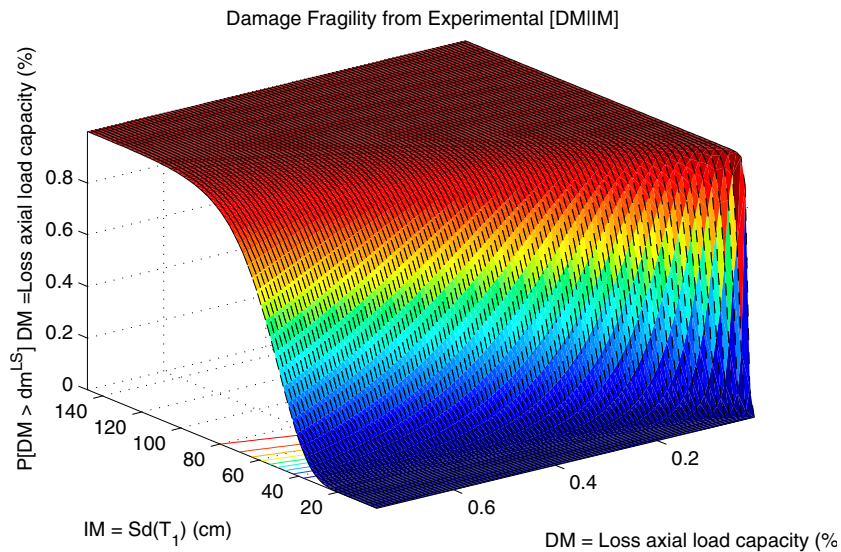
Fig. 4.47 Damage fragility surface derived from experimental damage model

However, this section provided a further method for obtaining better future damage and loss fragilities through the combined use of analytical and experimental data. By developing an experimentally verified two-step analytical process, it will be possible to better predict the loss of axial load-carrying capacity of more complex bridge structures in a highway network.
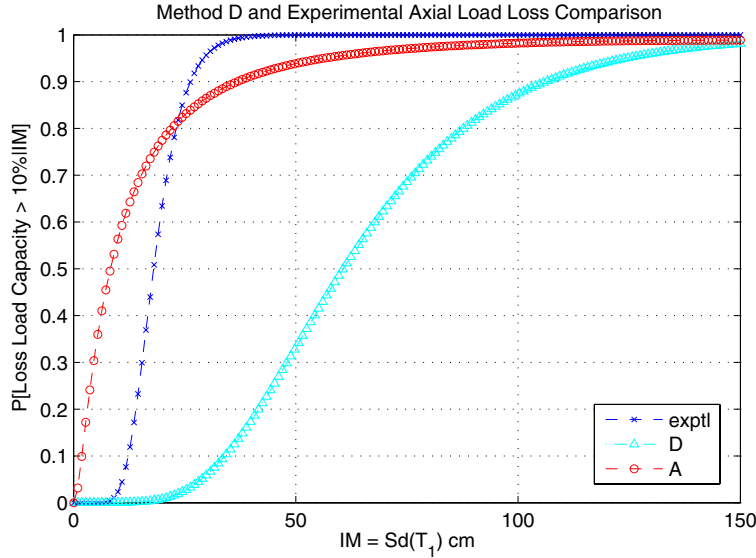
Fig. 4.48 Comparison of analytical and experimental damage fragilities

4.3   UNCERTAINTY

As with the demand chapter (Chapter 3), all of the damage models and resulting damage fragilities were constructed considering only the aleatory uncertainty. It is therefore instructive to demonstrate the inclusion of epistemic uncertainty in any of the damage fragilities or damage hazard curves generated in this chapter. Another item of interest stemming from the demand confidence intervals from Section 3.9 was the propagation of uncertainty due to the selection of the median. Some examples of damage fragility confidence intervals are presented at the end of this section.

Epistemic uncertainty was added to both the component- and bridge-level tracks established in this chapter. Integrating the damage and demand models to obtain damage fragilities required inclusion of uncertainty from both of these sources, according to Equation 4.23. A dispersion value of $\sigma_{PDM} = 0.20$ was assumed for all of the damage models to represent the epistemic uncertainty.

$$P_{DM|IM,Y}\left(dm^{LS} \mid im, y\right) = \Phi\left[\frac{\ln\left(dm^{LS}\right) - \ln\left(D\hat{M}(im)\right) - y\sqrt{d_{dm}^2\sigma_{PSDM}^2 + \sigma_{PDM}^2}}{\sqrt{d_{dm}^2\sigma_{EDP|IM}^2 + \sigma_{DM|EDP}^2}}\right] \quad (4.23)$$

The component-level damage state of bar buckling was selected from Figure 4.4. The median curve considers only the aleatory uncertainty ($y = 0$). The mean curve was obtained in the same

fashion; however, using the SRSS of the aleatory and epistemic uncertainty terms in Equation 4.1. The mean, median, and $y = \pm 1$ damage fragilities are shown together in Figure 4.49.
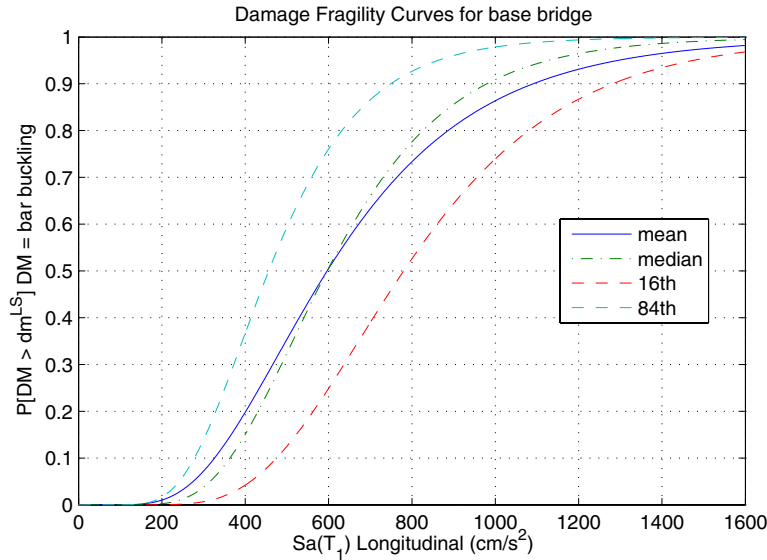
Fig. 4.49 Component damage fragility percentiles, base bridge longitudinal

Due to the relatively low aleatory and epistemic dispersion values, the median and mean were closely related. However, the effect of lack of knowledge on damage fragilities was evident when considering the 16th and 84th percentiles. At a given earthquake intensity, confidence in the damage fragility probability value was dependent on the width of the standard deviation bands. For example, for an earthquake with intensity of $Sa(T_1) = 600$ cm/s^2, the probability of bar buckling was an uncertain (lognormal) quantity with median value 0.5 and standard deviation 0.25. Such uncertainty (50% possible range of probability values between standard deviation bands) is undesirable and should motivate better and more rigorous demand and damage models.

A similar exercise was performed at the bridge level. At the bridge level (Fig. 4.50), the aleatory uncertainty of the demand model dominated the damage fragility form because the dispersion was 0.96. The net result was that the mean and median curves were approximately equal. In the case of reliability-analysis-based damage models, a higher value of epistemic uncertainty would be justified. The net effect would be slightly larger 16th and 84th percentile bands; however, the aleatory uncertainty would continue to dominate the final fragility form.

Finally, it is of interest to propagate the selection of the demand model median through to the damage fragility level. Using the demand model confidence intervals from Figure 3.82, confidence intervals on the damage fragility medians were obtained (Fig. 4.51). The damage fragility confidence intervals were not compounded by the confidence intervals inherent in the damage model alone. The figure simply shows the result of propagating the demand uncertainty to the damage fragility level. The 50% and 90% confidence intervals are nearly equivalent, indicating the extremely low level of confidence obtained in the selection of the median in Method A, the direct implication of the PEER integral described in Chapter 4.
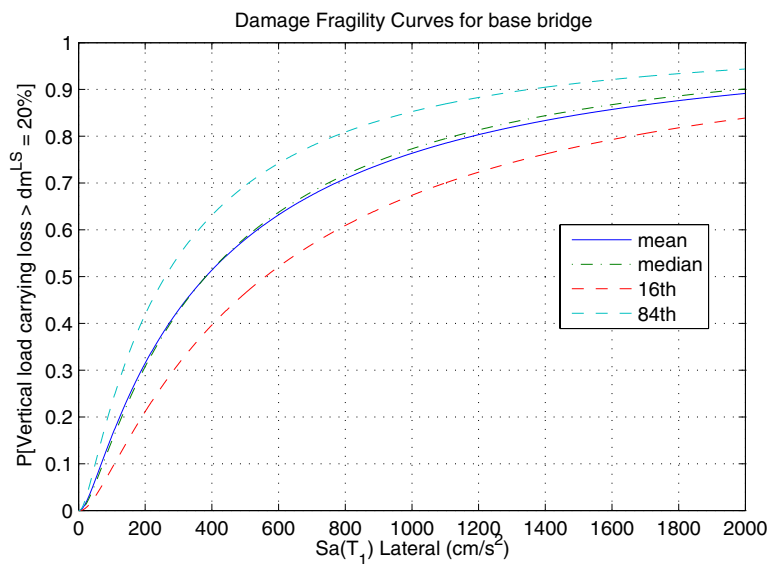
Fig. 4.50 Bridge-level damage fragility percentiles

Confidence can be increased using alternative methods developed in this chapter, specifically Method D. A comparison of confidence levels between Method A and D is shown for loss fragilities in Section 5.3.
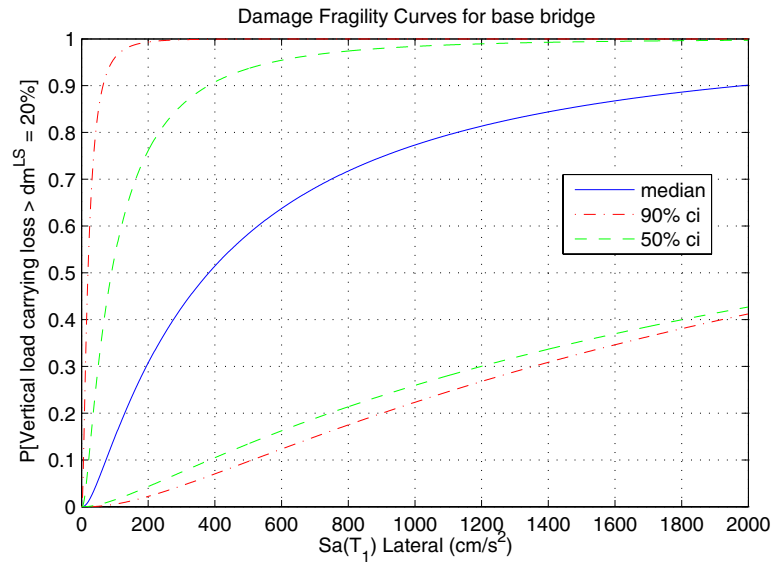
Fig. 4.51 Bridge-level damage fragility confidence intervals

5   Highway Bridge Loss Model

The introduction of the loss model attempts to address many of the questions posed by emergency managers, recovery planners, and structural engineers after an earthquake. These questions include whether traffic can access certain areas of a transportation network, how quickly, how heavy a load can be transported, how much money will it take to repair any damage, and how long will those repairs take? The answers are in the state of highway infrastructure in a region struck by an earthquake, of which bridges are an integral part. Today, answers to these questions are more qualitative than quantitative, based on experience and engineering intuition rather than results of analyses and engineering evaluations. Furthermore, after an earthquake decisions must be made quickly; there is often no time to perform extensive engineering investigations. This chapter focuses on more rigorous decision-making alternatives based on the ability of a typical highway bridge to function, or its need for repair after an earthquake.

The PEER framework defines a loss or decision-making measure as a decision variable (*DV*). Loss is defined as decision making based on cost and loss of function. As discussed in previous chapters, there are two types of *DV*s that can be applied to highway bridges. First, a bridge functional *DV* describes the post-earthquake operational state of the bridge. This implies a graded system of criteria involving lane closures, reduction in traffic volume, or complete bridge closure that are useful for traffic network modeling. Second, a bridge repair *DV* is the time (cost) of bridge repair and restoration. This *DV* is triggered only if the bridge function *DV* crosses the repair threshold. Therefore, the total cost due to a given earthquake scenario on a particular bridge is the sum of the indirect (or operational) costs from the loss of function, and the direct costs to restore previous functionality. The two sources of costs (or losses) are particularly relevant in the case of a highway network system, as the indirect losses to an urban area would likely exceed the direct losses (Moore 2000).

*DV*s are applicable not only to the first-shock earthquake scenario, but also to aftershocks. Further insight into post-earthquake decision making may be gained from the introduction of the probability of collapse during first-shocks and aftershocks. Barring collapse, the subsequent decrease in performance in an aftershock as compared to the initial performance goals may also be of interest. Aftershock residual capacity can be seen as another method of determining post-earthquake capacity such as the lateral load-carrying capacity described above.

Collapse of a modern bridge is an unacceptable performance goal for any seismic region, especially California. Therefore, it was necessary to define the collapse or collapse-prevention limit state in terms of global and local bridge performance. An approach for defining collapse in terms of observed damage and decision limit states is presented in this chapter. While it would be possible to arbitrarily assign a traffic volume (decision) loss limit state to the collapse-prevention state, it is more logical to use a combination of damage limit states. This combination involves both observable damage to bridge components and loss of overall bridge function.

Limit states for highway bridges loss models are formulated at two levels: component and system. The component level addresses the effect of damage to a specific structural component on the post-earthquake response strategy. Components are assessed for damage, and corresponding repair costs or repair times are estimated. For example, damage could be considered in piles, pile caps, columns, expansion joints, abutment wing walls, approach slab and embankment, and numerous other locations. The limit state formulated at the bridge level addresses the overall performance of the bridge as a whole in a post-earthquake scenario. For a highway overpass bridge, functionality is primarily measured in terms of the traffic load-carrying capacity, lane closures, allowed axle loads, and speed limits. The total cost due to a single bridge in the highway network in a post-earthquake scenario is the summation of the component, or direct losses, and the loss of functionality, or indirect losses.

As mentioned previously, empirical loss model data are sparse. Loss model data can be obtained from professional surveys and opinion, reconnaissance data from previous earthquakes, repair data from experimental projects and post-earthquake reconstruction, or inferred from policy decisions. Interestingly enough, such data exist but were not being systematically applied for the purpose of loss estimation. As with damage models, it may not be possible to describe a continuous relationship between *DM*s and *DV*s. Therefore, probabilistic loss models (PLMs) are often also in the form of probabilities of exceeding explicit discrete decision states given different *DM*s.

Individual PLMs are presented in this section. As with the PDMs, no single procedure (such as PSDA for the PSDMs) applies to the generation of all loss models; therefore each model is developed individually in the following sections. However, the main motivation for developing loss models is once again to convolve them with previous probabilistic models to yield fragility curves. The decision fragility formulation is independent of individual loss model generation, as shown in Equation 1.3. Conversely, it is also possible to build directly upon the damage fragilities presented in the previous chapter. Probabilities associated with discrete or continuous loss models are compatible with the decision fragility formulation in Equation 5.1.

$$P\left(DV < dv^{LS} \mid IM = im\right) = \int_{dm} P_{DV|DM}\left(dv^{LS} \mid dm\right) dP_{DM|IM}\left(dm \mid im\right) ddm \qquad (5.1)$$

The first term is the CDF obtained from whatever PLM is available. The second term is the derivative of Equation 4.1 with respect to the *DM* variable. Therefore, the damage fragility curves generated can be used directly in developing decision fragility curves. It should be noted, however, that simply taking the derivative of a damage fragility curve (with respect to *IM*) stemming from a single damage limit state does not provide the information needed in the second term of Equation 5.1. The derivative with respect to *DM* is required.

5.1 COMPONENT LEVEL

The process of deriving losses at the component level was limited by the selection of damage states used to generate damage models. In Section 4.1, only three discrete damage states were calculated, specifically spalling, bar buckling, and failure for the single-column bent in the sample bridge. Therefore, any discussion about repair costs or repair times related to damage to the roadway, embankments, or abutments was precluded. Because of this, a single sample *DV* was selected to generate a loss model.

5.1.1 Component Decision Variables

The component-level damage suggests direct cost economic variables such as repair cost. Alternatively, repair time could be considered, as it may be more significant to important arteries in a transportation network than repair cost. The loss model of this section considered a

relationship between repair cost, normalized by replacement cost, and damage. The repair cost ratio (RCR) was therefore a continuous *DV* variable, but with discrete input points.

5.1.2   Repair Cost

From data compiled for the Northridge earthquake, the HAZUS document reported a modified repair cost ratio as a function of damage for typical bridges (HAZUS 1997). The HAZUS damage states of slight damage, extensive damage, and complete damage were assumed to correspond to the *DM* values of spalling, bar buckling, and failure, respectively. This assumption was made based on more detailed damage descriptions for each damage state (Basöz 1999), even though the damage states were descriptive of bridge components not considered in this study. The slight damage state included minor spalling at the column, as well as minor cracks and spalling at the abutment, expansion joints, and deck. The extensive damage state included column degradation without collapse and large residual displacements. Finally, complete failure included possible column and deck collapse.

From the best mean RCR and range of RCRs reported (Basöz 1999), a mean and standard deviation were assumed for each damage state. A least-squares regression was performed to obtain the approximate (but continuous) form of a loss model (according to Eq. 6.6). A relationship between repair cost, normalized by replacement value, and damage is shown in Figure 5.1. By assuming that the value of the *DM* variable was, in fact, the median drift ratio for each damage limit state, it was possible to provide a smooth closed-form function with numerical values on the ordinate. A relatively large value of dispersion was adopted (0.50) based on the standard deviations reported. The large uncertainty in the model stemmed not only from the bridge-to-bridge variation in repair costs, but also due to bridge data from all classes considered by HAZUS being lumped together.

By using Equation 5.1, the repair cost loss model was integrated with the damage fragility curves from Figure 4.4. The results for several decision limit states (*RCR* values) as a percent of the replacement cost are shown in Figure 5.2. For example, for an earthquake with intensity of $Sa(T_1) = 1000$ cm/s^2, there is a 91% probability that the repair cost will exceed 25% of the replacement cost. This probability drops to 65% for exceeding the entire replacement cost. As would be expected, it is possible for the repair cost to exceed the replacement cost based on the model used (Fig. 5.1).
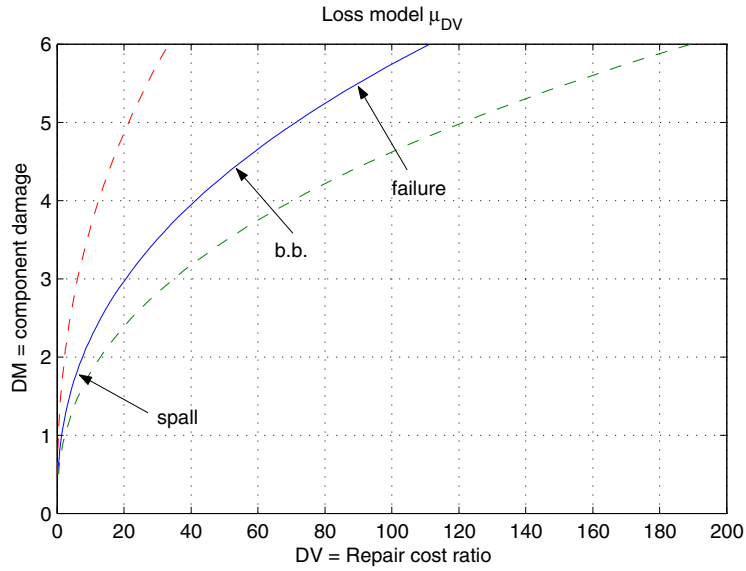
Fig. 5.1 Component repair cost loss model

It should be noted that it may not be possible to obtain a complete decision variable distribution function if the given discrete damage states do not cover the full range required for the decision variable limit states. For illustrative purposes, the *DM* was assumed continuous, as in Figure 5.1, to provide the complete fragility curves shown. Alternatively, discrete points on the fragility curves can be predicted using the discrete form of the decision fragility formulation (Eq. 5.2).

$$P\!\left(DV > dv^{LS} \mid IM = im\right) = \sum_{dm} G_{DV|DM}\!\left(dv^{LS} \mid dm_i\right) G_{DM|IM}\!\left(dm_i \mid im\right) \tag{5.2}$$
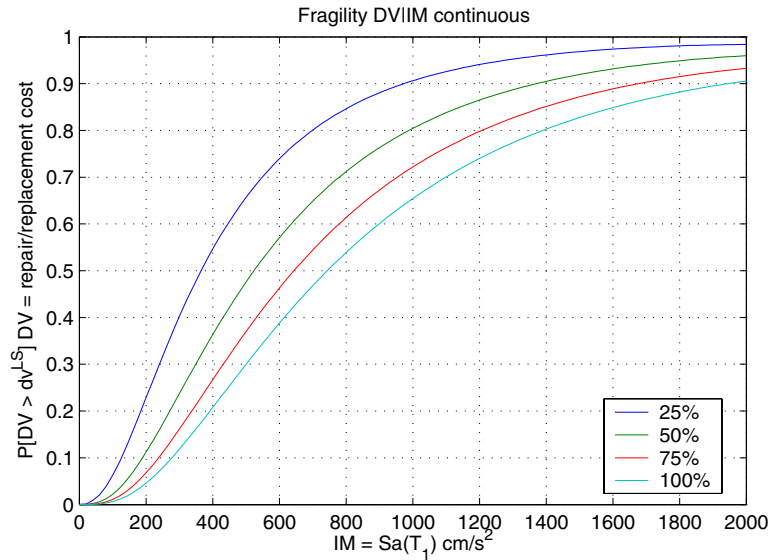
Fig. 5.2 Component decision fragility curves

The repair cost loss model was uncertain largely because it did not discriminate based on bridge class, nor on different configurations within each class. Due to the large amount of uncertainty in the loss model and the lack of other *DV* choices or cost data on other bridge components, component-level loss model derivation for reinforced concrete highway bridges cannot be done without additional research focused on damage assessment and repair cost modeling.

5.2   BRIDGE LEVEL

In previous PEER and Caltrans meetings (Porter 2002), several bridge system level outcomes were discussed. The bridge system variables all related to a graded system of bridge performance levels such those in ATC-49 (ATC 2001). These are discrete tables with traditional language such as "immediately operational," "emergency traffic only," and "closed." The goal was to provide a rational criterion for selection of these performance levels. On a more rational basis, loss in the vertical and lateral load-carrying capacity can better be used for separating bridges into different performance levels or decision criteria. These need not only be "open" and "closed," and can include a continuous distribution based on traffic load-carrying capacity relative to the initial or design value (e.g., Table 4.8). The issue of structural safety also arises when considering subsequent shocks. The decision to assign a damaged bridge to a certain

performance level may be more influenced by this safety factor, rather than its immediate load-carrying capacity.

5.2.1   Bridge Decision Variables

By choosing overall bridge system behavior as the *EDP* and *DM* of interest, it was desirable to generate a *DV* fragility curve that would provide information about loss of bridge performance in terms of traffic load-carrying capacity, and therefore indirect losses. The *DV* chosen in this section was the loss of traffic load-carrying capacity (in terms of traffic volume) as compared to the design traffic load. The loss of traffic load-carrying capacity is distinctly different to the loss of vertical or lateral load-carrying capacity in this sense. However, as with the component case, there is little information regarding loss models available for bridges today.

The traffic function limit state presented in this paper addressed the bridge system as a whole to generate information about loss of its functionality. Functionality was defined in terms of the lateral and vertical load-carrying capacity damage states of the bridge. It then remains up to researchers, decision stakeholders, engineers, and highway authorities to determine the form of the loss model that relates the losses in capacity to changes in traffic loading and speed. A sample loss model is presented in this section to facilitate application of the methodology and further discussion as to a more practical mathematical form.

5.2.2   Traffic Load

From PEER-Caltrans meeting minutes (Porter 2002), it has been suggested that a 10% loss in lateral capacity may constitute a life safety condition, but loss as high as 50% is a collapse-prevention performance objective. Therefore, a continuous model incorporating these data points was proposed that related the loss of lateral load-carrying capacity *DM* to the traffic load loss *DV* (Fig. 5.3). The loss of lateral load-carrying capacity was determined solely from the longitudinal direction in this example; however, the transverse direction could also be considered if critical in any given earthquake scenario.

For the case of the bridge vertical load-carrying capacity, a similar exercise can be performed to determine a relationship between the *DM* and a loss of traffic capacity. Once again, a continuous form of the loss model in the vertical direction was assumed and is shown in

Figure 5.4. The form of the loss model was once again guided by the proposed values in Table 4.8.
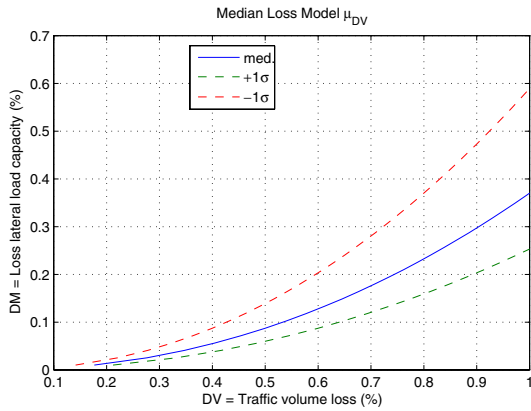
Fig. 5.3 Bridge traffic load loss model longitudinal
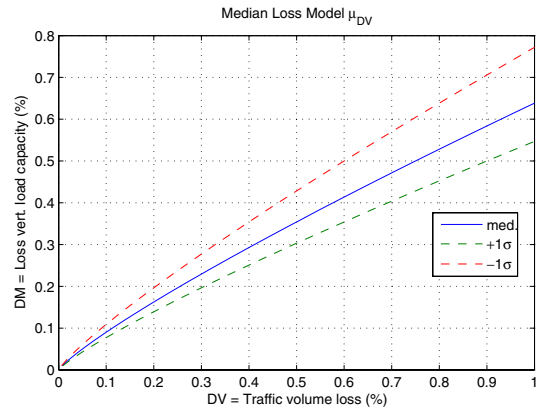
Fig. 5.4 Bridge traffic load loss model vertical

By using the decision fragility formulation of Equation 1.3 or 5.1, decision (or loss) fragilities can be derived for each of the bridge-level loss models presented. Several subsequent decision fragility curves are shown in Figure 5.5 from convolving the damage fragility and loss models for the longitudinal direction. The percentage in parenthesis (in the legend) refers to the loss in traffic volume associated with the proposed decision performance objectives. Loss fragility curves in the vertical direction are presented in Section 5.2.4.

The performance objectives shown on the plot are defined in terms of specific decision variable values (over a possible continuum of values), and they contain uncertainty information. In this manner, it was possible to construct a new set of bridge performance levels that are fully probabilistic and based on rational bridge performance criteria. These could be used to supplement existing information obtained from reconnaissance information during post-earthquake damage assessment. Or they can be used to give preliminary information about the transportation network functionality in a planning or design scenario.
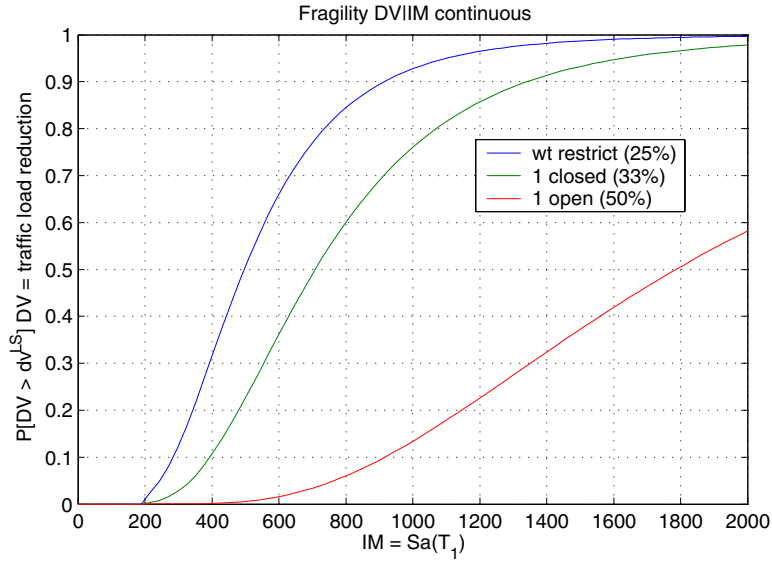
Fig. 5.5 Bridge decision fragility curves longitudinal

For an example of utilizing the decision fragility curves (in the longitudinal direction from Fig. 5.5), a design earthquake with intensity $Sa(T_1) = 900$ cm/s^2 was selected. The probability of weight restrictions (25% loss of traffic load capacity) is 0.9, the probability of lane closure is 0.7, but the probability of limited access (one lane open or emergency vehicles only) is only 0.1.

It should be noted, however, that this bridge-level example considers only the longitudinal lateral load-carrying capacity of the bridge. A complete set of decision-making tools would need to be more rigorous. Using the same procedure, the data in this example already exist for the transverse lateral and vertical load-carrying capacity of the same bridge (not shown in this section). This information can be used in conjunction with the longitudinal load-carrying capacity to create decision criteria based on the intersection of two or more of these quantities. For example, it was suggested (Porter 2002) that the loss of lateral load-carrying capacity could be acceptably large if the vertical capacity had not degraded significantly or if the bridge was shored.

At the bridge-level, the forms of both the *DM*s and *DV*s are yet to be defined. While existing documents focus on graded seismic performance objectives, the performance is not always rigorously defined. As an alternative, a new system of performance objectives based on the bridge-level example in this study was proposed in Table 4.8. Using decision fragility curves, the probability of exceeding any performance objectives can be determined at the seismic

level of interest. The specific values in the table (Table 4.8) are provided for illustration only and are meant to be refined through future research and discussion.

5.2.3   Collapse and Damage State Unions

Bridges are a crucial part of the transportation network in a region struck by an earthquake. The ability of a bridge to carry traffic load after an earthquake determines the weight of trucks that can cross it and the speed at which such traffic may move in the noncollapse scenario. However, the bridge reaches a certain critical point at which it is no longer able to sustain the traffic capacity. This point is defined as the collapse-prevention limit state, regardless of whether physical collapse has occurred. In a network simulation, however, whether the bridge has collapsed determines if a road is passable. Today, post-earthquake bridge evaluation is qualitative and empirical rather than quantitative. Therefore, this section provides an engineering basis for quick and reliable evaluation of the ability of a typical highway overpass bridge to function after an earthquake.

The collapse-prevention limit state used in this section was a combination of the loss of lateral and vertical load-capacity limit states shown in Table 4.8. A bridge would be considered closed, i.e., in a collapse-prevention limit state, if the lateral load-carrying capacity had been reduced by 25% or the vertical load-carrying capacity had been reduced by 50%. Thus, the remaining traffic volume crossing this bridge is zero. These values were used as an example and will be changed once more data become available. The damage fragility surfaces lateral (longitudinal) and vertical directions are presented in Section 4.2. For the purposes of this example, the direct method (Method A) was used to maintain consistency between the lateral and vertical directions. Both of the limit states are plotted in Figure 5.6 along with the probability of closure, defined as the union of the two damage limit states.

The probability of the union was approximated as a series system with the correlation coefficient computed using the response load-carrying data for the lateral and vertical directions. As would be expected, the correlation ($\rho = 0.85$) between vertical and lateral loss of load-carrying capacity was high. The probability was calculated using a two-dimensional multi-normal CDF. Only two damage limit states were chosen to allow closed-form integration of this CDF; however, it may be of further benefit to describe collapse in terms of both the loss of lateral and vertical load-carrying capacity and the residual displacement of the bridge piers.
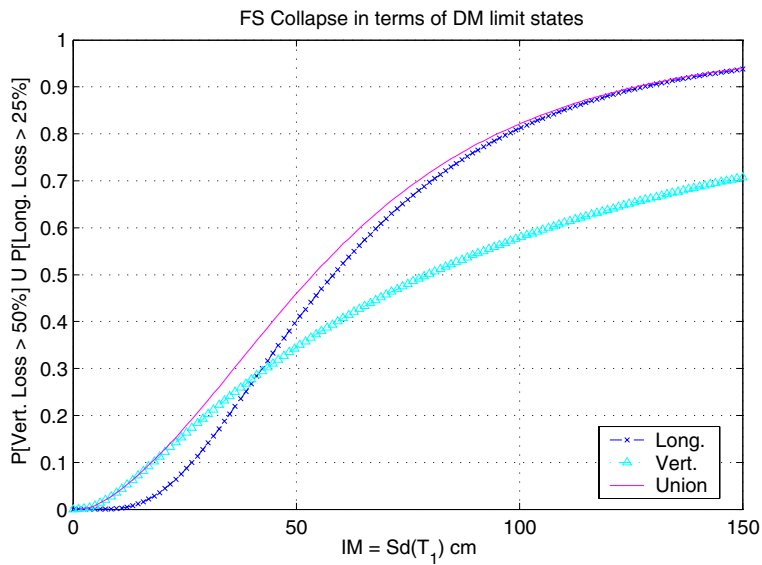
Fig. 5.6 Bridge collapse-prevention limit-state fragility curves

5.2.4   Improved Methods for Post-Earthquake Capacity

Four methods for predicting post-earthquake damage fragilities from first-shock earthquakes, the corresponding interim models, and interim variables were detailed in Section 4.2.3 for damage fragilities.   Only a brief summary of each method and their comparison are provided here, followed by extensions from damage to decision fragilities.   The four methods were applied to the bridge vertical direction only; therefore only the vertical loss model is considered in this section.   However, the methods remain general for the lateral directions as well.   The loss model, which relates a vertical damage variable to the loss of the traffic capacity decision variable, proposed herein, is shown in Figure 5.4.

5.2.4.1 Method A — Direct Method

The direct method was an application of the PEER framework (Eq. 1.3) directly to bridge-level interim models.   Therefore, the approach was the same as the one use for component-level decisions: Equation 1.3 is evaluated numerically for a range of *IM, EDP, DM,* and *DV* values to produce the *DV* fragility surface of Figure 5.7.   The fragility surface is a convenient method of visualizing numerous decision limit states on the same plot.   Each black line on the surface is a

single *DV* fragility curve. The major drawback of this method when applied to bridge-level decisions was a large model error. This resulted in low confidence (large dispersion) in predicting the median relationship between engineering response and earthquake intensity. This uncertainty was propagated through the subsequent models and resulted in a significant lack of confidence in the damage and decision fragilities.

Another shortcoming was also apparent: there is a large jump in probabilities of exceedance of a *DV* for small *IM* values. This was not realistic, as damage would start to accumulate only at higher earthquake intensities, not during the elastic response of the bridge. The result is an overprediction of the probability of traffic volume loss at lower earthquake intensities. Nevertheless, as these bridge-level models were derived by direct application of the PEER framework, they are useful as benchmarks for comparing subsequent methods.
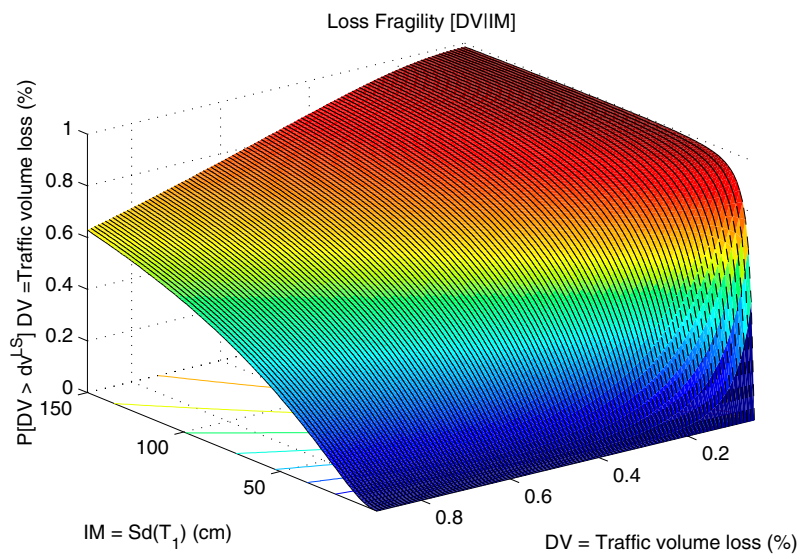
Fig. 5.7 Bridge loss fragility Method A vertical

5.2.4.2 Method B— MDOF Residual Displacement Method

This method introduced residual displacement u_{res} as an intermediate response parameter to improve the PSDM relating bridge-level engineering response parameters and earthquake intensity (*IM*). Analytical simulations were then used to relate residual displacement of the bridge and its vertical and horizontal load-carrying capacity degradation due to a combination of

material and geometric nonlinearities. The resulting *DV* fragility formulation is shown in Equation 5.3.

$$P\left(DV < dv^{LS} \mid IM = im\right) = \iiint P_{DV|DM}\left(dv^{LS} \mid dm\right) dP_{DM|EDP}(dm \mid edp) \cdot$$
$$dP_{EDP|U_{res}}\left(edp \mid u_{res}\right) dP_{U_{res}|IM}\left(u_{res} \mid im\right) du_{res} \cdot dedp \cdot ddm \qquad (5.3)$$

Once again, it was assumed that the *EDP* could be conditioned solely on u_{res}, without any additional *IM* information. While there was lower uncertainty in the *EDP*|u_{res} correlation, this method also suffered from large model error due to the large uncertainty in the residual displacement demand model. However, it did provide a more realistic prediction of the onset of bridge-level damage. The resulting fragility surface is shown in Figure 5.8. A comparison between all four methods for *DV* limit states of 25% and 50% traffic volume loss are shown in Figures 5.12 and 5.13, respectively.
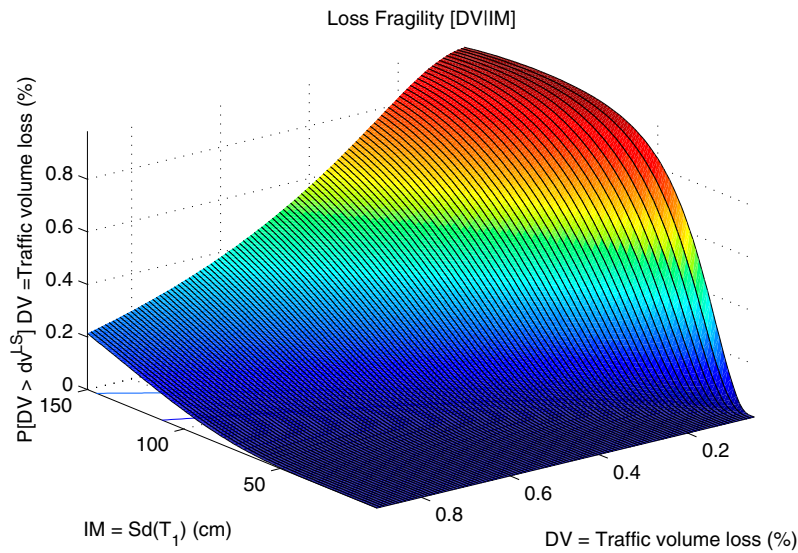
Fig. 5.8 Bridge loss fragility Method B vertical

5.2.4.3 Method C— SDOF Residual Displacement Method

This method was equivalent to Method B, except that the residual displacements were obtained from residual displacement spectra (Kawashima 1998) rather than analysis of actual bridge models. This method was effected to reduce the uncertainty in the residual displacement demand model. The single-degree-of-freedom (SDOF) oscillator properties were selected based on the

initial elastic period of the bridge and an *R*-factor obtained from demand model simulations. While the method did result in slightly reduced uncertainty, the median prediction was largely dependent on the selection of SDOF oscillator properties.

5.2.4.4 Method D— EDP Conditioning Method

In an attempt to further reduce the interim uncertainty (model error), maximum displacement u_{max} was introduced and correlated with residual displacement u_{res}. This was achieved by integrating over maximum displacement and residual displacement in the third term of Equation 1.3. The expanded third term is shown in Equation 5.4. Application of Equation 5.4 requires the *EDP* to be conditioned on u_{res} only (no u_{max} information), and u_{res} to be conditioned on u_{max} only (no *IM* information). This was verified by showing the dependence of the residuals on u_{max} and *IM* in Figures 5.9 and 5.10, respectively, is small. There was a trend between the *EDP*-u_{res} model and u_{max}, however, on average, the dependence was negligible, and the integration proposed by the PEER methodology was conducted without restrictions.

$$P_{EDP|IM}\left(edp\,|\,im\right)=\iint P_{EDP|U_{res}}\left(edp\,|\,u_{res}\right)dP_{U_{res}|U_{max}}\left(u_{res}\,|\,u_{max}\right)\cdot \\ dP_{U_{max}|IM}\left(u_{max}\,|\,im\right)du_{max}\,du_{res} \tag{5.4}$$
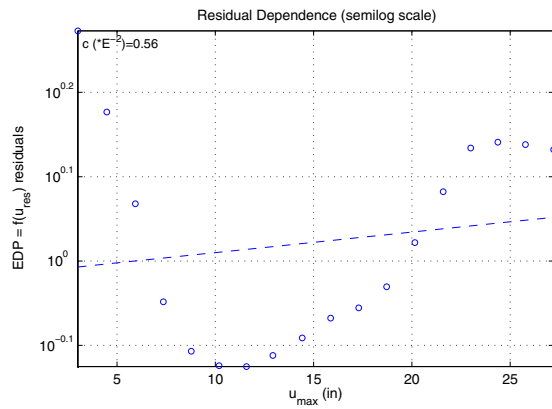
Fig. 5.9 EDP-u_{res}, u_{max} residual dependence   **Fig. 5.10 u_{res}-u_{max}, IM residual dependence**
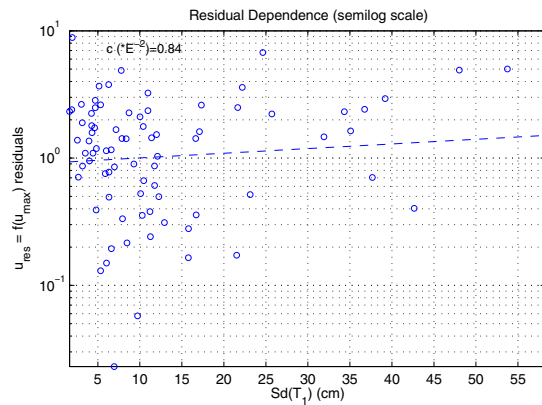
An efficient demand model relating maximum displacement u_{max} (or drift ratio) and $Sa(T_1)$ was used in the last term in Equation 5.4. The middle term in Equation 5.4 was derived using simulation (Section 4.2.3.4). The first term in Equation 5.4 was computed in Method B.

Combining all of the interim models numerically resulted in the loss fragility surface in Figure 5.11.
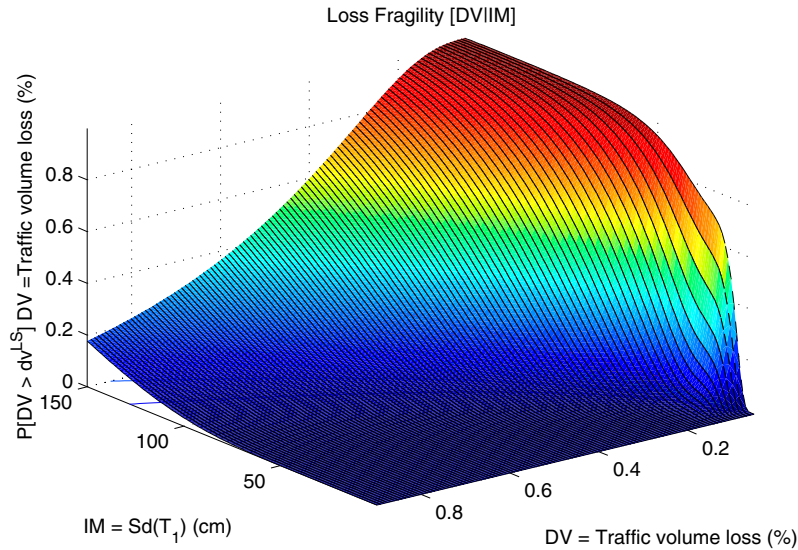
Fig. 5.11 Bridge loss fragility Method D vertical

By using *DV* limit states of 25% and 50% of traffic volume reduction, the four methods are compared in Figures 5.12 and 5.13, respectively. The values of ζ, the lognormal parameter that describes the dispersion of the *DV* model given *IM*, of the four methods were 0.96, 0.80, 0.73, and 0.46, respectively. Therefore, while even Method D had fairly high uncertainty, its prediction of the median value was better than the direct application of Equation 1.3.

The same trends evident in the damage fragility curves of Section 4.2.5 were also apparent in the figures above. Method A provided an unrealistic, yet conservative, upper bound. Methods B and C yielded less dispersion; however, Method D remained the best alternative of the improved methods presented. The bias in the median value of Method C was once again due to the use of the SDOF oscillator without a participation factor. Aftershock analysis at the loss fragility level could also be carried out using the procedure outlined in Section 4.2.4.
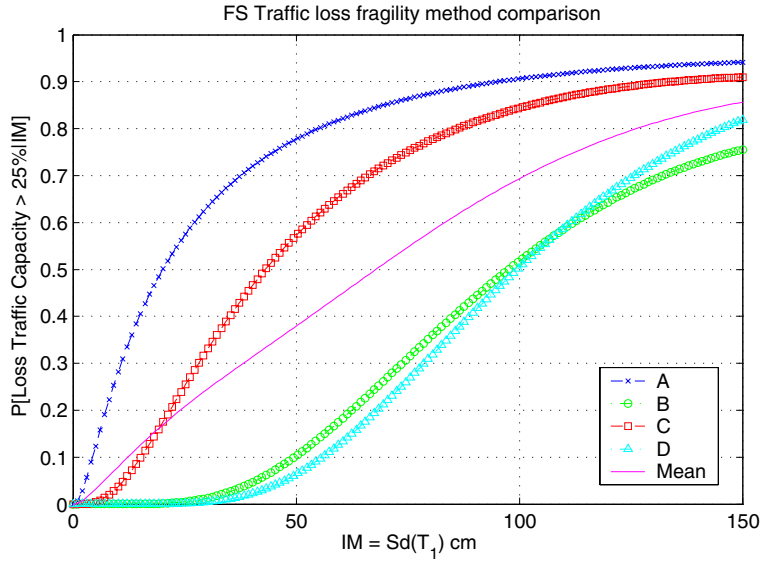
Fig. 5.12 Bridge decision fragility first-shock method comparison, $dv^{LS} = 25\%$

In summary, formulation of decision fragilities is hindered by lack of data at the loss model stage. At the component-level stage, this will involve future research on repair costs and time that improve the performance of the loss models in the framework. At the bridge-level, there is an even larger gap in the loss model, as the mathematical form of the loss model and the *DV*s of interest are yet to be agreed upon. Not only this, but the determination of loss fragilities suffers from the same lack of confidence as the bridge-level damage fragilities.
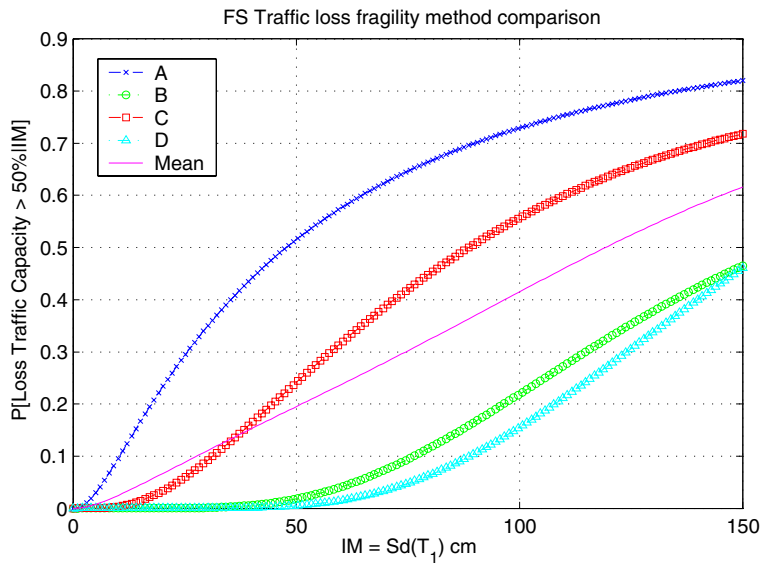
Fig. 5.13 Bridge decision fragility first-shock method comparison, $dv^{LS} = 50\%$

5.3   UNCERTAINTY

Epistemic uncertainty at the loss model level is introduced in this section. As in Sections 3.9 and 4.3, the dispersion term can be modified by SRSS to include the contribution of the aleatory and epistemic portions. This total dispersion can then be used without modification in all of the loss fragility and loss hazard curves of this chapter. The result of using the total uncertainty is the prediction of the mean fragility or hazard curve rather than the median curve. Alternatively, the two sources of uncertainty can be separated and the percentiles due to the epistemic uncertainty plotted around the median curve. This is illustrated for the loss fragility curve in Equation 5.5.

$$P_{DV|IM,Y}\left(dv^{LS} \mid im, y\right) = \Phi\left[\frac{\ln\left(dv^{LS}\right) - \ln\left(D\hat{V}(im)\right) - y\sqrt{d_{dm}^2 f_{lm}^2 \sigma_{PSDM}^2 + f_{lm}^2 \sigma_{PDM}^2 + \sigma_{PLM}^2}}{\sqrt{d_{dm}^2 f_{lm}^2 \sigma_{EDP|IM}^2 + f_{lm}^2 \sigma_{DM|EDP}^2 + \sigma_{DV|DM}^2}}\right] (5.5)$$

The Method A loss fragility curve is selected to illustrate the use of Equation 5.5. The loss (Fig. 5.14) and damage fragilities (Fig. 4.50) were very similar in form and dispersion. This is due to the dominance of the large aleatory uncertainty in the demand model for Method A. Hence, the mean and median curves were almost equivalent. A relatively small epistemic uncertainty (0.05) was assumed for the loss model, as the relationship between *DV* and *DM* is relatively certain, once agreed on by the decision-making stakeholders.
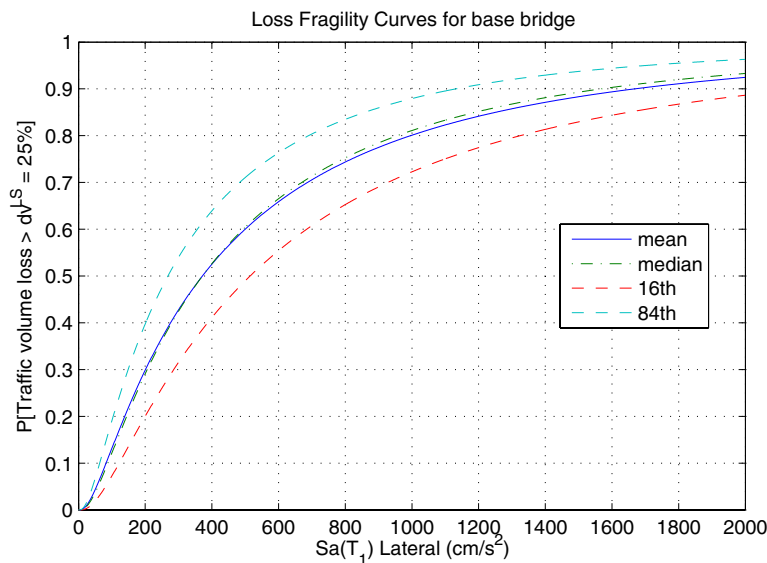
Fig. 5.14 Bridge-level loss model fragility curve percentiles

Continuing the confidence interval propagation example from Section 4.3, the 50% confidence intervals are shown in Figure 5.15 for the 15% traffic volume loss fragility curve. Once again, the confidence intervals stemmed only from the uncertainty in selecting the median demand model, not confidence intervals at each of the damage and loss model levels. To further illustrate the poor performance of Method A in predicting damage and loss fragilities, 50% intervals are shown for both methods A and D in Figure 5.15. While the median of Method D did not fall within the Method A confidence intervals, the width of the intervals is largely indicative of the better choice of method. The plot was simplified by removing the 90% confidence intervals. The Method D 90% confidence intervals were wider than the 50% intervals, as would be expected from a median with higher certainty.
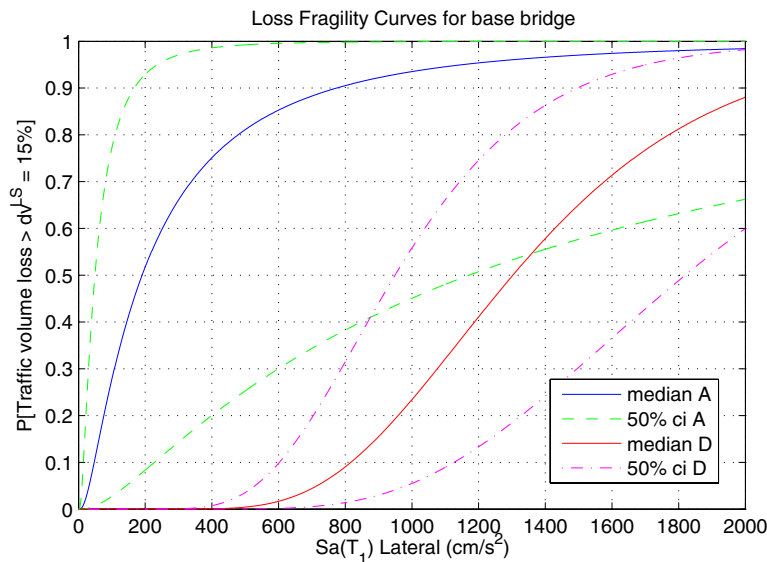
Fig. 5.15 Bridge-level loss model confidence intervals

An engineering basis for quantitatively evaluating the ability of a typical highway bridge to function after an earthquake was presented in this chapter for three limit states: repair cost, traffic function, and collapse-prevention. The PEER framework was utilized to cast these limit states in terms of damage and decision fragility curves. For the repair cost limit state, component-level (column) damage and loss data were used in a direct application of the PEER integral. However, for the bridge-level traffic function limit state, several methods of obtaining the decision fragilities were introduced, the best method using *EDP* conditioning (Method D).

Finally, an example of combining damage limit states to define the collapse-prevention limit state was presented. The resulting fragility curves for all limit states can be used by engineers and decision makers to assess the performance of a typical highway bridge in a given earthquake scenario, and evaluate the changes in bridge performance under varying earthquake intensity scenarios. Ongoing research is focused on refining the values of decision variables using feedback from bridge engineers and additional analytical studies.

6 General PBEE Formulation

This chapter provides a general formulation for the entire PBEE problem from the hazard (*IM*) to the decision variable (*DV*). Rather than using abstract models, the same bridge-level interim models derived in previous chapters were used. This general formulation includes closed-form solutions for intermediate hazard curves based on the power-law relationship, conditional lognormal distribution, and constant dispersion assumptions of the constituent variables. Specifically, the *DV*s were considered lognormally distributed when conditioned on *DM*. The same assumption was made regarding DMs conditioned on *EDP*s and *EDP*s conditioned on *IM*s. The goal of this chapter is provide an explicit example of how to generate loss hazard information and to illustrate the simplicity of evaluating the framing equation (Eq. 1.2) when the successive interim variables are assumed to be conditionally lognormal.

6.1 PSHA

In this example, probabilistic hazard assessment was obtained from USGS mapping data (USGS) for a site near the Berkeley campus of the University of California. While there may be numerous ways of obtaining these data, below is short description of the method used to obtain the median hazard curve. Spectral acceleration was chosen as the *IM* of concern throughout this example. As mentioned previously (Section 3.4.1), large amounts of previous research have shown $Sa(T_1)$ is an optimal choice among existing *IM*s to use during the integral evaluation.

The 2%-, 5%-, and 10%-exceedance in 50 years pseudo-acceleration equal hazard spectra are shown in Figure 6.1, along with each individual interpolated response spectra. The two-part fit used a $1/T$ relationship between $Sa(T)$ and T for periods greater than 0.5 sec and a capped spectral acceleration in the short-period range. The continuous fit was merely a function fitted to the given data points. The two-part fit was used for analysis. An example analysis was

performed using the single-bent base-bridge configuration with a fundamental period of $T_1 = 1.57$ sec. The values at the period of interest were used to determine the median hazard curve.
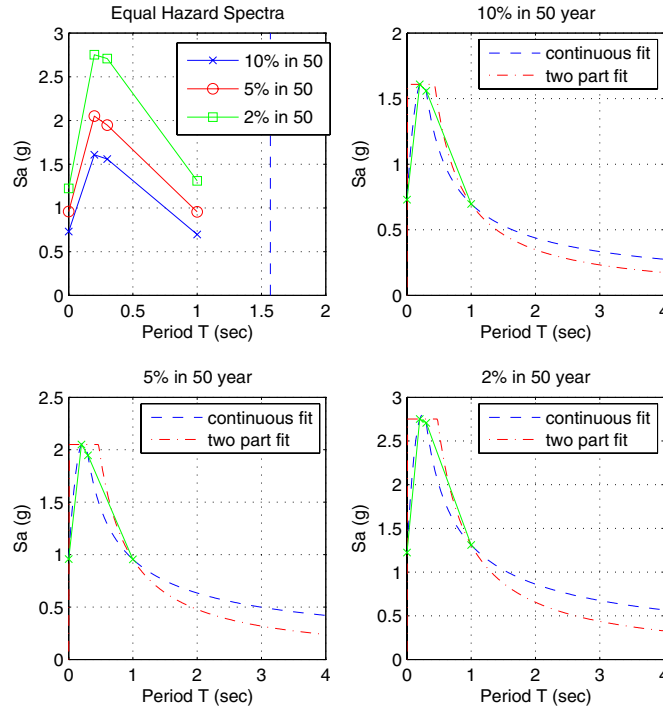
Fig. 6.1 USGS hazard curves for Berkeley, California

The hazard curve was assumed to have an exponential form with two unknown parameters (Eq. 3.4). The two-parameter approximation tends to overpredict frequencies of exceedance for both *IM* extremes. Therefore, care should be used when extrapolating any resultant hazard curves to extremely low (or high) frequencies of exceedance. Using a least-squares fit in log-log space (Eq. 3.5), the unknown parameters were determined to be $k = 2.61$ and $k_0 = 1.7e4$. The resulting hazard curve is shown in Figure 6.2. This hazard curve was used implicitly in Sections 3.8.2 and 4.1.2. Alternatively, coefficient determination is often performed by solving the equations using only two of the hazard levels (Eqs. 6.1, 6.2).

$$k = \frac{\ln\left(\dfrac{\nu_{Sa}(10\%,50\,yr)}{\nu_{Sa}(2\%,50\,yr)}\right)}{\ln\left(\dfrac{Sa_{2\%,50\,yr}}{Sa_{10\%,50\,yr}}\right)} \tag{6.1}$$

196

$$\ln(k_0) = \frac{\ln(Sa_{10\%,50yr})\ln(\nu_{Sa}(2\%,50yr)) - \ln(Sa_{2\%,50yr})\ln(\nu_{Sa}(10\%,50yr))}{\ln\left(\dfrac{Sa_{10\%,50yr}}{Sa_{2\%,50yr}}\right)} \qquad (6.2)$$
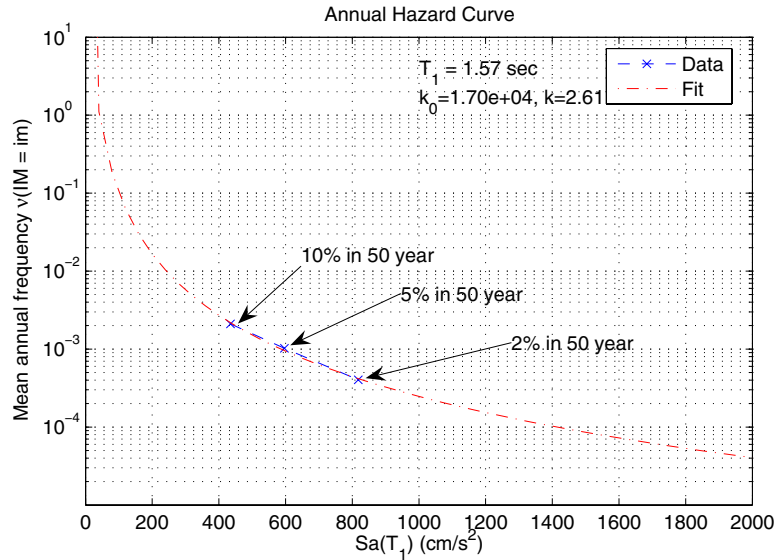
Fig. 6.2 Median annual hazard curve for T_1 = 1.57 sec in Berkeley, California

The uncertainty in the hazard curve (not shown here) is taken care of by using the mean hazard curve in order to estimate the mean annual frequency of exceeding an *EDP, DM,* or *DV* limit state (see Cornell 2002). The mean hazard curve must be derived from the hazard data, or estimated from the median hazard above based on a hazard uncertainty term. The hazard curves in this report do not include this uncertainty, only the aleatory uncertainty from each of the demand, damage, and loss models.

6.2 DEMAND MODEL

The demand model was fully described in Chapter 3 and therefore is mentioned only briefly here. The power-law form (Eq. 3.9) and conditional lognormal distribution of *EDP* given *IM* of the demand model was assumed to apply; therefore, the closed-form solution for the demand hazard curve (Eq. 3.34) was applicable. Probabilistic demand analysis was required only to produce the coefficients *a* and *b* of the median fit in order to fully describe both the median demand fragilities (Eq. 3.29) and the hazard curves (Eq. 3.34).

Sample demand fragility curves using the assumption of a lognormal demand model are shown in Figure 3.76 for the drift ratio *EDP*. The corresponding demand hazard curves are shown in Figure 3.80. At the bridge level, an example of applying Equation 3.34 is shown in Figure 6.3. The discrepancy between the numerical and closed-form solution arose due to the number and placement of numerical integration points. The approximations of Equation 1.2 should also be remembered, as it is equally applicable at the demand hazard curve level. Therefore, it should be expected that the hazard predicted at the lower *EDP*s is less accurate (especially for larger return periods).

6.3   DAMAGE MODEL

The median damage model developed for loss of vertical load-carrying capacity at the bridge-level in Section 4.2.2 was also assumed to follow a power-law relationship. The resulting general probabilistic damage model equations then become Equation 6.3 in linear space and Equation 6.4 in log space. The models were fully defined after deriving the coefficients c_{dm} and d_{dm}.

$$D\hat{M} = c_{dm}\left(EDP\right)^{d_{dm}} \tag{6.3}$$

$$\ln\left(D\hat{M}\right) = C_{dm} + D_{dm}\ln\left(EDP\right) \tag{6.4}$$

The damage model was simplified greatly because the coefficients d_{dm} and c_{dm} are simply 1 and -ln(P_{max}), respectively.
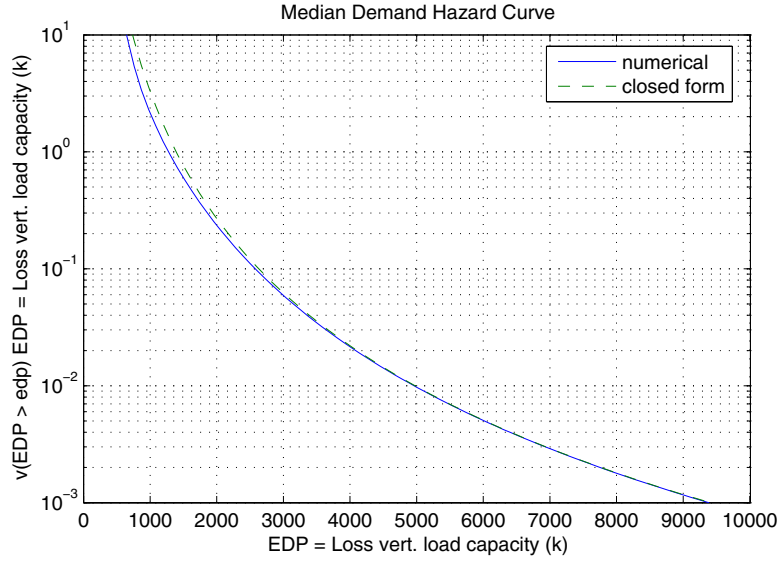
Fig. 6.3 Bridge-level demand hazard curves vertical

It was also assumed that the conditional probability distribution of *DM* on *EDP* was lognormal. In a similar manner to the demand model, it was possible to obtain a closed-form expression for the mean annual frequency of exceeding different *DM* values. The structural damage hazard curve is described by Equation 6.5.

$$\lambda_{DM}(dm) = k_0 \left[\frac{1}{a} \left(\frac{dm}{c_{dm}} \right)^{\frac{1}{d_{dm}}} \right]^{\frac{-k}{b}} \exp\left(\frac{k^2}{2b^2 d_{dm}^2} \left(d^2 \sigma_{EDP|IM}^2 + \sigma_{DM|EDP}^2 \right) \right) \qquad (6.5)$$

This closed-form expression was applied to the bridge-level damage hazard curve in Figure 4.19. The discrepancy arose from the numerical integration points, as described above, and was also compounded by the errors in the demand hazard curve. The numerical solution is obtained simply by differentiating the demand hazard curve; therefore, any errors in this curve were propagated forward.

6.4   LOSS MODEL

Similarly, the proposed median loss model for loss of traffic load-carrying capacity at the bridge-level in Section 5.2.2 was also assumed to follow a power-law relationship. The resulting general probabilistic loss model equations then become Equation 6.6 in linear space and

Equation 6.7 in log space. The models were fully defined after deriving the coefficients e_{lm} and f_{lm}.

$$D\hat{V} = e_{lm}(DM)^{e_{lm}} \tag{6.6}$$

$$\ln(D\hat{V}) = E_{lm} + F_{lm}\ln(DM) \tag{6.7}$$

Continuing from the damage hazard curve, and assuming that the *DV* was lognormally distributed when conditioned on *DM*, it was also possible to obtain a closed-form expression for the mean annual frequency of exceeding different *DV* values. The structural loss hazard curve is described by Equation 6.8. A comparison of the numerical and closed-form loss hazard curves is shown in Figure 6.4. The numerical solution was obtained from differentiation of the damage hazard curve in Figure 4.19.

$$\lambda_{DV}(dv) = k_0 \left[\frac{1}{a}\left\{ \frac{1}{c_{dm}}\left(\frac{dv}{e_{lm}}\right)^{\frac{1}{f_{lm}}} \right\}^{\frac{1}{d_{dm}}} \right]^{\frac{-k}{b}} e^{\left(\frac{k^2}{2b^2 d_{dm}^2 f_{lm}^2}\left(d_{dm}^2 f_{lm}^2 \sigma_{EDP|IM}^2 + f_{lm}^2 \sigma_{DM|EDP}^2 + \sigma_{DV|DM}^2\right) \right)} \tag{6.8}$$
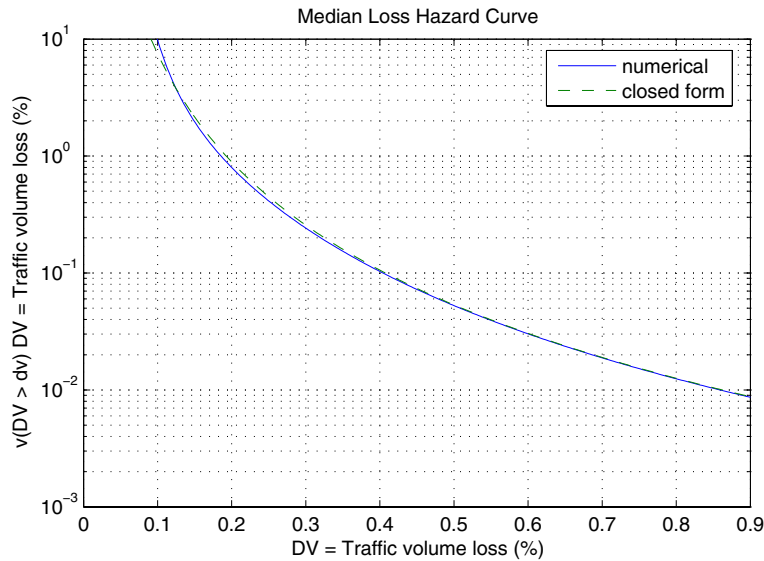
Fig. 6.4 Bridge-level loss hazard curve vertical

7   Conclusion

The problem of highway overpass bridge decision making due to seismic hazard is a complex one. For the reinforced concrete highway overpass bridges considered in this study, measures used to calculate loss included structural component repair costs and decrease in traffic volume compared to the pre-earthquake bridge state (the actual indirect costs due to lack of function were not calculated herein). However, there is no clear direct relationship between these loss-modeling measures and typical seismic hazard input parameters, such as earthquake magnitude, distance, and intensity. In addition, evolving design methodologies no longer focus on solely deterministic estimates of such loss-modeling measures. Rather, it is necessary to consistently describe loss in a probabilistic manner. The result is a performance-based approach to bridge design and assessment in an earthquake scenario.

To arrive at systematic and quantifiable measures that aid in decision-making or loss-modeling contexts, it is necessary to rigorously define the various contributing components. For fragility-based seismic decision making this includes expected response of the bridge structure to seismic excitation, subsequent damage and degradation of the structure, the loss of function after an earthquake event, and the need to restore the bridge to a predetermined level of functionality. To achieve the end goal, the probabilistic performance-based earthquake engineering framework of the Pacific Earthquake Engineering Research Center was adopted.

7.1   BASIC PROCEDURE

While previous bridge fragility studies have focused on demand-based limit states, subjective limit-state definitions, and compatibility with existing empirical fragilities, this study provides an analytical fragility formulation that is rigorous and probabilistically consistent. Not only this, but the problem of defining earthquake fragilities is disaggregated into interim models that are succinctly defined, and have associated fragilities. Therefore, it was possible to generate

demand, damage, and decision fragility curves. These are distinctly different from any existing fragilities for numerous reasons. First, the fragilities are in reference to exceeding specific rational values of *EDP*, *DM*, or *DV* variables in discrete or continuous fashion. Second, they are conditioned on an arbitrary *IM* variable that can be chosen to best suit the structure and site of interest. Finally, uncertainty in each model is propagated to each subsequent fragility curve.

The PEER PBEE framework disaggregates the decision-making procedure into three discrete models, combined using the total probability theorem (Eq. 1.1). The interim models can be treated separately if selected so as not to carry on conditional dependencies on previous models. The three interim models are the probabilistic seismic demand model (PSDM), probabilistic damage model (PDM), and the probabilistic loss model (PLM). The results of applying the PEER framework are either the annual frequencies of exceeding prescribed limit states (a hazard curve) or the probabilities of exceeding the same limit states, conditioned on earthquake intensity (a fragility curve). The decision-making procedure was applied to individual realizations of reinforced concrete highway bridges that account for the largest number of highway bridges in the California bridge inventory. The analytical finite element models used to represent this class of bridges were detailed in Chapter 2.

PSDMs relate measures of earthquake intensity (*IM*) to measures of structural response (*EDP*). The demand models (Chapter 3) can be formulated using either the cloud method (PSDA) or the incremental scaling method (IDA). The PSDA procedure was utilized exclusively in this study to investigate the selection of optimal *IM*s and *EDP*s as well as trends due to the variation of bridge design parameters. Of existing *IM*s, the first-mode spectral quantities (*Sa*, *Sv*, or *Sd*) were optimal. Optimal was defined as being practical, effective, efficient, sufficient, and robust. For more efficient *IM*s, the Class III *IM*s generated from using a bandpass filter were the most computationally efficient method of filtering ground motion records over a band of frequencies. The efficiency increase was equivalent to using an average of spectral quantities over a period band; however, the computation time is drastically reduced. Alternatively, first-mode period modification factors can be used to obtain more efficient results using only a single spectral analysis. However, these are structure specific and may not be applicable to a wide range of structures.

Performance changes were generated by varying bridge design parameters during demand analysis. Results were quantified in the PSDMs through the use of design equations (Eq. 3.17). Alternatively, probabilities of exceeding demand limit states were investigated for

different design parameters using parameterized demand fragility surfaces (Eq. 3.30). The drawback of comparing design parameters with highly optimal *IM*s is the period-dependence of the *IM*s. Therefore, the design equations and fragility surfaces were all generated with the best period-independent *IM*. For the bridges considered in this study, the best period-independent choice was *CAD* or *PGV*. Optimal PSDMs and design parameter variations were explored for the one-bent, two-bent, and three-bent bridges in the class of bridges selected. A complete treatment of uncertainty was made for each of the interim models. Each probabilistic model was formulated considering only randomness, or aleatory, uncertainty. At the end of each chapter, the inclusion of epistemic uncertainty was then introduced.

Damage models (Chapter 4) were formulated at two levels corresponding to localized decision goals and functional decision goals. The localized, or component-level damage models were generated using both an experimental and analytical approach. The experimental approach incorporated thousands of test results from a database used to predict component-level damage to columns at different levels of response. An analytical reliability-based approach was also employed to produce the same component damage models. The experimental database is currently limited to columns only and requires interpolation between design parameters of interest. The reliability approach is applicable to any component of interest but suffers from the inability to model complex natural phenomena using finite element models. Therefore, both methods have potential uses in future studies. Damage models were formulated only for the columns of the bridges considered; however for a complete damage assessment, damage models for other components would be required.

The functional, or bridge-level, damage models were generated entirely using reliability methods due to the lack of experimental data. Simulations were performed to predict the loss of lateral and vertical load-carrying capacity of the bridge in a post–first-shock or post-aftershock scenario. Large uncertainties were present in the direct method of predicting these damage models, therefore several other methods were introduced to improve the level of confidence in the final models. The most promising method (Method D) incorporated both the maximum and residual displacements (*EDP*s) on the bridge. These were then used to predict the loss of load-carrying capacity. However, all methods were largely dependent on the final element modeling choices and can be improved in the future.

Loss models (Chapter 5) continued the two-path approach (based on component- or bridge-level quantities) leading to direct and indirect earthquake losses. At the component level

(and related strictly to columns due to the damage models), a repair cost loss model was developed using data collected from the Northridge and Loma Prieta earthquakes. At the bridge level, the same improved methods used to generate bridge damage fragilities were used to predict loss fragilities in terms of traffic volume loss. The bridge-level loss model was inferred from Caltrans expected bridge post-earthquake performance. A possible mathematical form of the loss model and ordinates were presented as a motivation for further discussion between the engineers, owners, and authorities involved. The loss of function was presented as a basis for pre- and post-earthquake decision making as well as a tool for calculating indirect costs to a network.

As a further tool for relating loss of load-carrying capacity and such visible damage as residual displacements, a reconnaissance tool was presented that would supplement field decisions on the conditions of a bridge. The concept of collapse prevention was also introduced as a union of (load) capacity losses and residual displacements, rather than the actual onset of structural collapse. This is a more realistic definition of collapse (i.e., the loss of lateral and vertical load-carrying capacity) in terms quantifiable to both structural engineers and policy makers alike.

7.2 APPLICABILITY TO REDARS AND HAZUS

The methodology proposed in this report is rigorous and can be applied to any bridge (or structure) of interest. However, the value of bridge-level loss modeling is greatly increased if it can be utilized to predict the performance of numerous bridges in a highway network setting. While it is impractical to perform such a meticulous loss modeling procedure for every single bridge in a regional inventory, the grouping of bridges into classes that share common characteristics and performance trends is achieved in this study.

Using the most common class of bridges in California, the applicability of the fragilities derived in this study was made possible through the variation of bridge design parameters. The FHWA already classifies bridges according to numerous criteria in the NBI (national bridge inventory), such as year built, material type, and structural type. Basöz recommended improved parameters (Basöz 1996, 1999) that better categorized bridges into different performance classes, such as number of spans, skew, height. The bridge design parameters used in this study correlate

well with both these HAZUS database categories, and with those often used to assess damage to structural element on a component level (PEER Capacity Catalog).

With the general bridge classifications and damage and loss fragilities available from research, a future version of the NBI may feature a meta-database that includes entries for fragility curves parameterized by design parameter, as well as bridge specific data obtained from pre- and post-earthquake reconnaissance (recorded motion, documented damage, etc). This database would become very powerful in large-scale simulations on transportation networks, such as REDARS and HAZUS.

Not only would more comprehensive data be available for each bridge in the network, but also the fragilities generated in this study could be applied directly to calculation of network losses. This includes the direct use of loss fragilities, such as the repair cost ratio, in determining network direct losses. Alternatively, the repair cost data could be supplied in the network simulation and the damage fragilities used to predict probabilities of exceeding functional or structural component damage states. Currently, both HAZUS and REDARS make use of damage fragilities to classify the post-earthquake state of bridges. However, these fragilities are either empirically based, or based on simplified analytical tools applicable to a larger array of bridges. The current limitation, however, on the fragilities and methodology in this study is the lack of time dependence of the results. Therefore, the return to functionality due to repair and restoration is not addressed.

7.3   ANALYTICAL SHORTCOMINGS AND FUTURE WORK

A primarily analytical approach was assumed in generating most of the interim models of this study. The only experimental data used was for column component damage models as well as small-scale axial load loss experiments. The obvious caveat being that the resulting analytical models are only as good as the finite element models and the associated input. While some of the component-level damage models were validated with the experimental database, the analytical approach was adopted largely due to the lack of available data for bridge-level response.

However, experimental programs suffer from a variety of uncertainty sources, just as analytical programs do, albeit different sources. At the analytical level, lack of knowledge and choice of modeling procedure are the primary sources of uncertainty. Failure modes are required

a priori in order to predict them analytically. Therefore, the primary focus of this research was not on collapse and high-intensity earthquake events. Rather, reliability methods were introduced to address some sources of uncertainty in the analytical prediction of damage and loss.

The principal shortcoming uncovered during this study was the prediction of the loss of load-carrying capacity at the bridge level. While numerous attempts were made to improve confidence in the prediction through residual and maximum displacement, uncertainties in the final models were still large. For use as a decision-making guideline, the losses of load capacities are very important. Therefore, refinement of the methods and procedures used to predict these losses should be investigated in the future. This is especially true when applied to aftershocks, as there has been little treatment on the cumulative effect of multiple shocks on the load-carrying capacity of a bridge.

Numerous other improvements are also required to obtain a more complete picture of bridge-specific loss modeling. At the component level, only the column was considered. Especially in short bridges, the abutment response and subsequent damage should outweigh that of the column. There are also other components, such as the approach embankment, that determine post-earthquake functionality. These components need to be considered in future studies even though the methodology applied in this report is general. However, as more components are considered, not only are damage models required, but so are loss models (such as repair costs). This is indicative of the interdisciplinary nature of earthquake engineering.

REFERENCES

API. (1993). *Recommended practice for planning, designing, and constructing fixed offshore platforms - Load and resistance factor design*. Report No. RP2A-LRFD. American Petroleum Institute, Washington D.C.

Arias, A. (1970). A measure of earthquake intensity. R.J. Hansen, Editor. *Seismic design for nuclear power plants*. Cambridge: MIT Press, 438-483.

ATC. (1978). *Tentative provisions for the development of seismic regulations for buildings*. Report No. ATC 3-06. Applied Technology Council, Palo Alto, California.

ATC/MCEER. (2001). *Recommended LRFD guidelines for the seismic design of highway bridges*. ATC Report No. ATC-49a. Applied Technology Council and Multidisciplinary Center for Earthquake Engineering joint venture.

Basöz, N., and Kiremidjian, A.S. (1996). *Risk assessment for highway transportation systems*. Report No. 118. John A Blume Earthquake Engineering Center, Stanford University, Stanford, California.

Basöz N., and Kiremidjian A.S. (1997). *Evaluation of bridge damage data from the Loma Prieta and Northridge, CA earthquakes*. Report No. 127. John A Blume Earthquake Engineering Center, Stanford University, Stanford, California.

Basöz N., Kiremidjian, A.S., and King, S.A. (1999a). Statistical analysis of bridge damage data from the 1994 Northridge, CA, earthquake. *Earthquake Spectra*, 15(1): 25-54.

Basöz N., and Mander, J. (1999b). *Enhancement of the highway transportation lifeline module in HAZUS*. National Institute of Building Sciences.

Bazzurro, P. (1998). *Probabilistic seismic demand analysis*. PhD Dissertation. Stanford University, Stanford, California.

Bazzurro, P., Cornell, C.A., Menun, C., and Motahari, M. (2004). Guidelines for seismic assessment of damaged buildings. In *Proceedings of the 13th World Conference on Earthquake Engineering*, August 1-6 2004, Vancouver, Canada.

Berry, M.P., and Eberhard, M.O. (2004). *PEER structural performance database user's manual*. PEER Report. Submitted for publication, 2004. Pacific Earthquake Engineering Research Center, University of California, Berkeley.

Berry, M.P., and Eberhard, M.O. (2003). *Performance models for flexural damage in reinforced concrete columns*. Report No. 2003/18. Pacific Earthquake Engineering Research Center, University of California, Berkeley.

Boulanger, R.W., Curras, C.J., Kutter, B.L., Wilson, D.W., and Abghari, A. (1999). Seismic soil-pile-structure interaction experiments and analyses. *Journal of Geotechnical and Geoenvironmental Engineering*, ASCE, 125(9): 750-759.

Brinch-Hansen, J. (1961). *The ultimate resistance of rigid piles against transversal forces*. Bulletin No. 12, Danish Geotechnical Institute, Copenhagen, Denmark, 5-9.

Caltrans (1999). *Seismic Design Criteria 1.1*. California Department of Transportation, Sacramento, California.

Carballo, J.E, Cornell, C.A. (2000). *Probabilistic seismic demand analysis: Spectrum matching and design*. Reliability of Marine Structures Report No. RMS-41. Dept. of Civil and Envir. Engineering, Stanford University, California.

CEB (2003). *Displacement-based seismic design of reinforced concrete buildings*. Bulletin 25, International Federation for Structural Concrete, Lausanne, Switzerland.

Chopra, A.K. and Goel, R.K. (2001). *A Modal Pushover Analysis Procedure to Estimate Seismic Demands for Buildings*. Report No. 2001/03. Pacific Earthquake Engineering Research Center, University of California, Berkeley.

Cordova, P.P., Mehanny, S.S.F., Deierlein, G.G., and Cornell, C.A. (2000). *Development of a two-parameter seismic intensity measure and probabilistic assessment procedure*, The Second U.S.-Japan Workshop on Performance-Based Earthquake Engineering Methodology for Reinforced Concrete Building Structures. Report No. 2000/10. Pacific Earthquake Engineering Research Center, University of California, Berkeley.

Cornell, C.A. (1968). Engineering seismic risk analysis. *Bulletin of the Seismological Society of America*, 58: 1583-1606.

Cornell, C.A., and Krawinkler, H. (2000). Progress and challenges in seismic performance assessment. *PEER Center News*, 3(2).

Cornell, C.A., Jalayer, F., Hamburger, R.O., and Foutch, D.A. (2002). Probabilistic basis for 2000 SAC/FEMA steel moment frame guidelines. *Journal of Structural Engineering*, 128(4): 526-533.

Deodatis, G., and Shinozuka, M. (1997). Effects of spatial variation of earthquake ground motion on the dynamic response of highway bridges. In *Simulation for Civil Infrastructural Systems: Proceedings of US-Japan Seminar/Workshop*, November 22-23, 1997, Kyoto, Japan.

Der Kiureghian, A. (2005). Non-ergodicity and PEER's framework formula. *Earthquake Engineering and Structural Dynamics*, short communication, accepted for publication.

Eberhard, M.O., and Marsh, M.L. (1997). Lateral-load response of a Reinforced Concrete Bridge. *Journal of Structural Engineering*, 123(4): 451-460.

Elnashai, A.S., Borzit, B., and Vlachos, S. (2004). Deformation-based vulnerability functions for RC bridges. *Structural Engineering and Mechanics*, 17(2): 215-244.

Elwood, K.J. (2002). *Shake table tests and analytical studies on the gravity load collapse of reinforced concrete frames*. PhD Dissertation, University of California Berkeley.

Fajfar, P., Gaspersic, P., and Drobnic, D. (1997). A simplified nonlinear method for seismic damage analysis of structures. In *Proceedings of the International Workshop on Seismic Design Methodologies for the Next Generation of Codes*, June 24-27, 1997, Bled, Slovenia.

Fajfar, P., Vidic, T., and Fischinger, M. (1990). A measure of earthquake motion capacity to damage medium-period structures. *Soil Dynamics and Earthquake Engineering*, 9(5): 236-242.

FEMA-273. (1996). *NEHRP guidelines for the seismic rehabilitation of buildings*. Report No. FEMA-273. Federal Emergency Management Agency, Washington D.C.

FEMA-302. (1997). *NEHRP recommended provisions for seismic regulations for new buildings and other structures*. Report No. FEMA-302. Federal Emergency Management Agency, Washington D.C.

FEMA-356. (2000a). *Prestandard and commentary for the seismic rehabilitation of buildings*. Report No. FEMA-356. Federal Emergency Management Agency, Washington D.C.

FEMA-350. (July 2000b). *Recommended seismic design criteria for new steel moment-frame buildings*. Report No. FEMA-350. Federal Emergency Management Agency, Washington D.C.

FHWA. (2003). National Bridge Inventory. http://www.fhwa.dot.gov/bridge/nbi.htm. Web site. Federal Highway Administration.

Foutch, D.A., Yu, C.-Y., and Wen, Y.K. (1992). Reliability of steel frame buildings under seismic load. In *Proceedings of the Tenth World Conference on Earthquake Engineering*, July 19-24, 1992, Madrid, Spain. A.A. Balkema, Rotterdam, Vol. 8.

Gardoni, P., Der Kiureghian, A., and Mosalam, K.M. (2002). *Probabilistic models and fragility estimates for bridge components and systems*. PEER Report 2002/13. Pacific Earthquake Engineering Research Center, University of California, Berkeley.

Gupta, A., and Krawinkler, H. (2000). Behavior of ductile SMRFs at various hazard levels. *Journal of Structural Engineering*, 126(ST1): 98-107.

Haukaas, T. (2003). *Finite element reliability and sensitivity analysis of hysteretic degrading structures*. PhD Dissertation, University of California, Berkeley.

HAZUS. (1997). *Earthquake loss estimation methodology*. Technical Manual. National Institute of Building Sciences for Federal Emergency Management Agency.

Hose, Y., Silva, P., and Seible, F. (2000). Development of a performance evaluation database for concrete bridge components and systems under simulated seismic loads, *Earthquake Spectra*, 16(2): 413-442.

Housner, G.W. (1959). Behavior of structures during earthquakes. *Journal of Engineering Mechanics Division*, 85(EM14): 109-129.

Jalayer, F. (2003). *Direct probabilistic seismic analysis: implementing non-linear dynamic assessments*. PhD Dissertation, Stanford University, Stanford, California.

Karim, K.R., and Yamazaki, F. (2001). Effect of earthquake ground motions on fragility curves of highway bridge piers based on numerical simulation. *Earthquake Engineering and Structural Dynamics*, 30(12): 1839-1856.

Kato, D., and Ohnishi, K. (2002). *Axial load-carrying capacity of reinforced concrete columns under lateral load reversals*. PEER Report No. 2002/02: 247-255. Pacific Earthquake Engineering Research Center, University of California, Berkeley.

Kawashima, K., MacRae, G.A., Hoshikuma, J., and Nagaya, K. (1998). Residual displacement response spectrum, *Journal of Structural Engineering*, 124(5): 523-530.

Kent, D.C., and Park, R. (1971). Flexural members with confined concrete. *Journal of Structural Engineering*, 97(ST7): 1969-1990.

Kiremidjian, A.S., Hortacsu, A., and Williams, M. (2002). Implications of different site hazards on the highway network loss estimation. In *Proceedings of the Fourth China-Japan-USA Trilateral Symposium on Lifeline Earthquake Engineering*, October 28-31, 2002, Qindao, China.

Krawinkler, H. (2002). A general approach to seismic performance assessment. In *Proceedings of the International Conference on Advances and New Challenges in Earthquake Engineering Research*, August 19-20, 2002, Hong Kong.

Lee, K., and Foutch, D.A. (2002). Seismic performance evaluation of pre-Northridge steel frame buildings with brittle connections. *Journal of Structural Engineering*, 128(4): 546-555.

Luco, N., Cornell, C.A., and Yeo, G.L. (2001a). Annual limit-state frequencies for partially-inspected earthquake-damaged buildings, *In 8th International Conference on Structural Safety and Reliability*, June 2001, Newport Beach, California.

Luco, N. (2001b). *Probabilistic seismic demand analysis, SMRF connection fractures, and near source effects*. Ph.D. Dissertation. Dept. of Civil and Environmental Engineering, Stanford University, California.

Luco, N., Cornell, C.A. (2003). Structure-specific scalar intensity measures for near-source and ordinary earthquake ground motions. *Earthquake Spectra*. Resubmitted for publication, 2003.

Mackie, K., and Stojadinović, B. (2001). Probabilistic seismic demand model for California highway bridges. *Journal of Bridge Engineering*, 6(6): 468-481.

Mackie, K., and Stojadinović, B. (2002a). Optimal probabilistic seismic demand model for typical highway overpass bridges. In *Proceedings of the 12th European Conference on Earthquake Engineering*, September 9-13, 2002, London. Elsevier Science Ltd.

Mackie, K., and Stojadinović, B. (2002b). Design parameter sensitivity in probabilistic seismic demand models. In *Proceedings of the 7th US National Conference on Earthquake Engineering*, July 21-25, 2002, Boston, Massachusetts.

Mackie, K., and Stojadinović, B. (2002c). Relation between probabilistic seismic demand analysis and incremental dynamic analysis. In *Proceedings of the 7th US National Conference on Earthquake Engineering*, July 21-25, 2002, Boston, Massachusetts.

Mackie, K., and Stojadinović, B. (2003). *Seismic demands for performance-based design of bridges*. PEER Report No. 2003/16. Pacific Earthquake Engineering Research Center, University of California, Berkeley.

Mackie, K.R. (2004). *Fragility-based seismic decision making for highway overpass bridges*. Ph.D. Dissertation. Dept. of Civil and Environmental Engineering, University of California, Berkeley.

Mander, J.B., Priestley, M.J.N., and Park, R. (1988). Theoretical stress-strain model for confined concrete. *Journal of the Structural Engineering*, 114(ST8): 1804-1826.

Matlock, H. (1970) Correlations for design of laterally loaded piles in soft clay. In *Proceedings of the Second Annual Offshore Technology*, Houston, Texas, OTC 1204.

McKenna, F., and Fenves, G.L. (2000). An object-oriented software design for parallel structural analysis. In *Proceedings of the 2000 Structures Congress & Exposition: Advanced Technology in Structural Engineering*, May 8-10, 2000, Philadelphia, Pennsylvania.

Medina, R., Krawinkler, H., and Alavi, B. (2001). Seismic drift and ductility demands and their dependence on ground motions. In *Proceedings of the US-Japan Seminar on Advanced Stability and Seismicity Concepts for Performance-Based Design of Steel and Composite Structures*, July 23-27, 2001, Kyoto, Japan.

Mehanny, S.S.F., and Deierlein, G.G. (2001). Seismic damage and collapse assessment of composite moment frames. *Journal of Structural Engineering*, 127(9): 1045-1053.

Moore, J.E., Kiremidjian, A., and Chiu, S. (2000). *Seismic risk model for a designated highway system: Oakland/San Francisco Bay Area*. PEER Report No. 2002/02. U.S.-Japan

Workshop on the Effects of Near-Field Earthquake Shaking, March 20-21, 2000, San Francisco, California, 71-75. Pacific Earthquake Engineering Research Center, University of California, Berkeley.

Neuenhofer, A., and Filippou, F.C. (1998). Geometrically nonlinear flexibility-based frame finite element. *Journal of Structural Engineering*, 124(6): 704-711.

OpenSees. http://opensees.berkeley.edu. Web page.

Panagiotakos, T.B., and Fardis, M.N. (2001). Deformations of reinforced concrete members at yielding and ultimate. *ACI Structural Journal*, 98(2): 135-148.

Pantelides, C.P., Duffin, J.B., Ward, J., Delahanty, C., and Reaveley, L.D. (2002). In-situ tests at South Temple Bridge on Interstate 15. In *Proceedings of the 7th US National Conference on Earthquake Engineering*, July 21-25, 2002, Boston, Massachusetts.

PEER Capacity Catalog.

http://www.structures.ucsd.edu/PEER/CapacityCatalog/capacity catalog.html. Web page.

PEER SPD (Structural Performance Database). http://nisee.berkeley.edu/spd/. Web page.

PEER Strong Motion Catalog. http://peer.berkeley.edu/smcat. Web page.

Porter, K. (2002). Minutes and notes from PEER/Caltrans meetings, 2/27/02 and 5/14/02. California Department of Transportation and Pacific Earthquake Engineering Research Center.

RS Means. (2004). *Means Heavy Construction Cost Data 2004 Book*, 18th Edition. New York: RS Means.

Seed, H.B., Wong, R.T., Idriss, I.M, and Tokimatsu, K. (1984). *Moduli and damping factors for dynamic analyses of cohesionless soils*. Earthquake Engineering Research Center Report No. UCB/EERC 84/14. University of California, Berkeley.

Shin, Y.B., and Moehle, J.P.M. (2002). *Quarter-scale reinforced concrete specimen test*. Internal Report, University of California, Berkeley.

Shome, N., Cornell, C.A., Bazzurro, P., and Carballo, J.E. (1998). Earthquakes, records, and nonlinear responses. *Earthquake Spectra*, 14(3): 467-500.

Shome, N., and Cornell, C.A. (1999). *Probabilistic seismic demand analysis of nonlinear structures*. Reliability of Marine Structures Report No. RMS-35, Dept. of Civil and Envir. Engineering, Stanford University, California.

Tasai, A. (1999). *Residual axial capacity and restorability of reinforced concrete columns damaged due to earthquake*. PEER Report No. 1999/10: 191-202. Pacific Earthquake Engineering Research Center, University of California, Berkeley.

Tasai, A. (2000). *Residual axial capacity of reinforced concrete columns during shear degradation*. PEER Report No. 2000/10: 257-267. Pacific Earthquake Engineering Research Center, University of California, Berkeley.

Travasarou, T., Bray, J.D., and Abrahamson, N.A. (2003). Empirical attenuation relationship for Arias Intensity. *Journal of Earthquake Engineering and Structural Dynamics*, 32(7): 1133-1155.

USGS. National Seismic Hazard Mapping Project Zip Code Look-up for Ground Motion Values. http://eqint.cr.usgs.gov/eq/html/zipcode.shtml. Web page.

Vamvatsikos, D. and Cornell, C.A. (2002). Incremental dynamic analysis. *Earthquake Engineering and Structural Dynamics*, 31(3): 491-512.

Vardeman, S.B. (1994). *Statistics for Engineering Problem Solving*. Boston: PWS Publishing Co.

Vesic, A.S. (1961). Bending of beams resting on isotropic elastic solids. *Journal of Engineering Mechanics Division*, ASCE, 87(2): 35–53.

Von Thun, J.L., Rochim, L.H., Scott, G.A., and Wilson, J.A. (1988). Earthquake ground motions for design and analysis of dams. *Earthquake Engineering and Soil Dynamics II – Recent advances in ground motion evaluation*. New York: ASCE, 463-481.

Werner, S.D., Taylor, C.E., Sungbin, C., Lavoie, J-P., Huyck, C.K., Eitzel, C., Eguchi, R.T., and Moore, J.E. (2004). New developments in seismic risk analysis of highway systems. In *Proceedings of the 13th World Conference on Earthquake Engineering*, August 1-6 2004, Vancouver, Canada.

Yamazaki, F., Onishi, J., and Tayama, S. (1998). Damage estimation of highway structures due to earthquakes. In *Proceedings of Third China-Japan-US Trilateral Symposium on Lifeline Earthquake Engineering*, August 1998. Kunming China.

Yashinsky, M., and Ostrom, T. (2000). Caltrans' new seismic design criteria for bridges. *Earthquake Spectra*, 16(1): 285-307.

Yoshimura, M., and Nakamura, T. (2002). *Axial collapse of reinforced concrete short columns*. PEER Report No. 2002/21: 187-198. Pacific Earthquake Engineering Research Center, University of California, Berkeley.

Appendix Ground Motions

Specific information detailing all the ground motion records used in this study is contained in the tables of this appendix. The tables are separated according to bin. All of the records and record information were obtained from the PEER Strong Motion Catalog. Values of *PGA*, *PGV*, and *PGD* are shown for informational purposes only. In reality, values were calculated when the acceleration record was integrated by the *IM* processing routines.

Table A.1 LMSR ground motion bin record details

Record ID	Event	Year	M	R (km)	Station	Soil	Mechanism	fHP (Hz) x	y	z	fLP (Hz) x	y	z	PGA (g) x	y	z	PGV (cm/s) x	y	z
AGW	Loma Prieta	1989	6.9	28.2	Agnews State Hospital	D	reverse-oblique	0.20	0.20	0.20	30.0	30.0	42.0	0.159	0.172	0.093	17.6	26.0	8.3
CAP	Loma Prieta	1989	6.9	14.5	Capitola	D	reverse-oblique	0.20	0.20	0.20	40.0	48.0	50.0	0.443	0.529	0.541	29.3	36.5	19.4
G03	Loma Prieta	1989	6.9	14.4	Gilroy Array #3	D	reverse-oblique	0.10	0.10	0.10	40.0	33.0	50.0	0.367	0.555	0.338	44.7	35.7	15.5
G04	Loma Prieta	1989	6.9	16.1	Gilroy Array #4	D	reverse-oblique	0.20	0.20	0.20	30.0	28.0	42.0	0.212	0.417	0.159	37.9	38.8	14.6
GMR	Loma Prieta	1989	6.9	24.2	Gilroy Array #7	D	reverse-oblique	0.20	0.20	0.20	35.0	40.0	48.0	0.323	0.226	0.115	16.6	16.4	5.6
HCH	Loma Prieta	1989	6.9	28.2	Hollister City Hall	D	reverse-oblique	0.10	0.10	0.10	30.0	29.0	32.0	0.215	0.247	0.216	45.0	38.5	14.9
HDA	Loma Prieta	1989	6.9	25.8	Hollister Differential Array	D	reverse-oblique	0.10	0.10	0.10	33.0	40.0	38.0	0.279	0.269	0.154	35.6	43.9	8.4
SVL	Loma Prieta	1989	6.9	28.8	Sunnyvale - Colton Ave.	D	reverse-oblique	0.10	0.10	0.10	32.0	40.0	50.0	0.209	0.207	0.104	36.0	37.3	8.6
CNP	Northridge	1994	6.7	15.8	Canoga Park - Topanga Can.	D	reverse-slip	0.10	0.05	0.05	30.0	30.0	30.0	0.420	0.356	0.489	60.8	32.1	14.2
FAR	Northridge	1994	6.7	23.9	LA - N Faring Rd.	D	reverse-slip	0.13	0.13	0.20	30.0	30.0	30.0	0.242	0.273	0.191	29.8	15.8	8.9
FLE	Northridge	1994	6.7	29.5	LA - Fletcher Dr.	D	reverse-slip	0.15	0.13	0.30	30.0	30.0	30.0	0.240	0.162	0.109	26.2	10.7	6.9
GLP	Northridge	1994	6.7	25.4	Glendale - Las Palmas	D	reverse-slip	0.10	0.13	0.30	30.0	30.0	30.0	0.206	0.357	0.127	7.4	12.3	4.3
HOL	Northridge	1994	6.7	25.5	LA - Holywood Stor FF	D	reverse-slip	0.20	0.20	0.20	23.0	23.0	23.0	0.358	0.231	0.139	27.5	18.3	9.2
NYA	Northridge	1994	6.7	22.3	La Crescenta-New York	D	reverse-slip	0.10	0.30	0.13	30.0	30.0	30.0	0.159	0.178	0.106	11.3	12.5	3.9
LOS	Northridge	1994	6.7	13.0	Canyon Country - W Lost Cany	D	reverse-slip	0.10	0.05	0.20	30.0	30.0	30.0	0.482	0.410	0.318	45.1	43.0	20.3
RO3	Northridge	1994	6.7	12.3	Sun Valley - Roscoe Blvd	D	reverse-slip	0.10	0.10	0.10	30.0	30.0	30.0	0.443	0.303	0.306	38.2	22.1	12.5
PEL	San Fernando	1971	6.6	21.2	LA - Hollywood Stor Lot	D	reverse-slip	0.20	0.20	0.50	35.0	35.0	35.0	0.174	0.210	0.136	14.9	18.9	4.3
B-ICC	Superstition Hills	1987	6.7	13.9	El Centro Imp. Co. Cent	D	strike-slip	0.10	0.10	0.10	38.0	40.0	47.0	0.258	0.358	0.128	40.9	46.4	8.4
B-IVW	Superstition Hills	1987	6.7	24.4	Wildlife Liquef. Array	D	strike-slip	0.10	0.10	0.10	40.0	50.0	50.0	0.207	0.181	0.408	34.5	29.9	6.0
B-WSM	Superstition Hills	1987	6.7	13.3	Westmorland Fire Station	D	strike-slip	0.10	0.10	0.10	40.0	35.0	50.0	0.211	0.172	0.249	31.0	23.5	8.7

Given R is closest to fault rupture
red indicates hypocentral distance

Table A.2 LMLR ground motion bin record details

Record ID	Event	Year	M	R (km)	Station	Soil	Mechanism	fHP (Hz)			fLP (Hz)			PGA (g)			PGV (cm/s)		
								x	y	z	x	y	z	x	y	z	x	y	z
A-ELC	Borrego Mountain	1968	6.8	46.0	El Centro Array #9	D	strike-slip	0.20	0.20	0.20	12.8	12.5	16.4	0.057	0.130	0.030	13.2	26.3	3.3
A2E	Loma Prieta	1989	6.9	57.4	APEEL 2E Hayward Muir Sch.	D	reverse-oblique	0.20	0.20	0.20	25.0	30.0	40.0	0.139	0.171	0.095	11.5	13.7	3.8
FMS	Loma Prieta	1989	6.9	43.4	Fremont - Emerson Court	D	reverse-oblique	0.10	0.10	0.10	32.0	31.0	38.0	0.141	0.192	0.067	12.9	12.7	8.6
HVR	Loma Prieta	1989	6.9	31.6	Halls Valley	D	reverse-oblique	0.20	0.20	0.20	22.0	22.0	28.0	0.103	0.134	0.056	13.5	15.4	8.4
SJW	Loma Prieta	1989	6.9	32.6	Salinas - John & Work	D	reverse-oblique	0.10	0.10	0.10	28.0	30.0	42.0	0.112	0.091	0.101	15.7	10.7	6.7
SLC	Loma Prieta	1989	6.9	36.3	Palo Alto - SLAC Lab.	D	reverse-oblique	0.20	0.20	0.20	28.0	33.0	40.0	0.278	0.194	0.090	29.3	37.5	10.2
BAD	Northridge	1994	6.7	56.1	Covina - W. Badillo	D	reverse-slip	0.20	0.20	0.30	30.0	30.0	30.0	0.079	0.100	0.043	7.0	5.8	2.9
CAS	Northridge	1994	6.7	49.6	Compton - Castlegate St.	D	reverse-slip	0.20	0.20	0.40	30.0	30.0	30.0	0.136	0.088	0.046	7.1	6.8	2.6
CEN	Northridge	1994	6.7	30.9	LA - Centinela St.	D	reverse-slip	0.20	0.13	0.13	30.0	30.0	30.0	0.322	0.465	0.109	22.9	19.3	10.6
DEL	Northridge	1994	6.7	59.3	Lakewood - Del Amo Blvd.	D	reverse-slip	0.20	0.13	0.80	30.0	30.0	30.0	0.123	0.137	0.058	10.4	11.2	1.6
DWN	Northridge	1994	6.7	47.6	Downey - Co. Maint. Bldg.	D	reverse-slip	0.20	0.20	0.20	23.0	23.0	23.0	0.230	0.158	0.146	11.3	13.8	3.9
JAB	Northridge	1994	6.7	46.6	Bell Gardens - Jaboneria	D	reverse-slip	0.13	0.13	0.13	30.0	30.0	30.0	0.068	0.098	0.049	7.6	7.4	3.5
LH1	Northridge	1994	6.7	36.3	Lake Hughes #1	D	reverse-slip	0.12	0.12	0.12	23.0	23.0	23.0	0.077	0.087	0.099	9.5	9.4	7.0
LOA	Northridge	1994	6.7	42.4	Lawndale - Osage Ave.	D	reverse-slip	0.13	0.13	0.13	30.0	30.0	30.0	0.152	0.084	0.053	8.0	8.5	3.5
LV2	Northridge	1994	6.7	37.7	Leona Valley #2	D	reverse-slip	0.20	0.20	0.20	23.0	23.0	23.0	0.063	0.091	0.058	7.2	7.5	7.1
PHP	Northridge	1994	6.7	43.6	Palmdale - Hwy 14 & Palmdale	D	reverse-slip	0.20	0.20	0.20	46.0	46.0	46.0	0.067	0.061	0.040	16.9	14.8	8.0
PIC	Northridge	1994	6.7	32.7	LA - Pico & Sentous	D	reverse-slip	0.20	0.20	0.20	46.0	46.0	46.0	0.186	0.103	0.065	14.3	12.2	5.3
SOR	Northridge	1994	6.7	54.1	West Covina - S. Orange Ave.	D	reverse-slip	0.10	0.20	0.20	30.0	30.0	30.0	0.067	0.063	0.049	5.8	5.9	2.7
SSE	Northridge	1994	6.7	60.0	Terminal Island - S. Seaside	D	reverse-slip	0.13	0.13	0.13	30.0	30.0	30.0	0.194	0.133	0.048	12.1	13.7	3.1
VER	Northridge	1994	6.7	39.3	LA - E Vernon Ave.	D	reverse-slip	0.10	0.20	0.20	30.0	30.0	30.0	0.153	0.120	0.063	10.1	9.2	3.4

Given R is closest to fault rupture
red indicates hypocentral distance

Table A.3 SMSR ground motion bin record details

Record ID	Event	Year	M	R (km)	Station	Soil	Mechanism	fHP (Hz)			fLP (Hz)			PGA (g)			PGV (cm/s)		
								x	y	z	x	y	z	x	y	z	x	y	z
H-CAL	Imperial Valley	1979	6.5	23.8	Calipatria Fire Station	D	strike-slip	0.10	0.10	0.10	40.0	40.0	40.0	0.078	0.128	0.055	13.3	15.4	3.9
H-CHI	Imperial Valley	1979	6.5	28.7	Chihuahua	D	strike-slip	0.05	0.05	0.05	-	-	-	0.254	0.270	0.218	30.1	24.9	5.1
H-E01	Imperial Valley	1979	6.5	15.5	El Centro Array #1	D	strike-slip	0.10	0.10	0.10	40.0	40.0	40.0	0.134	0.139	0.056	10.7	16.0	3.8
H-E12	Imperial Valley	1979	6.5	18.2	El Centro Array #12	D	strike-slip	0.10	0.10	0.10	40.0	40.0	40.0	0.116	0.143	0.066	21.8	17.6	6.7
H-E13	Imperial Valley	1979	6.5	21.9	El Centro Array #13	D	strike-slip	0.20	0.20	0.20	40.0	40.0	40.0	0.139	0.117	0.046	13.0	14.7	3.2
H-WSM	Imperial Valley	1979	6.5	15.1	Westmorland Fire Station	D	strike-slip	0.10	0.10	0.10	40.0	40.0	40.0	0.110	0.074	0.082	21.9	21.2	6.8
A-SRM	Livermore	1980	5.8	21.7	San Ramon Fire Station	D	strike-slip	0.20	0.15	0.30	15.0	15.0	20.0	0.040	0.058	0.016	4.0	3.3	2.0
A-KOD	Livermore	1980	5.8	17.6	San Ramon - Eastman Kodak	D	strike-slip	0.20	0.08	0.40	20.0	20.0	30.0	0.076	0.154	0.042	6.1	18.9	2.8
M-AGW	Morgan Hill	1984	6.2	29.4	Agnews State Hospital	D	strike-slip	0.20	0.20	0.20	13.0	14.0	18.0	0.032	0.032	0.016	5.5	5.0	3.2
M-G02	Morgan Hill	1984	6.2	15.1	Gilroy Array #2	D	strike-slip	0.10	0.20	0.20	37.0	31.0	37.0	0.212	0.162	0.578	12.6	5.1	10.8
M-G03	Morgan Hill	1984	6.2	14.6	Gilroy Array #3	D	strike-slip	0.10	0.10	0.10	32.0	37.0	42.0	0.200	0.194	0.395	12.7	11.2	9.9
M-GMR	Morgan Hill	1984	6.2	14.0	Gilroy Array #7	D	strike-slip	0.10	0.10	0.10	30.0	31.0	40.0	0.113	0.190	0.428	6.0	7.4	5.4
PHN	Point Mugu	1973	5.8	25.0	Port Hueneme	D	reverse-slip	0.15	0.20	0.20	30.0	25.0	30.0	0.083	0.112	0.047	4.6	14.8	2.2
BRA	Westmorland	1981	5.8	22.0	5060 Brawley Airport	D	strike-slip	0.70	0.15	0.60	33.0	40.0	40.0	0.171	0.169	0.101	5.8	12.7	2.2
NIL	Westmorland	1981	5.8	19.4	724 Niland Fire Station	D	strike-slip	0.25	0.30	0.30	40.0	33.0	33.0	0.176	0.105	0.126	6.6	5.6	2.9
A-CAS	Whittier Narrows	1987	6.0	16.9	Compton - Castlegate St.	D	reverse	0.28	0.09	0.50	25.0	25.0	25.0	0.333	0.332	0.167	14.1	27.1	3.3
A-CAT	Whittier Narrows	1987	6.0	28.1	Carson - Catskill Ave.	D	reverse	0.55	0.18	0.50	25.0	25.0	25.0	0.059	0.042	0.037	2.4	3.8	1.3
A-DWN	Whittier Narrows	1987	6.0	18.3	14368 Downey - Co Maint Bldg	D	reverse	0.25	0.20	1.00	30.0	30.0	40.0	0.141	0.221	0.177	13.4	28.8	3.3
A-W70	Whittier Narrows	1987	6.0	16.3	LA - W 70th St.	D	reverse	0.20	0.30	0.30	25.0	25.0	25.0	0.151	0.198	0.077	8.7	19.5	2.8
A-WAT	Whittier Narrows	1987	6.0	24.5	Carson - Water St.	D	reverse	0.30	0.20	0.50	25.0	25.0	25.0	0.133	0.104	0.046	11.3	9.0	2.0

Given R is closest to fault rupture
red indicates hypocentral distance

Table A.4 SMLR ground motion bin record details

Record ID	Event	Year	M	R (km)	Station	Soil	Mechanism	fHP (Hz)			fLP (Hz)			PGA (g)			PGV (cm/s)		
								x	y	z	x	y	z	x	y	z	x	y	z
B-ELC	Borrego	1942	6.5	49.0	El Centro Array #9	D	unknown	0.10	0.10	0.10	15.0	15.0	20.0	0.044	0.068	0.033	4.0	3.9	1.1
H-C05	Coalinga	1983	6.4	47.3	Parkfield - Cholame 5W	D	reverse-oblique	0.20	0.20	0.50	22.0	22.0	30.0	0.131	0.147	0.034	10.0	10.8	2.3
H-C08	Coalinga	1983	6.4	50.7	Parkfield - Cholame 8W	D	reverse-oblique	0.50	0.20	0.20	21.0	23.0	27.0	0.100	0.098	0.024	8.0	8.6	3.3
H-CC4	Imperial Valley	1979	6.5	49.3	Coachella Canal #4	D	strike-slip	0.20	0.20	0.20	40.0	40.0	40.0	0.128	0.115	0.038	15.6	12.5	3.6
H-CMP	Imperial Valley	1979	6.5	32.6	Compuertas	D	strike-slip	0.20	0.20	0.20	-	-	-	0.147	0.186	0.075	9.5	13.9	2.9
H-DLT	Imperial Valley	1979	6.5	43.6	Delta	D	strike-slip	0.05	0.05	0.05	-	-	-	0.351	0.238	0.145	33.0	26.0	14.8
H-NIL	Imperial Valley	1979	6.5	35.9	Niland Fire Station	D	strike-slip	0.10	0.10	0.10	40.0	30.0	40.0	0.069	0.109	0.034	8.3	11.9	3.8
H-PLS	Imperial Valley	1979	6.5	31.7	Plaster City	D	strike-slip	0.10	0.10	0.10	40.0	40.0	40.0	0.057	0.042	0.026	5.4	3.2	2.4
H-VCT	Imperial Valley	1979	6.5	54.1	Victoria	D	strike-slip	0.20	0.05	0.05	-	-	-	0.167	0.122	0.059	8.3	6.4	1.6
A-STP	Livermore	1980	5.8	37.3	Tracy - Sewage Treatment Plant	D	strike-slip	0.08	0.15	0.20	15.0	20.0	20.0	0.073	0.050	0.021	7.6	7.5	3.1
M-CAP	Morgan Hill	1984	6.2	38.1	Capitola	D	strike-slip	0.20	0.20	0.20	28.0	30.0	35.0	0.142	0.099	0.045	8.1	4.9	2.1
M-HCH	Morgan Hill	1984	6.2	32.5	Hollister City Hall	D	strike-slip	0.20	0.20	0.20	24.0	19.0	25.0	0.071	0.071	0.118	9.0	7.4	3.9
M-SJB	Morgan Hill	1984	6.2	30.3	San Juan Bautista	C	strike-slip	0.10	0.10	0.10	21.0	21.0	21.0	0.036	0.044	0.052	4.4	4.3	2.7
H06	N. Palm Springs	1986	6.0	39.6	San Jacinto Valley Cemetery	D	strike-slip	0.20	0.20	0.50	31.0	38.0	40.0	0.063	0.069	0.053	4.4	3.1	1.8
INO	N. Palm Springs	1986	6.0	39.6	Indio	D	strike-slip	0.10	0.10	0.10	35.0	35.0	40.0	0.117	0.064	0.087	12.3	6.6	3.1
A-BIR	Whittier Narrows	1987	6.0	56.8	Downey - Birchdale	D	reverse	0.15	0.28	0.60	25.0	25.0	25.0	0.299	0.243	0.230	37.8	13.7	4.1
A-CTS	Whittier Narrows	1987	6.0	31.3	LA - Century City CC South	D	reverse	0.30	0.20	0.40	25.0	25.0	30.0	0.063	0.051	0.021	5.4	3.5	1.7
A-HAR	Whittier Narrows	1987	6.0	34.2	LB - Harbor Admin FF	D	reverse	0.25	0.60	0.20	25.0	30.0	25.0	0.071	0.058	0.028	7.3	4.1	1.6
A-SSE	Whittier Narrows	1987	6.0	35.7	Terminal Island - S. Seaside	D	reverse	0.28	0.20	0.28	25.0	25.0	25.0	0.041	0.042	0.021	3.1	3.9	1.2
A-STC	Whittier Narrows	1987	6.0	39.8	Northridge - Saticoy St.	D	reverse	0.20	0.23	0.25	25.0	25.0	25.0	0.118	0.161	0.084	5.1	8.4	2.4

Given R is closest to fault rupture
red indicates hypocentral distance
Borrego magnitude not from Silva database

Table A.5 Near (field) ground motion bin record details

Record ID	Event	Year	M	R (km)	Station	Soil	Mechanism	fHP (Hz) x	y	z	fLP (Hz) x	y	z	PGA (g) x	y	z	PGV (cm/s) x	y	z
I-ELC	Imperial Valley	1940	7.0	8.3	El Centro Array #9	D	strike-slip	0.20	0.20	0.20	15.0	15.0	15.0	0.215	0.313	0.205	30.2	29.8	10.7
C08	Parkfield	1966	6.1	5.3	Cholame #8	D	strike-slip	0.20	0.20	0.20	20.0	20.0	24.0	0.273	0.246	0.116	11.3	10.2	4.3
H-AEP	Imperial Valley	1979	6.5	8.5	Aeropuerto Mexicali	D	strike-slip	0.20	0.20	0.20	-	-	-	0.260	0.327	0.142	24.9	42.8	5.6
H-BCR	Imperial Valley	1979	6.5	2.5	Bonds Corner	D	strike-slip	0.10	0.10	0.10	40.0	40.0	40.0	0.775	0.588	0.425	45.9	45.2	12.2
H-CXO	Imperial Valley	1979	6.5	10.6	Calexico Fire Station	D	strike-slip	0.20	0.10	0.10	40.0	40.0	40.0	0.202	0.275	0.187	16.0	21.2	6.7
H-ECC	Imperial Valley	1979	6.5	7.6	EC County Center FF	D	strike-slip	0.10	0.10	0.10	35.0	40.0	50.0	0.235	0.213	0.246	68.8	37.5	18.1
H-E05	Imperial Valley	1979	6.5	1.0	El Centro Array #5	D	strike-slip	0.10	0.10	0.10	40.0	40.0	40.0	0.379	0.519	0.537	90.5	46.9	38.5
H-SHP	Imperial Valley	1979	6.5	11.1	SAHOP Casa Flores	D	strike-slip	0.20	0.20	0.20	-	-	-	0.506	0.287	0.379	30.9	19.6	9.2
H-PVP	Coalinga	1983	6.4	8.5	Pleasant Valley P.P. - bldg	D	reverse-oblique	0.20	0.20	0.20	22.0	20.0	30.0	0.285	0.380	0.206	19.1	32.4	12.3
M-HVR	Morgan Hill	1984	6.2	3.4	Halls Valley	D	strike-slip	0.20	0.20	0.20	30.0	26.0	28.0	0.312	0.156	0.110	39.4	12.5	12.2
A-JAB	Whittier Narrows	1987	6.0	9.8	Bell Gardens - Jaboneria	D	reverse-slip	0.10	0.25	0.40	25.0	25.0	25.0	0.212	0.219	0.095	21.8	18.9	2.7
A-SOR	Whittier Narrows	1987	6.0	10.5	West Covina - S. Orange Ave.	D	reverse-slip	0.23	0.23	0.50	25.0	25.0	25.0	0.179	0.137	0.131	7.0	10.6	3.7
GOF	Loma Prieta	1989	6.9	12.7	Gilroy - Historic Bldg.	D	reverse-oblique	0.20	0.20	0.20	40.0	38.0	52.0	0.241	0.284	0.149	24.0	42.0	11.1
G02	Loma Prieta	1989	6.9	12.7	Gilroy Array #2	D	reverse-oblique	0.20	0.20	0.20	31.0	40.0	40.0	0.322	0.367	0.294	39.1	32.9	14.6
JEN	Northridge	1994	6.7	6.2	Jensen Filter Plant	D	reverse-slip	0.20	0.08	0.30	-	-	-	0.593	0.424	0.400	99.3	106.2	34.1
NWH	Northridge	1994	6.7	7.1	Newhall - Fire Station	D	reverse-slip	0.12	0.12	0.12	23.0	23.0	23.0	0.590	0.583	0.548	97.2	75.5	31.5
RRS	Northridge	1994	6.7	7.1	Rinaldi Receiving Station	D	reverse-slip	-	-	-	-	-	-	0.472	0.838	0.852	73.0	166.1	50.7
SPV	Northridge	1994	6.7	8.9	Sepulveda VA	D	reverse-slip	0.00	0.10	0.10	-	-	-	0.939	0.753	0.467	76.6	84.8	33.2
SCS	Northridge	1994	6.7	6.2	Sylmar - Converter Station	D	reverse-slip	-	-	-	-	-	-	0.897	0.612	0.586	102.8	117.4	34.6
SYL	Northridge	1994	6.7	6.4	Sylmar - Olive View Med FF	D	reverse-slip	0.12	0.12	0.12	23.0	23.0	23.0	0.843	0.604	0.535	129.6	78.2	19.1

Given R is closest to fault rupture
red indicates hypocentral distance

Table A.6 PEER aftershock ground motion bin record details

Record ID	Event	Year	M	R (km)	Station	Soil	Mechanism	fHP (Hz)			fLP (Hz)			PGA (g)			PGV (cm/s)		
								x	y	z	x	y	z	x	y	z	x	y	z
A-BPL	Chalfant Valley	1986	6.2	23.0	Bishop - Paradise Lodge	A	strike-slip	0.10	0.20	0.10	40.0	30.0	50.0	0.161	0.165	0.127	12.4	4.9	5.9
A-LAD	Chalfant Valley	1986	6.2	9.2	Bishop - LADWP South St	D	strike-slip	0.10	0.10	0.10	30.0	40.0	40.0	0.175	0.248	0.140	19.4	19.2	6.7
A-ZAK	Chalfant Valley	1986	6.2	18.7	Zack Brothers Ranch	D	strike-slip	0.10	0.10	0.20	33.0	33.0	50.0	0.400	0.447	0.321	44.5	36.9	12.5
C-LAD	Chalfant Valley	1986	5.6	14.0	Bishop - LADWP South St	D	strike-slip	0.30	0.23	0.40	20.0	25.0	40.0	0.070	0.106	0.057	6.5	4.9	2.2
F-CHP	Coalinga	1983	5.2	12.7	46T04 CHP	D	reverse normal	0.10	0.30	0.30	40.0	40.0	40.0	0.733	0.431	0.332	37.6	18.7	8.4
F-CSU	Coalinga	1983	5.2	14.7	Sulphur Baths	A	reverse normal	0.30	0.30	0.40	25.0	30.0	30.0	0.230	0.152	0.139	10.9	8.5	6.5
A-BCR	Imperial Valley	1979	5.2	15.6	Bonds Corner	D	strike-slip	0.30	0.80	3.00	30.0	30.0	35.0	0.100	0.084	0.052	8.2	3.6	0.9
A-E04	Imperial Valley	1979	5.2	14.4	El Centro Array #4	D	strike-slip	0.45	0.50	0.60	35.0	40.0	40.0	0.157	0.262	0.097	35.0	40.0	40.0
A-E05	Imperial Valley	1979	5.2	13.8	El Centro Array #5	D	strike-slip	0.60	0.70	0.50	35.0	35.0	50.0	0.239	0.238	0.079	13.3	10.7	0.1
A-E06	Imperial Valley	1979	5.2	13.1	El Centro Array #6	D	strike-slip	0.35	0.60	0.40	30.0	30.0	50.0	0.366	0.189	0.080	20.8	12.1	1.7
A-HVP	Imperial Valley	1979	5.2	12.2	Holtville Post Office	D	strike-slip	0.50	0.60	0.80	30.0	30.0	40.0	0.211	0.127	0.044	15.4	7.3	1.0
B-LFA	Livermore	1980	5.4	3.6	Fagundas Ranch	D	strike-slip	0.30	0.30	0.30	20.0	25.0	30.0	0.233	0.258	0.098	11.4	9.6	2.5
B-LMO	Livermore	1980	5.4	8.0	Livermore - Morgan Terr Park	C	strike-slip	0.40	0.25	0.40	30.0	30.0	30.0	0.252	0.198	0.078	9.8	11.7	4.1
J-CVK	Mammoth Lakes	1980	5.7	16.3	Convict Creek	D	strike-slip	0.50	0.50	0.50	35.0	35.0	47.0	0.178	0.160	0.129	12.2	11.3	9.0
J-MLS	Mammoth Lakes	1980	5.7	14.2	Mammoth Lakes H.S.	D	strike-slip	0.10	0.50	0.10	52.0	50.0	60.0	0.390	0.442	0.264	23.9	22.5	9.0
B-CVK	Mammoth Lakes	1980	5.7	3.0	Convict Creek	D	strike-slip	0.20	0.20	0.20	35.0	35.0	40.0	0.432	0.380	0.345	21.0	13.3	6.2
C-FIS	Mammoth Lakes	1980	4.9	5.5	Fish & Game	D	strike-slip	0.11	0.20	0.20	40.0	50.0	50.0	0.098	0.103	0.038	5.2	4.2	1.7
C-XGR	Mammoth Lakes	1980	4.9	4.7	3 Green Church	D	strike-slip	0.30	0.25	0.80	30.0	25.0	30.0	0.170	0.167	0.079	12.1	10.7	2.2
G-CVK	Mammoth Lakes	1983	5.4	10.8	Convict Creek	D	strike-slip	0.20	0.40	0.30	30.0	30.0	40.0	0.101	0.150	0.073	7.1	8.4	5.7
D-DWR	Oroville	1975	4.7	6.5	DWR Garage	A	Normal	3.00	1.50	5.00	40.0	50.0	40.0	0.209	0.141	0.106	1.8	1.1	0.7

Given R is closest to fault rupture
red indicates hypocentral distance

PEER REPORTS

PEER reports are available from the National Information Service for Earthquake Engineering (NISEE). To order PEER reports, please contact the Pacific Earthquake Engineering Research Center, 1301 South 46th Street, Richmond, California 94804-4698. Tel.: (510) 231-9468; Fax: (510) 231-9 461.

PEER 2005/12   *PEER Testbed Study on a Laboratory Building: Exercising Seismic Performance Assessment.* Mary C. Comerio, editor. November 2005.

PEER 2005/11   *Van Nuys Hotel Building Testbed Report: Exercising Seismic Performance Assessment.* Helmut Krawinkler, editor. October 2005.

PEER 2005/10   *First NEES/E-Defense Workshop on Collapse Simulation of Reinforced Concrete Building Structures.* September 2005.

PEER 2005/06   *Global Collapse of Frame Structures under Seismic Excitations.* Luis F. Ibarra and Helmut Krawinkler. September 2005.

PEER 2005/02   *Fragility Basis for California Highway Overpass Bridge Seismic Decision Making.* Kevin R. Mackie and Bozidar Stojadinovic. June 2005.

PEER 2005/01   *Empirical Characterization of Site Conditions on Strong Ground Motion.*   Jonathan P. Stewart, Yoojoong Choi, and Robert W. Graves. June 2005.

PEER 2004/09   *Electrical Substation Equipment Interaction: Experimental Rigid Conductor Studies.*   Christopher Stearns and André Filiatrault. February 2005.

PEER 2004/08   *Seismic Qualification and Fragility Testing of Line Break 550-kV Disconnect Switches.* Shakhzod M. Takhirov, Gregory L. Fenves, and Eric Fujisaki. January 2005.

PEER 2004/07   *Ground Motions for Earthquake Simulator Qualification of Electrical Substation Equipment.* Shakhzod M. Takhirov, Gregory L. Fenves, Eric Fujisaki, and Don Clyde. January 2005.

PEER 2004/06   *Performance-Based Regulation and Regulatory Regimes.* Peter J. May and Chris Koski.   September 2004.

PEER 2004/05   *Performance-Based Seismic Design Concepts and Implementation: Proceedings of an International Workshop.* Peter Fajfar and Helmut Krawinkler, editors. September 2004.

PEER 2004/04   *Seismic Performance of an Instrumented Tilt-up Wall Building.* James C. Anderson and Vitelmo V. Bertero. July 2004.

PEER 2004/03   *Evaluation and Application of Concrete Tilt-up Assessment Methodologies.* Timothy Graf and James O. Malley. October 2004.

PEER 2004/02   *Analytical Investigations of New Methods for Reducing Residual Displacements of Reinforced Concrete Bridge Columns.* Junichi Sakai and Stephen A. Mahin. August 2004.

PEER 2004/01   *Seismic Performance of Masonry Buildings and Design Implications.* Kerri Anne Taeko Tokoro, James C. Anderson, and Vitelmo V. Bertero. February 2004.

PEER 2003/18   *Performance Models for Flexural Damage in Reinforced Concrete Columns.* Michael Berry and Marc Eberhard. August 2003.

PEER 2003/17   *Predicting Earthquake Damage in Older Reinforced Concrete Beam-Column Joints.* Catherine Pagni and Laura Lowes. October 2004.

PEER 2003/16   *Seismic Demands for Performance-Based Design of Bridges.* Kevin Mackie and Božidar Stojadinovic.   August 2003.

PEER 2003/15   *Seismic Demands for Nondeteriorating Frame Structures and Their Dependence on Ground Motions.* Ricardo Antonio Medina and Helmut Krawinkler. May 2004.

PEER 2003/14   *Finite Element Reliability and Sensitivity Methods for Performance-Based Earthquake Engineering.* Terje Haukaas and Armen Der Kiureghian. April 2004.

PEER 2003/13   *Effects of Connection Hysteretic Degradation on the Seismic Behavior of Steel Moment-Resisting Frames.* Janise E. Rodgers and Stephen A. Mahin. March 2004.

PEER 2003/12 *Implementation Manual for the Seismic Protection of Laboratory Contents: Format and Case Studies.* William T. Holmes and Mary C. Comerio. October 2003.

PEER 2003/11 *Fifth U.S.-Japan Workshop on Performance-Based Earthquake Engineering Methodology for Reinforced Concrete Building Structures.* February 2004.

PEER 2003/10 *A Beam-Column Joint Model for Simulating the Earthquake Response of Reinforced Concrete Frames.* Laura N. Lowes, Nilanjan Mitra, and Arash Altoontash. February 2004.

PEER 2003/09 *Sequencing Repairs after an Earthquake: An Economic Approach.* Marco Casari and Simon J. Wilkie. April 2004.

PEER 2003/08 *A Technical Framework for Probability-Based Demand and Capacity Factor Design (DCFD) Seismic Formats.* Fatemeh Jalayer and C. Allin Cornell. November 2003.

PEER 2003/07 *Uncertainty Specification and Propagation for Loss Estimation Using FOSM Methods.* Jack W. Baker and C. Allin Cornell. September 2003.

PEER 2003/06 *Performance of Circular Reinforced Concrete Bridge Columns under Bidirectional Earthquake Loading.* Mahmoud M. Hachem, Stephen A. Mahin, and Jack P. Moehle. February 2003.

PEER 2003/05 *Response Assessment for Building-Specific Loss Estimation.* Eduardo Miranda and Shahram Taghavi. September 2003.

PEER 2003/04 *Experimental Assessment of Columns with Short Lap Splices Subjected to Cyclic Loads.* Murat Melek, John W. Wallace, and Joel Conte. April 2003.

PEER 2003/03 *Probabilistic Response Assessment for Building-Specific Loss Estimation.* Eduardo Miranda and Hesameddin Aslani. September 2003.

PEER 2003/02 *Software Framework for Collaborative Development of Nonlinear Dynamic Analysis Program.* Jun Peng and Kincho H. Law. September 2003.

PEER 2003/01 *Shake Table Tests and Analytical Studies on the Gravity Load Collapse of Reinforced Concrete Frames.* Kenneth John Elwood and Jack P. Moehle. November 2003.

PEER 2002/24 *Performance of Beam to Column Bridge Joints Subjected to a Large Velocity Pulse.* Natalie Gibson, André Filiatrault, and Scott A. Ashford. April 2002.

PEER 2002/23 *Effects of Large Velocity Pulses on Reinforced Concrete Bridge Columns.* Greg L. Orozco and Scott A. Ashford. April 2002.

PEER 2002/22 *Characterization of Large Velocity Pulses for Laboratory Testing.* Kenneth E. Cox and Scott A. Ashford. April 2002.

PEER 2002/21 *Fourth U.S.-Japan Workshop on Performance-Based Earthquake Engineering Methodology for Reinforced Concrete Building Structures.* December 2002.

PEER 2002/20 *Barriers to Adoption and Implementation of PBEE Innovations.* Peter J. May. August 2002.

PEER 2002/19 *Economic-Engineered Integrated Models for Earthquakes: Socioeconomic Impacts.* Peter Gordon, James E. Moore II, and Harry W. Richardson. July 2002.

PEER 2002/18 *Assessment of Reinforced Concrete Building Exterior Joints with Substandard Details.* Chris P. Pantelides, Jon Hansen, Justin Nadauld, and Lawrence D. Reaveley. May 2002.

PEER 2002/17 *Structural Characterization and Seismic Response Analysis of a Highway Overcrossing Equipped with Elastomeric Bearings and Fluid Dampers: A Case Study.* Nicos Makris and Jian Zhang. November 2002.

PEER 2002/16 *Estimation of Uncertainty in Geotechnical Properties for Performance-Based Earthquake Engineering.* Allen L. Jones, Steven L. Kramer, and Pedro Arduino. December 2002.

PEER 2002/15 *Seismic Behavior of Bridge Columns Subjected to Various Loading Patterns.* Asadollah Esmaeily-Gh. and Yan Xiao. December 2002.

PEER 2002/14 *Inelastic Seismic Response of Extended Pile Shaft Supported Bridge Structures.* T.C. Hutchinson, R.W. Boulanger, Y.H. Chai, and I.M. Idriss. December 2002.

PEER 2002/13 *Probabilistic Models and Fragility Estimates for Bridge Components and Systems.* Paolo Gardoni, Armen Der Kiureghian, and Khalid M. Mosalam. June 2002.

PEER 2002/12   *Effects of Fault Dip and Slip Rake on Near-Source Ground Motions: Why Chi-Chi Was a Relatively Mild M7.6 Earthquake.* Brad T. Aagaard, John F. Hall, and Thomas H. Heaton. December 2002.

PEER 2002/11   *Analytical and Experimental Study of Fiber-Reinforced Strip Isolators.* James M. Kelly and Shakhzod M. Takhirov. September 2002.

PEER 2002/10   *Centrifuge Modeling of Settlement and Lateral Spreading with Comparisons to Numerical Analyses.* Sivapalan Gajan and Bruce L. Kutter. January 2003.

PEER 2002/09   *Documentation and Analysis of Field Case Histories of Seismic Compression during the 1994 Northridge, California, Earthquake.* Jonathan P. Stewart, Patrick M. Smith, Daniel H. Whang, and Jonathan D. Bray. October 2002.

PEER 2002/08   *Component Testing, Stability Analysis and Characterization of Buckling-Restrained Unbonded Braces^{TM}.* Cameron Black, Nicos Makris, and Ian Aiken. September 2002.

PEER 2002/07   *Seismic Performance of Pile-Wharf Connections.* Charles W. Roeder, Robert Graff, Jennifer Soderstrom, and Jun Han Yoo. December 2001.

PEER 2002/06   *The Use of Benefit-Cost Analysis for Evaluation of Performance-Based Earthquake Engineering Decisions.* Richard O. Zerbe and Anthony Falit-Baiamonte. September 2001.

PEER 2002/05   *Guidelines, Specifications, and Seismic Performance Characterization of Nonstructural Building Components and Equipment.* André Filiatrault, Constantin Christopoulos, and Christopher Stearns. September 2001.

PEER 2002/04   *Consortium of Organizations for Strong-Motion Observation Systems and the Pacific Earthquake Engineering Research Center Lifelines Program: Invited Workshop on Archiving and Web Dissemination of Geotechnical Data, 4–5 October 2001.* September 2002.

PEER 2002/03   *Investigation of Sensitivity of Building Loss Estimates to Major Uncertain Variables for the Van Nuys Testbed.* Keith A. Porter, James L. Beck, and Rustem V. Shaikhutdinov. August 2002.

PEER 2002/02   *The Third U.S.-Japan Workshop on Performance-Based Earthquake Engineering Methodology for Reinforced Concrete Building Structures.* July 2002.

PEER 2002/01   *Nonstructural Loss Estimation: The UC Berkeley Case Study.* Mary C. Comerio and John C. Stallmeyer. December 2001.

PEER 2001/16   *Statistics of SDF-System Estimate of Roof Displacement for Pushover Analysis of Buildings.* Anil K. Chopra, Rakesh K. Goel, and Chatpan Chintanapakdee. December 2001.

PEER 2001/15   *Damage to Bridges during the 2001 Nisqually Earthquake.* R. Tyler Ranf, Marc O. Eberhard, and Michael P. Berry. November 2001.

PEER 2001/14   *Rocking Response of Equipment Anchored to a Base Foundation.* Nicos Makris and Cameron J. Black. September 2001.

PEER 2001/13   *Modeling Soil Liquefaction Hazards for Performance-Based Earthquake Engineering.* Steven L. Kramer and Ahmed-W. Elgamal. February 2001.

PEER 2001/12   *Development of Geotechnical Capabilities in OpenSees.* Boris Jeremi . September 2001.

PEER 2001/11   *Analytical and Experimental Study of Fiber-Reinforced Elastomeric Isolators.* James M. Kelly and Shakhzod M. Takhirov. September 2001.

PEER 2001/10   *Amplification Factors for Spectral Acceleration in Active Regions.* Jonathan P. Stewart, Andrew H. Liu, Yoojoong Choi, and Mehmet B. Baturay. December 2001.

PEER 2001/09   *Ground Motion Evaluation Procedures for Performance-Based Design.* Jonathan P. Stewart, Shyh-Jeng Chiou, Jonathan D. Bray, Robert W. Graves, Paul G. Somerville, and Norman A. Abrahamson. September 2001.

PEER 2001/08   *Experimental and Computational Evaluation of Reinforced Concrete Bridge Beam-Column Connections for Seismic Performance.* Clay J. Naito, Jack P. Moehle, and Khalid M. Mosalam. November 2001.

PEER 2001/07   *The Rocking Spectrum and the Shortcomings of Design Guidelines.* Nicos Makris and Dimitrios Konstantinidis. August 2001.

PEER 2001/06   *Development of an Electrical Substation Equipment Performance Database for Evaluation of Equipment Fragilities.* Thalia Agnanos. April 1999.

PEER 2001/05   *Stiffness Analysis of Fiber-Reinforced Elastomeric Isolators.* Hsiang-Chuan Tsai and James M. Kelly. May 2001.

PEER 2001/04   *Organizational and Societal Considerations for Performance-Based Earthquake Engineering.* Peter J. May. April 2001.

PEER 2001/03   *A Modal Pushover Analysis Procedure to Estimate Seismic Demands for Buildings: Theory and Preliminary Evaluation.* Anil K. Chopra and Rakesh K. Goel. January 2001.

PEER 2001/02   *Seismic Response Analysis of Highway Overcrossings Including Soil-Structure Interaction.* Jian Zhang and Nicos Makris. March 2001.

PEER 2001/01   *Experimental Study of Large Seismic Steel Beam-to-Column Connections.* Egor P. Popov and Shakhzod M. Takhirov. November 2000.

PEER 2000/10   *The Second U.S.-Japan Workshop on Performance-Based Earthquake Engineering Methodology for Reinforced Concrete Building Structures.* March 2000.

PEER 2000/09   *Structural Engineering Reconnaissance of the August 17, 1999 Earthquake: Kocaeli (Izmit), Turkey.* Halil Sezen, Kenneth J. Elwood, Andrew S. Whittaker, Khalid Mosalam, John J. Wallace, and John F. Stanton. December 2000.

PEER 2000/08   *Behavior of Reinforced Concrete Bridge Columns Having Varying Aspect Ratios and Varying Lengths of Confinement.* Anthony J. Calderone, Dawn E. Lehman, and Jack P. Moehle. January 2001.

PEER 2000/07   *Cover-Plate and Flange-Plate Reinforced Steel Moment-Resisting Connections.* Taejin Kim, Andrew S. Whittaker, Amir S. Gilani, Vitelmo V. Bertero, and Shakhzod M. Takhirov. September 2000.

PEER 2000/06   *Seismic Evaluation and Analysis of 230-kV Disconnect Switches.* Amir S. J. Gilani, Andrew S. Whittaker, Gregory L. Fenves, Chun-Hao Chen, Henry Ho, and Eric Fujisaki. July 2000.

PEER 2000/05   *Performance-Based Evaluation of Exterior Reinforced Concrete Building Joints for Seismic Excitation.* Chandra Clyde, Chris P. Pantelides, and Lawrence D. Reaveley. July 2000.

PEER 2000/04   *An Evaluation of Seismic Energy Demand: An Attenuation Approach.* Chung-Che Chou and Chia-Ming Uang. July 1999.

PEER 2000/03   *Framing Earthquake Retrofitting Decisions: The Case of Hillside Homes in Los Angeles.* Detlof von Winterfeldt, Nels Roselund, and Alicia Kitsuse. March 2000.

PEER 2000/02   *U.S.-Japan Workshop on the Effects of Near-Field Earthquake Shaking.* Andrew Whittaker, ed. July 2000.

PEER 2000/01   *Further Studies on Seismic Interaction in Interconnected Electrical Substation Equipment.* Armen Der Kiureghian, Kee-Jeung Hong, and Jerome L. Sackman. November 1999.

PEER 1999/14   *Seismic Evaluation and Retrofit of 230-kV Porcelain Transformer Bushings.* Amir S. Gilani, Andrew S. Whittaker, Gregory L. Fenves, and Eric Fujisaki. December 1999.

PEER 1999/13   *Building Vulnerability Studies: Modeling and Evaluation of Tilt-up and Steel Reinforced Concrete Buildings.* John W. Wallace, Jonathan P. Stewart, and Andrew S. Whittaker, editors. December 1999.

PEER 1999/12   *Rehabilitation of Nonductile RC Frame Building Using Encasement Plates and Energy-Dissipating Devices.* Mehrdad Sasani, Vitelmo V. Bertero, James C. Anderson. December 1999.

PEER 1999/11   *Performance Evaluation Database for Concrete Bridge Components and Systems under Simulated Seismic Loads.* Yael D. Hose and Frieder Seible. November 1999.

PEER 1999/10   *U.S.-Japan Workshop on Performance-Based Earthquake Engineering Methodology for Reinforced Concrete Building Structures.* December 1999.

PEER 1999/09   *Performance Improvement of Long Period Building Structures Subjected to Severe Pulse-Type Ground Motions.* James C. Anderson, Vitelmo V. Bertero, and Raul Bertero. October 1999.

PEER 1999/08   *Envelopes for Seismic Response Vectors.* Charles Menun and Armen Der Kiureghian. July 1999.

PEER 1999/07   *Documentation of Strengths and Weaknesses of Current Computer Analysis Methods for Seismic Performance of Reinforced Concrete Members.* William F. Cofer. November 1999.

PEER 1999/06   *Rocking Response and Overturning of Anchored Equipment under Seismic Excitations.* Nicos Makris and Jian Zhang. November 1999.

PEER 1999/05   *Seismic Evaluation of 550 kV Porcelain Transformer Bushings.* Amir S. Gilani, Andrew S. Whittaker, Gregory L. Fenves, and Eric Fujisaki. October 1999.

PEER 1999/04   *Adoption and Enforcement of Earthquake Risk-Reduction Measures.* Peter J. May, Raymond J. Burby, T. Jens Feeley, and Robert Wood.

PEER 1999/03   *Task 3 Characterization of Site Response General Site Categories.* Adrian Rodriguez-Marek, Jonathan D. Bray, and Norman Abrahamson. February 1999.

PEER 1999/02   *Capacity-Demand-Diagram Methods for Estimating Seismic Deformation of Inelastic Structures: SDF Systems.* Anil K. Chopra and Rakesh Goel. April 1999.

PEER 1999/01   *Interaction in Interconnected Electrical Substation Equipment Subjected to Earthquake Ground Motions.* Armen Der Kiureghian, Jerome L. Sackman, and Kee-Jeung Hong. February 1999.

PEER 1998/08   *Behavior and Failure Analysis of a Multiple-Frame Highway Bridge in the 1994 Northridge Earthquake.* Gregory L. Fenves and Michael Ellery. December 1998.

PEER 1998/07   *Empirical Evaluation of Inertial Soil-Structure Interaction Effects.* Jonathan P. Stewart, Raymond B. Seed, and Gregory L. Fenves. November 1998.

PEER 1998/06   *Effect of Damping Mechanisms on the Response of Seismic Isolated Structures.* Nicos Makris and Shih-Po Chang. November 1998.

PEER 1998/05   *Rocking Response and Overturning of Equipment under Horizontal Pulse-Type Motions.* Nicos Makris and Yiannis Roussos. October 1998.

PEER 1998/04   *Pacific Earthquake Engineering Research Invitational Workshop Proceedings, May 14–15, 1998: Defining the Links between Planning, Policy Analysis, Economics and Earthquake Engineering.* Mary Comerio and Peter Gordon. September 1998.

PEER 1998/03   *Repair/Upgrade Procedures for Welded Beam to Column Connections.* James C. Anderson and Xiaojing Duan. May 1998.

PEER 1998/02   *Seismic Evaluation of 196 kV Porcelain Transformer Bushings.* Amir S. Gilani, Juan W. Chavez, Gregory L. Fenves, and Andrew S. Whittaker. May 1998.

PEER 1998/01   *Seismic Performance of Well-Confined Concrete Bridge Columns.* Dawn E. Lehman and Jack P. Moehle. December 2000.